ZDES simulations of propulsive jets : physical analysis and influence of upstream turbulence

Jonas Verrière

Doctoral dissertation of UNIVERSITÉ PIERRE ET MARIE CURIE

Doctoral School of « Mechanics, Acoustics, Electronics and Robotics »
Field : **Fluid Mechanics**

Presented by

Jonas Verrière

Submitted in partial fulfillment of the requirements for the degree of :

Doctor of UNIVERSITÉ PIERRE ET MARIE CURIE

ZDES simulations of propulsive jets: Physical analysis and influence of upstream turbulence

---

Defended on September 23, 2016 in front of the committee composed of :

Dr. Christophe BOGEY	**LMFA, École Centrale Lyon**	**Reviewer**
Pr. Éric LAMBALLAIS	**Insitut PPrime, Université de Poitiers**	**Reviewer**
Pr. Jean-Christophe ROBINET	**DynFluid, Arts et Métiers ParisTech**	**Examiner**
Pr. José-Maria FULLANA	**IJLRA, Université Pierre et Marie Curie**	**Examiner**
Dr. Sébastien DECK	**ONERA**	**Director**
Dr. Fabien GAND	**ONERA**	**Examiner**
Mr. Christophe BOURDEAU	**Airbus Operations**	**Invited member**
Mr. Vincent BRUNET	**Safran**	**Invited member**

À mes parents.

Remerciements

Au moment d'écrire les remerciements, je me dis parfois que passées les premières lectures par les gens de notre entourage, il est probable que se trouvent parmi les futurs lecteurs de parfaits inconnus, de jeunes thésards ou des acteurs du monde scientifique. Comme me l'a rappelé mon directeur de thèse, les deux choses les plus lues d'un manuscrit de thèse sont la conclusion et les remerciements. L'exercice me parait ainsi légèrement impudique. J'ai donc volontairement fait des remerciements à rallonge dans l'espoir d'effrayer les lecteurs initialement intéressés par le contenu scientifique. Néanmoins, je ne sais pas si ils seront nombreux, je peux donc m'épancher sereinement. Et puis je dois bien ça au gens qui ont gravité autour de cette thèse. De surcroit c'est une des rares occasions d'écrire un petit mot sympa aux gens qui pèsent.

Alors voilà, il y a une certaine fierté à aboutir, mais aussi du soulagement. Une aventure qui se termine. Une dure aventure qui se termine. Cinq années quasiment jour pour jour après avoir été retenu pour ce mandat de doctorant, le procès verbal final tombe enfin. Si j'ai toujours eu la sensation d'être parfaitement adapté pour réussir dans le système éducatif français jusqu'au diplôme d'ingénieur, voilà bien une formation qui m'a poussé dans mes retranchements. Je savais l'aventure difficile techniquement, je savais les risques de se retrouver dans l'impasse scientifique, du désaccord avec l'encadrement, de l'arbitrage délicat entre aspiration de l'industriel et exigences de l'encadrement académique. Je n'avais à aucun moment présagé des difficultés administratives et logistiques de cette affaire. Elles m'ont mené à un nombre conséquent de changements de plans, à une escapade inattendue (mais fort enrichissante) en Belgique avant de lancer véritablement les hostilités, ainsi qu'à un nombre un peu trop considérable de déménagements. Je souhaite d'ailleurs en premier lieu remercier les personnes qui m'ont hébergés pendant mes périodes sans domicile fixe, à Toulouse (Ponpon, Alex, Isanka, Adrien, Jordi) puis à Paris (Opwal, Denis, Greg, Aline, Martin, Florian, Charlotte). Je dois dire que la place la plus confortable reste sans conteste le matelas au pied du lit de Ponpon, qui n'a pas souvent raté l'occasion de commencer sa journée en piétinant mon oreiller.

Il est de coutume de remercier les rapporteurs, mais c'est une vrai reconnaissance que j'ai vis à vis de Messieurs Lamballais et Bogey pour leurs rapports écrits pendant leur période de congés estivale et leur intérêt pour mon travail. Je tiens également à remercier Messieurs Robinet et Fullana pour leur présence dans le jury.

J'ai passé mes premières années de thèse au service de design aérodynamique d'Airbus à Toulouse et c'est indéniablement la bonne entente et l'ambiance entre les membres de l'équipe qui m'a permis de tenir lorsque je ne voyais pas encore très clair dans ma thèse. Merci donc aux Thomas et aux Guillaume, à André, au Prince de Cadours, à Stève, à SHU (ex-tuteur d'un stage sur les hélices qui a tout lancé), à Benoit et à tous les autres pour l'atmosphère qu'ils ont contribué à créer, que ce soit lors des pauses, autour des croissants, au self ou autour d'un verre pour un quizz. Je remercie les membres du service des méthodes aérodynamiques qui m'ont apporté leur aide, notamment Cyril Gacherieu et Simon Trapier pour les discussions sur les schémas numériques et les calculs DES, Loïc Tourrette qui m'a sorti d'affaire plusieurs fois en particulier par l'installation d'une version spécifique d'elsA, et Alain Soulard pour sa grande disponibilité et sa persévérance sans faille dans l'affaire de la ligne informatique. Je remercie les personnes qui se sont investies sur le volet administratif de la thèse, David Grossein, Marie-jo et Jenny, notamment au lancement et pour la mise en place d'une extension de financement. Je tiens également

à saluer mon prédécesseur sur le sujet, Pierre Giner. Enfin, je tiens à remercier très chaleureusement Christophe mon encadrant industriel qui m'a guidé dans les méandres de (feu ?) la chaîne de calcul EGAT et dont je ne peux que louer la disponibilité, l'altruisme, la rigueur et les ressources inépuisables de dépatouilleur. J'ai particulièrement apprécié ses grandes qualités humaines et sa personnalité incomparable, entre coups de sang et trait d'humours, et ses récits de parapentes 10 fois répétés avec un enthousiasme inaltérable. Son aide me fut précieuse, sa fréquentation réjouissante.

La fin de ma thèse s'est déroulée à l'ONERA au sein du Département d'Aérodynamique APpliquée (DAAP) et j'y ai côtoyé beaucoup de monde qu'il me faut remercier.

Tout d'abord, j'adresse une pensée émue à la famille de Michel Gazaix, dont je viens d'apprendre la disparition, et que je souhaitais remercier pour son aide lors de l'installation d'une version spécifique d'elsA sur les calculateurs d'Airbus.

Ensuite, je remercie Joël Reneaux et Gérald Carrier, pour m'avoir accueilli au DAAP et permis mon extension de thèse. J'ai apprécié travailler avec Vincent Brunet qui a supporté ce projet et m'a encadré pendant ma première année, bien que ce ne soit pas simple à distance, et qui a largement œuvré pour faire avancer la partie politico-administrative (ce dont je lui suis particulièrement reconnaissant). Merci également à tous les membres de l'équipe et plus particulièrement, Christelle, Jean-luc, Fred, Fulvio (et son petit ballon de rugby qui a occupé mes instants de réflexion au bureau), Michel et Antoine (dont la joie de vivre, le dynamisme et la gentillesse sont un must).

C'est en arrivant à l'ONERA que j'ai pris conscience du cadre privilégié que constitue le DAAP pour la réalisation d'une thèse, et que l'on retrouve plus difficilement dans le monde industriel. Hormis, une flexibilité accrue des outils et de l'environnement, l'élément le plus important, avant même la proximité avec les encadrants académiques, est la proximité avec d'autres thésards. En tous cas pour moi ce fut l'énorme plus que j'ai ressenti en arrivant au DAAP. Les discussions et questionnements scientifiques que nous avons eu devant écrans informatiques et tableaux blancs, l'écoute, le partage des galères, les résolutions de problèmes respectifs, les astuces python, Tecplot, shell, les vidéos débiles, les cafés, bref, plein de choses qu'on partage bien plus facilement avec des thésards. Et je dois avouer que je n'ai pas à me plaindre de mes co-thésards au DAAP. le sens de l'entraide y est sévère et la cohésion importante. Je tiens à les saluer et les remercier pour ces bons moments. Merci donc à Aurélien, à Mehdi, à Loïc et Mickael, les deux zigotos MHL du fond du couloir, le premier d'une sérénité qui m'a toujours parue imparable (sans doute car il avait les mains propres), l'autre un peu moins serein (ah ouais mais on fait pas des missiles impunément !), pour leur humour libérateur, à Hélène, que j'comprends toujours pas comment qu'elle a fait pour être toujours dans les temps dans sa thèse, à Nico, le Fox, avec une majuscule parce que quand même, pour les discussions techniques et ta culture aéronautique partagée avec passion, à Amaury, petit prince irrévérencieux de la course en chaussures à orteils séparés, pour ton enthousiasme et tes blagues potaches, à Edoardo, expansif italien (pléonasme) encore plus rital que celui de mon bureau à tel point qu'on l'a calé dans le bureau stagiaire au fond du couloir, à Anthony le trottinetteman local. Il en manque deux qui méritent un remerciement particulier pour l'aventure singulière vécue ensemble au bureau AY-02-22. Deux chics types. Andrea, italien papadipupi, généreux en tout, dans l'amitié, l'aide, la théâtralité, le rire, l'écoute, les commentaires de l'actualité, les puttana troia, les coglioni, les Que cazzo, et Ilias, grec, calme, cool, rigoureux dans le développement limité et qui maitrise magnifiquement l'art de lancer un sujet politique avant de s'en extirper. Ces débats intenses avec Andrea, s'ils n'ont pas manqué de nuire à notre productivité, restent d'excellents souvenirs de la vie au bureau. Autant que la

blue ball, les Johnny Culo, la touche two. Je m'excuse auprès d'eux pour les nombreux craquages suite aux pénibles (je crois que c'est le mot) pertes de connexion informatique, ainsi que pour le nombre inadmissible d'absences aux sorties impromptues, bar ou resto, mais je pouvais pas j'avais poney.

Merci également aux thésards du premier étage, en particulier Cédric le bug-finder, pour sa gentillesse et ses coups de fils depuis le "bureau stagiaires". Je tiens aussi à rendre hommage aux précédentes générations de thésards du DAAP, qui d'une manière ou d'une autre ont nourri mon travail, en particulier la promotion 2007 des Trapier, Chauvet, Simon,... Je salue également, Enric et Romain que je n'ai fait que croiser au DAAP, mais fréquentés plus largement en dehors.

Cette thèse, si elle est mon travail, reflète aussi toute l'implication de mes encadrants à l'ONERA. Nous avons toujours entretenu de très bonnes relations et je tiens à leur exprimer toute ma gratitude. D'une part, Fabien, qui a repris l'encadrement de ma thèse en cours de route et a parfaitement géré cette tâche. Il faut dire que Fabien est très bon dans ce qu'il fait. Par sa maitrise technique, sa disponibilité, la rapidité et la qualité de ses corrections, ses qualités humaines, il a grandement contribué à la réussite de cette thèse. J'admire également son zen au bureau, qui lui permet de cohabiter avec une pile électrique comme Antoine et de rester concentré quand celui ci se chamaillent avec Andrea sur la méthode adjointe. D'autre part, Sébastien, qui a accepté la direction de cette thèse CIFRE, et qui, malgré l'énergie lâchée en route avec le Fox, s'est largement investi dans mon travail. C'est une chance de l'avoir eu pour directeur de thèse. Pour son souci du détail et, capable d'être piquant comme de reconnaitre le travail bien fait (ce qui n'est pas l'apanage de tous les directeurs de thèse), pour avoir su me booster et maintenir ma motivation quand pointait la lassitude. J'ai aussi apprécié sa préoccupation de l'avenir des doctorants qui l'entourent et toutes les discussions que l'on a pu avoir à ce propos.

Bien sûr, il m'est impossible d'écrire des remerciements sans souligner l'influence des personnes fréquentées en dehors de la mécanique des fluides durant ces années de thèse mais aussi avant et qui ont fait la personne que je suis. On ne se fait ni en un jour, ni tout seul hein ! En dehors de mes études ou de mon travail, j'ai toujours bénéficié d'un cadre impeccable.

Mes amis y ont beaucoup contribué. J'ai le privilège d'avoir pu rester proche autant de mes amis de classe préparatoire que de mes amis d'école, notamment du X6. Ils occupent une place importante pour moi. Ça fait une tripotée de zouaves et la plupart sont sur Paris, ce qui m'a permis à de nombreuses reprises de m'évader en leur compagnie. Je tiens à tous les remercier pour tout ce qu'on a pu vivre jusque là. Merci aussi aux toulousains, notamment mes colocs, Isanka, Alex, Jordi, Camille avec qui j'ai partagé beaucoup de moments forts.

J'ai également une formidable reconnaissance pour ma famille, en premier lieu pour mes parents. Ils ont depuis toujours su m'offrir un environnement privilégié à tous points de vue et inculqué cette envie d'apprendre, cette soif de comprendre, cette curiosité intellectuelle. Je leur dois énormément. Même si le but n'était pas là, qu'ils soient un peu fiers, mes parents et ma soeur, c'est bien le moins que je puisse leur rendre. Merci à eux de m'avoir toujours soutenu.

Enfin, merci à ma chère Chloé.

PS : Avant de terminer cet encart, je souhaiterais vivement me repentir pour mon action néfaste vis à vis de la population mondial de pingouin. En effet, les grandes ressources informatiques dont j'ai bénéficié sur les calculateurs d'Airbus (Alors dans le top 30 des plus gros calculateurs mondiaux) pendant cette thèse m'ont conduit à une utilisation intempestive de processeurs et à une consommation énergétique honteuse de la part d'un seul thésard. Considérant une estimation d'environ 1000 processeurs utilisés en permanence pendant 1 ans et demi, on peut évaluer la consommation électrique à plus de 150000 kWh, soit la consommation électrique totale pendant la même période d'une vingtaine de foyers français ... L'impact sur la fonte de la banquise reste dur à quantifier, mais je tiens malgré tout à préciser aux pingouins que j'ai tenté d'éviter les centrales à charbon allemandes en lançant mes calculs sur les POD de Toulouse plutôt que sur ceux d'Hambourg... pouf pouf !

Toulouse m'a rempli
de rêves et d'amis,
Toulouse c'est fini,
Demain, c'est Paris.

Et la nostalgie,
Envahit mon lit,
Ce lit trop petit,
Pour ma nostalgie.
Car même si je sais
Que je vais trouver
Des rêves nouveaux
Pour leur faire écho,
Et d'autres poteaux,
Pour châtier mes maux,
Me remonte au coeur
Cette sourde torpeur.

Toulouse m'a rempli
De rêves et de joie,
Mais c'est à Paris
Que demain j'échoie.

(Fini tisséo,
Bonjour navigo,
3M et barbots
Pour les apéros ☺)

Toulouse, 13 octobre 2014

Contents

Nomenclature

ρ	density
$\boldsymbol{q}$	velocity vector
u, v, w	velocity components
p	static pressure
C_p	specific pressure heat
γ	ratio of specific heats
μ	dynamic viscosity
μ_t	turbulent viscosity
ν	kinematic viscosity
p_a	ambient static pressure
p_e	jet exit static pressure
P_i	stagnation pressure $p_i = p\left(1 + \frac{\gamma-1}{2}M^2\right)^{\frac{\gamma}{\gamma-1}}$
T	temperature
T_i	stagnation temperature $T_i = T\left(1 + \frac{\gamma-1}{2}M^2\right)$
$\boldsymbol{q_h}$	heat flux vector
$\boldsymbol{q_h^{tur}}$	turbulent heat flux vector
$\underline{\boldsymbol{\tau}}$	viscous stress tensor
$\underline{\boldsymbol{\tau^{tur}}}$	turbulent stress tensor
$\underline{\boldsymbol{\tau^{SGS}}}$	subgrid scale stress tensor
D	diameter
Δ	characteristic cell size
Δt	time step
Δ_{vol}	subgrid length scale based on the cell volume $\Delta_{vol} = (\Delta_x \Delta_y \Delta_z)^{1/3}$
Δ_ω	subgrid length scale based on the cell sizes and the local vorticity $\Delta_\omega = \sqrt{S_\omega}$
δ_ω	vorticity thickness $\delta_\omega = \dfrac{\Delta u}{(\partial u/\partial y)_{max}}$
θ_0	nozzle exit boundary layer momentum thickness

Normalized numbers

M	Mach number
Re_D	diameter based Reynolds number $Re_D = \frac{UD}{\nu}$
Re_{θ_e}	Reynolds number based on the initial boundary layer momentum thickness $Re_{\theta_e} = \frac{U\theta_0}{\nu}$
JPR	Jet Pressure Ratio JPR=$\frac{p_e}{p_a}$
NPR	Nozzle Pressure Ratio NPR=$\frac{p_i}{p_a}$
St_D	Strouhal number $St_D = \frac{fD}{U}$
St_{θ_e}	Strouhal number based on the initial boundary layer momentum thickness $St_{\theta_e} = \frac{f\theta_0}{U}$

Acronyms

CFD	Computational Fluid Dynamics
HPC	High Performance Computing
RANS	Reynolds Averaged Navier Stokes
URANS	Unsteady Reynolds Average Navier Stokes
LES	Large Eddy Simulation
WMLES	Wall-Modeled Large Eddy Simulation
DES	Detached Eddy Simulation
DDES	Delayed Detached Eddy Simulation
ZDES	Zonal Detached Eddy Simulation
RFG	Random Flow Generation

Chapter 1

Introduction

1.1 General context

Since the entry in service of the Boeing 707 in the late fifties, the propulsion system integration of commercial aircraft has not significantly changed, with podded engines located under swept wings. In this common configuration, engines are embedded in nacelles which are fixed to wings by pylons, as depicted in figure 1.1(a).

Conversely, the technology of engines powering large commercial aircraft has been constantly evolving, from turbojets toward dual-stream turbofans currently in use as those of the CFM-56 family or of the Rolls-Royce Trent family (see figure 1.1(b)). The design of these turbofans and their integration on aircraft must meet different requirements.

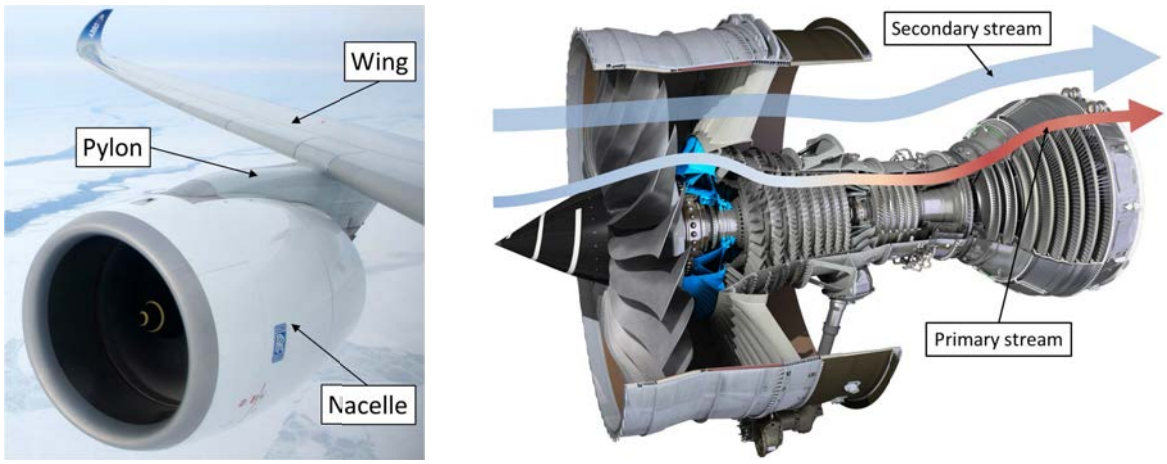

(a) A350 XWB engine integration

(b) Schematic of a dual-stream turbofan

Figure 1.1: Large commercial aircraft engines: (a) Under swept wing podded engine of the Airbus A350 XWB entered in service in 2015, adapted from [1], (b) Schematic of a dual-stream turbofan, adapted from [4].

As a matter of fact, for many decades the design of new airplanes and their engines has mainly been driven by objectives of specific fuel consumption (sfc), since fuel burns are the main part of aircraft operating costs. In the framework of a constantly increasing air traffic, very ambitious goals have been set by the ACARE [2] in order to reduce the environmental footprint of aviation by 2020:

- a 50% reduction of the far field aircraft noise;

- a 80% reduction of Nitrogen Oxide (NOx) emissions;
- a 50% decrease of carbon dioxide (CO_2) emissions.

This last objective regarding CO_2 emissions in the atmosphere involves directly a reduction of the specific fuel consumption as well. According to ACARE, while 20 to 25% of the sfc gain should lie in the overall aircraft optimization, 15 to 20% should lie in the increase of engine efficiency. Thus, engine manufacturers endorse a large responsibility in the achievement of these ambitious objectives, which induces new constraints early in the design process of future propulsive systems.

In order to fulfill these requirements, several technological choices have been made to increase the efficiency of turbofans. Considering that the overall efficiency of an aircraft is the product of the thermodynamic cycle efficiency and the propulsive efficiency, two main orientations are followed concomitantly:

- The first significant evolution aims at increasing the thermodynamic cycle efficiency by increasing both engine cycle temperatures and global pressure rates;
- The second trend is the continuous increase of turbofan bypass ratio, i.e. the ratio of the secondary stream mass flow rate to the primary one. As depicted in figure 1.2, the overall efficiency of turbofans increases with the bypass ratio. The main explanation for this lies in the increase of the propulsive efficiency due to a reduction of the engine jet velocity. In addition to reduced sfc, it must also be noted that increasing turbofan bypass ratio provides an acoustic advantage.

Current commercial aircraft are already equipped with significantly high bypass ratio (between 8-11) engines and the trend toward higher engines seems to continue as Ultra High Bypass Ratio (UHBR 15-20) are considered by engine and aircraft manufacturers.

The advantages of high bypass ratio engines in terms of overall efficiency and jet noise are nevertheless balanced by an increase of weight and size of the engine, which leads to new integration challenges.

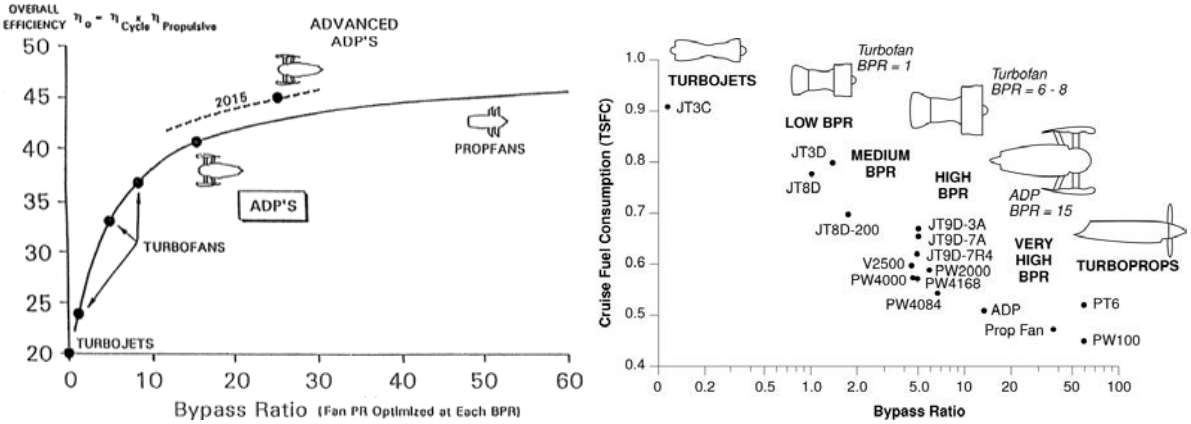

(a) Overall efficiency vs bypass ratio

(b) Specific fuel comsumption vs bypass ratio

Figure 1.2: Trends in large commercial bypass ratio engines. (a) overall efficiency, from [5], (b) fuel consumption, from [3]

The increase of engine size has led to close-coupling configurations (between the nacelle and the pylon/wing) which involve much stronger interactions between hot engine jets and the airframe. Indeed, as the nacelle trailing edge is closer to the wing, mixing layers are likely to impact wing devices such as flaps or flap track fairings and provoke vibrational

issues. Pylon elements such as the aft pylon fairing (APF) (see figure 1.3), which are licked by engine jets, are also subject to this kind of issues because of high pressure fluctuations at the interface with jet mixing layers. Such a "sonic fatigue" phenomenon can lead to dramatic damages such as cracks in the structure.

Stronger interactions between jets and airframe also raise the issue of thermal stress on elements licked by hot engine jets, which is amplified by the current increase of primary jet temperatures. For instance, some areas of the APF are submitted to important wall temperatures as evidenced by marks on the fairing in figure 1.3. Consequently, the introduction of lighter materials such as composites with lower thermal resistance is limited in these areas or must be operated with extreme care. In particular, one of the objectives of the engine integration design is to shield the APF from an intense licking by hot engine jets issued from the core nozzle. Several patents have already been filed to do so, but the use of new materials remains limited.

Last, though noise emitted by dual-stream jets with high bypass ratios is reduced for isolated jets, the close-coupling integration of modern installations generate a lot of acoustic interactions in the jet vicinity. These interactions generally produce additional noise and their understanding and accurate prediction is mandatory to achieve ACARE acoustic objectives.

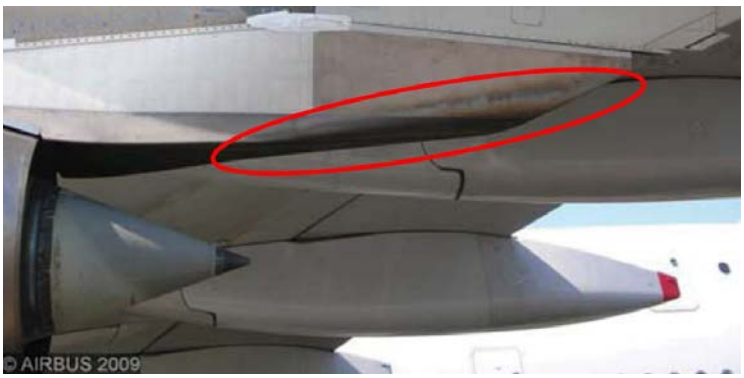

Figure 1.3: Intense temperature stress on the rear part of the APF

1.2 Industrial motivations in numerical predictions

The part of simulations in the aerodynamic design process has been constantly increasing since the beginning of Computational Fluid Dynamics (CFD), following the growth of computational capabilities. Even though wind tunnel tests remain necessary to validate numerical methods and maintain a high level of reliability, the use of CFD in the design process presents many advantages. First, wind tunnel test campaigns are extremely expensive and rather long to prepare and carry out. Numerical simulations enable to obtain aerodynamic data much faster and at a significantly lower cost, especially with the development of massively parallel and high performance computers, which makes them particularly suited for daily iteration loops of a conception process. Another asset of CFD lies in the capability to simulate in flight conditions with the complete aircraft geometry, which is not possible in wind tunnel since the model is maintained by struts and flight conditions are extremely tough to reproduce [82].

The current CFD methods in use in the industry, especially during the design process, are mainly based on Reynolds Averaged Navier-Stokes (RANS) approaches. In this framework, the influence of turbulence on the mean flow is modeled and RANS simulations

are used to obtain a steady-state flow solution. These steady methods have proven to be reliable to predict the aerodynamic performance of an aircraft in cruise conditions, but are not suited to properly simulate massively separated and strongly unsteady flows.

In particular, in propulsive jet configurations, the interactions between engine jets and the airframe are driven by highly unsteady mechanisms. Thus, the development of jets mixing layers in presence of pylon fairings is likely to be poorly predicted by RANS simulations, while it is a fundamental requirement regarding the vibrational and acoustic issues raised by close-coupling configurations. The level of confidence in RANS simulations is currently limited for such configurations and leads to use large safety factors during the design process for pylon and wing parts in the jet area. An increased confidence in numerical predictions would improve safety margin definitions, bringing higher safety and potential weight savings.

In this general framework of the improvement of the reliability of simulations, another key requirement lies in the accurate prediction of wall pressure fluctuations and temperature levels. Indeed, the local maxima of these quantities can temporarily reach values unsupported by the pylon or flap fairing materials. Since RANS simulations only provide steady-state data, it is therefore necessary for these industrial applications to move toward turbulence-resolving simulations. This is all the more relevant since large computational means now available in the industry.

Although the computational cost of such simulations remains prohibitive to be integrated in an iterative design process, such simulations could bring serious insights into the flow physics of complex configurations. It could otherwise be used to validate the design in presence of strong unsteady features.

1.3 Scientific motivations

A large number of jet simulations using turbulence-resolving approaches can be found in the literature, mostly using Large Eddy Simulation (LES).

However, among all LES of turbulent round jets encountered in the literature, most of the studies focused on academic configurations at Reynolds numbers smaller than 10^5. Many physical and numerical parameters have been studied, including the initial state of the mixing layer, the mesh resolution of LES, and their effect of the farfield noise. Conversely, configurations at Reynolds numbers typical of civil aircraft, i.e. higher than 10^6 or 10^7 are less investigated.

For the simulation of complex configurations at such Reynolds numbers, hybrid methods coupling RANS and LES appear today as the most feasible approach in terms of implementation and accuracy. Indeed, significant progress has been achieved in hybrid RANS-LES methods since the introduction of the Detached Eddy Simulation (DES)[202] in 1997. Based on the DES idea of treating the boundary layer with the RANS modeling and the detached flow with the LES approach, several methods have emerged to improve the transition between modeled and resolved areas, to ensure the robustness of the RANS treatment of attached boundary layers, and to increase the resolution level in the LES areas, as RANS-ILES (ILES for implicit LES)[235, 91], Delayed DES (DDES) [201] or Zonal DES (ZDES)[81] for instance. The use of such approaches for the prediction of propulsive jets have shown promising results and permitted to reach realistic Reynolds numbers [237, 92, 57].

Nevertheless, before considering RANS-LES simulations as a reliable prediction tool in the framework of propulsive jets, an important work of validation remains necessary.

Hybrid RANS-LES methods are classically dedicated to the treatment of massively separated flows in which a strong and sudden instability is likely to generate the LES content of the detached flow. Consequently, the resolved turbulent fluctuations are not immediately existing at the RANS-to-LES interface.

In particular, due to the RANS treatment of the nozzle exit boundary layers, the mixing layers at the nozzle exit present a turbulent mean profile (i.e. a shape factor around 1.4) but no resolved turbulent fluctuations. Therefore the RANS-to-LES transition in the early development of the mixing layers occurs in a similar fashion as a laminar/turbulent transition, which is not the case in real mixing layers initially turbulent at high Reynolds numbers. Several recent works underlined this issue of RANS-to-LES transition in weakly unstable flows and suggested improvements to reduce it. In the case of shear layers, resolved turbulent fluctuations remain essentially triggered by Kelvin-Helmholtz instabilities whose intensity depend on the velocity difference at the origin of the shear-layer.

Thus, it appears all the more difficult to obtain significant resolved fluctuations at the beginning of a mixing layer when this latter one is induced by a small velocity difference. For example, the mixing layers between primary and secondary jets of an aircraft engine jets are typically subject to this issue. Thus, as a too large transition area downstream of the nozzle exit can have dramatic consequences on the development of mixing layers, it is important to reduce as far as possible the transition length.

Besides, even though the influence of turbulent levels in the nozzle exit boundary layers has regularly been addressed in the literature, no study thoroughly investigated the influence of upstream turbulence in the whole inflow plane on the jet development of a dual-stream jet. However, real engine jets exhibit a large upstream turbulence rate in the core of jets and some recent numerical studies that took into account upstream turbulence suggested a noticeable effect on the jet development due to the increased mixing [55, 213].

1.4 PhD objectives and organization of the thesis

The present work aims at fulfilling these gaps in the literature of jet simulations and making hybrid RANS-LES approaches more mature for simulating propulsive jets in an industrial environment. Therefore, the study focuses on numerical ingredients that can improve the representativity of mixing layers and enhance their transition from laminar state toward fully developed turbulence. In particular, in the frame of mode 1 and mode 2 of ZDES, an hybrid RANS-LES approach developed at ONERA, the effects on the resolved jet physics of a low dissipation spatial scheme as well as the interest of a subgrid length-scale based on local vorticity are analyzed. This thesis work also investigates the influence of inflow turbulence on the development of the jet by means of synthetic turbulence added at inlet boundary conditions.

In the first chapter, the main features of the subsonic and supersonic jet physics are reminded prior to providing an overview of the state of the art for turbulence-resolving jet simulations.

The second chapter introduces the numerical modeling of turbulent flows and the MARTEL experiment which is used as a validation test case throughout the thesis. In particular, RANS and hybrid RANS/LES approaches are described as well as the numerical solver elsA, spatial schemes and the synthetic turbulence method used during the PhD work. The experimental means are also described in the last section of this chapter.

The study of the ZDES numerical setup influence on the resolved jet physics is carried out in the third chapter. The results obtained with the time-honored subgrid length scale Δ_{vol} are compared to the ones obtained with the subgrid length scale definition

Δ_ω introduced by Chauvet et al. [65] and the effect of the spatial scheme is studied by comparing the flow field obtained with the Jameson scheme to the one obtained with the lower dissipative scheme AUSM+(P) developed by Edwards & Liou [94] and modified by Mary & Sagaut [151]. Eventually, in the framework of the industrialized implementation of eddy-resolving approaches, the ZDES mode 2 is assessed.

The fourth chapter investigates the influence of accounting for upstream turbulence in ZDES simulations of propulsive jets by using the Random Flow Generation (RFG) technique of Smirnov et al. [197]. Different turbulent characteristic length scales and turbulence rate have been prescribed at nozzle inlets and their effects on the mixing layer development and shock-cell pattern are analyzed.

A discussion of the salient findings of this work together with some proposals of future work are addressed in the conclusion.

Chapter 2

Literature review

This chapter aims at providing an overview of the main characteristics of jets that can be obtained from the literature, in order to summarize salient points for the sake of analysis and comparison.

Contents

Civil aircraft propulsive jets are characterized by the development of mixing layers in both subsonic and supersonic regimes, with high flow temperatures. The first part of this literature review aims at educing the main features of jets. Single stream configurations are studied first and then the effect of initial conditions, compressibility, temperature gradients and a co-flow are investigated. Eventually, the special features of dual stream jets are analyzed. In the second part of this chapter, the numerical approaches that can be used for jet simulations are presented. Let us be reminded that the main concerns of this PhD thesis regard aerodynamic purposes, and thus acoustic results will not be thoroughly presented.

2.1 General remarks about jet physics

This section focuses on single-stream jets, and more specifically round jets, as they represent the most common configuration of propulsive jets. Besides, a large part of their physics is common with co-axial propulsive jets.

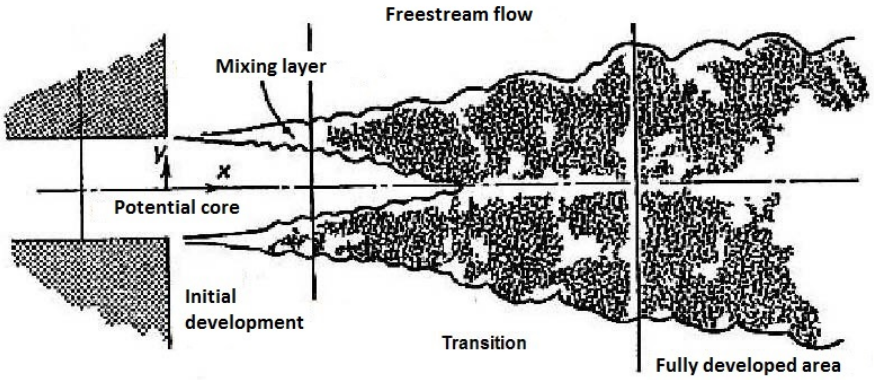

Figure 2.1: Round jet in transition, from Tennekes & Lumley(1976)

Basically, the jet exiting from a nozzle is bounded by mixing layers, the zone of strong velocity gradients and shear at the interface with the freestream flow (away from the jet).

As sketched in figure 2.1, several areas can be identified in a jet:

- The **initial development zone** where the instabilities in the shear-layers (Kelvin-Helmholtz instabilities that might be followed by vortex-coupling or 3D destabilization, depending on the Reynolds number and the initial boundary conditions)appear.

- The potential core, within the core of the jet before mixing layers meet up on the axis line. Several studies, for instance Kleinstein (1964)[129], Witze (1974)[234] or Lau et al. (1979)[140], established empirical correlations for the potential core length and the centerline velocity. According to Lau et al. the potential core length follows the relation:

$$L_c = 4.2 + 1.1M_e^2 \tag{2.1.1}$$

  with M_e the jet exhaust Mach number. Eq (2.1.1) is valid in the range $M_e = 0.3$ - 1.4.

- The **transition area**, starting slightly upstream from the end of the potential core, a region where mixing-layers grow until meeting each other. In this region, the spreading rate of the mixing-layer is important and vortical structures tend to be more and more three-dimensional, with a consequent broadening of the turbulent spectrum. Lau et al. determined that the centerline velocity $u(r = 0)$ follows the relation:

$$\frac{u(r=0)}{u_e} = 1 - exp\left(\frac{1.35}{1 - \frac{x}{L_c}}\right) \tag{2.1.2}$$

  with u_e the jet exit velocity.

- The **fully developed region**, where the turbulence is often assimilated to isotropic homogeneous turbulence and where the velocity on the jet axis decreases proportionately to $1/x$.

2.1.1 Main features of mixing-layers

At the nozzle exit and downstream from the thick trailing edge, the flow presents a strong velocity gradient at the interface between the engine jet and the ambient flowfield, which in turn results in an intense shear process. Thus, the mixing-layer is largely dependent on the velocity difference between the internal and the external flows. The thickness of this mixing layer increases as the large scale structures are convected downstream.

In initially laminar shear layers, i.e. originating from 2 laminar co-flows, it is generally possible to identify 3 regions, the initial vortex sheet roll-up, the transitional zone and the fully turbulent mixing layer. At very high diameter based Reynolds numbers (around 10^6), the boundary layer at the nozzle exit is already fully turbulent and the mixing-layer is almost characterized by a fully developed turbulent regime.

2.1.1.1 Useful definitions

For the sake of simplicity, let us consider the axi-symmetric case, with x the axial coordinate, r the radial and z the tangential ones. In the following, the index 1 will always refer to the flow with the highest mean velocity and the index 2 to the lowest.

Velocity and density ratios The ratios of velocity and density are of primary importance in the mixing layer development, therefore we define:

$$\kappa = \frac{u_2}{u_1} \qquad s = \frac{\rho_2}{\rho_1} \tag{2.1.3}$$

It is also useful to define the jet exit velocity u_e, the mean velocity u_m and the shear velocity Δu:

$$u_e = u(x=0) \qquad u_m = \frac{u_1 + u_2}{2} \qquad \Delta u = u_1 - u_2 \tag{2.1.4}$$

The velocity ratio R_u related to the shear velocity Δu is:

$$R_u = \frac{\Delta u}{2u_m} \tag{2.1.5}$$

Mixing layer thickness To evaluate the size and eventually the growth rate of the mixing layer, several definitions of the mixing layer thickness have been proposed:

- δ_{pit} the Pitot thickness which is the width of the total pressure profile between the points reaching respectively 0.5% and 95% of the external flow pressure (Papamoschou & Roshko (1988)[167], Murakami & Papamoschou(2002),[161], Bellaud's PhD thesis (1999)[21])

- θ_m the momentum thickness, whose general expression for a two-dimensional mixing layer is given by:

$$\theta_m = \int_{-\infty}^{\infty} \left(\frac{u(r) - u_2}{\Delta u}\right)\left(\frac{u_1 - u(r)}{\Delta u}\right) dr \tag{2.1.6}$$

  which for a jet discharging in a static environment becomes:

$$\theta_m = \int_{0}^{\infty} \frac{u(r)}{u_e}\left(1 - \frac{u(r)}{u_e}\right) dr \tag{2.1.7}$$

- δ_ω the vorticity thickness or thickness of maximal slope. Its more general definition for a two-dimensional mixing-layer, as shown in Bailly & Comte-Bellot 2015[16], is given by:

$$\delta_\omega = \frac{1}{\Omega_{max}} \int_0^\infty \Omega(r) dr \tag{2.1.8}$$

where Ω is the mean vorticity and Ω_{max} its maximum value in the plane at the axial position considered. It characterizes the maximum of the velocity gradient in the mixing-layer since it can generally be reduced to:

$$\delta_\omega = \frac{\Delta u}{(\partial u/\partial y)_{max}} \tag{2.1.9}$$

This last definition is widely spread in the literature and it is generally acknowledged that the visual thickness of a mixing-layer (as could be observed on a photography) is twice δ_ω. It must also be noted that for canonical mixing layers characterized by hyperbolic tangent velocity profiles, the vorticity thickness is four times as large as the momentum thickness ($\delta_\omega = 4\theta_m$)[16].

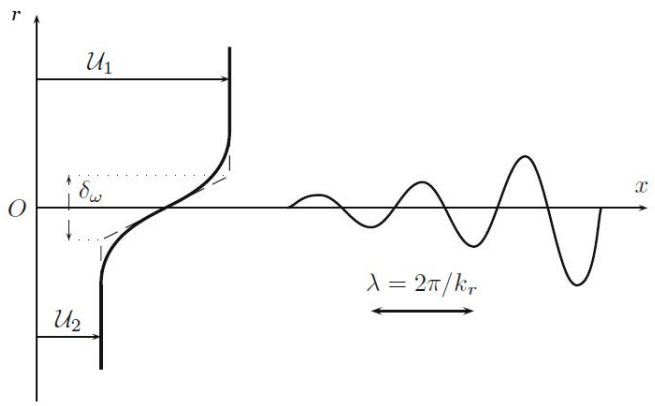

Figure 2.2: Illustration of vorticity thickness in the case of an hyperbolic tangent profile and of the instability wave growth, from Bailly & Comte-Bellot (2015)[16]

In the following, this quantity will be the main one used for the measure of the encountered mixing layer thicknesses.

2.1.1.2 Kelvin-Helmholtz instabilities

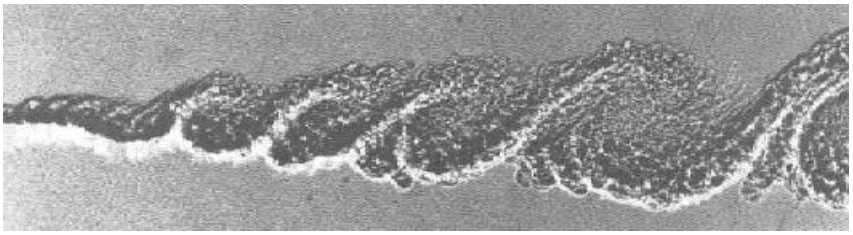

Figure 2.3: Mixing layer snapshot exhibiting Kelvin-Helmholtz instabilities, from Brown & Roshko(1974)[54]

These instabilities are characteristic of shear-layers. They are recognizable by the development of eddies as exhibited fig 2.3. Due to the difference of velocities, a primary instability, also called Kelvin-Helmholtz instability, produces the roll-up of the vortical sheet as presented in the sketch figure 2.4. In the early stages of shear-layer development, these vortices occur with a spatial wavelength λ_0 which can be determined by a linear stability analysis (see for instance Michalke (1964)[154], (1965)[155] in function of the local thickness of the shear-layer, following eq 2.1.10 (Bailly & Comte-Bellot 2015[16]):

$$f_{KH} \simeq 0.033\frac{u_m}{\theta_m} \simeq 0.132\frac{u_m}{\delta_\omega} \tag{2.1.10}$$

with u_m the mean velocity defined in eq. (2.1.4).

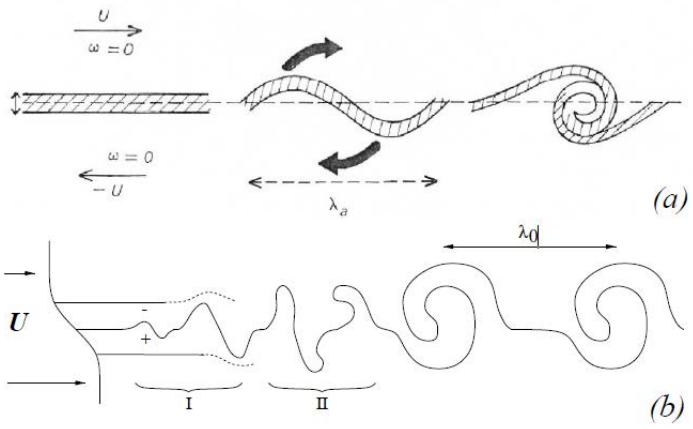

Figure 2.4: Sketches from the origin of Kelvin-Helmholtz instabilities, from Lesieur[142] (a) and Balarac[17] (b)

2.1.1.3 Evolution of the mixing-layer thickness: spreading rate

During the mixing-layer development, turbulent structures of various sizes are generated and participate to the mixing of the jet with the external flow. Thus, the mixing-layer thickness increases as it is convected donwstream. This enlargement is characterized by the spreading rate $\delta' = \frac{d\delta_\omega}{dx}$. Brown & Roshko (1974)[54], Bogdanoff (1983)[28], Dimotakis(1986)[88] and Papamoschou & Roshko (1988) among others have studied the mixing-layer in the relative frame linked to the convected structures. In this approach, according to Dimotakis (1986, 1991)[88, 87]:

$$\frac{d\delta_\omega}{dt} \propto u_1 - u_2 \tag{2.1.11}$$

Considering the frame transformation defined by $x = u_c t$, with u_c the convection velocity of turbulent structures, the following spreading rate definition writes:

$$\delta' = \frac{d\delta_\omega}{dx} \propto \frac{u_1 - u_2}{u_c} \tag{2.1.12}$$

Assuming the existence of a stagnation point in the frame linked to vortices [88] [72], it leads,assuming an incompressible flow, to the following expression for vortex convection velocity:

$$u_c = u_1\frac{1+\sqrt{s}\kappa}{1+\sqrt{s}} \tag{2.1.13}$$

Thus,

$$\delta'_\omega = C_\delta \frac{(1-\kappa)(1+\sqrt{s})}{1+\sqrt{s}\kappa} \tag{2.1.14}$$

This formulation has been obtained by Brown (1974)[54] with C_δ in the range $0.16 - 0.18$, whereas Aupoix & Bézard found it to lie rather between 0.175 and 0.185 [14]. Regarding the value of C_δ associated to Pitot thickness $\delta_{pit.}$, Papamoschou & Roshko (1988)[167] found 0.14. This model correctly describes the temporal evolution of the mixing-layer in the moving frame but does not take into account the asymetrical entrainment of fluid on both sides of the mixing, which is characteristic of its spatial evolution. Dimotakis (1986) provides various arguments to achieve the more general expression:

$$\delta'_\omega \propto \left(\frac{(1-\kappa)(1+\sqrt{s})}{1+\sqrt{s}}\right)\left[1 - \frac{(1-\sqrt{s})/(1+\sqrt{s}\kappa)}{1+2.9(1+\kappa)/(1-\kappa)}\right] \tag{2.1.15}$$

which is in a good agreement with Konrad's experimental work (1977)[134].

The strong influence of compressibility effects on the spatial evolution of δ'_ω is presented in the next section.

2.1.1.4 Influence of compressibility on the mixing layer: the convective Mach number

Usually, at high Mach numbers, close to 1 or above, compressibility effects can be observed on the mixing layer development. The various turbulent structures developing in the shear-layer are convected donwstream with a velocity u_c which is characteristic of the mixing layer. As mentioned previously, in the case of incompressible flows, the convection velocity can be linked to the velocity ratio and to the density ratio, using the assumption that a stagnation point exists in the frame related to turbulent structure's motion (see sect 2.1.1.3). In order to take compressibility effects into account, Bogdanoff (1983)[28], followed by Papamoschou & Roshko (1988)[167], introduced the convective Mach number as a parameter of similitude. The convective Mach numbers based on the sound speeds c_1 and c_2 in both flows around the mixing layer are defined by:

$$M_{c_1} = \frac{u_1 - u_c}{c_1} \text{ and } M_{c_2} = \frac{u_c - u_2}{c_2}$$

The same step as in the incompressible case (balancing of stagnation and static pressures at the stagnation point) leads to the following equality:

$$\left(1 + \frac{\gamma_1 - 1}{2} M_{c_1}^2\right)^{\frac{\gamma_1}{\gamma_1 - 1}} = \left(1 + \frac{\gamma_2 - 1}{2} M_{c_2}^2\right)^{\frac{\gamma_2}{\gamma_2 - 1}} \tag{2.1.16}$$

Since in most of the flow fields encountered, the values of γ_1 and γ_2 are very close, the γ dependency is often neglected and it comes:

$$M_{c_1} = M_{c_2} \tag{2.1.17}$$

Eventually, the convective Mach number is given by:

$$M_c = \frac{u_1 - u_2}{c_1 + c_2} \tag{2.1.18}$$

Also, as in the incompressible case, the mixing layer's growth rate is given by:

$$\frac{d\delta_\omega}{dx} = C_\delta \frac{(1-\kappa)(1-\sqrt{s})}{2(1+\kappa\sqrt{s})}. \tag{2.1.19}$$

where $\kappa = u_2/u_1$ is the velocity ratio and $s = \rho_2/\rho_1$ is the density ratio. The difference with respect to the incompressible case lies in the dependence of C_δ on the convective Mach number. For compressible cases, Dimotakis [87] proposed an expression for $C_\delta(M_c)$ as a function of the convective Mach number:

$$\frac{C_\delta}{C_\delta(M_c=0)} = 0.8e^{-3M_c^2} + 0.2, \tag{2.1.20}$$

This representation is plotted on the chart figure 2.5 (from Aupoix [13]), together with experimental values compiled by Aupoix [13]. When M_c rises, the decrease of C_δ, and thus of the spreading rate, can be observed up to $M_c = 1.5$. This result reveals the stabilization effect of compressibility on the mixing layer. For convective Mach numbers higher than approximately 1.4 (the same value appears in the works of Schadow et al.[186]), the coefficient C_δ remains constant at 0.25-0.3 time the incompressible value.

Equation 2.1.20 has been refined by Murakami & Papamoschou, with respect to experimental results of Goebel & Dutton [105] Elliott *et al* [95], Hall *et al* [107]:

$$\frac{C_\delta}{C_\delta(M_c=0)} = 0.77e^{-3.5M_c^2} + 0.23. \tag{2.1.21}$$

Slessor *et al* [195] have also remarked that with this definition of the convective Mach number, if both flows have very different temperatures, the convective Mach number is managed by the hottest flow (since its sound speed is higher), even though it is not the fastest flow, which is the flow undergoing the most the compressibility. They proposed another definition for the convective Mach number:

$$\Pi_c = max\left(\frac{\sqrt{\gamma}_i - 1}{c_i}\right)(u_1 - u_2) \tag{2.1.22}$$

with γ_i the heat capacity ratio and c_i the sound speed in the flow i. The evolution of C_δ with Π_c is also plotted in figure 2.5.

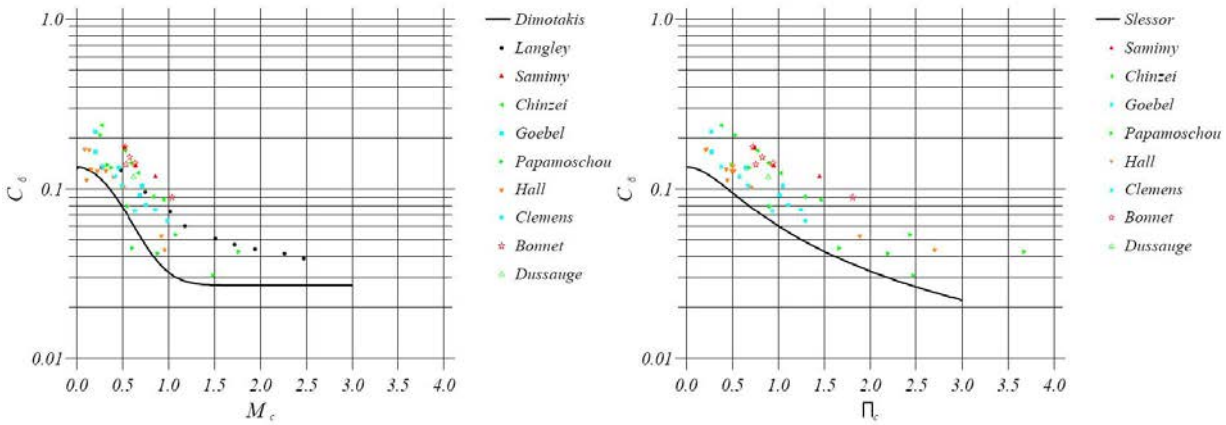

Figure 2.5: Evolution of C_δ as a function of M_c and of Π_c, Dimotakis' formulation [87] (left) correction from Slessor *et al* [195] (right), from Aupoix (2004) [13]

As reported by Simon (2007)[193, 194], several authors investigated the origin of the stabilization effect due to compressibility on the mixing layers. If some authors primarily searched for it in the modification of the dilatation affecting the total dissipation (Zeman [244],[245]), more recent works have identified it in the reduction of pressure fluctuations and thus of the pressure-strain term in the kinetic energy transport equation (Vreman et al. [228], Pantano & Sarkar (2002)[166]). Pantano & Sarkar [166] explain that the reduced pressure-strain term leads to inhibited energy transfer from the streamwise to cross-stream fluctuations. Hence, turbulence levels and growth rates are reduced.

2.1.2 Subsonic jets

2.1.2.1 Physical instabilities in jets

The main instabilities of a jet are often classified in 2 categories: Instabilities characteristic of shear-layer birth and instabilities characteristic of global jet development.

The shear-layer instability mode is associated with a high frequency phenomenon dominated by the Kelvin-Helmholtz instability and its periodical vortical development in the shear-layer. In round jets, due to the axi-symmetry, these Kelvin-Helmholtz vortices initially form vortical rings. The Strouhal number frequently used in the literature to describe the shear-layer instabilities is:

$$St_{\theta_m} = \frac{f\theta_m}{\Delta u} \tag{2.1.23}$$

with θ_m the momentum thickness of the shear-layer and Δu the velocity difference between the flows on both sides of the shear-layer. In the case of studies about initial boundary conditions of jets, a similar normalization is used but θ_0 is the momentum thickness of the boundary layer at the nozzle exit and Δu is equal to the streamwise velocity at the nozzle exit boundary layer edge u_e:

$$St_{\theta_e} = \frac{f\theta_0}{u_e} \tag{2.1.24}$$

This normalization allows to characterize vortex pairing due to the shear-layer instability. Theoretical analyses (Michalke (1964)[154], (1965)[155]) determined the most amplified shear-layer mode at the frequency $St_{\theta_e} = 0.017$, characteristic of the roll-up process. In practice however, the most energetic frequency for non-excited jet is lower due to viscosity, and some experimental measurements reached $St_{\theta_e} = 0.012$ (Zaman & Hussain (1981)[243]) or $St_{\theta_e} = 0.013$ (Bridges & Hussain (1987)[49]). Once the first vortex pairing occurs, the first sub-harmonic around $St_{\theta_e} = 0.065$ becomes preponderant, and so on, with a reduction of the dominant frequency by a factor 2 at each new pairing.

Azimuthal modes

During the Kelvin-Helmholtz pairing process, it is also possible to determine the most amplified modes using an azimuthal decomposition. The varicose (axisymetric) mode corresponds to the mode 0, the helical or sinuous mode corresponds to the mode 1, following ones being referred to as helical modes of order m. Many experimental (Raman *et al* 1994[176], Cohen & Wygnanski 1987[71]) and theoretical studies (Michalke & Hermann[157], Batchelor & Gill[19]) showed that all unstable modes grow close to the exit, with modes 0 and 1 being preponderant, but further downstream of the potential core only mode 1 remains unstable. The varicose or sinuous nature of the most amplified

mode seems to be dependent on the jet boundary layer momentum thickness and in particular of the ratio R/θ_0 with R the jet radius. For high values of R/θ_0, the varicose mode is dominant, while below $R/\theta_0 \simeq 6.25$ (Michalke & Hermann (1982)[157]), the sinuous mode is the most amplified. Regarding the evolution of a mixing layer in a real jet, the value R/θ_m is initially important and then decreases further downstream, which is coherent with the mode 1 dominant downstream the potential core.

Jet-preferred mode

The second main instability found in jets is the jet-preferred mode at the frequency f_p. It is a low-frequency oscillation due to the evolution of the large-scale coherent structures. Since these coherent structures are linked to the occurence of vorticity rings, Bridges and Hussain (1987)[49] have also called these large-scale structures "jet column vortices". They are often observed around the end of the potential core. Some studies (for instance Hussain & Zaman (1981)[119]) suggested that this instability is quite independent of initial conditions and depends merely on the Reynolds number based on the exit diameter $Re_D = U_{jet}D/\nu$. Therefore the most popular Strouhal number in the study of such instabilities is:

$$St_D = \frac{f_p D}{u_e} \tag{2.1.25}$$

where D denotes the jet diameter. Bridges & Hussain found values between 0.3 and 0.5. In his experiment, Zaman (1985)[240] obtained that the "jet column mode" was characterized by a Strouhal number St_D between 0.65 and 0.85, but most of experimental and numerical works, at various Re_D, exhibited values between 0.3 and 0.6. (See the table established by Gutmark & Ho (1983)[106], and the recent work of Kim & Choi (2009)[128]). It has been observed that generally, an excitation at this frequency induces an amplification of the spreading rate and of the noise due to this instability.
However, Crighton & Gaster (1976)[75] and Petersen & Samet(1988)[168] suggested that

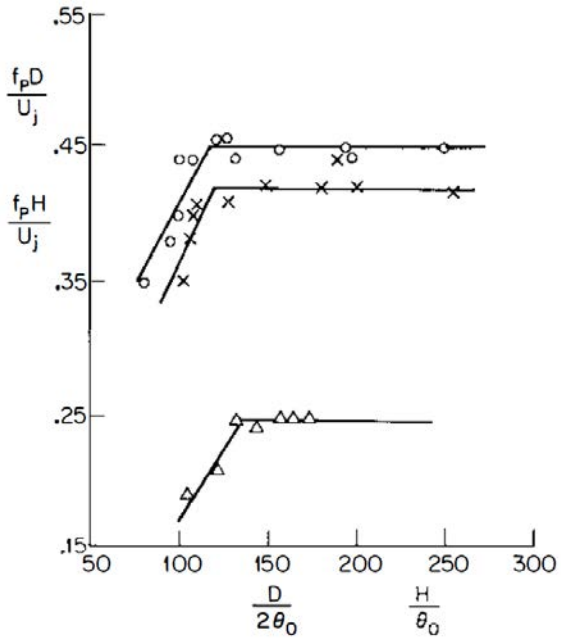

Figure 2.6: Strouhal number of preferred mode in jets versus characteristic length scale ratio:round jets (circles[126] and cross[89]) and planar jets (triangles[113]). From Ho & Huerre (1984)[112]

the jet preferred mode could be the shear-layer mode that becomes unstable near the end of the potential core. In such an approach, they used the normalization:

$$\frac{f_p \theta_s}{u_e} \tag{2.1.26}$$

where θ_s is the momentum thickness of the shear-layer at the end of the potential core. Actually, this idea is strengthened by the results of many authors (Kibens (1981)[126], Drubka(1981)[89], Ho & Hsiao (1983)[113]) who have established experimentally that the Strouhal number of the preferred mode is proportional to the Strouhal number St_{θ_e} of the shear-layer mode for low values of R/θ_0. This can be explained by the successive vortex pairings mentioned in the previous paragraph that occur up to the end of the potential core and would lead to a theoretical dominant frequency :

$$f_p = f_{KH}/2^n \tag{2.1.27}$$

where f_{KH} is the natural frequency of the initial vortex shedding and n is the number of vortex pairings existing between the nozzle lip and the end of potential core. Nonetheless, for higher ratios R/θ_0 typically beyond 120, which is the case of most of jets at very high Reynolds number, the Strouhal number St_D remains constant (at a value around 0.4 in the cases of figure 2.6). This Strouhal number locking is not fully understood yet.

Further downstream, an azimuthal secondary instability dominated by streamwise vorticity also exists, but it is generally tough to distinguish for very high Reynolds numbers as the ones we are going to consider for aircraft engine jets and therefore is not developed here. More information can be found in the study of Liepmann & Gharib (1992)[144] or in the one of Brancher et al. (1994)[43].

2.1.2.2 Effects of inflow conditions and Reynolds number effect

It is well-known since the work of Crow & Champagne(1971)[76] and Brown & Roshko (1974)[54] that shear-layer development is influenced by the state of the inflow boundary conditions. The influence of the ratio R/θ_0, which can partly be predicted by inviscid stability analysis, has already been evoked, but there are two additional factors which can affect jet development: the viscous effects, quantified by the Reynolds number, and the turbulent state of the nozzle exit boundary layer, characterized by the ratio $u'_e/u_e/u_e$ where u'_e is the maximum value of axial velocity fluctuations in the boundary layer. Furthermore, the influences of these parameters are not independent.

Two Reynolds numbers are generally used to investigate the viscous effects on the flow field downstream the nozzle. The Reynolds number based on the jet diameter, $Re_D = \frac{u_e D}{\nu}$, and the one based on the boundary layer momentum thickness at the nozzle exit, $Re_\theta = \frac{u_e \theta_0}{\nu}$. Let us remind that both are linked by the ratio R/θ_0 since $Re_D = 2Re_\theta \frac{R}{\theta_0}$.

Boundary layer state: Laminar or turbulent

The most relevant parameter to study the boundary layer state should be the Reynolds number based on the boundary layer momentum thickness Re_θ. However, the range of transitional Re_θ for the boundary layer is not clearly defined. Even though the Re_θ of transition can be estimated for a flat plate boundary layer, this value is highly dependent on the local pressure gradient and free-stream turbulence level and the range of variation appears wide enough to make the characterization of the nozzle exit boundary layer state difficult.

Several authors tried instead to estimate the state of the boundary layer depending on the value of Re_D. According to Bogey & Bailly (2012)[41], from the work of Zaman (1985)[240], jets can indeed be considered as initially laminar for $Re_D \lesssim 10^5$ (as in Crighton (1981)[74]) with some fluctuations of velocity u'_e lower than 1% of the jet velocity u_e. For $10^4 \lesssim Re_D \lesssim 5 \cdot 10^5$, they are initially transitional with $1\% \leqslant u'_e/u_e \leqslant 10\%$. Lastly, for $Re_D \gtrsim 5 \cdot 10^5$, the jets are initially fully turbulent with $u'_e/u_e \geqslant 10\%$.

Nevertheless, similarly as Re_θ, Zaman (1985)[240] and Bridges & Hussain (1987)[49] mention that the value Re_D for which the jet is considered initially fully turbulent could differ depending on wind tunnel characteristics and operating conditions of the experiment. Hence, a certain correlation exists between Re_D and the nozzle exit boundary layer thickness. Harper-Bourne (2010)[108] also pointed out the differences between academic and industrial test-facilities, in particular the larger contraction ratios of nozzles in university-type facilities that could lead, at same Re_D, to a nominally laminar boundary layer, whereas the industrial types may involve a turbulent boundary layer, according to Zaman(2012)[241]. These last authors suggest also that the nozzle geometry would also play an important role. Accordingly, Bogey and Marsden (2016)[38] suggest that the laminar or turbulent boundary layer state could depend on the adverse or favorable pressure gradient that can appear at the exit of nozzles, such as conic nozzles.

Effect on the spreading rate of the mixing layer and the potential core length

The nature of the boundary layer is expected to impact the jet development significantly. Some thorough studies have shown that the spreading rate and potential core length are largely affected by the turbulence rate of the nozzle exit boundary layer as well as by its momentum thickness. In particular, they investigated these influences by means of different sources of excitation, experimentally and numerically.

For instance, in their experiments, Hussain & Zedan (1978)[117] generated axial velocity fluctuations in turbulent and laminar boundary layers of identical Re_θ using various nozzle shapes, Hill et al (1976)[111] used thick tape trip at the entrance of the nozzles whereas Husain & Hussain (1979)[116] used trip rings close to the nozzle exit. Zaman (1985)[240] generated excitation in the boundary layer by means of loudspeakers. However, in all the experiments it is difficult to isolate a single parameter and to vary it without

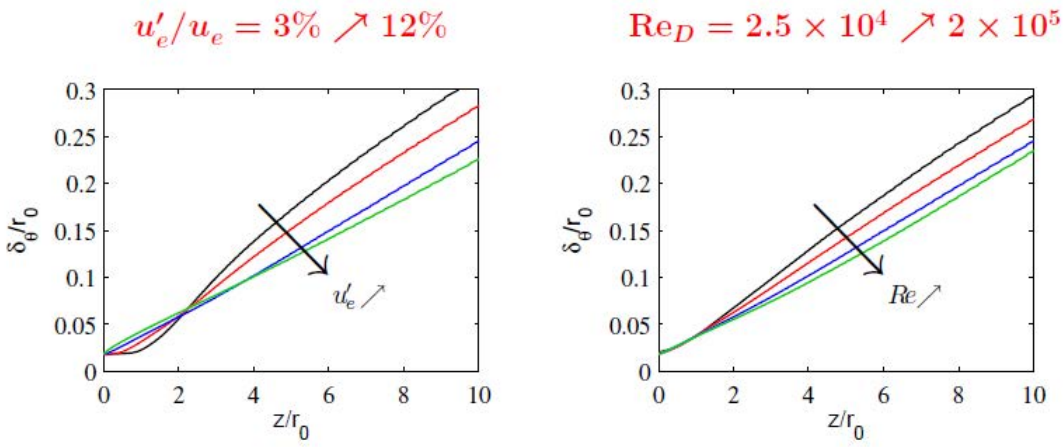

Figure 2.7: Effect of the fluctuation level $\frac{u'_e}{u_e}$ in nozzle exit boundary layer[41] and of Re_D[40] on the spreading rate of a round jet mixing layer, from Bogey(2013)[30]

affecting the others. With recent progress in turbulence-resolving simulations, it has become possible to investigate the effect of each parameter more independently. Among all the numerical studies investigating turbulent level in nozzle boundary layers, the important work of Bogey et al. (2012)[41] can be cited, in which turbulent perturbations are added thanks to random low level vortical disturbances decorrelated in azimuth.

As a general result, it has been observed that initially turbulent boundary layers provide a lower spreading rate and a longer potential core than initially laminar or transitional ones. For instance, Hill et al (1976)[111], Raman *et al* (1994)[176] and Antonia & Zhao (2001)[11] and Xu & Antonia (2002)[239], among others, have remarked that jets with an initially transitional mixing-layer exhibit a shorter potential core than jets with a mixing-layer that is initially fully turbulent. These results have been confirmed by works of Bogey & Bailly [33]. More recently Bogey et al. (2012)[41] have numerically investigated the effect of u'_e/u_e, with both Re_D and Re_θ fixed ($Re_D = 10^5$ and $Re_\theta \simeq 900$), and actually observed the opposite trend. They indeed found that the higher the fluctuation level, the longer the potential core length, and the lower the spreading rate. In a similar way, they made variations of Re_D between $2 \cdot 10^4$ and $2 \cdot 10^5$, keeping a constant fluctuation level to $u'_e/u_e = 9\%$[40]. Globally, they observed the same effect in increasing the diameter based Reynolds number than by increasing the fluctuation level in the nozzle exit boundary layer (see figure 2.7). This behavior is attributed to the weakening of large-scale structures and the strengthening of fine-scale structures.

Hussain & Zedan (1978)[118] investigated the effects of boundary layer thickness and of turbulent peak level in quasi-laminar nozzle exit boundary layers. Experimentally they found that the effect of boundary layer thickness is much lower than the one caused by different values of u'_e/u_e. Bogey & Bailly (2010)[34] also investigated the effect of boundary layer thickness and established that jets with a thinner boundary layer develop earlier but at a slower rate, yielding longer potential cores. However, Kim & Choi (2009) [128] established that as for the boundary layer state, an inter-dependency between Re_D and R/θ_0 exists regarding the development of initially laminar jets. Depending on the value of Re_D, the influence of the exit boundary layer on the jet development is different. In particular, they obtained for a Re_D of 3600 that a boundary layer thickness decrease induces the generation of large structures earlier downstream the exit, which in turn enhances the mixing and the turbulent intensity. Conversely, for higher Reynolds numbers (beyond 10^4), when the boundary layer thickness is decreased, the early growth of the mixing-layer generates numerous small scale structures, due to early shear-layer saturation, producing lower turbulent intensity and mixing. In particular, Bridges & Hussain (1987)[49] observed for Re_D around $2 \cdot 10^5$ that when the ratio R/θ_0 increases, the vortex pairing process of the shear-layer mode does not have the time to occur and transitions immediately toward jet column vortices.

2.1.2.3 Influence of temperature gradients

Even though most of the studies on round jets have been performed for cold jets, several ones have focused on the effect of temperature on its downstream development, as for example, Witze (1974)[234], Lau (1981)[139], Tanna (1977)[210] and more recently, Bridges & Wernet (2003, 2007)[50, 53], Bodony & Lele, (2005)[25] or Bogey & Marsden (2013)[36]. These studies have shown some recurring trends in the development of the jet, although it is difficult to identify the part which is due to the temperature gradient and the part which is due to the change of other jet parameters. Indeed, increasing the jet temperature decreases density and thus the value of $Re_D = \frac{u_e D}{\nu}$ for instance. The temperature parameter often considered in the dedicated studies, is the ratio of temperature $TR = T_e/T_a$ or the Total

Authors	Re_D	Re_θ	$\frac{u'_e}{u_e}(\%)$	$\frac{R}{\theta_0}$	M_j
Hussain & Zedan[117]	$5 \cdot 10^4$ - $1.4 \cdot 10^5$	200	8.4 - 17.2	132 - 340	0.03 -0.07
Hussain & Zedan[118]	$6.6 \cdot 10^4$ - $1.4 \cdot 10^5$	180 - 350	6 - 11.7	108 - 355	0.03 -0.07
Husain & Hussain [116]	$2.4 \cdot 10^5$	432 - 1445	2.5 - 3.2	100 - 300	0.1
Zaman [240]	$5 \cdot 10^4$ - $3 \cdot 10^5$		0.2 0.3- 10	135	0.1 - 0.5
Bridges & Hussain [49]	$2 \cdot 10^5$	300 - 1600	0.2 - 4	87 - 250	0.15 - 0.35
Raman & Zaman [177]	$6 \cdot 10^5$		0.15 - 5		0.05 - 0.44
Bogey & Bailly [31]	$4 \cdot 10^5$	600 & 1000		20 - 33	0.9
Kim & Choi [128]	$3600, 10^4, 10^5$	200 - 2000		25 - 90	
Morris & Zaman [159]	$2.8 \cdot 10^5$	90 - 270	6.7 - 7.5	260 - 770	
Bogey *et al* [34]	10^5	900	0 - 12	40 - 180	0.9
Bogey & Bailly [41]	10^5	900	0 - 1.9	53 - 57	0.9
Bogey & Bailly [40]	$2.5 \cdot 10^4$ $2 \cdot 10^5$	900	0 - 1.9	56	0.9

Table 2.1: Noticeable studies of initial conditions on the development of subsonic jets. $\frac{u'_e}{u_e}$ refers to velocity fluctuations in the boundary layer at the nozzle exit.

Temperature Ratio $TTR = T_0/T_a$ (T_a referring to the ambient temperature and T_0 being the jet total temperature).

As a first result, all authors report that for jets of the same nozzle diameter and velocity, the increase of temperature induces a quicker development of the jet, with higher spreading rates and turbulence intensity and shorter potential core lengths. However, Bogey & Marsden (2013)[36] have shown that the major cause of this behavior is the decrease of Re_D. Indeed, comparing two jets of different temperature ratio but of similar Re_D (by increasing the diameter) they obtained much less discrepancies on jet development.

Saxena & Morris also investigated the evolution of temperature development in the jet through the thermal core length L_T defined as the distance from the nozzle exit to the point where the relative normalized temperature:

$$\Theta(x, r = 0) = \frac{T(x, r = 0)/T_0 - 1}{T_e/T_0 - 1} \tag{2.1.28}$$

falls to 0.98. They observed that the thermal core length is shorter than the potential core length, but follows the same trend depending on the temperature ratio.

We can also notice regarding noise emission, that many studies (Tanna (1977)[210], Bodony & Lele (2005)[25]), highlighted a Mach number $M_a = u_e/c_a$ from which the effect of temperature changes. Hot jets are less noisy than cold ones only beyond $M_a > 0.7$. This noise reduction due to jet heating at high Mach numbers has regularly been observed in the literature.

2.1.2.4 Effect of an external co-flow

The effect of an external co-flow enables to investigate the flight effect on the development of the jet. In the following, the core jet will be referred to as the primary jet while the co-flow will be referred to as the secondary stream.

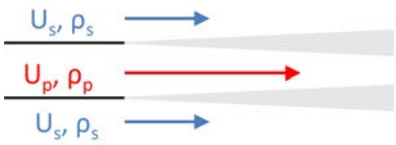

Figure 2.8: sketch of a jet with an external co-flow

Classically the driving parameter for jets with co-flow is the momentum ratio $\rho_s u_s^2/\rho_p u_p^2$. However, considering the same fluid in both streams and neglecting the temperature variations here, the main parameter to characterize jets with co-flow and coaxial jets becomes the ratio of initial secondary velocity to primary exit velocity $r_u = u_s/u_p$.

As a first observation, the existence of an external flow involves a lengthening of the potential core. It can be established from the measures of Forstall & Shapiro (1950) that the potential core length L_p of the primary jet depending on r_u, is given by :

$$\frac{L_p(r_u)}{L_p(r_u=0)} = 1 + 3r_u \tag{2.1.29}$$

This expression has been later refined by Murakami & Papamoschou (2002)[161] based on the spreading rate evolution of the mixing layers and accounting for compressibility effects:

$$\frac{L_p(r_u)}{L_p(r_u=0)} = \frac{1}{\delta'_{r_u}} = \left[0.14\frac{(1-r_u)(1+\sqrt{s_u})}{1+r_u^{3/2}}\right]^{-1}\left[0.23+0.77exp\left(-3.5M_{c_u}^2\right)\right]^{-1} \tag{2.1.30}$$

where δ'_{r_u} and M_{c_u} are respectively the spreading rate and the convective Mach number of the mixing layers. Based on different experimental datasets, they also developed a correlation for the determination of the secondary potential core length L_s in coaxial jets (see ref. [161]).

2.1.3 Supersonic jets

2.1.3.1 Influence of the exit Mach number and of the nozzle pressure ratio

As presented in sect 2.1.1.4, compressibility impacts the mixing layer development. In the case of high subsonic and supersonic jets, shock and expansion waves are likely to influence jet development. Therefore it is essential here to distinguish whether the jet flow is supersonic or subsonic.

The jet exiting from a cylindrical pipe is fully determined by its exit Mach number M_e and by its Jet Pressure Ratio (JPR) given by $JPR = p_e/p_a$, where p_e is the nozzle exit pressure and p_a the ambient pressure. If $p_e = p_a$, the nozzle is called adapted.

In the more general case of non-uniform flow at the nozzle exit, the generative conditions at the nozzle inlet p_i and T_i (respectively the total pressure and the static temperature) are rather used. The Nozzle Pressure Ratio (NPR) is thus given by NPR=p_i/p_a.

Different kind of nozzle geometries exist, generally referenced in three categories: divergent, convergent and convergent-divergent nozzles. In practice, mostly convergent and convergent-divergent are encountered in aeronautics. The nozzle throat is the location of minimum passage section. Depending on the NPR of the nozzle, the flow velocity at the nozzle throat can be either subsonic or sonic. If the flow is subsonic at the throat, it is at the nozzle exit as well, and the pressure at the nozzle outlet is the ambient pressure $p_e = p_a$. If the flow is sonic (M=1) at the nozzle throat, the nozzle exit pressure depends on the geometry of the nozzle:

Convergent nozzle

In purely convergent nozzles as depicted in figure 2.9, the critical value of NPR which determines the flow nature at the nozzle throat is defined by:

$$NPR_c = (1+\frac{\gamma-1}{2})^{\frac{\gamma}{\gamma-1}} \tag{2.1.31}$$

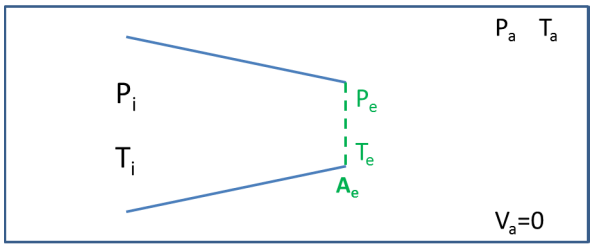

Figure 2.9: Sketch of a convergent nozzle

For the air considered as a perfect gas with $\gamma = 1.4$, the value of $\text{NPR}_c \simeq 1.89$.

- if $\mathbf{NPR} < \mathbf{NPR}_c$, the flow is subsonic at the throat, $p_e = p_a$ and the nozzle is adapted;
- if $\mathbf{NPR} = \mathbf{NPR}_c$, the flow is sonic at the throat, the flow is perfectly expanded $p_e = p_a$ and the nozzle is adapted;
- if $\mathbf{NPR} > \mathbf{NPR}_c$, the flow is sonic at the throat, $p_e > p_a$ and the flow is thus under-expanded. The return to ambient pressure occurs through oblique expansion waves at the trailing edge of the nozzle, which involves shock cells.

Convergent-divergent nozzle

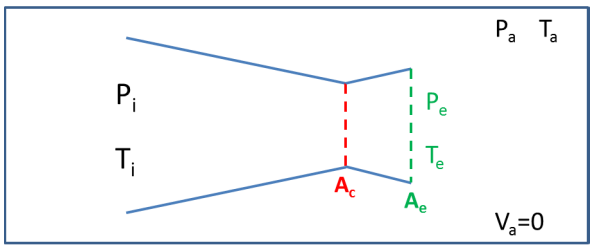

Figure 2.10: Sketch of a convergent-divergent nozzle

In a convergent-divergent nozzle as depicted in figure 2.10, the flow pattern downstream of the throat is much more complex since the flow is choked depending on both the NPR and the area ratio A_e/A_c. The several situations that can exist in the divergent part are summarized in sketches in figure 2.11. Three operating conditions enables to reach the nozzle adaptation:

- an entirely subsonic regime (case (a)), up to the flow becomes choked (case (b)). The NPR value for achieving this later case depends on A_e/A_c;
- a transsonic regime, existing once the flow is choked. In this regime, the supersonic flow downstream of the throat returns to a subsonic regime and to the ambient pressure thanks to a strong shock in the divergent part (case (c)). The limit of this regime appears when the shock reaches the nozzle exit (case (d)), thus when $NPR = NPR_c$;
- a supersonic regime, corresponding to design conditions, thus at a specific design pressure ratio $NPR = NPR_d$, in which no shock occurs neither in the divergent part nor in the jet (case (f)).

Last, it is important to note that in supersonic regime two cases can exist:

- if $NPR_c < NPR < NPR_d$, then $p_e < p_a$ and the nozzle is overexpanded (case (e));
- if $NPR_d < NPR$, then $p_e > p_a$ and the nozzle is underexpanded (case (g)).

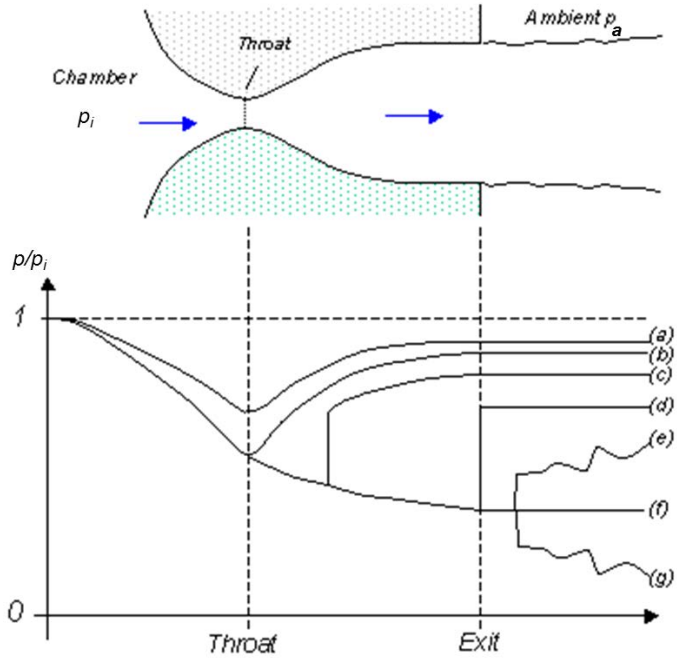

(a)

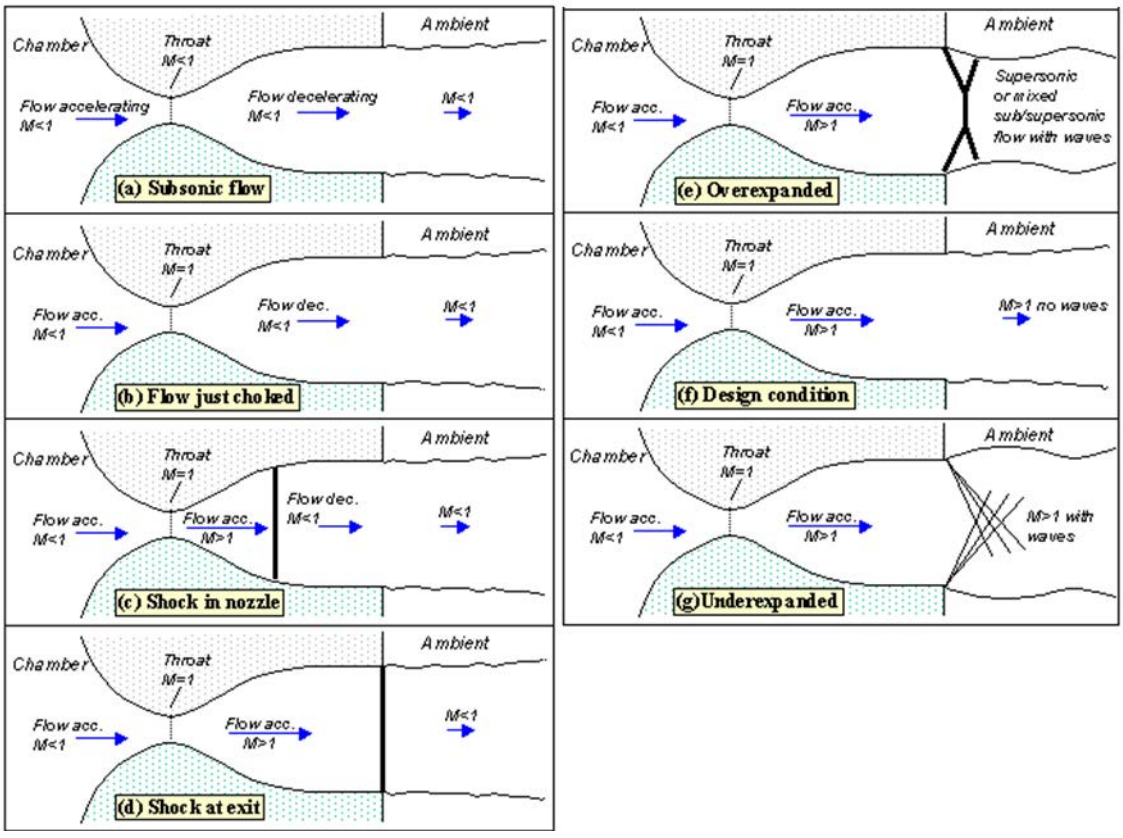

(b)

Figure 2.11: Different operating conditions in convergent-divergent nozzles, from Virginia Tech. University [6]

2.1.3.2 Shock-cell structure of under-expanded jets

Within the framework of the present thesis, only purely convergent underexpanded jets are considered. To analyze the shock-cell structure of such jets, the simple case of a supersonic jet with a uniform exit is considered in this section. In such a case, as mentioned previously, the nozzle exit values are determined by M_e and JPR only.

First, in under-expanded jets, the isobar lines constituting the outer boundary of the jet are curved as shown figure 2.12. An increase of JPR increases the curvature of the isobar line, as well as its outward initial deviation (It can be noticed that for a pure convergent nozzle without parallel walls, the flow at the exit is always non-uniform while the sonic line is curved and the nozzle cannot be adapted).

In low supersonic regimes and JPR just above 1, the expansion waves issuing from the nozzle lip reflect on the isobar lines, producing compression waves. These in turn reflect on the isobar lines, and so on, giving the periodic pattern in figure 2.13.

With an increase of the JPR, some shocks appear before compression wave reflections on the outer boundary of the jet, and a further increase leads to shock reflections on the jet axis. In the end, for high JPR, the regular shock reflections on the jet axis are replaced by a Mach disk, whose size increases up to more than half of the jet width for highly under-expanded jets, as represented in figure 2.12. It can be noted that the addition of a small divergent part at the nozzle exit induces a reduction of the Mach disk size, as well as of the shock-cell length. It is a similar effect to decreasing the JPR. This effect is also observed in presence of an external parallel flow. The higher the external Mach number, the smaller the deviation angle and the closer to nozzle adaptation.

Case of axisymmetric sonic jets

Regarding a sonic round jet exiting from a convergent nozzle, for instance a conic one, most of the previous behaviors also exist, but some specifics due to the axisymmetry are noteworthy.

First of all, in axisymmetrical cases, the deviation of the flow at the nozzle exit is lower that in planar jets, and the sonic line at the throat is less curved. It follows that the oblique shocks are also less "deviated". Then, at equivalent exit conditions of M_e and JPR, the wave length of the shock-cells is smaller than in the planar case. It is also observed that in conical flows, the focusing of compression waves to form a shock converging toward

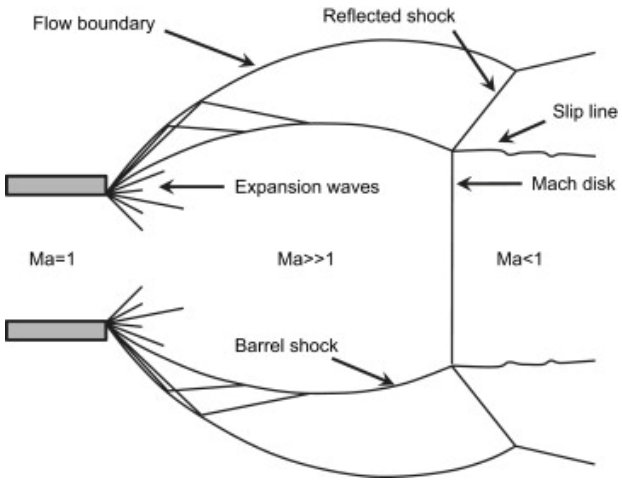

Figure 2.12: Different zones of a highly under-expanded jet, from Verhelst et Wallner (2009)[219]

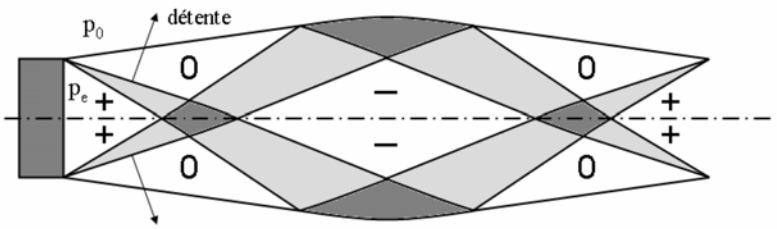

Figure 2.13: Sketch of the expansion/compression wave pattern in under-expanded jets, from Chauvet PhD Thesis (2007)[65]

the axis is accelerated, which is consistent with smaller shock-cell widths. Conversely, the diverging shocks are weakened. Last, an important characteristic of axisymmetric jets lies in the impossibility of a regular reflection of a shock on the jet axis. Instead, the shock curves and turns into a shock normal to the axis. It is thus more frequent to observe Mach disks in round jets than in planar jets.

Shock-cell width

As it can be observed in figure 2.14, representing a schlieren visualization of an under-expanded jet, the shock-cell pattern appears quasi-periodic. This quasi-periodic repetition

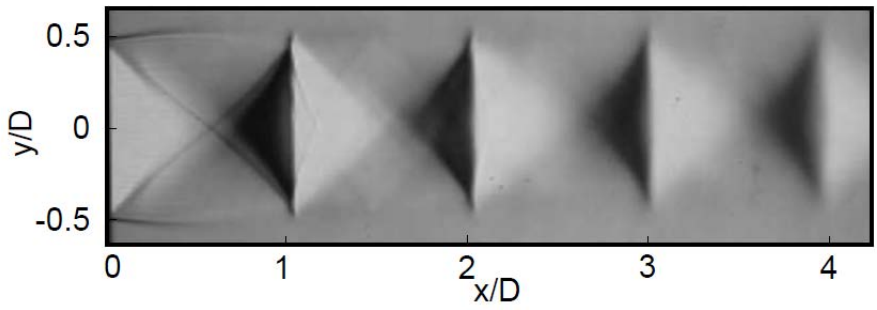

Figure 2.14: Schlieren image of a supersonic shocked jet, issuing from a convergent nozzle., from André (2012)[8]

of shocks in under-expanded jets has been investigated analytically by several authors since the beginning of the twentieth century.

The first to focus theoretically on this question is Prandtl in 1904 [172], based on previous experimental observations of Emden (1899). In the case of slightly under-expanded jets, he linearized the Euler equations around the conditions of the adapted jet and solved them using Bessel's functions. Pack (1950)[162] refined the demonstration, changing some Prandtl's hypotheses, in particular regarding the Mach number to consider for adapted conditions. Whereas Prandtl initially thought the exit Mach number was relevant, Pack introduced the perfectly expanded Mach number M_j, which is obtained for a jet of similar NPR, but which would be adapted. Its expression is:

$$M_j = \sqrt{\frac{2}{\gamma - 1}\left[JPR^{\frac{\gamma-1}{\gamma}}(1 + \frac{\gamma - 1}{2}M_e^2) - 1\right]} \tag{2.1.32}$$

The expression of the shock-cell length for a slightly underexpanded sonic jet obtained by

Pack :

$$\lambda/D \simeq 1.22\sqrt{M_j^2 - 1} \tag{2.1.33}$$

where D is the jet exit diameter, fitted much more the experimental measurements and has proven to be a good approximation in many cases.

Actually, the last improvement in the theoretical description of the shock-cell structure results from the work of Tam (1972)[207], which describes the complete evolution of pressure oscillations in an axisymmetrical jet:

$$p(x,r) = \sum_{n=1}^{\infty} A_n J_0\left(\frac{2\mu_n r}{D_j}\right) cos(k_n x) \tag{2.1.34}$$

where J_0 refers to the Bessel's function of order 0 and D_j the diameter of the equivalent fully expanded jet. The expressions of A_n and k_n can be found in Tam (1972)[207].

Tam et al. (1985) [208] later developed another model taking into account the shortening of the shock-cells further downstream due to viscous and turbulence effects and by the merging of mixing layers. They found that turbulence and viscosity attenuate pressure fluctuations but do not affect the shock cell length. This one would be essentially reduced by the mean velocity profile diffusion, as the mixing layers spread. The same results have been later obtained by Choi & Lele (2001) [70] thanks to parabolized stability equations (PSE).

2.1.3.3 Shock/mixing layer interactions and shock associated noise

The interactions between the shocks and the mixing layer are an important field of investigation since the first observations of Powell in 1951 [171], since they are known to be strongly related to shock associated noise.

A phenomenon primarily addressed is the emission of tonal noise by the jet in the presence of shock cells. This shock associated noise is referred to as the screeching tones. Many authors addressed this phenomenon in the second part of the twentieth century and a large review can be found in Raman (1999) [175]. More recently, Panda [164] [165] and André et al. [10] [9] have investigated the noise production mechanisms experimentally, particularly focusing on shock oscillation detection.

Jet screech

According to Powell [171], screech is the result of a resonance feedback loop. Some large turbulent structures advected in the mixing layer interact with shocks when passing through them, generating an acoustic wave in the upstream direction. When this acoustic wave encounters the nozzle lip, it gives birth to embryo disturbances in the mixing layer. This mechanism can be separated into 4 distinct phases [175]:

1. Instability wave growth in a shock-containing jet
2. Instability-shock interaction
3. Acoustic feedback
4. Mixing layer excitation in the vicinity of the nozzle exit

Powell [171] proposed a model to predict screech frequency, based on the idea that the characteristic time scale of the screech process is the sum of the time needed for instabilities to reach the shock and the time for acoustic wave to radiate up to the nozzle lip:

$$T_s = \frac{L_s}{U_c} + \frac{L_s}{c_0} \tag{2.1.35}$$

where T_s is the screech period, L_s the shock cell length, U_c the convective velocity of turbulent structures in the mixing layer and c_0 the speed of sound outside the jet. This leads to the following expression for the screech frequency f_s:

$$f_s = \frac{U_c}{L_s(1+M_c)} \tag{2.1.36}$$

with $M_c = U_c/c_0$ the convective Mach number [1]. This formula has been widely acknowledged in the literature. The remaining issues regard the expressions of U_c and L_s.

It must be noted that Tam et al. [206] find the same result by directly linking the screech and the broadband noise through the interaction between shocks and turbulent structures. From there, they assume that the screech frequency must be the broadband central frequency for the upstream direction. Tam et al. [206] also rewrote the formula according to jet exit characteristics, D_j, M_j and U_j, considering $U_c = 0.7U_j$ and $L_s = 0.8 \cdot 1.306\sqrt{M_j^2 - 1}D_j$ (i.e. 0.8 times the shock cell length of the Prandtl model):

$$\frac{f_s D_j}{U_j} = \frac{0.67}{\sqrt{M_j^2 - 1}} \left[1 + \frac{0.7M_j}{\sqrt{1 + \frac{\gamma-1}{2}M_j^2}} \right]^{-1} \tag{2.1.37}$$

Broadband noise In the literature, the broadband shock-associated noise (BBSAN) is also explained by the interaction, weak but coherent, of turbulent large scale structures of the mixing layer with the shocks in the jet (Seiner & Norum 1979, Tam & Tanna 1982, Choi & Lele 2001).

According to Harper-Bourne & Fisher (1974)[109], BBSAN exhibits a broad-band spectrum with a theoretical peak:

$$f_p = \frac{n \cdot u_c}{L(1 - M_c cos\theta)} \tag{2.1.38}$$

with $M_c = u_c/c_a$ the ratio of convective velocity of the mixing layer turbulent structure to the ambient sound speed, θ the emission angle of acoustic waves with the jet axis, L the shock width and n the number of the harmonic.

2.1.4 Coaxial jets

The present thesis focuses on propulsive jets issued from civil aircraft engines which share many characteristics with coaxial jets. In the literature, coaxial jet studies have most of the time been motivated by the reduction of jet noise. In the first part of this section, studies based on academic cases are presented. Then, more technical configurations, representative of the ones usually encountered in the industry, are investigated.

2.1.4.1 Academic configurations of coaxial flows

To generate co-axial jets, some authors have used an external co-flow (fig 2.15(a)) but most interesting configurations involve two separated streams discharging in a rested environment. In the following, subscripts p and s refer to primary and secondary streams respectively. In the case of coaxial jets, a potential core in the secondary stream also exists as depicted in figure 2.1.21, taken from Murakami & Papamoschou (2002).

1. NB: the convective Mach number here is different from the one defined in the case of canonical shear layers subsection 2.1.1

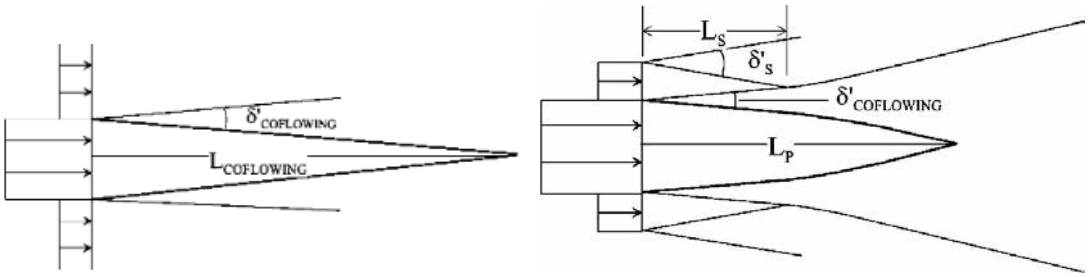

(a) (b)

Figure 2.15: Sketch of mixing layers in a jet with co-flow (a) and of a coaxial jet (b), with $r_u < 1$, from Murakami & Papamoschou (2002)

In the following, it is assumed that both streams involve the same fluid at the same temperature. The parameter $r_u = u_s/u_p$ is therefore considered, with the addition of the ratio of densities $s_u = \rho_s/\rho_p$ when necessary, in order to maintain the formalism previously adopted for mixing layers. The primary jet refers to the core jet and the secondary jet to the co-flowing jet around.

Two exit velocity profiles patterns can be observed in coaxial jets, as represented in figure 2.16, depending on the value of r_u:

If $r_u < 1$ the initial outer stream is slower than the primary one and the configuration is classified as having a Normal Velocity Profile (NVP).

If $r_u > 1$ the initial outer stream is faster than the primary one and the configuration is classified as having an Inverted Velocity Profile (IVP).

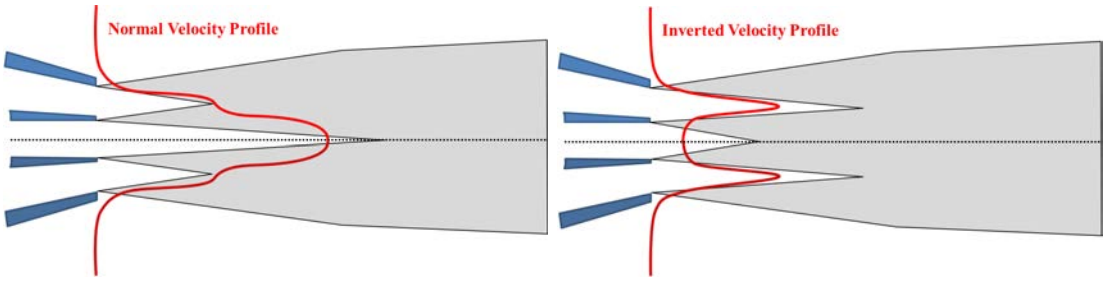

(a) (b)

Figure 2.16: Two kinds of velocity profiles in coaxial configurations: (a) Normal velocity profile (NVP), (b) Inverted Velocity Profile (IVP)

Ko & Kwan (1976)[130] and Kwan & Ko (1977) [136]have identified 3 zones in the development of coaxial jets as depicted in figure 2.17:

- The initial merging zone, starting from the jet exit up to the end of the secondary potential core.
- The fully developed zone, starting when both jets have totally merged and that the flow is self-similar and comparable to the one of a simple round jet.
- The intermediate zone that connects both previous zones, and which represents the transition between them.

This representation of coaxial jets was primarily established for NVP flows, but remains valid for IVP ones, as noted by Ko & Au (1981[131], 1982[132], 1985[133]) and Au & Ko (1987)[12].

NVP jets are by far the most studied case, in particular since Williams et al. (1969), observed that a low speed annular flow around the core jet can reduce the radiated noise. This result has been verified several times, but as initially addressed by Tanna (1980)[211] and more recently by Zaman & Dahl (2007)[160], noise must always be compared to the noise produced by an equivalent simple jet of similar momentum, mass flow rate, thrust, etc [2]. Thus, the interest of NVP configurations is not always obvious. Besides, IVP jets have also shown interesting noise reductions for values of r_u close to unity, mainly due to a faster decrease of the maximum mean velocity value. If the velocity ratio r_u becomes significantly larger than unity, the noise emitted by the outer shear layer dominates the previous effect, which results in an overall noise increase.

Several studies of imperfectly expanded supersonic jets have also investigated the effect of a co-flowing stream on the shock associated noise. For example, Tam et al (2009)[209] thoroughly studied the noise of dual-stream jets while André et al. (2012) [8] investigated the flight effect on the noise emitted by underexpanded jets. In particular Tam et al. proposed a model to account for shock/mixing layer interactions including both outer and inner mixing layers when the secondary stream is underexpanded (see figure 2.18).

2.1.4.2 Characteristics of civil aircraft engine jets

The characteristics of a civil aircraft engine are more dependent on operating conditions than on nozzle geometry, which rarely varies significantly from one aircraft to another. However, as presented in the introduction, the quasi-totality of current engines jets are dual-streams jets, with a hot primary flow.

Geometric characteristics

Regarding the geometry, the current trend in commercial aviation features externally mixed jets (i.e. the primary and secondary streams are separated in the nozzle, and only merge downstream from the exhaust), but primary and secondary flows mixed inside the nacelle before the exhaust can also be encountered. Such a mixing can be accelerated by an internal "mixer" nozzle as represented figure 2.19(a). All externally mixed engine jets present a primary exit plane located downstream of the secondary or fan exit plane. Thus, the outer shear-layer starts to develop earlier than the inner shear-layer, as represented

2. Different definitions of equivalent simple jet exist in the literature

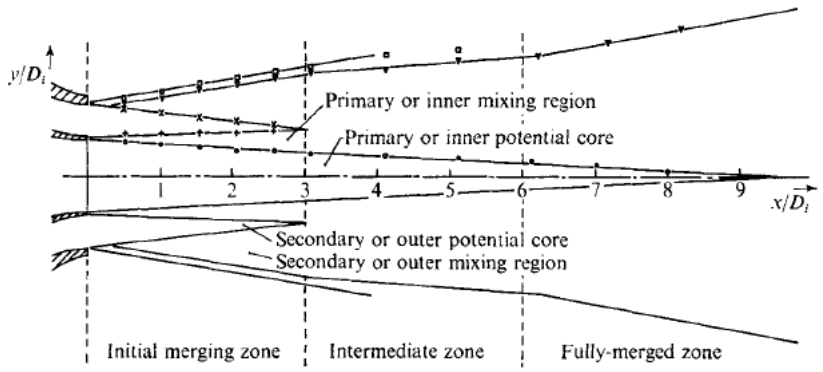

Figure 2.17: Three zone decomposition of a coaxial jet, in the case of $r_u < 1$, from Ko & Kwan (1976)

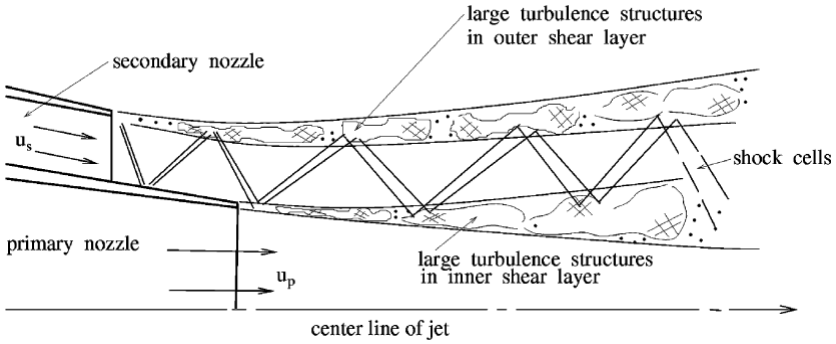

Figure 2.18: Sketch of shock-cell interactions in a dual-stream jet, from Tam et al. (2009)[209]

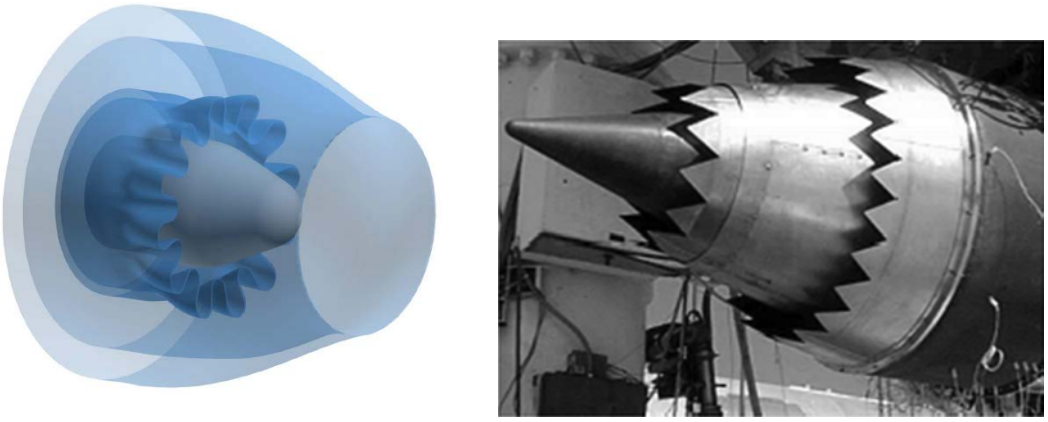

(a) (b)

Figure 2.19: Noise reduction devices: (a) Nozzle geometry of an internally mixed jet, from Fosso Pouangué et al. (2014)[97], (b) Nozzle with chevrons (NASA), from Bianchi et al. (2014)[22].

in the figure 2.18. In addition, some devices are sometimes added to reduce jet noise by accelerating the mixing (as chevrons in figure 2.19(b)) and thus limit acoustic sources due to large structures in the mixing layers. Furthermore, modern engines generally exhibit an external plug for aerodynamic performance reasons, which is also observable in figure 2.19(b).

Another point that characterizes the geometry of the nozzle and significantly affects the evolution of the flow is the design of internal ducts. Generally, the primary duct is purely convergent, but both convergent and convergent-divergent are used for the bypass duct. Most of the time the ratio of the bypass radius to the core radius is between 1.8 and 2.3.

Such complex configurations have been investigated experimentally in the eighties, by Janardan et al. (1984)[121] in particular, who studied some nozzle concepts to reduce the shock noise at supersonic operating points. More recently, noise reduction research at lower regimes has motivated experimental campaigns of such dual-stream configurations with an external plug (Saiyed et al. (2003)[183], Huber et al. (2014)[115]) using sometimes some chevrons (Bridges et al. (2003)[51]), beveled nozzles Viswanathan(2004)[221] or with

an internal mixer nozzle (Bridges & Wernet (2004)[52]) at conditions more typical of cruise or take-off. Some noise reductions have been achieved, but the complete understanding of the turbulent physics of such configurations is still an important area of research. In particular, flight effects, installation effects and interactions with the pylon remain subjects of primary interest as suggested by the recent studies of Viswanathan et al.(2011)[223], Huber et al. (2014)[115] or Brichet et al. (2015)[48].

In the present study, only the case of pure convergent primary and secondary ducts, with an external plug and no noise reduction device will be considered.

Operating conditions

The most critical design points for concerns of jet-pylon interaction are the "max take-off" conditions and the cruise conditions. At max take-off conditions, the jet thrust at its maximum, whereas the airplane velocity is not significant, which results in high shear velocity in the outer shear-layer, that involves high turbulent levels and a high spreading rate.

On the contrary, during cruise, the velocity difference between the external flow velocity and the fan jet velocity is much lower but the external pressure is extremely low, which enables the fan nozzle pressure ratio (NPR_{fan}) to reach more than the critical value $NPR_{fan} = 1.89$, inducing critical shock-cell patterns in the fan jet as described by Tam et al. (see figure 2.18).

Cruise conditions will constitute the core of this study. In the generation of engines that equipped aircraft up to the generation of the A350, the NPR_{fan} associated to relatively moderate bypass ratios was high enough (see sec 2.1.3) to produce shocks in the fan jet at cruise and to provide a higher speed in the fan jet than in the core jet. Engines jets thus exhibit an IVP profile as depicted in figure 2.21. Various characteristic values of engine conditions at cruise are given in the table 2.20.

$M_{e_{core}}$	0.7 - 0.8
$M_{e_{fan}}$	1
M_{ext}	0.75 - 0.85
NPR_{core}	1 - 2
NPR_{fan}	2.3 - 2.6
Tt_{core}/T_{ext}	2 à 3
Tt_{fan}/T_{ext}	1.25 à 1.3

Figure 2.20: Characteristic values of a civil aircraft engine at cruise conditions

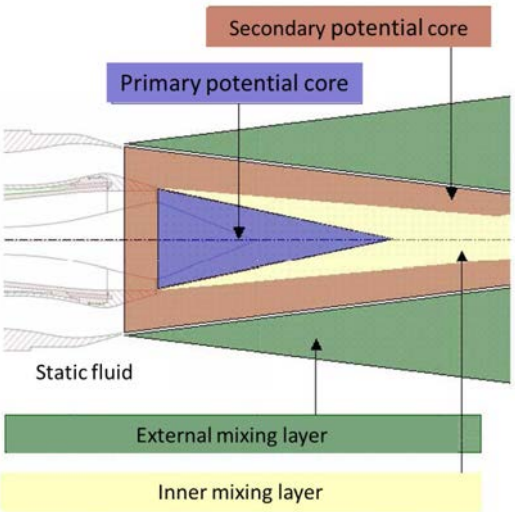

Figure 2.21: Sketch of mixing layers location in a IVP dual-stream jet of civil aircraft engine, from Giner (2011)[103].

Typical maximum exit velocity values in the fan jet at cruise lie in the range $300 - 400$ m/s with a secondary nozzle diameter between 2 and 3 meters. This leads to Re_D values higher than 10^7, which means that the nozzle exit boundary layer is expected to be already

fully turbulent. Nonetheless, it must be noted, that depending on the flight point and engine rates, since convergent nozzles with a strong contraction of the duct induce a favorable pressure gradient, a relaminarization of the boundary layers in the ducts is not totally excluded.

2.1.5 Summary on jet physics

In this section a review of the physical characteristics of the simple and coaxial jets has been performed.

First, it has been seen that jets can be characterized by:

- The vorticity thickness of the mixing layers;
- The potential core length;
- The turbulent intensity and turbulent spectra in mixing layers and downstream of the potential core, on the jet axis line;
- The convective Mach number, which characterizes the compressibility effects in mixing layers;
- The existence or not of shocks in the jet, depending on the exit Mach number and the NPR.

In particular, the early development of shear layers, dominated by Kelvin-Helmholtz instabilities has been described. The different frequencies involved have also been given.

The main parameters, JPR, M_e, R/θ_0, Re_D, u'_e/u_e, defining the jets have been referenced and a review of the literature regarding the jet sensitivity to these parameters has been given. For single stream round jets, the following effects are noteworthy:

- **The diameter based Reynolds number**: experimental results seem to indicate that below $Re_D = 10^5$, if the boundary layer is not tripped, jets are initially laminar and above $Re_D = 5 \cdot 10^5$, they are initially fully turbulent. Between these two values, the jet is likely to be transitional, with a strong dependence to the wind tunnel particularities. However, the ratio R/θ_0 also strongly influences the nature of the exit boundary layer;
- **The nozzle exit boundary layer thickness**: the effect of the nozzle exit boundary layer thickness, characterized by the ratio R/θ_0, is dependent on Re_D, but for $Re_D > 10^5$, the higher R/θ_0 the earlier the development of the shear layer instabilities. Then, small dissipative scales limit the downstream turbulent levels and spreading rate compared to lower values of R/θ_0;
- **The turbulence rate in the nozzle exit boundary layer**: initially laminar or transitional jets involve higher downstream turbulent levels and larger turbulent structures. They also exhibit a shorter potential core than initially turbulent jets. Indeed, the higher the perturbation level u'_e/u_e in the boundary layer, the thicker the early mixing layer, but the smaller the spreading rate. For significant perturbation levels (typically $u'_e/u_e > 5\%$), the influence of boundary layer thickness seems to be less significant;
- **The compressibility**: when the Mach number is high, some compressibility effects appear in the mixing layers, characterized by the convective Mach number. The compressibility has a stabilizing effect on the development of mixing layers by reducing the spreading rate when the convective Mach number increases;
- **The jet temperature**: the higher the difference of temperature with the outer flow, the higher the spreading rate. Moreover, the thermal potential core end is shorter than the velocity potential core;

- **The exit Mach number and the NPR**: if $M_e < 1$, the jet flow is subsonic, and the spreading rate is fairly proportional to the velocity difference between the jet flow and the outer flow If $M_e > 1$, the flow downstream of the nozzle is supersonic and the NPR is close to or higher than a critical value of 1.89. In that case, depending on the $JPR = p_e/p_a$, the jet can be adapted, overexpanded or underexpanded. The underexpanded case ($JPR > 1$) has been detailed, with an emphasis on the existence of shock-cells and the initial outward deviation of the sliding isobar line (the outer boundary of the jet);
- **The shock - mixing layer interaction**: like the main mechanisms of interaction, the main results related to shock associated noise are explained as well as the screech phenomena.

In a second step, the characteristics of coaxial jets have enabled to differentiate Normal Velocity Profiles (NVP) jets, in which the primary exit velocity is higher than the secondary exit velocity, and Inverted Velocity Profiles (IVP) jets, in which the faster flow is the secondary one. It appears that the development of coaxial jets exhibits 3 typical areas, bounded by the end of the different potential cores and finishing by a fully merged zone. Eventually, the characteristics of current civil aircraft engine jets were discussed.

As the jet physics have been presented, it is necessary to provide an overview of the different techniques used for the practical simulations of jets and found in the literature.

2.2 Numerical simulation of turbulent jets

Since the middle of the nineties, the progress of LES and the increase of computational resources, round jets have been a recurrent subject of numerical investigations. Indeed, in addition to being an interesting validation test case for the simulation of free shear flows, with a large volume of available experimental data, it has been seen previously that experimental campaigns fail to isolate the effect of one parameter at a time. Computational Fluid Dynamics (CFD) is much more flexible regarding initial boundary conditions and flow field characterization, which offers a possibility to get a deeper insight to the physics of the jet itself. Nonetheless, the numerical modeling of initial boundary conditions remains a key point to ensure the simulated flow is representative of actual conditions.

2.2.1 Numerical modeling strategy

Motivated by acoustic considerations, first works of turbulent round jets have involved DNS and LES in the whole computational domain. Due to the very high constraint on mesh size and CPU cost, only low to moderate Reynolds number jets were initially simulated, typically at $Re_D < 5000$ for DNS (Boersma et al. (1998), Freund et al (2000)[99, 100]) and Stanley & Sarkar (2000)[204]) and $Re_D < 7 \cdot 10^4$ for LES (e.g. Constantinescu & Lele (2001)[73], Zhao et al. (2001)[246], Bogey et al. (2003)[35]). Only Debonis & Scott (2002)[79] attempted an early LES simulation of an explicit nozzle at high Reynolds number Re_D, around 10^6, but with a very coarse mesh. Thus, due to the very low values of Re_D achievable with DNS and despite the increase of computational means, this numerical approach is not considered as a mature strategy to simulate realistic engine jets. On the contrary, many improvements have been achieved with LES over the last two decades and LES has proven to be an interesting approach for jet noise prediction.

Regarding the subgrid modeling, both explicit and implicit filtering are encountered in the literature. For instance, Bogey et al.[38], Bodony & Lele [26], Kim & Choi [127] or Brès et al. [46] used explicit filtering whereas Shur et al. [187] Uzun & Hussaini [215] or Xia et al. [237] used implicit LES. No consensus exists about this point, but implicit LES seems to be used mostly in the treatment of industrial applications when attached boundary layers do not play a major role.

A key element in LES computations of round jets lies in the specification of the inflow boundary condition. In particular, a first difference between the several studies of the literature lies in the inclusion or not of the explicit nozzle geometry in the computational domain.

As reminded by Bogey & Marsden[38], the explicit nozzle geometry was excluded (except in Debonis (2002) [79]) in the first studies involving LES of round jets. The usual approach was to specify a mean velocity profile (generally hyperbolic-tangent) representative of the nozzle exit flow, onto which some disturbances or instability modes were added to initiate turbulence. The grid count saving due to the exclusion of nozzle boundary layer in LES enables to reach significant values of Re_D, up to $5 \cdot 10^5$. As an example, Bogey & Bailly (2005)[32] and Kim & Choi (2009)[128] have investigated the sensitivity to initial conditions, at $Re_D = 4 \cdot 10^5$ and $Re_D = 10^5$ respectively. Nonetheless, such an approach induces an uncertainty in the origin of the jet exit and the difficulty to insure that the inlet profile is representative of the real flow arises. Furthermore, for real flow, measurements of the initial turbulent state are generally performed slightly downstream of the exit. Therefore, it has appeared necessary to take into account the nozzle geometry so as to improve the treatment of inflow conditions.

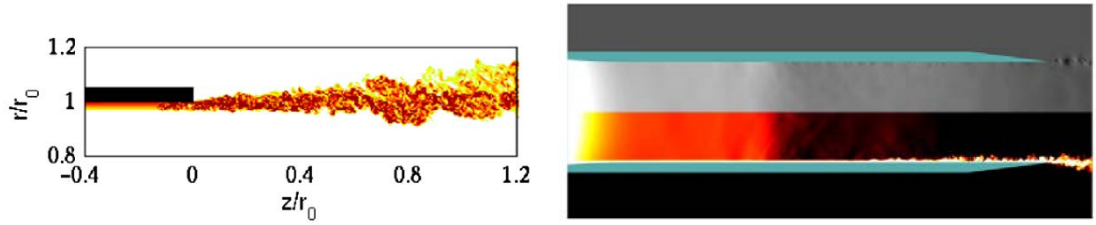

(a) (b)

Figure 2.22: Pipe boundary layer simulated with wall-resolved LES (WRLES) and wall-modeled LES (WMLES): vorticity contour a triggered boundary layer treated with WR-LES by Bogey & Marsden (2016)[38] (left), pressure and temperature contours of a pipe nozzle flow treated with WMLES, from Brès et al. (2015)[46] (right).

One approach directly includes either the final part of the nozzle geometry as in Andersson et al. (2005)[7] or a pipe nozzle in the computational domain of a full LES computation. Such an approach enables turbulence to develop in the pipe whereas, as pointed out by Bodony & Lele (2008) [27], the nozzle lip is supposed to offer "the necessary receptivity location for generated and reflected acoustic waves to scatter into vortical, entropic and acoustic disturbances within the jet's initial shear layers". In practice, obtaining a proper boundary layer development with the expected exit momentum thickness and satisfactory turbulent levels is by far not trivial. In particular, it might be necessary to introduce forcing in order to obtain a satisfactory shear layer development. Although this strategy has been adopted by Bogey et al. [34, 39, 41, 40, 36] to simulate initially laminar and highly disturbed jets up to $Re_D = 2 \cdot 10^5$, or by Uzun & Hussaini (2007)[215] to simulate initially transitional round jets at $Re_D = 10^5$, its computational cost is high. Therefore, the treatment of fully turbulent pipe flow with this approach has lead to simulations of jets with a relatively moderate diameter based Reynolds number, up to $Re_D = 5 \cdot 10^4$ (Bogey & Marsden (2014)[37]). More recently, Bogey & Marsden performed simulations of initially fully turbulent canonical round jets at a Reynolds number $Re_D = 2 \cdot 10^5$, close to experimental values, but their mesh size of almost 3.1 billion points is still out of reach for the industry and real configurations. To reduce the number of cells within the nozzle, some authors use WMLES (Brès *et al* [45, 47, 44, 46], Le Bras et al. (2015)[141]) with good results.

On the other hand, a two-step RANS-LES approach introduced by Shur et al (2005)[187], uses a precursor RANS simulation including the nozzle, which provides the mean inflow to prescribe the inlet boundaries of a second step LES computation (see figure 2.23(a)). This second step does not encompass nozzle geometry but only the isolated jet. This method has been employed by several authors to simulate increasingly complex jets (Viswanathan *et al* [224][226], Shur *et al* [191] and Cai *et al*[60], among others). Nonetheless, this approach still induces important uncertainties in the origin of the jet for comparisons with experimental results. Morevoer, since the first RANS simulation provides only mean data, turbulence generation is required as for an LES simulation that excludes the nozzle geometry. Last, no feedback from the jet simulated in LES mode inside the nozzle simulated in RANS mode is possible. Such a disadvantage can have detrimental effects, especially if pressure changes between the RANS and the LES jet are significant.

As emphasized by Debonis (2007)[78], another approach which offers large expectations for jet simulations is the one-stage fully coupled hybrid RANS/LES simulation of both the nozzle duct and the exiting jet. Indeed, since pure LES for the treatment of very

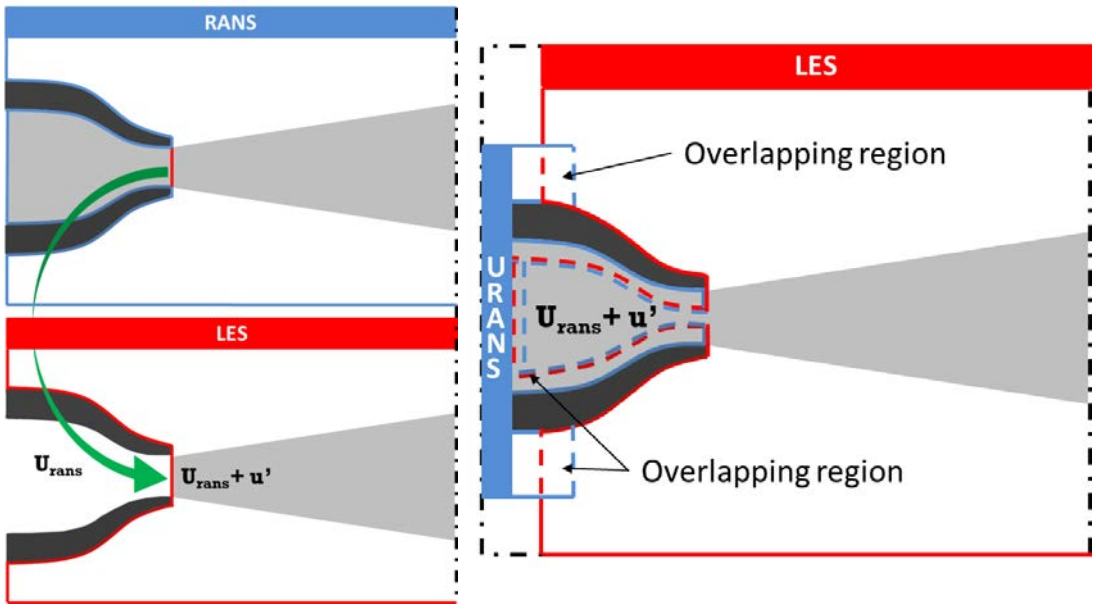

(a) (b)

Figure 2.23: Hybrid zonal RANS-LES strategies: (a) two-stage semi-coupled and (b) one-stage fully coupled approaches.

high Reynolds number wall-bounded flows is very restricting in terms of computational cost, its use in the simulation of explicit nozzles is limited to very simple configurations, like jets exiting from a pipe flow. Even in such configurations, it seems difficult to reach Re_D significantly higher than 10^5 in the near future. To investigate much more complex cases, like dual-stream jets with an external plug at Reynolds number higher than 10^6, the coupling of LES with a RANS modeling in the boundary layer appears as a good alternative strategy. Several methods have been developed since the introduction of the Detached Eddy Simulation (DES) by Spalart et al. in 1997. Sagaut *et al* (2013)[182] reviewed most of the methods currently available such as DES-like approaches (e.g. DDES [201], IDDES[189] or ZDES [80]) and assessed them with regards to validation criteria and the ease of implementation on industrial unsteady flows. Such methods have shown many capabilities for simulating jets. Chauvet et al. (2007) [67], Xia *et al* (2008)[236], Eastwood (2010) *et al* [93], Saxena and Morris (2012) [185], Brunet (2012) [55], for instance, performed jet predictions using such approaches for Re_D higher than $5 \cdot 10^5$. The possible delay in the LES content development has been identified as a critical issue [81] that will be discussed in the following.

In the following, only approaches explicitly modeling a part of the nozzle geometry will be considered, with a particular focus on hybrid RANS/LES methods.

2.2.2 Numerical schemes

Regarding the numerical settings of the LES used in jet simulations, it must be noted that a very wide variety exists in the literature. A first element to take into consideration is the difference of requirements between simulations for aeroacoustic purposes and simulations for aerodynamic purposes. In both cases turbulent lengthscales must be resolved, but in addition, in aeroacoutic simulations, acoustic waves must be propagated up to the limit of the far field, either directly or more usually thanks to an acoustic analogy in the frame of computational aeroacoustics (CAA) [15]).

In particular, aeroacoustic simulations impose strong constraints on mesh refinement in order to propagate a wide range of wavelengths and are much more sensitive to the accuracy and the dissipation of numerical schemes. Therefore, jet noise simulations generally involve very high-order spatial schemes with explicit time integration. As an example, Bogey & Bailly (2006)[29] used a 13-point stencil optimized finite-difference scheme for spatial discretization associated with an optimized six-stage Runge-Kutta explicit algorithm for time integration. The CPU time and memory requirements of this kind of scheme is prohibitive and not necessary to solve aerodynamic problems. Besides, their lack of robustness is also a critical limitation to their use in industrial configurations. Low-dispersive, low-dissipative Taylor-Galerkin finite-element schemes have also been recently employed by Fosso Pouangué et al. (2015)[98] with unstructured grid, but this setup is too binding for aerodynamic purpose.

In purely aerodynamic simulations, more simple and robust schemes, able to deal with complex geometry, are preferable and are mostly used in the frame of finite volume approaches with implicit time integration. For instance, among the most technical configurations treated, Brunet (2010, 2012[57][55]) carried out dual-stream jet simulations thanks to the second order centered spatial scheme of Jameson [120], which is widely adopted in the industry and a second order backward Gear scheme with an implicit LU-SSOR sub-iteration process. In a more accurate approach, another spatial discretization commonly employed is to modify the upwinding part of a second order upwind scheme (Bui (2000[59]), Mary & Sagaut (2002)[151]). This kind of modified scheme, less dissipative than classical spatial schemes used in the industry to carry out RANS simulations (i.e. Roe's and Jameson's), has been used several times over second order accurate spatial schemes, for instance in Gand et al. (2015)[101], in Eastwood & Tucker (2011)[92], in Xia et al. (2012)[237] or in Tyacke et al. (2015)[213].

2.2.3 Inflow conditions and modeling of the internal boundary layer

The modeling of the inner boundary layer has been an intense area of research in the recent years, which still remains challenging as proved by the various strategies enforced by Brès et al (2013,2014)[45, 47, 44], Bogey et al (2014)[37], Liu et al (2013)[147], etc. Eastwood et al(2012) specifically underlined the complexity of modeling the numerous small near-wall streaklike structures with an affordable CPU cost. Depending on the Reynolds number Re_D and the complexity of the jet, the boundary layer can be calculated in LES, in RANS, modeled by a wall function or partially skipped. For example, Bogey et al. directly resolved laminar (2012)[41, 40, 38] or transitional (2016)[38] boundary layers perturbed by vortical disturbances, whereas Brès et al (2013,2014) [45, 47, 44] used a wall model approach developed by Bodart & Larsson [24], in which the boundary layer is calculated with a RANS approach on a specific structured grid and coupled with the LES calculated on the global grid. Le Bras et al. (2015)[141] also enforced a WMLES approach based on the model of Bocquet et al. (2012)[23], while Chauvet et al. (2007) [67], Brunet (2010, 2012)[57, 55], Eastwood et al (2011)[92], Tyacke et al (2015)[213] among other, used an hybrid RANS/LES approach in which the boundary layer is treated with RANS following DES-like principles. On the contrary, Liu et al (2012)[147] have chosen to impose a slipping condition on the inner wall of the ducts, before triggering fluctuations thanks to wall roughness.

2.2.3.1 Inlet mean flow profile

Most of the time the computational domain inside the ducts starts between 0.5 and 1 diameters upstream of the exit, as in the studies of Uzun & Hussaini [215] or Bogey et al. [34, 39, 41, 40, 36, 38].

In such jets exhausting from a short pipe flow, the exit boundary layer thickness is controlled thanks to the prescription of a mean velocity profile at the inlet boundary condition, which in turn determines the boundary layer thickness at the nozzle exit. In the case of initially laminar shear layers, the Blasius laminar boundary-layer profile has been widely used by Bogey et al. [34, 39, 41, 40, 36, 38] through the polynomial approximation:

$$\frac{u_{inlet}}{u_j} = \frac{(r_0 - r)}{\delta_{BL}} \left[2 - 2 \left(\frac{(r_0 - r)}{\delta_{BL}} \right)^2 + \left(\frac{(r_0 - r)}{\delta_{BL}} \right)^3 \right] \quad if \quad r \geqslant r_0 - \delta_{BL} \tag{2.2.1}$$

$$\frac{u_{inlet}}{u_j} = 1 \qquad if \quad r \leqslant r_0 - \delta_{BL} \tag{2.2.2}$$

with δ_{BL} the prescribed Blasius boundary layer thickness.

Bogey & Marsden (2014)[37] investigated the influence of the mean velocity profile used to simulate transitional exit boundary layers. They calibrated their profiles to match experimental transitional profiles and obtained results of the form:

$$\frac{u_{inlet}}{u_j} = \left(sin \left[\frac{\pi}{2} \left(\frac{(r_0 - r)}{\delta_T} \right)^{\beta_T} \right] \right)^{\gamma_T} \quad if \quad r \geqslant r_0 - \delta_T \tag{2.2.3}$$

$$\frac{u_{inlet}}{u_j} = 1 \qquad if \quad r \leqslant r_0 - \delta_T \tag{2.2.4}$$

with δ_T the prescribed transitional boundary layer thickness. This type of profile has also been used in Bogey & Marsden (2016)[38] to simulate a jet issuing from a conical nozzle at $Re_D = 2 \cdot 10^5$, with an exit boundary layer presenting a shape factor of 1.52.

To prescribe mean velocity profiles of turbulent boundary layers, Uzun & Hussaini [215] have preferred to use profiles given by the Spalding law [203].

Last, in every study involving compressible flows, the velocity profile prescription is accompanied by a temperature and density evaluation through the Crocco-Busemann relation.

However, some authors consider the beginning of the computational domain further upstream, e.g. Andersonn et al. (2005) who used 6 diameters. It can be noted also that hybrid RANS modeling of the boundary layer or WMLES allow to simulate a larger part of the nozzle. For instance, using wall-modeled LES, Brès et al. [47] fixed the inlet boundary condition 10 Diameters upstream from the nozzle exit. In these latter cases, as in studies of industrial configurations (Brunet (2010,2012)[57, 55], Eastwood[92]), no special mean flow profile is applied. Instead, simply uniform total pressure and enthalpy (or total temperature) are prescribed at the inlet.

In the studies following the approach of Shur et al. (2005)[187], in which a precursor RANS simulation is run, the inflow profiles that are imposed in the final turbulence-resolving simulation are directly extracted from the RANS solution.

2.2.3.2 Turbulent forcing

As seen paragraph 2.1.2.2, many authors performed numerical investigations of the effects of the turbulence rate in the exit boundary layer. As previously mentioned, some authors have initially considered that the nozzle lip receptivity to acoustic waves was sufficient to sustain the Kelvin-Helmholtz instabilities (Andersonn et al. 2005[7]). However, in practice, the introduction of turbulent fluctuations to the nozzle mean velocity profile to trigger efficiently the shear layer development. To do so, the turbulent inlet boundary must satisfy certain conditions: it must be stochastically varying, on a large range of time and length scales, while ensuring compatibility with the Navier-Stokes equations ; in terms of accuracy, it should also provide the shortest possible adaptation length to establish realistic turbulence and, in aeroacoustic purposes to avoid the creation of significant spurious noise ; at the same time, the inlet condition must be easy to implement, must provide flexibility in the turbulent properties setup, and should not increase the CPU cost.

Several methods have been developed over the last two decades to treat turbulent boundary conditions of LES/DNS simulations (see the reviews of Keating et al. (2004)[125] and Tabor & Baba-Ahmadi (2010)[205]). Tabor & Baba-Ahmadi classified turbulent inlet conditions for LES computations in two main categories:

- The precursor simulation methods, that store the results of a preliminary computation to re-use it at the inlet of the actual computation.

- The synthesized turbulence methods, that try to generate a random field at the inlet which has suitable turbulence-like properties.

Precursor simulation methods

Regarding the methods of the first category, it can be divided in methods storing the results of a precursor DNS or LES in a pre-prepared library and the recycling methods. The drawbacks of a precursor LES or DNS, despite the advantage that it provides a realistic turbulence quasi-immediately downstream the interface, lie in its Reynolds number restriction which make it unusable for high Reynolds number industrial configuration, its computational cost (CPU and memory load) and the fact that it is not self-sufficient. Recycling methods, originally introduced by Lund et al. (1998)[148] and latter adapted in Xiao et al. (2010)[238], Deck et al. (2008)[85] or Shur et al. (2011)[190] for instance, consist in extracting data at a further downstream plane before re-injecting it at the inlet boundary. A re-scaling of turbulence is generally required for flows spatially evolving in the streamwise direction (see figure 2.24). This technique can provide a turbulence of very high quality and has the advantage of exhibiting a very short adaptation length (equal to a few times the boundary layer thickness), but it suffers from a lack of generality for the treatment of more complex flow with strong adverse pressure gradients. Last, it can generate peaks in the turbulence spectra at the recycling frequency.

Those methods have rarely been used in jet simulations. Nevertheless, it can be mentioned that Uzun & Hussaini used a rescaling/recycling method to simulate a round jet (2007, 2010)[215, 216] and a chevron nozzle jet (2011)[214] at $Re_D = 10^5$ while in a similar way, Wang et al. (2013)[232] used the rescaling/recycling method developed by Xiao et al. (2010)[238] to perform LES of some underexpanded jets issuing from a rectangular convergent-divergent nozzle at $Re_D = 1.58 \cdot 10^6$ and $Re_D = 1.7 \cdot 10^6$.

Synthesized turbulence methods

Regarding the methods of synthesized turbulence, the methods of artificial forcing can

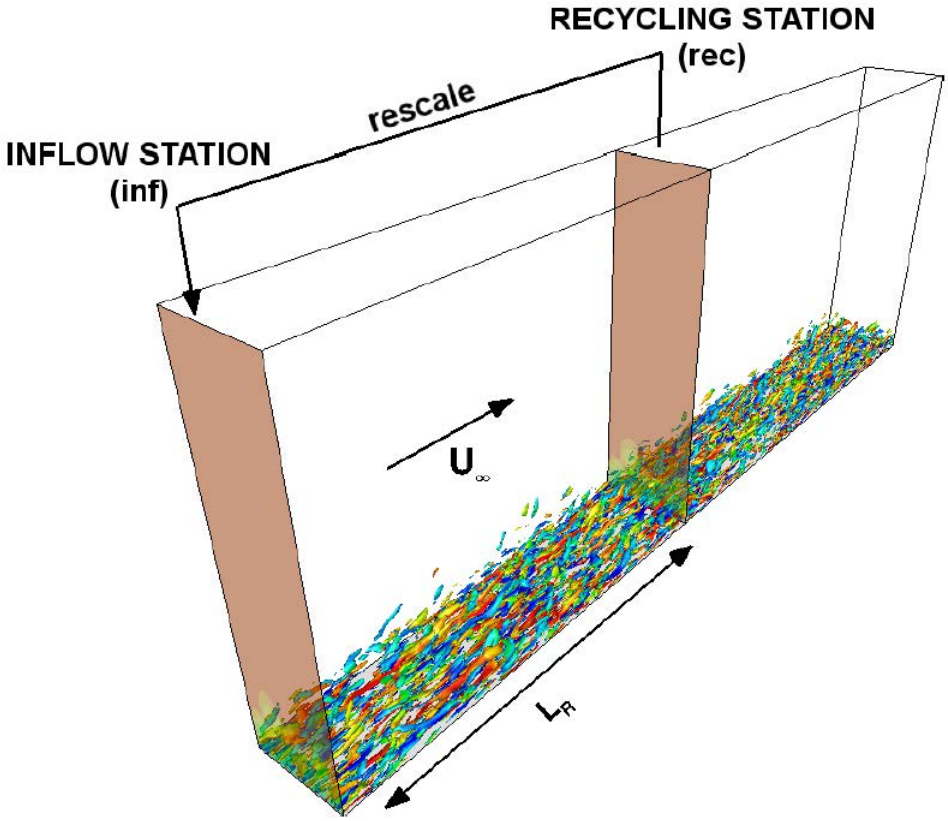

Figure 2.24: Sketch illustrating a recycling technique in which data from an interior plane is mapped backward to the inlet, from Sagaut et al. (2013)[182].

be distinguished from conventional synthetic methods. The latter consist in creating a stochastic field at the inlet interface whereas the first ones can also deal with volume sources or dynamic control forcing in the cells downstream of the interface to shorten the adaptation length. This latter type of method has produced very accurate results with relatively short adaptation length, around 8 times the boundary layer thickness (Laraufie (2011)[138]) or up to 2-3 times (Roidl et al.(2012)[180]). Nevertheless, this kind of approach has been validated on grids satisfying LES requirements but it has been shown that the adaptation distance is increased on coarser grids [86]. Besides, such methods greatly increase the implementation complexity and CPU cost.

As noticed by Shur et al. (2014)[192], in the frame of aerodynamic computations,

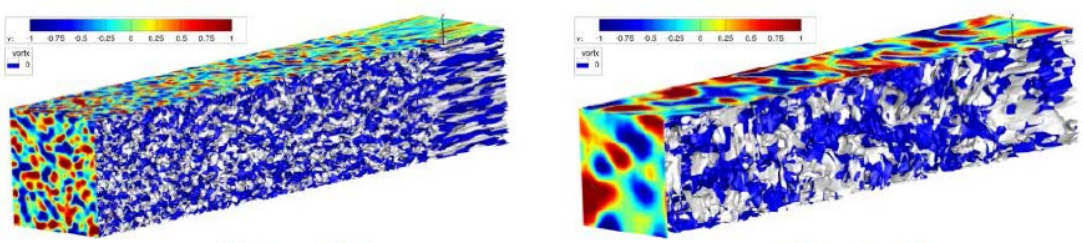

(a) $\sigma = L/20$ (b) $\sigma = L/5$

Figure 2.25: Flow visualizations of the convection of turbulence issuing from an SEM inlet, prescribing different turbulent characteristic length scales, from Gand et al. (2015)[101].

synthetic turbulence generation methods are currently the most suitable technique for treating complex industrial flows with RANS-LES modeling. They are basically much simpler, but a large variety of methods exist. If white noise is very simple to implement, its lack of coherence does not satisfy the Navier-Stokes equations and it is either quickly killed or takes a very long distance to establish a realistic turbulence. On the contrary, the most complex synthetic methods are based on the creation of coherent turbulent structures of controlled shapes and sizes, as for instance the Synthetic Eddy Method (SEM) (see figure 2.25) developed by Jarrin et al. (2006, 2009)[122, 123] and Pamiès et al. (2009)[163]. The ease of implementation is reduced but such methods are much more accurate and their adaptation length can reach 5-6 boundary layer thicknesses (Pamiès et al. (2009)[163]). Based on an idea of Kraichnan (1970)[135] another synthetic method has been developed by several authors as Smirnov et al.(2001)[197], Batten et al. (2004)[20] or Huang et al. (2010)[114] and provides a stochastic turbulent flow field by superimposing spatio-temporal Fourier modes with random amplitudes and phases. This last approach is relatively simple to implement and provides short adaptation length. More recently, this approach inspired Shur et al. (2014)[192] to develop a new turbulent boundary condition dedicated to RANS-LES simulations for aerodynamic purposes when a LES domain is located downstream of a RANS domain. This exercise has not to be confused Wall-Modeled LES (WMLES) where only the outer part of the boundary layer is treated in LES mode.

In jet applications, several synthetic methods have also been specifically developed to introduce fluctuations in the boundary layer. In the frame of initially laminar shear layers, Bogey et al injected some azimuthal modes in the exhausting boundary layer (Bogey & Bailly (2003)[35], using a method which has also been used by Lew et al (2005)[143] and Uzun et al (2004)[217]). In a following work dealing with the simulation of the boundary layer development inside the nozzle, these authors chose to add random low level vortical disturbances decorrelated in azimuth (Bogey et al (2012)[41], Bogey & Marsden (2016)[38]), to avoid the forcing of unstable modes. A forcing based on linear stability analysis has also been used by Bodony & Lele (2005)[25] and Zhao et al (2001)[246] but without calculating the explicit nozzle.

Nonetheless, let us keep in mind that all the aforementioned techniques of turbulent boundary condition have generally been developed and validated on configurations of spatially evolving boundary layer, or to trigger resolved turbulent fluctuations in the nozzle boundary layer. However, for more technical configurations or in industrial-type facilities, the turbulence levels in the jet core (so-called turbulence rate) are likely to be significant (up to 10-20%). This should be accounted for in simulations since it can impact the whole jet development. Therefore, in simulations explicitly modeling the nozzle at higher diameter-based Reynolds number, the question of turbulence injection in the whole inflow plane has gained some interest in recent years. From this point of view, synthetic methods seem to be the most user-friendly approach, as they easily allow the generation of an accurate isotropic homogeneous turbulence.

Actually, few authors have enforced these methods to simulate some turbulence in the core of the inlet section. The most valuable work of this kind is likely the one carried out at the ONERA in the frame of ZDES simulations. Gand et al. (2015)[101] performed ZDES simulations of a round jet at $Re_D = 2.10^5$ by injecting turbulent velocity fluctuations in the whole inlet plane thanks to the Synthetic Eddy Method (SEM) developed by Jarrin et al. (2009)[123]. Brunet (2012)[55] enforced the Random Flow Generation (RFG) technique of Smirnov et al. (2001)[197] to perform ZDES simulations of a dual-stream jet with an external plug in both isolated and installed configurations. These last studies underlined

the interest of accounting for the upstream core turbulence (not only the turbulent state of the boundary layer) to improve the prediction of the potential core length and shock-cell positioning.

2.2.4 Treatment of complex geometries

As mentioned previously, two main approaches can be referenced in the literature concerning the treatment of complex jets as twin jet, co-axial jets, close-coupled nacelle-to-wing configuration, etc. An approach developed by Shur et al. [187] is to use a first RANS simulation of both the explicit nozzle geometry and the downstream jet to extract the flow field at the nozzle exit and impose it at the inlet of a second Implicit LES (ILES) calculation of the jet flow. Another approach is to simulate both the explicit nozzle and the jet in one hybrid RANS/LES simulation.

2.2.4.1 Mixing devices

Pure LES has already allowed to accurately simulate some chevron nozzles (structured grid as Uzun & Hussaini (2011)[214], unstructured grid as Brès et al. (2012)[58]) and, less accurately, mixer nozzles (unstructured grid as Fosso Pouangué et al. (2014)[97]). However, up to now, several nozzle devices have been simulated through an hybrid RANS/LES approach. Shur et al. (2006)[188] for instance simulated a chevron nozzle using their two-stage approach. Fully coupled approaches also demonstrated their capabilities for treating such devices, as proved in Chauvet et al.(2007)[65, 66, 67] who used ZDES to simulate a propulsive jet controlled by fluid injections and tabs and Xia et al. (2011)[235] who performed computations of a chevron nozzle with an hybrid RANS-NLES approach (Numerical-LES, without explicit subgrid scale filtering in LES region). Due & Morris [91] simulated supersonic chevron nozzle jets through a similar approach (URANS with deactivation of the turbulence model in free shear flows) using immersed boundary conditions.

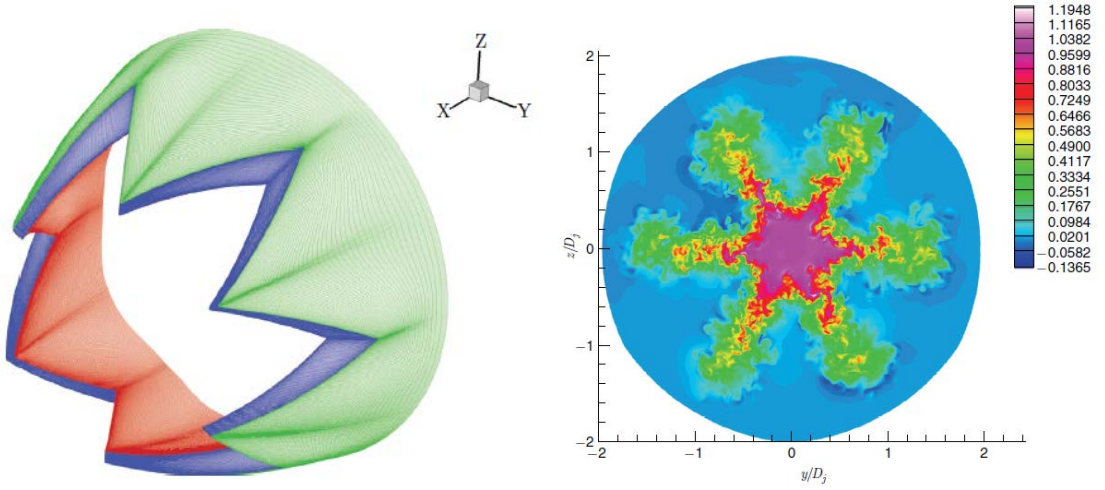

(a) (b)

Figure 2.26: Simulation of a chevron nozzle using LES: (a) surfacic mesh, (b) instantaneous velocity contours 2 diameters donwstream the exit, from Uzun et al.(2011)[214].

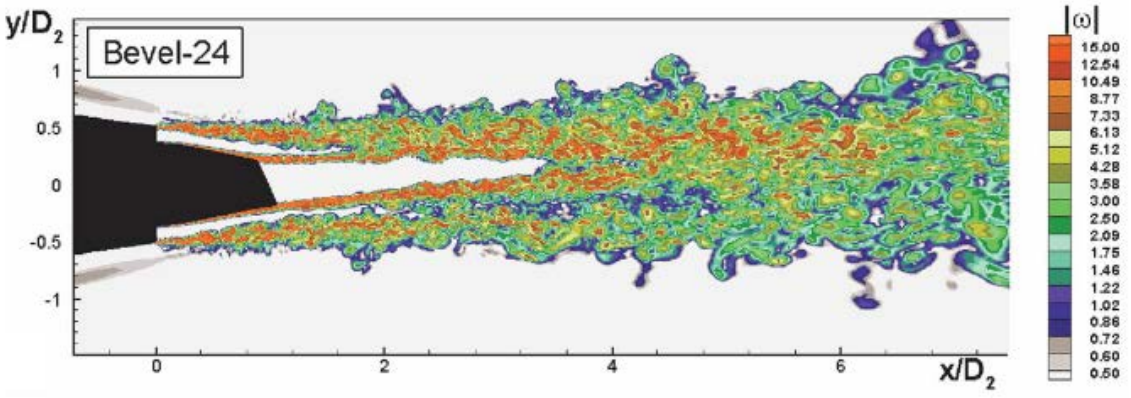

Figure 2.27: Dual-stream jet simulation of staggered nozzles, with a beveled primary nozzle, using the two-stage semi-coupled approach developed by Shur et al., from Viswanathan et al. (2008)[225].

2.2.4.2 Dual-stream configurations

Several dual-stream jets typical of the aircraft engine jet category have been simulated with a turbulence-resolving approach, with and without plug.

Viswanathan et al [225] investigated several jet noise reduction concepts for dual-stream jets using the two-step approach developed by Shur et al. However, they noticed that the two-stage semi-coupled approach is not perfectly adequate to treat dual-stream staggered nozzles, since the boundary layer on the external side of the primary nozzle undergoes an adverse pressure gradient and cannot correctly be captured by this kind of implicit LES. A wall-resolved LES in this region remains prohibitive.

Regarding dual-stream jet simulations with a central body, fully coupled methods have been used by Brunet (2010,2012) [57, 55], Eastwood & Tucker (2010)[93] or, more recently, Du & Morris (2015)[91]. Pure LES has rarely been used due to the grid count requirements of such approach which often leads to under-resolved simulations and not satisfying results (Fosso Poungué, et al. (2014)[97]). It can also be noted that Casalino & Lele (2014)[63] performed the simulation of a dual-stream jet with an external plug using a Lattice-Boltzmann approach. However, the method does not yet seem mature enough for transsonic and high Reynolds number jet simulations.

Actually, the only numerical studies encountered in the consulted literature that deal with dual-stream jets with a secondary underexpanded jet are the ones of Shur et al.

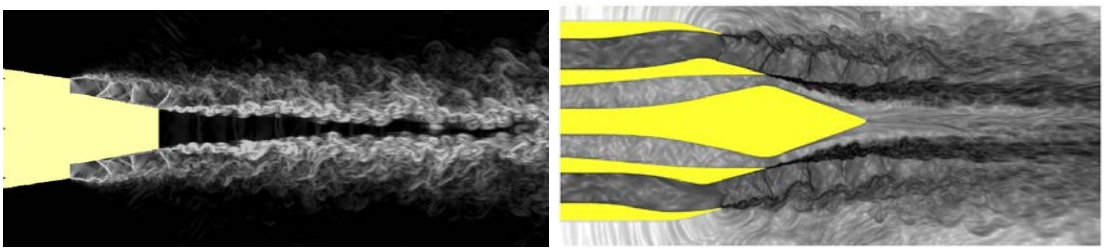

(a) (b)

Figure 2.28: Underexpanded secondary jet simulation (similar to flight conditions): (a) two-step RANS-LES approach of Shur et al. (2011)[191], (b) one-step fully coupled RANS-LES simulation with turbulent injection of Brunet (2012)[55]

(2011)[191] and of Brunet (2010, 2012)[57, 55]. In the work of Brunet, without introducing a turbulent inlet condition, the shock-cell positioning exhibits an important phase-lag compared to experimental results starting from the third shock-cell. Taking the inflow turbulence into account radically changes the location of shocks and at the same time enables a quick development of instabilities in both the internal and external shear-layers.

2.2.4.3 Installed configuration

Vuillot et al. (2010)[231] have used unstructured LES to simulate a configuration of dual-stream nozzle with pylon, but the LES setup was highly under-resolved and the mixing layers exhibited a nonphysically strong laminar behavior along a distance of several diameters downstream of the exit. Ramamurti et al. (2015)[173] performed simulations using also unstructured LES on a nozzle-pylon configuration and simulated only the core jet in underexpanded conditions, but the same issue, even though less critical, seems to occur.

Eastwood & Tucker (2011)[92] performed a RANS-NLES simulation on the same kind of configuration but with a dual-stream subsonic jet. No turbulent forcing at the nozzle inlet was prescribed, leading to initially laminar shear-layers with strong Kelvin-Helmholtz vortices and little small-scale turbulence.

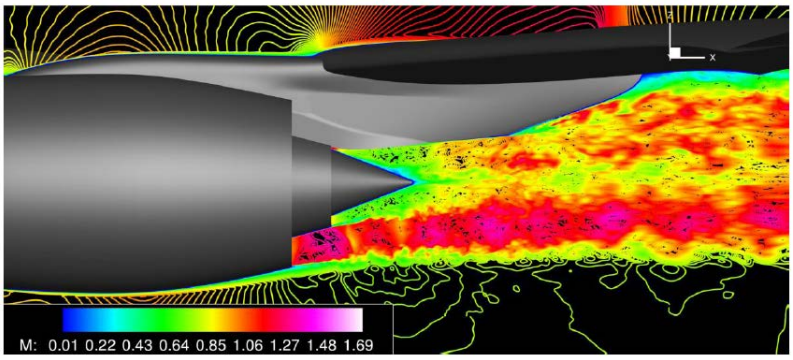

(a)

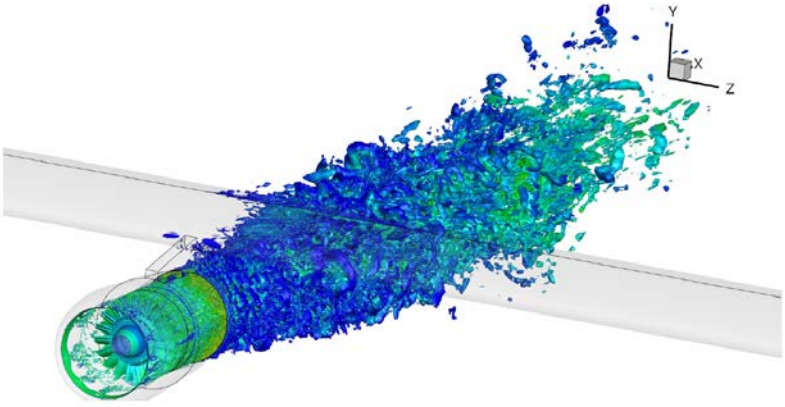

(b)

Figure 2.29: Hybrid RANS-LES simulations of installed configurations taking into account the upstream turbulence: (a) computation of Brunet (2012)[55] using Random Flow Generation at inlets, (b) computation of Tyacke et al. (2015)[213] using Immersed Boundaries and Body Force Modeling to simulate the effect of fan and gear-box in the ducts.

Brunet et al.(2010)[57] and Brunet (2012)[55] performed ZDES simulations of nacelle-to-wing simulations, with and without turbulent injection, reaching a rather good agreement with experimental measurements. Brunet (2012) imposed turbulent inlet thanks to the Random Flow Generation Technique (RFG) and emphasized the interest of the injection of turbulence to improve the fidelity of the simulation.

In the same spirit, but without any turbulent inlet forcing, Tyacke, Mahak and Tucker (2015) [213] have simulated a realistic fan-to-flap configuration using hybrid RANS-NLES. The particularity of this work lies in the simulation of the explicit upstream geometry of the nozzle up to the air intake of the nacelle. All the effects of the internal elements (FAN, OGV, gear-box shaft,...) on the duct flow are taken into account thanks to Immersed Boundary (IB) and Body Force modelling (BFM). As a result, added features generate wakes and turbulent structures in the duct, and thus the exhaust flow exhibits a more complex azimuthal non-uniformity and increased turbulence levels. The authors observed that the main effect appears on the turbulent variables in the outer shear layers, accelerating their mixing and widening. However, the inner shear-layers between the fan and the core streams are still strongly laminar with an important delay in the development of instabilities.

2.2.5 Summary on numerical simulations of jets

In this section, the different approaches developed for the resolution of turbulent jets have been presented, emphasizing on the difference in requirements between aeroacoustic and aerodynamic calculations. LES appears as the privileged approach to resolve turbulent fluctuations but its computational cost to resolve the small structures in boundary layers makes it prohibitive for complex configurations. Thus, in the literature of jet simulations, LES has originally been used without explicitly modeling the nozzle geometry. Instead, a mean velocity profile was prescribed at the inlet boundary with additional turbulent perturbations. To obtain a better representation of the nozzle exit boundary layer, and acknowledging the important sensitivity of the jet to this parameter, first LES simulations modeling an explicit nozzle have been performed, but the diameter-based Reynolds number remains moderate and the geometries relatively academic.

Another approach developed over the past fifteen years to overcome the CPU cost of LES of wall bounded flows while maintaining a LES resolution in free shear flows is the hybrid RANS-LES approach. In the simulation of jets, two methods have been widely used. On one hand, a two-stage approach in which a precursor RANS computation of the nozzle flow is used to prescribe the inlet condition of an actual LES calculation without the nozzle. On the other hand, a one-stage fully coupled RANS-LES method in which RANS is used to treat the boundary layers. These hybrid methods have shown good capabilities in the treatment of jet configurations and appear as an affordable alternative to pure LES for industrial computations. Nonetheless, most of high Reynolds number dual-stream jet simulations continue to exhibit an initially laminar inner mixing layer due to the lack of resolved turbulence in the nozzle boundary layer since it is treated in RANS. In addition, it appears that few authors have performed simulations which take into account upstream turbulence in the jet core and have instead mostly focused on using turbulence generation techniques to trigger turbulence in the exit boundary layers.

These findings have motivated the investigations of the present PhD thesis, which aims at improving the accuracy of technical jet simulations and assessing the effect of upstream turbulence on a dual stream jet configuration. To this effect, the hybrid RANS/LES

method developed at ONERA, ZDES, is used as it has proven to be a efficient approach to deal with complex geometries at high Reynolds numbers.

Authors	Year	Test Case	Re_D	Method
Viswanathan et al. [225]	2008	Staggered nozzles with beveled primary nozzle		two-stage RANS + ILES
Vuillot et al. [231]	2010	Dual-stream jet with external plug and pylon	$5.7 \cdot 10^6$	unstruct. LES
Eastwood et al. [93]	2010	Dual-stream jet with external plug	$0.3 \cdot 10^6$	RANS-NLES
Brunet et al. [57]	2010	Dual-stream jet with external plug, both isolated. Nacelle-to-wing installed configuration with cruise external Mach number	$2 \cdot 10^6$	ZDES
Eastwood & Tucker [92]	2011	Dual-stream jet with external plug and pylon	$0.3 \cdot 10^6$	RANS-NLES
Shur et al. [191]	2011	Staggered nozzles with underexpanded secondary jet		two-stage RANS + ILES
Xia et al. [237]	2012	Dual-stream jet with external plug, nacelle-to-wing configuration, no external flow.	$0.3 \cdot 10^6$	RANS-NLES
Brunet et al. [55]	2012	Dual-stream jet with external plug, both isolated. Nacelle-to-wing installed configuration with cruise external Mach number	$2 \cdot 10^6$	ZDES + RFG
Fosso Pouangué et al. [97] Sanjosé et al. [184]	2014	Dual-stream jet with internal mixer and dual-stream jet with external plug		unstruct. LES
Tyacke et al. [213]	2015	Dual-stream jet with external plug + nacelle-to-wing configuration + fan and internal elements, no external flow	$0.3 \cdot 10^6$	RANS-NLES + IBC + BFM
Ramamurti et al. [173]	2015	Single-stream jet with external plug and pylon. Adapted and underexpanded conditions	$3 \cdot 10^6$	unstruct. LES

Table 2.2: Main hybrid RANS-LES and LES simulations of complex jet configurations: dual-stream jets and installed configurations.

Chapter 3

Numerical and experimental methods

This chapter introduces the different tools and methodologies used in this thesis work to study a dual-stream propulsive jet. The first sections focus on the numerical modeling of turbulence and the methods used in the simulations. The last section is devoted to the description of the experimental dataset used in this work.

Contents

3.1 Numerical modeling of turbulent flows

Numerical simulations constitute the major part of this thesis work and this section aims at presenting the Computational Fluid Dynamics (CFD) framework used, by first giving an overview of the fundamentals of fluid mechanics and then describing the methods that have been utilized.

3.1.1 The Navier-Stokes equations for compressible flows

In the frame of continuum mechanics, Navier-Stokes equations are the classical model to describe the dynamics of a viscous fluid and heat conducting. They are derived from the conservation laws applied to an arbitrary control volume without external force:

Mass conservation equation:

$$\frac{\partial \rho}{\partial t} + \frac{\partial}{\partial x_i}(\rho u_i) = 0 \tag{3.1.1}$$

with t the time and u_i the velocity components.

Momentum conservation equation:

$$\frac{\partial(\rho u_i)}{\partial t} + \frac{\partial}{\partial x_i}(\rho u_i u_j) = -\frac{\partial p}{\partial x_i} + \frac{\partial \tau_{ij}}{\partial x_j} \tag{3.1.2}$$

with τ_{ij} the viscous shear stress tensor:

$$\tau_{ij} = \mu\left(\frac{\partial(u_i)}{\partial x_j} + \frac{\partial(u_j)}{\partial x_i}\right) - \frac{2}{3}\mu\frac{\partial(u_k)}{\partial x_k}\delta_{ij} \tag{3.1.3}$$

Energy conservation equation:

$$\frac{\partial(\rho E)}{\partial t} + \frac{\partial}{\partial x_i}[(\rho E + p)u_i)] = \frac{\partial}{\partial x_j}(\tau_{ij}u_i) - \frac{\partial q_{h_i}}{\partial x_i} \tag{3.1.4}$$

where q_{h_i} are the heat flux components and ρE is defined by:

$$\rho E = \rho\left(e + \frac{1}{2}u_i u_i\right) \tag{3.1.5}$$

with e the internal energy.

Such a set of partial derivative equations exhibits more unknowns than equations and requires additional equations to close the system and link p, τ_{ij} and q_{h_i} to ρ, E and u_i. Laws governing the physical properties of the fluid are thus introduced. In the framework of this study, we consider the fluid as a calorically perfect gas.
The **perfect gas law** reads:

$$p = \rho r T \tag{3.1.6}$$

where r is the ratio of the universal ideal gas constant $R = 8.3145\ J.mol^{-1}.K^{-1}$ to the molar mass of the considered gas and T is the temperature. Moreover, the expression of the internal energy as a function of the temperature, $e = C_v T$ yields to:

$$p = \rho(\gamma - 1)e \tag{3.1.7}$$

with γ defined by $\gamma = \frac{C_p}{C_v}$. For a diatomic gas $\gamma = 7/5$.

The **Fourier's law** provides an expression for the heat flux:

$$q_{h_i} = -\kappa(T)\frac{\partial T}{\partial x_i} \tag{3.1.8}$$

with κ the thermal conductivity. Introducing the Prandtl number, we can link the thermal conductivity and the molecular viscosity:

$$\kappa(T) = \frac{\mu(T)C_p}{Pr} \tag{3.1.9}$$

Pr is supposed constant and its values is fixed to 0.72, according to the literature.

The **Sutherland's law**, finally, links the molecular viscosity to the temperature:

$$\mu(T) = \mu_0\left(\frac{T}{T_0}\right)^{\frac{3}{2}}\frac{T + 110.4}{T_0 + 110.4} \tag{3.1.10}$$

with $T_0 = 273.16$ K and $\mu_0 = 1.711.10^{-5}$ kg.m^{-1}.s^{-1}.

3.1.2 Turbulence modeling

If the viscosity is neglected, the governing equations for the flow field can be simplified to the Euler equations, with no turbulence involved. However, when the non-linear mechanisms are preponderant at high Reynolds numbers, turbulent flows are dominated by vorticity dynamics and involve many different spatial and temporal scales which are correlated. The resolution of the Navier-Stokes equations up to the smallest scales implies many constraints. The computational cost of such a Direct Numerical Simulation (DNS) becomes rapidly prohibitive and must be restricted to academic configurations at low Reynolds numbers, up to few thousands. For example, Spalart et al. [202] estimates that a DNS on a complete aircraft would require about 10^{16} mesh points. Thus, the current computing capabilities impose to model turbulent interactions.

In the Kolmogorov cascade theory, the major part of the kinetic energy is conveyed by the biggest structures, which interact with the mean motion and whose kinetic energy is too high to be dissipated by the viscosity. This energy is transferred to the smaller structures by a mechanism of eddy stretching, up to a certain scale of eddy, the scale of Kolmogorov, permitting the viscous dissipation. This smallest length-scale for eddy structures is noted η. We can distinguish three ranges of scales depicted in figure 3.1:

- the integral scales, enclosing the biggest structures, carrying the major part of the energy and interacting with the mean flow;
- the inertial scales which are involved in the cascade mechanism;
- the disspative scales.

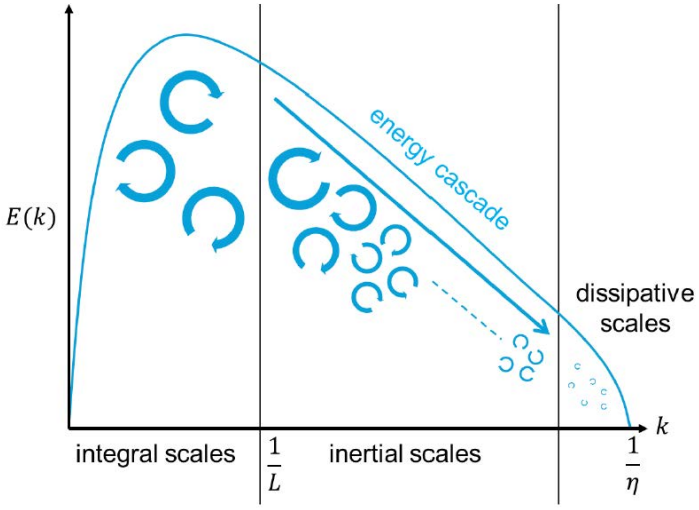

Figure 3.1: Spectral distribution of kinetic energy of isotropic homogeneous turbulence, adapted from Toubin [212]

The cascade theory has been developed in the framework of isotropic homogeneous turbulence, but such a representation can also be adopted for the fully developed turbulence of a shear flow.

In order to avoid resolving the whole spectrum of the turbulence, two main approaches have widely been used in the literature, the Reynolds Averaged Navier-Stokes (RANS) approach and the Large Eddy Simulation (LES) approach. These two approaches are both based on a separation of scales, but present a very different level of modeling. Therefore, hybrid RANS-LES more recently emerged, combining the best features of RANS and LES in order to offer a good compromise between the level of turbulence modeling and computing cost.

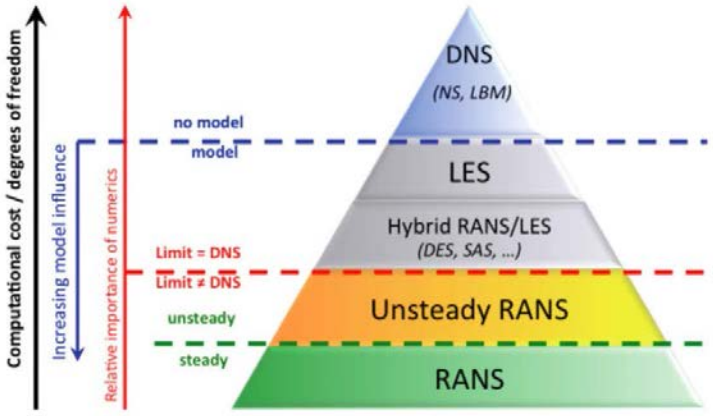

Figure 3.2: Classification of unsteady approaches according to levels of modeling and readiness, from Laraufie [137], adapted from Sagaut et al. [182]

3.1.2.1 Filtering of the Navier-Stokes equations

In order to mitigate the CPU cost of DNS, most approaches rely on a scale separation, which leads to the follwong decomposition of a flow variable f:

$$f = \overline{f} + f' \tag{3.1.11}$$

with $\overline{f}$ the resolved part of the variable and f' the unresolved part of the variable. Such a decomposition applied to a set of equations corresponds to a filtering of the equations by the operator $\overline{\cdot}$. For compressible flows, it is useful to introduce the Favre decomposition:

$$\widetilde{f} = \frac{\overline{\rho f}}{\overline{\rho}} \tag{3.1.12}$$

yielding to the decomposition between resolved and unresolved scales:

$$f = \widetilde{f} + f" \tag{3.1.13}$$

the unresolved part $f"$ is defined so that $\overline{\rho f"} = 0$. Nonetheless, it must be noted that $\overline{f"} \neq 0$.

The introduction of this decomposition in the Navier-Stokes equations gives the following set of equations:

$$\frac{\partial \overline{\rho}}{\partial t} + \frac{\partial}{\partial x_i}(\overline{\rho}\widetilde{u_i}) = \mathcal{A} \tag{3.1.14}$$

$$\frac{\partial}{\partial t}(\overline{\rho}\widetilde{u_i}) + \frac{\partial}{\partial x_j}(\overline{\rho}\widetilde{u_i}\widetilde{u_j} + \overline{p} - \widetilde{\underline{\tau_{ij}}}) = \frac{\partial {\underline{\tau_{ij}}^{tur}}}{\partial x_i} + \mathcal{B} \tag{3.1.15}$$

$$\frac{\partial \widehat{\rho E}}{\partial t} + \frac{\partial}{\partial x_i}\left[(\widehat{\rho E} + \overline{p})\widetilde{u_i} - \widetilde{\underline{\tau_{ij}}}\widetilde{u_j} + \widetilde{q_{hi}}\right] = -{q_{hi}}^{tur} + \frac{\partial}{\partial x_i}({\underline{\tau_{ij}}}^{tur}\widetilde{u_j}) + \mathcal{C} \tag{3.1.16}$$

The new energy equation is obtained by defining:

$$\widehat{\rho E} = \frac{\overline{p}}{\gamma - 1} + \frac{1}{2}\overline{p}\widetilde{u_i}\widetilde{u_i} \tag{3.1.17}$$

$$\widetilde{q_{hi}} = -\kappa(\widetilde{T})\frac{\partial \widetilde{T}}{\partial x_i} \tag{3.1.18}$$

In comparison with the original Navier-stokes equations structure, some additional terms appear on the right member. These terms originate from the non-linearity of the exact Navier-Stokes equations and from potential commutation errors of the filtering. In particular, the terms $\mathcal{A}$, $\mathcal{B}$ and $\mathcal{C}$ represent some possible commutation errors between the scale separation operator and the spatial derivation. They are neglected in the RANS and LES approaches used in this work. A discussion of the relative importance of these terms is provided in the work of Vreman et al. [229]. The two other terms, ${\underline{\tau_{ij}}}^{tur}$ and ${q_{hi}}^{tur}$ encompass the turbulent part of the resolved flow:

The term ${\underline{\tau_{ij}}}^{tur}$ results from the non-linear convection term in the exact Navier-Stokes equations and is called turbulent stress tensor. According to the Leonard's decomposition, the interactions between resolved and unresolved scales can be interpreted as follows:

$${\underline{\tau_{ij}}}^{tur} = \underbrace{\overline{\rho}(\widetilde{\widetilde{u_i}\widetilde{u_j}} - \widetilde{u_i}\widetilde{u_j})}_{\underline{L_{ij}}} + \underbrace{\overline{\rho}(\widetilde{\widetilde{u_i}u_j"} - u_i"\widetilde{u_j})}_{\underline{C_{ij}}} + \underbrace{\overline{\rho}\widetilde{u_i"u_j"}}_{\underline{\tau_{Re}}} \tag{3.1.19}$$

- The Leonard's tensor $\underline{L_{ij}}$ represents the interactions between resolved scales;
- The crossed tensor $\underline{C_{ij}}$ represents the crossed interactions between resolved scales and non-resolved scales;
- The Reynolds tensor $\underline{\tau_{Re}}$ represents the interactions the effect of unresolved scales on the resolved ones.

The term ${q_{hi}}^{tur}$ represents the diffusion of total energy by turbulence and is often called the turbulent heat flux. By analogy with the Fourier's law, a turbulent thermal conductivity κ^{tur} is introduced:

$${q_{hi}}^{tur} = \kappa^{tur}\frac{\partial \widetilde{T}}{\partial x_i} \tag{3.1.20}$$

The main point of divergence between RANS and LES approaches lies in the computation of the turbulent stress tensor, in other words, the choice of the scale separation operator.

3.1.2.2 RANS approach

In the RANS approach, the scale separation operator $< . >$ is the statistical average. In practice, it is assimilated to a temporal average operator, based on the ergodicity hypothesis. Thus, the resolved part of the field is the mean field and the unresolved part

of the field is the fluctuating field. As the statistical average operator has the property of idempotence ($<< a > \cdot b >=< a > \cdot < b >$), the turbulent stress tensor becomes:

$$\underline{\tau_{ij}}^{tur} = \underline{\tau_{Re}} =< \rho > \widetilde{u_i"u_j"} \tag{3.1.21}$$

Therefore, in order to close the set of RANS equations, the only remaining term to be computed is the Reynolds tensor. To this effect, several approaches can be considered as described in the following section.

Reynolds tensor modeling To estimate the Reynolds tensor, different approaches have been developed.

On one hand, some RANS models, called as RSM models, are based on Reynolds stress transport equations. These models require to solve 7 transport equations, and for that reason, are quite expensive in term of computational cost.

On the other hand, models as Algebraic Reynolds Stress Models (ASM) or Explicit Algebraic Reynolds Stress Models (EARSM) propose to link the Reynolds tensor to the strain rate tensor by non-linear relations. Non-linear terms are determined by means of experimental data and thanks to the analysis of terms in the Reynols stress transport equations. This class of model does not require additional transport equations, which limits their cost.

Another way is to further reduce the problem through the concept of turbulent viscosity developed by Boussinesq in 1897 [42]. The turbulent viscosity enables to link the Reynolds stress tensor to the mean field by the equation:

$$- < \rho > \widetilde{u_i"u_j"} - \frac{2}{3} < \rho > \widetilde{k} = \mu_t \left(\frac{\partial \widetilde{u_i}}{\partial x_j} + \frac{\partial \widetilde{u_j}}{\partial u_i} - \frac{2}{3} \frac{\partial \widetilde{u_k}}{\partial x_k} \delta_{ij} \right) \tag{3.1.22}$$

with $\widetilde{k} = \frac{1}{2} \widetilde{u_i} \widetilde{u_i}$. The analogy with the cinematic viscosity clearly appears, but it is important to notice that the cinematic viscosity is a property of the fluid whereas the turbulent viscosity is a property of the flow. The turbulent conduction is evaluated thanks to the turbulent Prandtl number:

$$Pr_t = \frac{\mu_t C_p}{\kappa_{tur}} \tag{3.1.23}$$

The value commonly used for RANS models is $Pr_t = 0.9$.

Thus, most of common RANS models based on the Boussinesq assumption try to express μ_t with the mean field to close the system. Many ways have been developed in the literature: algebraic models, models with transport equations of one or more variables,etc.

In the following paragraph, only the Spalart-Allmaras model, used in this work, is presented in more details.

The Spalart-Allmaras turbulence model The Spalart-Allmaras model is a one-equation turbulence model based on the Boussinesq assumption. The model proposes to solve a transport equation for the quantity $\rho\tilde{\nu}$:

$$\frac{\partial \tilde{\nu}}{\partial t} + u_j \frac{\partial \tilde{\nu}}{\partial x_j} = c_{b1}(1 - f_{t2})\tilde{S}\tilde{\nu} - \left[c_{w1} f_w - \frac{c_{b1}}{K^2} f_{t2}\right] \left(\frac{\tilde{\nu}}{d}\right)^2 + \frac{1}{\sigma}\left[\frac{\partial}{\partial x_j}\left((\nu + \tilde{\nu})\frac{\partial \tilde{\nu}}{\partial x_j}\right) + c_{b2}\frac{\partial \tilde{\nu}}{\partial x_i}\frac{\partial \tilde{\nu}}{\partial x_i}\right] \tag{3.1.24}$$

The different terms of the right hand side have been determined heuristically and calibrated from more and more complex flows. The turbulent eddy viscosity is computed from:

$$\mu_t = \rho \tilde{\nu} f_{v1} \tag{3.1.25}$$

where

$$f_{v1} = \frac{\chi^3}{\chi^3 + c_{v1}^3} \tag{3.1.26}$$

$$\chi = \frac{\tilde{\nu}}{\nu} \tag{3.1.27}$$

ρ is the density, $\nu = \mu/\rho$ is the molecular kinematic viscosity, and μ is the molecular dynamic viscosity. The other terms of eq 3.1.24 are given by:

$$\tilde{S} = \Omega + \frac{\tilde{\nu}}{K^2 d^2} f_{v2} \tag{3.1.28}$$

where d is the distance to the nearest wall, $\Omega = \sqrt{2\omega_{ij}\omega_{ij}}$ is the vorticity magnitude with

$$\omega_{ij} = \frac{1}{2}\left(\frac{\partial u_i}{\partial x_j} - \frac{\partial u_j}{\partial x_i}\right) \tag{3.1.29}$$

and

$$f_{v2} = 1 - \frac{\chi}{1 + \chi f_{v1}} \qquad f_w = g\left[\frac{1 + c_{w3}^6}{g^6 + c_{w3}^6}\right]^{1/6}$$
$$g = r + c_{w2}(r^6 - r) \qquad r = \frac{\tilde{\nu}}{\tilde{S} K^2 d^2} \qquad f_{t2} = c_{t3} \exp\left(-c_{t4}\chi^2\right) \tag{3.1.30}$$

The different constants involved in this model have been calibrated to fit experimental and DNS results of plane free-shear flows, wake flows and boundary layers. The standard values used within this model in most of industrial applications are given in table 3.1. This model is commonly used in the industry, but often tends to predict too massive separations, due to an overestimation of the turbulent viscosity in the vortices cores.

Many versions of the Spalart-Allmaras model have been developed to take into account compressibility or curvature effects, for instance, but have not been used in this work. For further investigations regarding the choice of numerical settings in steady RANS simulations the reader is invited to consult the PhD thesis of Giner [103].

3.1.2.3 LES Approach

In the RANS approach, all the turbulent scales are modeled, which provides very low computing costs by lowering the mesh resolution required. Conversely, the LES approach aims at resolving the turbulence production mechanisms, i.e. the large scale eddies (cf. fig 3.1), hence the name of this approach. It is assumed that in the inertial range and beyond,

Constant	Value
C_{b1}	0,1355
C_{b2}	0,622
σ	2/3
K	0,41
C_{w1}	$C_{b1}/K^2 + (1 + C_{b2})/\sigma$
C_{w2}	0,3
C_{w3}	2
C_{v1}	7,1
C_{t3}	1,2
C_{t4}	0,5

Table 3.1: Standard values of Spalart-Allmaras model constants

the turbulence is locally isotropic, which justifies the modeling of the smallest turbulent length scales compared to RANS. Thus, the decomposition operator $\overline{\cdot}$ in equation 3.1.11 is akin to a low-pass filter of width Δ (in the wave number space).

$$\overline{f(x,t)} = (G \star f)(x,t) = \int_{-\infty}^{\infty} G(x-\xi,\Delta) f(\xi,t) d\xi \tag{3.1.31}$$

With G the convolution kernel of a low-pass filter, whose filter width is Δ.

To capture a certain length scale of turbulent structures, it is required to get a sufficiently refined mesh, at least as small as the length scale. In some ways, the grid acts as a filter. According to the Shannon theorem, the cutoff wave length Δ_c is twice the characteristic grid spacing Δ_g.

Some authors take profits of this grid filtering and from the dissipation of numerical schemes which are used as an "implicit filtering" of turbulent length scales. The transfer function of the filter is then not well-known. Such LES is often called Implicit LES (ILES). However, the filtering can also be applied separately using an explicit operator with a filter width Δ larger than Δ_c, leading to a better control of the filter width and characteristics. This approach is referred to as "explicit filtering". Several filters exist in the literature, the most common of them being:

- The "box" or top-hat filter, providing a spatial average on a given length. It is a cardinal sinus in the spectral space;
- The "spectral or sharp cutoff" filter, representing a cardinal sinus in the physical space but which is an ideal low-pass filter in the spectral space (and owns the idempotence property);
- The Gaussian filter whose representation in both the physical and spectral spaces is a Gaussian distribution.

Once the filtering applied with the Favre decomposition, it has been seen in chapter 3.1.2.1 that only the term τ_{ij}^{tur} remains to be modeled. In the LES approach, τ_{ij}^{tur} can be written τ_{ij}^{SGS}, where SGS means Sub-Grid Scales (since the modeling only involves scales lower or equal to the cell size). Sagaut [181] classified the several existing ways to model this tensor. In particular, two main family are identified: structural and functional models.

The structural models aim at keeping the mathematical structure of the turbulent tensor. Either by means of series expansions of the different terms in filtered Navier-

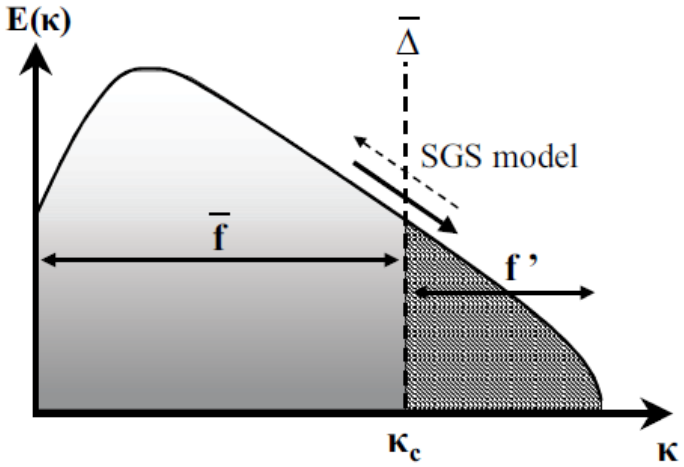

Figure 3.3: LES turbulent field decomposition (sharp cutoff filter), adapted from Sagaut et al. [182]

Stokes equations or by extrapolating the characteristics of the finest turbulent length scales resolved, in application of the scale similarity hypothesis (Bardina et al. [18]).

In the functional models all the tensor τ_{ij}^{SGS} is modeled in order to reproduce the behavior of the sub-grid turbulence and its interactions with resolved scales. Such an approach requires a very fine analysis of the physics of turbulent interactions and is largely based on the Kolmogorov's cascade. A popular, but strong, hypothesis is that effects of subgrid scales on resolved scales are essentially dissipative. The action of subgrid scales can thus be summarized by the energy equilibrium with the resolved scales. It is then assumed that subgrid scales have locally an isotropic behavior, which is not strictly right except for isotropic homogeneous turbulence. In this frame, it leads to introduce the notion of subgrid viscosity $\mu_{sgs} =< \rho > \nu_{sgs}$ to model the energy transfer mechanisms from the resolved to the subgrid scales, by analogy with the molecular mechanisms, which is similar to the Boussinesq hypothesis used in RANS:

$$\tau_{ij}^{SGS} - \frac{1}{3}\tau_{kk}^{SGS}\delta_{ij} = -\overline{\rho}\nu_{sgs}\left(\frac{\partial(\widetilde{u_i})}{\partial x_j} + \frac{\partial(\widetilde{u_j})}{\partial x_i} - \frac{2}{3}\frac{\partial(\widetilde{u_k})}{\partial x_k}\delta_{ij}\right) \tag{3.1.32}$$

A closure equation remains to be provided to evaluate ν_{sgs}. Many subgrid viscosity models have been developed in the literature. Only the Smagorinsky model is detailed below.

The Smagorinsky model The Smagorinsky model [196] is a functional model which is based on the resolved scales, in the viscosity subgrid model classification of Sagaut [181]. These models exhibit a viscosity expression of the form:

$$\nu_{sgs} = \nu_{sgs}(\Delta, \widetilde{\varepsilon}) \tag{3.1.33}$$

where Δ is the characteristic cutoff length of the filter and $\widetilde{\varepsilon}$ the instantaneous energy flux through the cutoff. In addition to the hypothesis previously described regarding the energetic nature of interscale relations, the Smagorinsky formulation assumes the following hypothesis:

- Only the forward energy cascade process is taken into account, i.e. the action of subgrid scales on the resolved scales (backward process) is neglected;
- A characteristic length l_0 and a characteristic time t_0 are sufficient to describe the subgrid scales;
- There exists a total separation between the subgrid and resolved scales;
- The energy spectrum of the flow is in equilibrium, there is no accumulation of energy at any frequency.

These assumptions lead Smagorinsky to suggest the following expression for ν_{sgs}:

$$\nu_{sgs} = (C_s\Delta)^2\|\widetilde{S}^d\| \tag{3.1.34}$$

where $\|\widetilde{S}^d\| = \sqrt{2\widetilde{S_{ij}}^d\widetilde{S_{ij}}^d}$ with $\widetilde{S_{ij}}^d$ the deviatoric part of the filtered strain-rate tensor, defined by

$$\widetilde{S_{ij}}^d = \frac{1}{2}\left(\frac{\partial(\widetilde{u_i})}{\partial x_j} + \frac{\partial(\widetilde{u_j})}{\partial x_i} - \frac{2}{3}\frac{\partial(\widetilde{u_k})}{\partial x_k}\delta_{ij}\right) \tag{3.1.35}$$

The constant C_s can be determined by different manners but is often estimated assuming an equilibrium between production and dissipation terms in isotropic homogeneous turbulence. The common value of C_s is $C_s = 0.18$, but its value is often tuned according to the application, between 0.1 and 0.2.

LES mesh requirements It is commonly admitted [64, 83], that the LES simulation of a free shear layer, requires a minimal grid size in the streamwise and spanwise directions satisfying $\Delta_x \approx \Delta_z \approx \delta_\omega/2$ whereas in the velocity gradient direction a minimal grid length $\Delta_y \approx \delta_\omega/20$ is required.

Regarding attached boundary layers, the turbulent length scales participating to the dynamics of the boundary layer and which must be resolved can be very small. Hence, LES mesh requirements are much more binding. In the direction normal to the wall, it is similar to RANS requirements and is estimated to $\Delta_y^+ \approx 1$. Conversely, in the streamwise and spanwise directions LES requires a much finer grid than RANS. Indeed, in boundary layers. In the streamwise direction, $\Delta_x^+ \approx 50$ is recommended instead of about $\Delta_x^+ \approx 500$ in RANS. In the spanwise direction, $\Delta_z^+ \approx 15$ to 20 is recommended instead of $\Delta_z^+ \approx 1000$ in RANS [65]. It clearly appears that the computing cost of LES is much higher than the RANS one, especially in boundary layers. Thus, this computing cost becomes prohibitive when the Reynolds number increases (see for instance Choi & Moin [68] or Deck et al. [84]). The use of full LES computations on industrial cases for most of which the Reynolds number is higher than $Re = 10^6$ is therefore out of reach of current computing capabilities. Nevertheless, the need to increase the level of resolved physics for complex flows lead to the development of hybrid approaches.

3.1.2.4 Hybrid RANS/LES approaches

As previously mentioned, the current calculation capabilities do not allow to use the LES approach to simulate flows at high Reynolds numbers for wall-bounded flows. In order to reduce this CPU cost, the idea has grown to combine the best features of the RANS with the best features of the LES to solve complex flows. Hence, the hybrid approaches combine the efficiency of the RANS for wall bounded flows and the high resolution level of the LES in separated areas.

As an example, hybrid RANS/LES methods take advantage of the similarity of filtered equations in both approaches, in which only the scale separation operator changes

(see eq 3.1.19). Although the mechanisms modeled in the tensor τ_{ij}^{SGS} and τ_{ij}^{RANS} are very different, the common formalism enables to switch from one modeling to the other. Switching from one model to another is equivalent to change the effective filtering [182], in other words, to change the characteristic length scale. The challenge for such approach is to manage the transfer from one model to the other, as they do not represent the same physics.

A very large number of hybrid RANS/LES strategies has been developed over the last two decades, such as "SDM", "LNS", "VLES", "XLES", "DES", "SAS", "ZDES",... and can not all be described here. The reader is invited to report to the review of Sagaut, Deck and Terracol [182] to get a quite exhaustive insight on these methods. In the following, only DES-like models based on the Spalart-allmaras turbulence model are described.

Detached-Eddy Simulation (DES97) One of the most popular hybrid approach for simulating industrial flows is the Detached-Eddy Simulation (DES), originally developed by Spalart [202]. Considering that RANS modeling is very efficient close to walls to simulate an attached boundary layer, but exhibits many difficulties to provide realistic solutions of massively separated flows and that LES requirements are prohibitive in the boundary layer, the main idea of this approach lies in the modification of the transport equation of the turbulent variables depending on the wall-distance. Thus, a RANS model is imposed close to the wall and a LES model further. In the original DES of Spalart *et al.* (DES97) the initial turbulent viscosity of the RANS model, close to the wall, progressively turns into a subgrid viscosity of Smagorinsky type in the free stream and flow separated areas. This is done thanks to a new characteristic length scale $\widetilde{d}$ which replaces the wall distance d_w in the pseudo-viscosity transport equation. The equation (3.1.24) becomes:

$$\frac{D\widetilde{\nu}}{Dt} = c_{b1}\widetilde{S}\widetilde{\nu} - c_{w1}\left[\frac{\widetilde{\nu}}{\widetilde{d}}\right]^2 + \frac{1}{\sigma}\left[\nabla\cdot((\nu+\widetilde{\nu})\nabla\widetilde{\nu}) + c_{b2}\nabla\widetilde{\nu}\cdot\nabla\widetilde{\nu}\right] \tag{3.1.36}$$

where the destruction term depends on $\widetilde{d}$:

$$\widetilde{d} = min(d_w, C_{DES}\Delta) \tag{3.1.37}$$

with $\Delta = \Delta_{max} = max(\Delta_x, \Delta_y, \Delta_z)$ the characteristic mesh length and C_{DES} a constant calibrated to 0.65. Far away from the wall, when the production and destruction terms are preponderant and balanced, it leads to an expression of the turbulent viscosity of the form:

$$\nu_t = f_{v1}\frac{c_{b1}}{c_{w1}}C_{DES}^2\Delta^2\|\widetilde{S}\| \tag{3.1.38}$$

Thus, $\nu_t \propto \|\widetilde{S}\|\Delta^2$, which is similar to the Smagorinsky's subgrid viscosity $\nu_{sgs} = (C_s\Delta)^2\|\widetilde{S}\|$. [1] The definition of $\widetilde{d}$ based on Δ_{max} induces a switch from the RANS modeling to the LES modeling according to the local mesh refinement. It allows the use of a RANS grid close to the wall (which is a very strong advantage of this approach) while also satisfying LES grid standards far from the solid walls. Nevertheless an uncertainty remains in the transition area between the two models when $d_w \approx \Delta$, the "grey area" as called by the authors of DES [202], [198] (see figure 3.1.2.4). In particular, if this grey area is located inside the boundary layer, i.e. Δ_x or $\Delta_z \approx \delta$ the boundary layer thickness, a drop of the eddy

1. It has to be noted that $\|\widetilde{S}\|$ does not refer to the same tensor in the Spalart's formulation, where $\|\widetilde{S}\| = \|\widetilde{\Omega_{ij}}\|$ is the magnitude of vorticity, and the Smagorinsky's one, in which $\|\widetilde{S}\| = \|\widetilde{S_{ij}}\|$ is the magnitude of the local strain rate. In an isotropic homogeneous turbulence, both expressions are equivalent, $\|\widetilde{\Omega_{ij}}\| = \|\widetilde{S_{ij}}\|$.

viscosity occurs in this area. But at the same time, as the mesh is not yet adapted to the LES mode, there is no mechanism to convert modeled turbulent kinetic energy into resolved one, yielding to under-estimated Reynolds stress levels, what Spalart *et al.* call a "Modelled-Stress-Depletion" (MSD) [201]. This issue is accompanied by a decrease of the skin friction coefficient. In the worst cases, it can lead to a premature separation, that has been identified by Menter *et al.* as a "Grid Induced Separation" (GIS) [153]. Such a highly undesired feature is not acceptable in applied aerodynamics.

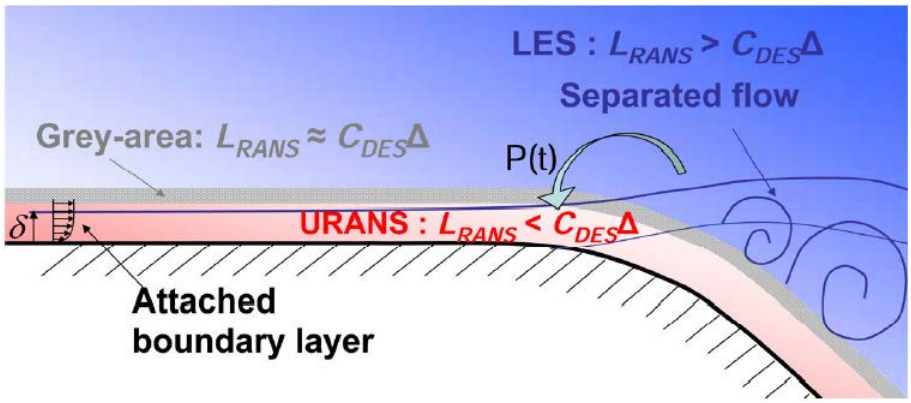

Figure 3.4: Sketch of RANS and LES regions in a DES approach, from [182].

Delayed Detached-Eddy Simulation (DDES) The drawbacks of the DES97 as described in the previous paragraph led to different strategies to work around the model-stress depletion issue [152], [62], [96]. After having prescribed recommendations about the grid [199], Spalart et al. developed a significant improvement to the original DES called Delayed Detached-Eddy Simulation (DDES), in order to ensure that the RANS mode is enforced in the attached boundary layers, no matter the local grid density. [201]. They introduced the blending function f_d defined by:

$$f_d = 1 - tanh\left([8r_d]^3\right) \tag{3.1.39}$$

with

$$r_d = \frac{\nu_t + \nu}{\sqrt{U_{i,j}U_{i,j}}K^2 d_w^2} \;;\; K = 0.41 \tag{3.1.40}$$

where ν_t and ν are respectively the eddy and molecular viscosity, $U_{i,j}$ the velocity gradients and d_w the distance to the wall. This function f_d enables to redefine the DES length scales in the following manner:

$$\widetilde{d} = d_w - f_d \max(0, d_w - C_{DES}\Delta) \tag{3.1.41}$$

The behavior of r_d and f_d, depends both on the distance to the wall and on the time-dependent eddy viscosity. Consequently, $\widetilde{d}$ does not depend only on the grid but also on the flow solution. The function f_d is null at the wall, leading to RANS mode, and is equal to 1 outside the attached boundary layers, where the standard DES behavior is therefore used. Hence, the RANS treatment of the attached boundary layer is preserved. DDES has been enforced on various complex cases with a quite good success. Nevertheless, a drawback of this approach is a potential delay to the development of instabilities [81].

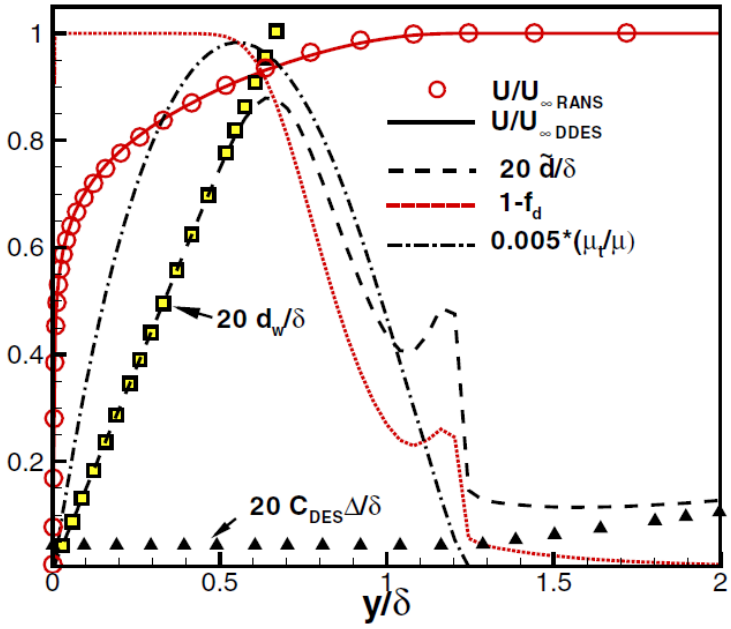

Figure 3.5: DDES behavior in flat plate boundary layer with LES-like resolution $\Delta x+ \approx 50, \Delta y+ \approx 1, \Delta z+ \approx 15$. Note that the modified length scale $\widetilde{d}$ follows the LES branch farther away from the wall than it would in DES97. More precisely, one can notice that $\widetilde{d} = d_w$ over more than half of the boundary layer thickness and at its peak, exceeds $C_{DES}\Delta$ by more than an order of magnitude. The second peak near $y/\delta \approx 1.11.2$ is due to the shear rate reaching zero at the edge of the boundary layer and entering rd. However, it is not noticeably disturbing the eddy viscosity, from [182].

Zonal Detached-Eddy Simulation (ZDES) The Zonal Detached Eddy Simulation (ZDES) was first proposed by Deck [80] and the complete formulation that proposes an efficient solution to prevent delay in the formation of instabilities has been published in Ref. [81]. In this formulation, it is possible to specify RANS and LES regions, but also to use various physical resolutions within the same calculation. Thus, ZDES offers an attractive flexibility in the treatment of turbulent flows in technical applications and has been applied often with good results over a range of Mach numbers and configurations (see [84]).
Three specific hybrid length scale formulations, also called modes, are then optimized to be employed on three typical flow field topologies (see figure 3.6). Mode 1 concerns flows where the separation is triggered by a relatively abrupt variation in the geometry; mode 2 is retained when the location of separation is induced by a pressure gradient on a gently-curved surface and mode 3 for flows where the separation is strongly influenced by the dynamics of the incoming boundary layer. This latter mode is often referred to as Wall-Modelled Large Eddy Simulation (WMLES) mode (see Ref. [82]). The ZDES method aims at treating all classes of flow problems indicated in figure 3.6 in a single model, which length scale reads as :

$$\tilde{d}_{ZDES} = \begin{cases} d_w & (mode = 0) \\ \tilde{d}^{I}_{DES}(\widetilde{\Delta}) & (mode = 1) \\ \tilde{d}^{II}_{DES}(\widetilde{\Delta}) & (mode = 2) \\ \tilde{d}^{III}_{DES}(\widetilde{\Delta}) & (mode = 3) \end{cases} \tag{3.1.42}$$

where $\widetilde{\Delta}$ is the subgrid lengthscale entering $\tilde{d}_{ZDES}$. The length scale definition originally proposed for $\widetilde{\Delta}$ was the cube root of the cell:

$$\Delta_{vol} = (\Delta_x \Delta_y \Delta_z)^{1/3} \tag{3.1.43}$$

Whereas the original proposal of Chauvet et al. [65] to also take into account the local flow is defined by:

$$\Delta_\omega = \sqrt{N_x^2 \Delta_y \Delta_z + N_y^2 \Delta_x \Delta_z + N_z^2 \Delta_x \Delta_y} \tag{3.1.44}$$

with $\overrightarrow{N} = \frac{\overrightarrow{\omega}}{\|\omega\|}$ the unit vectors giving the orientation of the vorticity $\overrightarrow{\omega}$. In this work, both length scales are used. Note that Eq. (3.1.44) has been generalized by Deck[81] in the frame of unstructured grids:

$$\Delta_\omega = \sqrt{S_\omega} \tag{3.1.45}$$

where S_w is the averaged area normal to the local vorticity orientation.

In the framework of ZDES, the new proposal of $\widetilde{\Delta}$ is not a minor adjustment of the DES formulation because $\widetilde{\Delta}$ depends not only on the grid $(\Delta_x, \Delta_y, \Delta_z)$ but also on the velocity gradients $(u_{i,j})$ and eddy viscosity field (ν_t) since $\widetilde{\Delta} = \widetilde{\Delta}(\Delta_x, \Delta_y, \Delta_z, u_{i,j}, \nu_t)$. It is worth noting that within mode 2 of ZDES, which clearly borrows ideas from DDES [201], especially the blending function f_d, it is permitted to operate in an "automatic" manner. The improvement of mode 2 compared with standard DDES comes from $\widetilde{\Delta}$ becoming the new lengthscale instead of Δ_{max}. Moreover, to prevent a "Modeled-Stress Depletion" (MSD)[182], the former lengthscale Δ_{max} is used when f_d is less than the threshold value $f_{d_0} = 0.8$ and Δ_ω or Δ_{vol} is only used for $f_d > f_{d_0}$:

$$\tilde{\Delta} = \begin{cases} \Delta_{max} & if \quad f_d < f_{d_0} \\ \Delta_\omega \ or \ \Delta_{vol} & if \quad f_d > f_{d_0} \end{cases} \tag{3.1.46}$$

It is noteworthy that eq. (3.1.46) allows the ZDES mode 2 to keep the same attached flow shielding properties as DDES. Eventually, the mode 2 of the ZDES is "non-zonal" with regards to the automatic switch between RANS and LES areas, but "zonal" with regards to the length scale used in these areas. In the frame of ZDES, the source terms of the turbulence model are therefore discontinuous but the solution $(\widetilde{\nu})$ is continuous which confers the robustness of the method for technical applications. An example where the

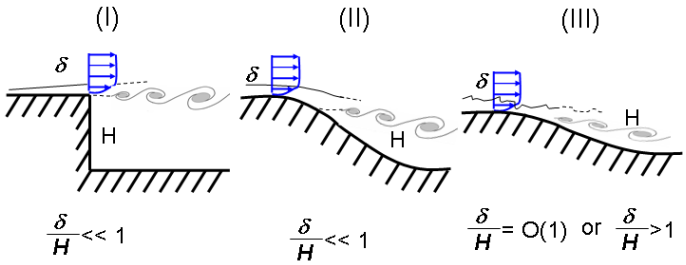

Figure 3.6: Classification of typical flow problems. I: separation fixed by the geometry, II: separation induced by a pressure gradient on a curved surface, III: separation strongly influenced by the dynamics of the incoming boundary layer (adapted from [81]).

three modes of ZDES are used at the same time on a curvilinear geometry (three-element airfoil with deployed slat and flap) can be found in Deck and Laraufie [83]. In the present configuration, only mode 0, mode 1 and mode 2 are used. Let us remind that within this strategy, the whole boundary layer is treated in RANS mode (see figure 3.6).

3.1.3 Solving of Navier-Stokes equations

The Navier-Stokes equations system is a partial differential equations system describing a problem of continuum mechanics. Its exact solution is not known. The numerical solving of these equations is carried out with the elsA software developed at ONERA [61] and requires both following steps:

- A step of spatial discretization that enables to transform the partial differential system to an ordinary differential system;
- A second step in which this ordinary differential system is transformed into recursive sequences by time integration. These sequences represent the field $\mathbf{q}$ at every point of the spatial discretization and every discrete time.

In the following paragraphs, only the methods used in the thesis work are described.

3.1.3.1 Spatial discretization

Finite Volume method

The finite volume method is one of the most popular method to solve problems of fluid dynamics thanks to their properties of conservativity and robustness which is essential in the frame of technical applications.

The finite volume method takes advantage of the conservative form of Navier-Stokes equations. Indeed, it is possible to rewrite the equations in a compact way. Once the scale separator RANS or LES has been applied, it is possible to develop the conservative form separating the flux matrix in a convective flux term and a non-viscous flux term:

$$\frac{\partial \boldsymbol{q}}{\partial t} + \nabla \cdot \underline{\boldsymbol{F}}(\boldsymbol{u}) - \nabla \cdot \underline{\boldsymbol{F}}^{v}(\boldsymbol{u}) = 0 \tag{3.1.47}$$

with $\boldsymbol{q}$, $\underline{\boldsymbol{F}}(\boldsymbol{u})$ and $\underline{\boldsymbol{F}}^{v}(\boldsymbol{u})$ defined by:

$$\boldsymbol{q} = \begin{bmatrix} \overline{\rho} \\ \overline{\rho}\widetilde{u_1} \\ \overline{\rho}\widetilde{u_2} \\ \overline{\rho}\widetilde{u_3} \\ \widehat{\rho E} \end{bmatrix} ; \quad \underline{\boldsymbol{F}}(\boldsymbol{u}) = \begin{bmatrix} \overline{\rho}\widetilde{u_i} \\ \overline{\rho}\widetilde{u_1}\widetilde{u_i} + \overline{p}\delta_{1i} \\ \overline{\rho}\widetilde{u_2}\widetilde{u_i} + \overline{p}\delta_{2i} \\ \overline{\rho}\widetilde{u_3}\widetilde{u_i} + \overline{p}\delta_{3i} \\ \widehat{\rho E}\widetilde{u_i} + \overline{p}\widetilde{u_i} \end{bmatrix}_{i=1,2,3} ; \quad \underline{\boldsymbol{F}}^{v}(\boldsymbol{u}) = \begin{bmatrix} 0 \\ \widetilde{\tau_{1i}} + \tau_{1i}^{tur} \\ \widetilde{\tau_{2i}} + \tau_{2i}^{tur} \\ \widetilde{\tau_{3i}} + \tau_{3i}^{tur} \\ q_{h\ i} + q_{h\ i}^{tur} + (\widetilde{\tau_{ij}} + \tau_{ij}^{tur})\widetilde{u_j} \end{bmatrix}_{i=1,2,3} \tag{3.1.48}$$

From this form, it is possible to integrate the system on a volume Ω of border S and of normal $\mathbf{n}$. The Green-Ostrograski theorem gives:

$$\iiint_{\Omega} \frac{\partial \boldsymbol{q}}{\partial t} d\Omega + \iint_{S} (\underline{\boldsymbol{F}} - \underline{\boldsymbol{F}}^{v}) \cdot \mathbf{n} dS \tag{3.1.49}$$

The continuous domain is then split into ijk hexaedrical cells of volume Ω_{ijk} to obtain a spatially discretized domain. In this frame, the cell center approach assumes that the value of $\boldsymbol{q}$ is constant in the whole ijk cell and that the fluxes $\underline{\boldsymbol{F}}_{ijk}$ and $\underline{\boldsymbol{F}}^{v}_{ijk}$ are constant on each of the 6 faces of the ijk cells. It is thus possible to rewrite the previous balance on the ijk cell:

$$\frac{\partial \Omega_{ijk} \boldsymbol{q}_{ijk}}{\partial t} + \sum_{l=1}^{6} (\underline{\boldsymbol{F}}_{ijk} - \underline{\boldsymbol{F}}^{v}_{ijk}) S_l = 0 \tag{3.1.50}$$

with S_l the cell faces.

The equation (3.1.50) shows fluxes at each interface remain to be evaluated to get an ordinary differential system that can be integrated in time. To this end, the methods usually

enforced take advantages of the physical nature of the fluxes: the convective and viscous fluxes are treated differently.

Viscous fluxes discretization Due to the dissipative nature of viscous fluxes, it is possible to discretize them by using a second order centered scheme, assuming that viscous flux value at the interface between the cell ijk and $ijk+1$ is the arithmetical sum of fluxes from each side of the interface:

$$\iint_{S_l} \underline{\boldsymbol{F}}^v \cdot \mathbf{n} dS = \frac{1}{2}(\underline{\boldsymbol{F}}^v_{\Omega_{ijk}} + \underline{\boldsymbol{F}}^v_{\Omega_{ijk+1}}) \cdot \mathbf{n}_{S_l} \tag{3.1.51}$$

where $\boldsymbol{n}_{S_l}$ is the unit vector normal to the surface S_l.
In order to estimate the expression (3.1.51), it is required to calculate the velocity gradients and temperatures acting in the expression of the fluxes at the centers of cells Ω_{ijk} and Ω_{ijk+1}. To achieve this, the Green-Ostrograski theorem gives:

$$\nabla \mathbf{u} \simeq \sum_{l=1}^{6} \iint_S \nabla \mathbf{u} \cdot \mathbf{n} dS = \left[\frac{(u_i\rfloor_{j+1} + u_i\rfloor_j)/2 - (u_i\rfloor_j + u_i\rfloor_{j-1})/2}{\Delta_i} \right] \tag{3.1.52}$$

where indexes $j-1$ and $j+1$ refers to side cells of the cell Ω_{ijk}.

Convective fluxes discretization Due to their non-linearity, convective fluxes require a more complex treatment. To obtain a unique value of the flux at the interface S_l from the conservative values at left and right sides of this one is a problem of Riemann that must be solved thanks to an approximated solver.
Two types of schemes can be used: centered schemes and upwind schemes.

Centered scheme: the Jameson scheme Centered schemes used to discretize the convective fluxes are expressed as the sum of a centered term as (3.1.51) and of a numerical dissipation term. Indeed, the centered scheme (3.1.51) is unconditionally unstable in the case of convective fluxes and requires the addition of a dissipation term. The generic formulation for this type of scheme is thus:

$$\iint_{S_l} \underline{\boldsymbol{F}} \cdot \mathbf{n} dS = \frac{1}{2}(\underline{\boldsymbol{F}}_{\Omega_{ijk}} + \underline{\boldsymbol{F}}_{\Omega_{ijk+1}}) \cdot \mathbf{n}_{S_l} - \mathbf{D}_{S_l} \tag{3.1.53}$$

In the frame of the thesis, the second order scheme of Jameson [120] has been used within the **elsA** software.

Modified upwind scheme: the AUSM+(P) scheme Upwind schemes are based on the fact that convective fluxes propagate the information in some preferred directions (characteristics theory). Two types of solvers based on upwind schemes exist: schemes of Flux Difference Splitting (FDS) type (Roe, Osher...) and schemes of Flux Vector Splitting (FVS) type (Van Leer, etc...). FVS schemes are generally more robust in the treatment of shock waves and high intensity expansions but their precision is lower. Their use in the treatment of a large variety of flows (turbulent, reactive, hypersonic,...) has lead to an increased interest in FVS schemes of the AUSM (Advection Upstream Splitting method) family. Indeed, the modifications introduced by Liou [145] to the AUSM scheme to obtain the AUSM+ enables to reach the accuracy of FDS schemes while keeping the robustness of the original FVS scheme in case of shock waves and expansion fans.

In the frame of this thesis work, ZDES computations have been performed using the scheme AUSM+(P) developed by Edwards & Liou [94] and modified by Mary & Sagaut [151]. The main idea of AUSM schemes is based on the decomposition of convective fluxes at the cell interface S_l in one convective term $\underline{F^c}\rfloor_{S_l}$ and one term of pressure $\underline{P}\rfloor_{S_l}$:

$$\underline{\mathbf{F}}\rfloor_{S_l} = \underline{\mathbf{F}^c}\rfloor_{S_l} + \underline{\mathbf{P}}\rfloor_{S_l} \tag{3.1.54}$$

As an illustration, we focus on the mono-dimensional case. The vector of variables is defined by :

$$\boldsymbol{q} = \begin{bmatrix} \overline{\rho} \\ \widetilde{\overline{\rho} u_1} \\ \widetilde{\rho E + \overline{p}} \end{bmatrix} \tag{3.1.55}$$

The Euler flux, as it is calculated in **elsA** is then, with L and R exponents respectively referring to left and right sides:

$$\underline{\mathbf{F}}\rfloor_{S_l} = \underbrace{\frac{U_{int}}{2}(\mathbf{q}\rfloor^L + \mathbf{q}\rfloor^R) - \Phi \; max(U_{int}, C_1 U_{ref})(\mathbf{q}\rfloor^L - \mathbf{q}\rfloor^R)}_{\underline{\mathbf{F}^c}\rfloor_{S_l}} + \underbrace{\frac{1}{2}(\begin{pmatrix} 0 \\ p\rfloor^L + p\rfloor^R \\ 0 \end{pmatrix}}_{\underline{\mathbf{P}}\rfloor_{S_l}} \tag{3.1.56}$$

where U_{int} can be considered as the normal velocity at the interface :

$$U_{int} = \frac{u_1\rfloor^L + u_1\rfloor^R}{2} - \underbrace{max\left(0, 1 - 2\frac{u_1\rfloor^L + u_1\rfloor^R}{2c}\right) C_2 \frac{p\rfloor^L + p\rfloor^R}{\rho_{ref} U_{ref}}}_{pressure-velocity\ correlation\ term} \tag{3.1.57}$$

Thus, the pressure-velocity correlation term, which is similar to the one introduced by Rhie & Chow [178], is active for interface Mach numbers $(u_1\rfloor^L + u_1\rfloor^R)/(2c)$ lower than 0.5.
C1 and C2 are some constants whose value has been determined according to the works of Mary [150] to limit the dissipation of the scheme:

$$C1 = C2 = 0.04 \tag{3.1.58}$$

At last, the quantity Φ in eq (3.1.56) is a sensor that depends on the smoothness of the primitive variables in $\mathbf{q}$. If no spurious oscillation is detected on these variables, the value of Φ is 0 and the scheme is thus centered. Otherwise, Φ is set to 1 in order to damp oscillations and the scheme is then upwind.

Actually, an extrapolation method MUSCL (*Monotonic Upwind-Centered Schemes for Conservative Laws*) is used to increase the effective order of the schemes. In this procedure introduced by Van Leer [218], instead of considering a piecewise constant approximation for each cell, a piecewise linear approximation is used. As this method can induce spurious oscillations in the presence of strong gradients, it is generally associated to a slope limiter in order to respect the TVD (*Total Variation Diminishing*) criterion introduced by Harten [110].

3.1.3.2 Time integration

Once the spatial discretization is done, the remaining system of Navier-Stokes equations can be written:

$$\begin{aligned}\frac{d\mathbf{q}_{ijk}}{dt} &= -\frac{1}{\Omega_{ijk}}\sum_{l=1}^{6}[\underline{\mathbf{F}}(\mathbf{q}_{ijk}) + \underline{\mathbf{F}^v}(\mathbf{q}_{ijk})]\cdot\mathbf{n}_{S_l} \\ &= -\frac{1}{\Omega_{ijk}}\sum_{l=1}^{6}[\mathbf{F}_{ijk,l} + \mathbf{F}^v_{ijk,l}] \\ &= -\frac{1}{\Omega_{ijk}}\mathbf{R}_{ijk}\end{aligned} \tag{3.1.59}$$

where Ω_{ijk} and S_l are respectively the volume and the surface of the *ijk* cell. The residual $\mathbf{R}_{ijk}$ has been introduced to simplify the notation.

The objective of the time integration is to solve the equation (3.1.59). Therefore, the exact solution $\mathbf{q}_{ijk}(t)$ is replaced by its discrete values $(q_{ijk})_n$ at every time $t_n = n\Delta t$. To estimate the sequence $(\mathbf{q}_{ijk})_n$, explicit formulations can be used in which the calculation of $(\mathbf{q}^{n+1}_{ijk})$ involves only $(\mathbf{q}^n_{ijk})$, i.e only values at the previous time step t_n. The knowledge of the initial condition, $\mathbf{q}_0$ then enables to calculate all the values of the sequence $(\mathbf{q}_{ijk})_n$. Despite the ease of implementation of such methods, they are submitted to the CFL (Courant-Friedrich-Levy) stability condition that drastically limits the choice of the time step. This constraint can be written:

$$\Delta t < CFL_{max}\frac{\Delta}{|u| + c} \tag{3.1.60}$$

with $\Delta = \min_{\chi\in(i,j,k)}\Delta_\chi$ the local characteristic length scale of the mesh, u the characteristic velocity of the flow, c the local sound speed and CFL_{max} a constant depending on the time integration scheme.

In the case of unsteady simulations dealing with low frequency phenomena, it is mandatory to get a sufficiently long time of simulation. Unfortunately, the condition of stability of explicit schemes imposes extremely small time steps which are not compatible with simulations over a long period. It is thus necessary to move toward implicit time integration schemes that are unconditionally stable. Indeed, due to the less restrictive constraint on the time step, implicit schemes can provide an important saving of computational time.

Backward Euler scheme used for RANS computations The time integration scheme chosen for RANS computations is the backward Euler scheme that can be written:

$$\mathbf{q}^{n+1}_{ijk} - \mathbf{q}^n_{ijk} = -\frac{\Delta t}{\Omega_{ijk}}\mathbf{R}^{n+1}_{ijk} \tag{3.1.61}$$

The flux encompassed in the implicit term $\mathbf{R}^{n+1}_{ijk}$ are then linearized by neglecting the terms whose order is higher or equal to 2 in its Taylor development:

$$\mathbf{R}^{n+1}_{ijk} = \mathbf{R}^n_{ijk} + \frac{\partial\mathbf{R}_{ijk}}{\partial\mathbf{q}_{ijk}}\,|^n\,\Delta\mathbf{q}^{n+1}_{ijk} + \mathcal{O}(\Delta t^2) \tag{3.1.62}$$

with $\Delta\mathbf{q}^{n+1}_{ijk} = \mathbf{q}^{n+1}_{ijk} - \mathbf{q}^n_{ijk}$.
The jacobian matrix of the flux $\underline{\mathbf{J}}^n_{ijk}$ is introduced to obtain the expression:

$$\left(\frac{\Omega_{ijk}}{\Delta t}\underline{\mathbf{I}} - \underline{\mathbf{J}}^n_{ijk}\right)\Delta\mathbf{q}^{n+1}_{ijk} = \mathbf{R}^n_{ijk} \tag{3.1.63}$$

where $\mathbf{R}_{ijk}^n$ is called the explicit residual, and whose value at the time t_n is known from the spatial integration process.

As the calculation of a jacobian matrix is computationally expensive and generally leads to a wrong conditioning, jacobian matrices are approximated in **elsA** thanks to the LU-SSOR method.

Then, the simplified linear system is solved by using a sub-iteration process to increase the time integration accuracy. The idea is to solve the system for intermediate time steps between times t_n and t_{n+1} until obtaining the convergence of $\mathbf{q}_{ijk}^{n+1}$. To do so, an LU factorization is used. The obtained sequence $(\mathbf{q}_{ijk})_n$ thus represents the time evolution of the aerodynamic field at each point of the mesh. In steady RANS simulation, the time is considered as an iteration parameter that enables to converge toward a steady solution. A first order scheme in time is thus achieved.

Gear scheme for ZDES computations Computations involving turbulence-resolving approaches requires a higher order of accuracy in time than RANS computations. Therefore, for ZDES computations performed with the **elsA** software, a second order accurate scheme of Gear has been used. The reference to the inner iteration loop is omitted in the following for the sake of simplicity in the notation. Within that scheme the system is expressed by:

$$\frac{3}{2}\Delta\mathbf{q}_{ijk}^{n+1} - \frac{1}{2}\Delta\mathbf{q}_{ijk}^{n} = -\frac{\Delta t}{\Omega_{ijk}}\mathbf{R}_{ijk}^{n+1} \tag{3.1.64}$$

The resolution of this system is similar to the one of the backward Euler scheme used in RANS computations:

1. The flux are linearized from their Taylor development by neglecting terms of order higher than 2 in time;
2. The jacobian matrix are simplified, using the LU-SSOR method;
3. A sub-iteration process allows to resolve the system with a second-order accuracy in time. Each sub-iteration is resolved using an LU factorization.

The use of implicit schemes for unsteady computations can be questioned, but numerous studies have shown the relevance of such schemes for the aerodynamic purposes ([69], [163],[233],[83]...). These studies have established that the time step must be chosen in order to respect to the empirical rule:

$$\frac{CFL_{max}}{N_{sub-iterations}} \leqslant 4 \tag{3.1.65}$$

The number of sub-iterations $N_{sub-iterations}$ is fixed to verify, *a posteriori*, that for each time step the residual decreases at least of one order of magnitude following the L_2 norm.

3.1.4 Random Flow Generation technique

In order to generate turbulence representative of upstream turbulence inside the nozzle, the Random Flow Generation (RFG) technique developed by Smirnov et al.[197] has been used in this work. This method, derived from an idea of Kraichnan [135], is based on the superposition of harmonic functions. The main advantage of this approach is to keep a small number of parameters to set, which fits well the requirements of industrial applications and seems acceptable for upstream turbulence that is supposed to be rather isotropic and homogeneous. Indeed, the only user-defined parameters are the Reynolds stress tensor, a characteristic turbulence length, a characteristic turbulence time scale and

the number of random sample accounting for the stochastic behavior of the turbulent flow. In this approach the velocity fluctuations are generated according to following steps:

- The Reynolds stress tensor of the desired turbulence flow field has to be imposed:

$$r_{ij} = \overline{u_i' u_j'} \tag{3.1.66}$$

from which an orthogonal transformation through the tensor a_{ij} enables to reduce it to a diagonal tensor:

$$a_{mi} a_{nj} r_{ij} = \delta_{mn} c_n^2 \tag{3.1.67}$$

- Then a three-dimensional transient flow field $\{\upsilon_i(x_j,t)\}_{i,j\in[1,3]}$ is generated using the modified method of Kraichnan [135]:

$$\upsilon_i(x_j,t) = \sqrt{\frac{2}{N}} \sum_{n=1}^{N} \left[p_i^n cos(\widetilde{k_j^n}\widetilde{x_j} + \omega_n \widetilde{t}) + q_i^n sin(\widetilde{k_j^n}\widetilde{x_j} + \omega_n \widetilde{t}) \right] \tag{3.1.68}$$

with N corresponding to the number of a random sampling used to generate random variables,

$$\widetilde{x_j} = \frac{x_i}{l} \ , \ \widetilde{t} = \frac{t}{\tau} \ , \ c = \frac{l}{\tau} \ , \ \widetilde{k_j^n} = k_j^n \frac{c}{c_j} \tag{3.1.69}$$

where l and τ are the length and time-scales of turbulence, and

$$p_i^n = \epsilon_{ijm} \zeta_j^n k_m^n \ , \ q_i^n = \epsilon_{ijm} \xi_j^n k_m^n \tag{3.1.70}$$

where, noting $N(M,\sigma)$ the normal distribution of mean M and standard deviation σ, $k_j^n \in N(0,1/2)$ and $\omega_n, \zeta_j^n, \xi_j^n \in N(0,1)$. Last, ϵ_{ijm} is the permutation tensor used in vector product operation. These random perturbation variables are generated separately from the main time iteration loop of the flow solver with only the assembly of the velocity components in eq (3.1.68) performed for each iteration. This ensures a spatial and time consistency for the different computational domains and simulations.

- Then the final perturbation is obtained by applying the scaling and orthogonal transformations to the perturbation flow field υ_i to obtain a new flow-field u_i'

$$w_i(x_j,t) = c_i \upsilon_i(x_j,t) \tag{3.1.71}$$

$$u_i'(x_j,t) = a_{ik} w_k(x_j,t) \tag{3.1.72}$$

In the **elsA** software, the RFG method is implemented with a boundary condition formulation that respects the characteristics boundary relations for subsonic boundary conditions. Close to walls, a damping function ensures the physical influence of walls. The validation of the technique in the **elsA** software has been carried out by Brunet for a simple advection test case and later for double flux engine ZDES simulations [55, 56]. Marty also used the RFG technique in the framework of LES of low pressure turbine blades [149].

3.2 Experimental data set: MARTEL

To study the jet physics and validate the numerical study of a dual-stream jet, the experimental data used in this thesis comes from the JEDI-MARTEL engine jet campaign that was carried out at the *Laboratoire d'Etudes Aerodynamiques* (LEA, now part of the P' Institut) in Poitiers, France [104]. In this section, the geometry is presented, as well as operating conditions and experimental means.

3.2.1 Geometry and operating conditions

3.2.1.1 Geometry

In this experiment, an isolated heated dual-stream coaxial jet, representative of current aircraft nozzles, is investigated, without external wind. As illustrated in figure 3.7, it consists in a short-cowl nacelle, with staggered primary and secondary nozzles and an external plug. The secondary and the primary final ducts are purely convergent.

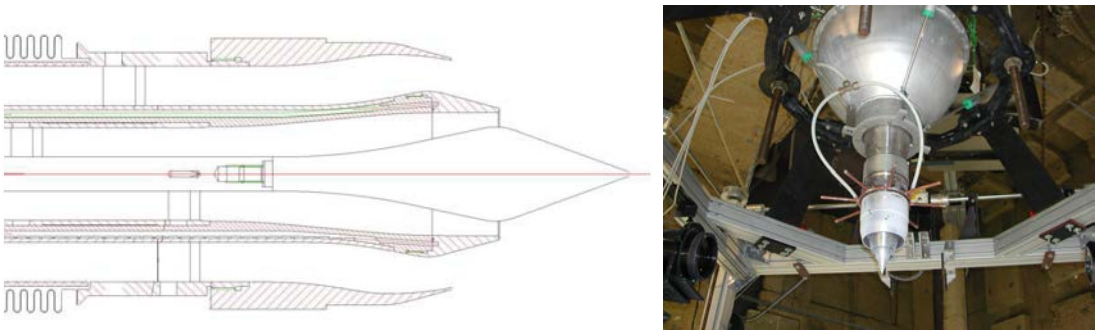

(a) (b)

Figure 3.7: Martel test rig: (a) geometry of the coxial nozzle, (b) JEDI nozzle installed on the MARTEL Test Rig

3.2.1.2 Operating conditions

The primary flow is heated up to $T_c = 500K$, its total pressure ratio is $NPR_c = 1.6$ and its nominal mean flow velocity at nozzle exit is $V_c = 300\ m/s$. The secondary flow is at ambient temperature ($T_f = 282K$), its total pressure ratio is $NPR_f = 2.425$ and its reference mean velocity is $V_f = 350\ m/s$. In these operating conditions, the flow stream exhibits an Inverted Velocity Profile (IVP) with $\rho_c < \rho_f$ and the secondary jet gets an under-expanded structure with the secondary flow shocked, followed by a shock-cells pattern downstream the nozzle as decribed in sec 2.1.3. The external mixing layer between static external field and the secondary flow is characterized by a convective Mach number of 0.52, while the internal mixing layer's one is 0.06. A summary of the operating conditions is given table 3.2.

Flow	Primary	Secondary	Outter
Reference velocity (m/s)	295	350	0
NPR (P_{i_0}/P_a)	1.6	2.425	1
Total Temperature (K)	500	283	280
Fully expanded jet Mach number M_j	0.85	1.2	0

Table 3.2: Summary of the operating conditions

3.2.2 Experimental test rig

The MARTEL Test Rig enables to generate relatively high mass flow rates , up to 2.5 kg/s, thanks to the high pressure air network of the CEAT in Poitiers and the maximal generative temperature that can be reached is 1850 °C. The rig is hold in a semi-anechoic

hall, represented in figure 3.8(a), and the air supply network is connected to two tranquilization chambers, one per stream. These chambers ensure the interface between the supply system and the model, as shown in figure 3.8(b). Some displacement sensors have also been installed to take into account the dilatation effects due to the heating of the primary flow. The measures are carried out only once the signals issuing from these sensors are stabilized.

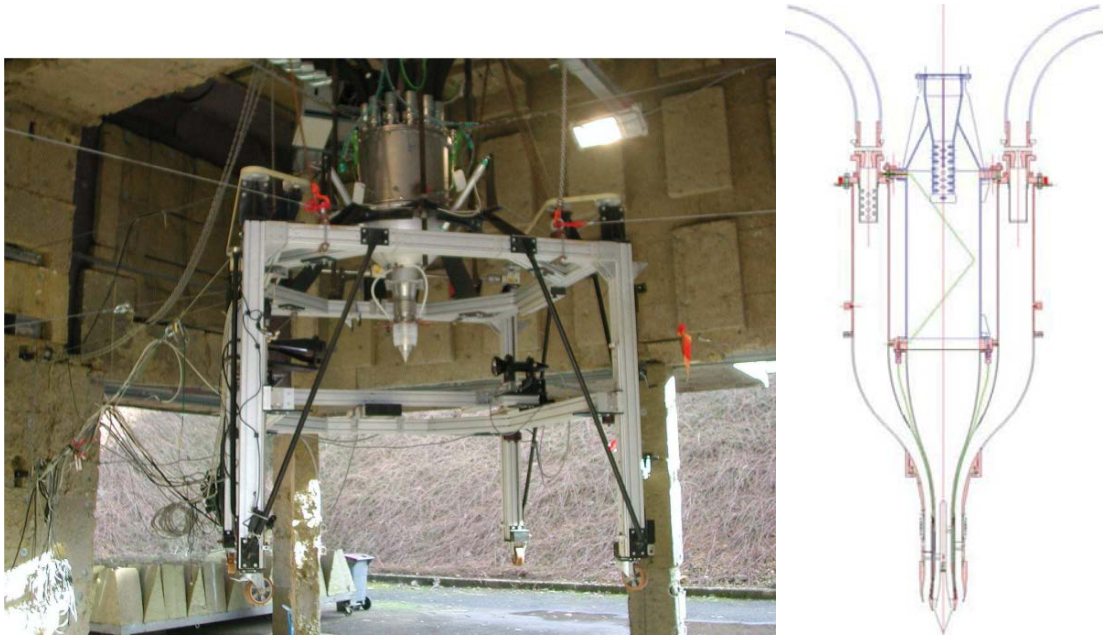

(a) (b)

Figure 3.8: Complete MARTEL test rig within the semi-anechoic hall

3.2.3 Measurements

Measurements are performed by means of a two-component Laser-Doppler Velocimetry (LDV), thermocouples, and a “triple" probe (total temperature, static and total pressures) as shown figure 3.9. The two-component LDV process provides the velocity components in the axial and radial directions. The averaged values of these components $\overline{u_x}$ and $\overline{u_r}$, as well as the RMS (Root Mean Square) average of their fluctuations $\sqrt{\overline{u_x'^2}}$ and $\sqrt{\overline{u_r'^2}}$ are obtained from a sampling signal of 20000 points. Last, these velocity signals in two directions of the flow provide also the shear-stress component $\overline{u_x' u_r'}$. These quantities will be normalized by the reference velocity ΔU, which is the velocity difference between the secondary jet and the outer flow.

As illustrated in figure 3.9, several radial velocity profiles have been measured every 0.5 diameter up to $x/D = 6$. For all these profiles, LDV measurements have been conducted. In addition, for some of them, the temperature has been acquired with a thermocouple. LDV measurements along two axial lines, respectively whithin the primary and secondary jets, have also been performed in order to characterize the shock-cell system.

All the measurement lines are represented in figure 3.10. The measurement lines plotted in blue refer to sets of data provided only by LDV and the red lines refer to sets of data obtained both by LDV and thermocouple. It is worthwhile to mention, as indicated in figure 3.10, that not all profiles have been discretized with the same number of points.

3.3 Conclusion

In this chapter, both numerical methods and experimental data used in the PhD work have been described.

Regarding numerical methods, the main approaches allowing to solve the Navier-stokes equations have been presented. They involve different levels of modeling, with different mesh requirements and computational time constraints. On one hand, the RANS approach models all the turbulence thanks to closure equations of a turbulence model but provides few fluctuating properties, on the other hand, the LES approach models only small scales but requires very fine mesh and induces a prohibitive CPU cost in the boundary layers.

Not all these approaches are adapted to simulate complex flows, and the choice of an approach is highly related to the objectives of the simulation. The RANS approach is actually a satisfactory way to perform steady aerodynamic simulations in a daily iterative process, whereas LES, due to its computational cost, remains limited to low-to-moderate Reynolds number applications, on relatively simple geometries. The DES-like approaches that have last been detailed, among which the ZDES developed at ONERA and used in this study, enable to couple both modelings in a same calculation and to restrict turbulence-resolving methods, computationally expensive, only to the areas of interest. These fully coupled hybrid RANS-LES approaches now appear as a promising tool to accurately sim-

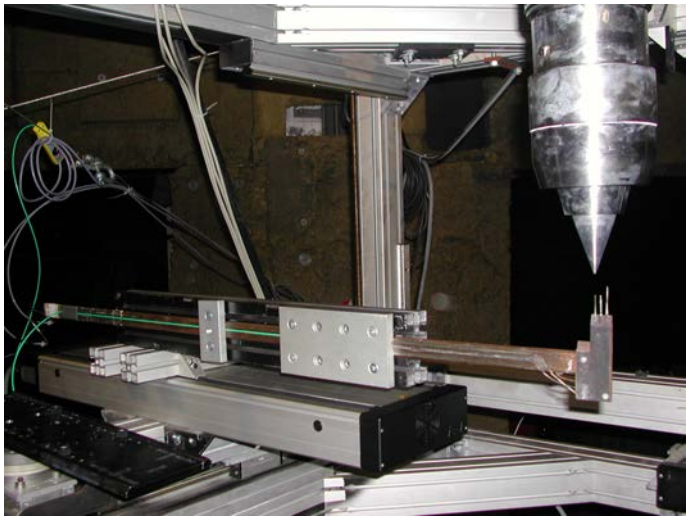

Figure 3.9: Measurements carried thanks to a “triple" probe

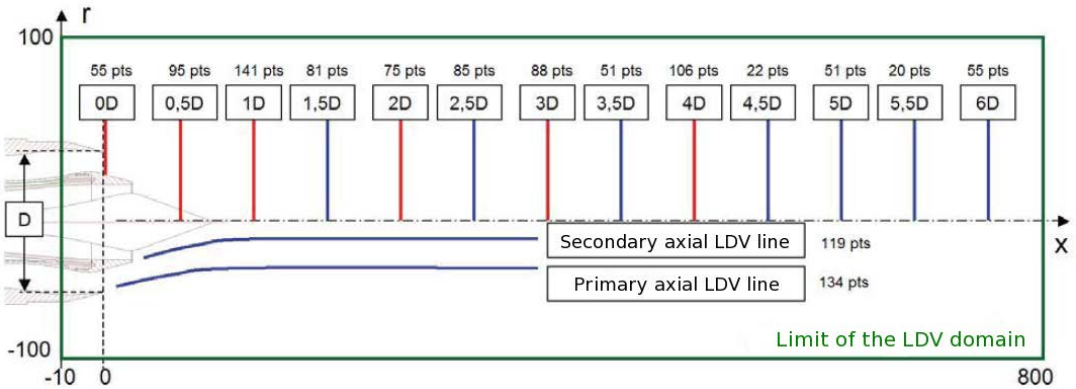

Figure 3.10: Measurement lines: blue = measurement lines with LDV only; red = measurement lines with LDV and thermocouples, adapted from Giner [102]

ulate unsteady flows for complex configurations at high Reynolds numbers. The Random Flow Generation technique used in this work to take into account upstream turbulence has also been presented.

The experimental configuration used in this work is a dual stream nozzle with an external plug, representative of current aircraft engines (MARTEL test campaign). The operating conditions chosen enable to reproduce the NPR and the associated shock-cell system of a cruise flight, although the external flow speed is not taken into account. The mean and turbulent velocities have been measured thanks to a LDV process, and offers a large data set for the study of propulsive jets and the validation of the simulations performed.

Chapter 4

Effect of ZDES numerical setup on the resolved jet physics

In this chapter, Zonal Detached Eddy Simulation (ZDES) is used to simulate the flow of the dual-stream nozzle presented in the previous chapter. The present chapter focuses on the effects on the mixing layer development and the shock-cells positioning of a low dissipative spatial scheme as well as the interest of a subgrid length-scale based on local vorticity, in the frame of mode 1 and mode 2 of ZDES.

Contents

4.1 Introduction

As mentioned in chapter 2, several RANS/LES approaches have been proposed to treat dual-stream nozzles, but all suffer - to some extent - from a laminar mixing layer between the core and the fan flow. To prevent this recurring issue, the present chapter explores three ways to improve jet flow simulations with ZDES as presented below.

First, a possible origin of the delay in the development of instabilities lies partly in the inevitable anisotropy of the mesh in the vicinity of complex flows and geometries that can affect the local subgrid viscosity. Therefore, taking into account this anisotropy in the definition of the subgrid length scale appears as a way of improvement for mixing layer development in jet flow simulations. As presented in sect 3.1.2.4, the original formulation of the ZDES has been proposed with the time-honored subgrid length scale Δ_{vol} only based on the local grid spacing. This subgrid length scale has proven to reduce the delay in the birth of instabilities, frequently evidenced with the original DES and DDES length-scale Δ_{max} [81]. However, in axisymetrical cases with shear-layers simulated on structured grid,

it is difficult to reduce the tangential cell size compared to axial and radial ones, which can lead to an overestimation of the subgrid viscosity causing a remaining delay in the development of instabilities. Preventing this behavior was one of the motivation leading to the proposal of Chauvet et al. [65] to use the subgrid length scale Δ_ω based on the local grid spacing as well as on the local vorticity orientation. Several studies[65, 81] have shown the efficiency of this length scale to resolve shear-layers. Therefore, the length scale Δ_ω is assessed in this study because it is expected to promote the development of small scale turbulence in the internal mixing layer. Results are compared with simulations using the subgrid length-scale Δ_{vol}.

Second, this chapter investigates the role of the numerical dissipation due to the spatial scheme in the jet development. Most of the studies using eddy resolving simulations on simple configurations are based on low dissipation schemes. However, currently in industrial environment, the most popular schemes are the second order accurate centered scheme of Jameson [120] and the second order accurate upwind scheme of Roe [179] as a result of a trade-off between robustness and accuracy. These numerical schemes are known to be quite dissipative, which makes them rarely used in pure LES simulations, and a possible weakness of hybrid RANS/LES calculations using them. The use of a low dissipation scheme could improve the accuracy of eddy resolving simulations. Therefore the present work aims at investigating the possible advantages and limitations of using in the framework of complex geometries a modified AUSM+P scheme (developed by Edwards & Liou [94] and modified by Mary & Sagaut [151]), which has been used as a standard method for ZDES developments[81, 101] and for academic studies [84].

Eventually, in the framework of the industrialized implementation of eddy-resolving approaches, the ZDES mode 2 is assessed, since it provides an automatic switch between RANS and DES areas as required for complex applications.

The chapter is organized as follows. First, the mesh, the numerical setup and the different simulations carried out are presented. Then the effect of the spatial scheme, of the subgrid length scale and of the mode 2 of ZDES are successively assessed, in terms of instantaneous and time averaged contents, mean and turbulent fields. Finally, a spectral analysis is performed, focusing on the shear-layers development.

4.2 Mesh generation for ZDES

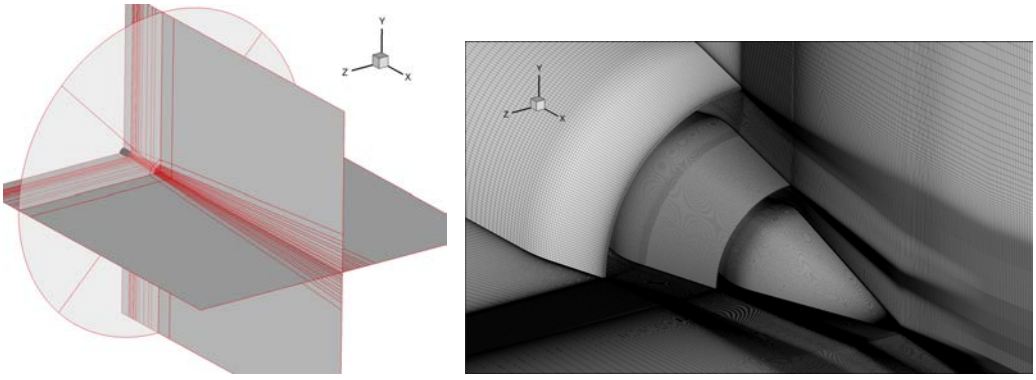

(a) 3D nozzle and block topology (b) mixing layer refinement downstream the nozzle

Figure 4.1: 3D mesh: (a) 3D mesh topology, (b) mixing layers refinement

ZDES simulations are carried out are carried out within the elsA software on a 3D

structured multi-block coincident mesh of around 205 million grid points. A H-type block topology is used at the nozzle axis to avoid centerline singularity. The mesh is discretized with 416 points in azimuthal direction and in radial direction the grid points are clustered close to the thick trailing edges, at the initial stages of the Kelvin-Helmholtz instabilities. To evaluate the refinement in mixing layers and ensure they are correctly captured, the vorticity thickness defined by:

$$\delta_\omega = \frac{\Delta u}{(\partial u/\partial r)_{max}} \tag{4.2.1}$$

is used.

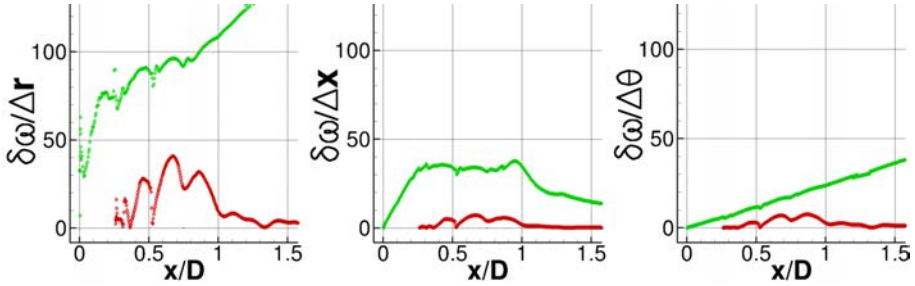

Figure 4.2: Local ratio of vorticity thickness over the grid length in the 3 directions : (green) external mixing layer , (red) internal mixing layer. $\Delta_\theta = r\Delta_\phi$ denotes the azimutal cell size at a constant radial location r with a constant azimutal discretization Δ_ϕ (rad).

In mixing layers, the radial spacing target target chosen for the present study is about $\Delta_r = \delta_\omega/40$, beyond the minimal value commonly acknowledged for this type of simulation $\delta_\omega/20$[83], and axial and azimuthal spacings verify $\Delta_{x,z} < \delta_\omega/2$. Considering the vorticity thickness extracted from the RANS computation, it can be seen in figure 4.2 that this goal is fully achieved in the external mixing layer, but criteria are partially verified in the internal mixing layer between fan and core flows where the radial spacing oscillates between $\delta_\omega/5$ and $\delta_\omega/40$. However, let us remind that in the core cowl trailing edge region, as the velocity difference between fan and core flows is low, the nature of the flow is rather similar to a base flow wake than to a mixing layer and the criterion using the vorticity thickness appears very hard to reach. Nevertheless, the mesh density in this region is very high, able to capture strong velocity gradients and, with 205 millions of grid points, lies at the limit of refinement that can be accepted in terms of CPU cost. The expansion ratio in the streamwise direction is maintained inferior to 1.05 up to approximately $x/D = 2$ and to 1.1 further downstream. The rise of the axial cell length seems however significant from $x/D = 1$, as shown figure 4.2. Furthermore, the Erikssonn skewness is very satisfactory (more than 0.7 everywhere and more than 0.95 for 99% of cells).

4.3 Numerical setup

4.3.1 Restrictions for the choice of time steps

As mentioned in section 3.1.3, the choice of the time step must satisfy stability conditions associated to the CFL number. Nonetheless, with implicit time integration schemes, no stability condition has to be fulfilled. A CFL higher than 1 can thus be reached, keeping in mind that a precision loss accompany the CFL number increase. The time step choice generally results from a trade-off between precision, robustness and computational time. For instance, Daude et al. [77] recommend to limit the CFL to 15-20 with a sufficient

number of inner-iterations N to verify CFL/N $\leqslant 4$. For reminder, the CFL number is defined by:

$$CFL = \frac{(u+c)\Delta t}{min(\Delta_x, \Delta_y, \Delta_z)} \tag{4.3.1}$$

where Δt is the physical time step, u the local velocity and c the sound speed. A first RANS calculation enables to more precisely estimate the local values of sound speed and velocity in the domain. Considering a physical time step of $1.5 \cdot 10^{-7}s$, maximal CFL number values lies around 15 as presented in figure 4.3. These maximal values of the CFL number are located within the vicinity of the trailing edge, where the grid cell sizes remain verya small, due to the propagation of the boundary layers refinement. These values of CFL number are compliant with the implicit time integration used, and similar to maximal values encountered in this kind of simulations [233, 57] and advocate by Daude et al. [77].

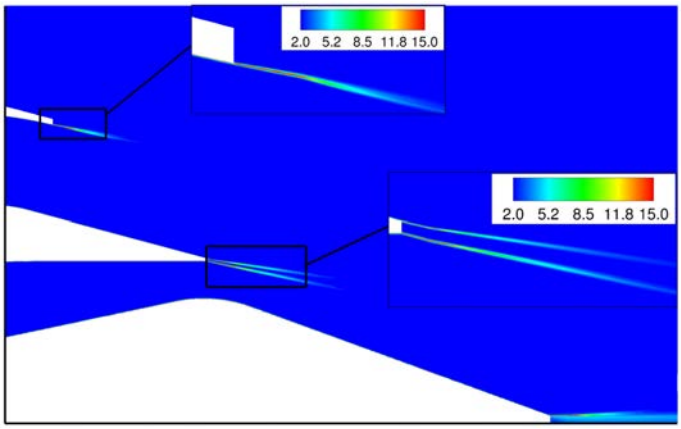

Figure 4.3: Acoustic CFL number using a time step $\Delta t = 1.5.10^{-7}s$

However, in order to limit the computational time of simulations, some attempts have been made at increasing the time step. Computations have thus been performed with time steps $\Delta t = 5 \cdot 10^{-7}s$ and $\Delta t = 3 \cdot 10^{-7}s$ to divide the computational time by a factor 2 or around 3. Unfortunately, the development of instabilities in those last cases was highly damped compared to the case using $\Delta t = 1.5 \cdot 10^{-7}s$. The origin could lie in the dissipative behavior of the time integration scheme when increasing the time step, but the reason may rather be that such time step values are to high to capture the physical characteristic time scales in the early beginning of the inner shear-layer.

In the end, the value $\Delta t = 1.5 \cdot 10^{-7}s$ is conserved for all unsteady simulations, leading to the reduced time step $\widetilde{\Delta t} = \frac{\Delta t \Delta U}{D}$ of $4.86.10^{-4}$.

The post-processing providing statistical results is carried out as follows: once the transient phase is evacuated, the statistical average is performed over a period of 200000 iterations, *i.e.* $T = 30$ms corresponding approximately to $\widetilde{T} = \frac{T \Delta U}{D} = 100$. The notation $\overline{\cdot}$ refers to the time average.

The spectral analysis has been carried out using a time signal of $T = 36$ms corresponding to $\widetilde{T} = \frac{T \Delta U}{D} = 116$.

4.3.2 Computational description

The RANS and ZDES simulations are both based on the Spalart-Allmaras turbulence model. Regarding boundary conditions, far field free-stream conditions are modelled by non-reflective conditions while the skin boundaries are modelled by adiabatic no-slip conditions. At upstream boundaries, the total pressure and temperature are imposed while the pressure is prescribed at the downstream interface.

First, a RANS computation is carried out, to provide a fast solution with a low CPU cost and to initialize the field of ZDES computations. Then, as mentioned previously, three types of numerical parameters have been investigated : two subgrid length scales, Δ_ω and Δ_{vol}, and two numerical schemes, namely the scheme of Jameson and the scheme AUSM+(P) in its modified version of Mary & Sagaut, as well as the use of ZDES mode 2 are compared in this study.

- In order to assess the spatial scheme effects on the jet flow field, two ZDES simulations using both spatial scheme AUSMP+(P) and Jameson are performed;
- in order to investigate the subgrid length scale in the frame of ZDES mode 1, two ZDES simulations, implementing respectively Δ_ω and Δ_{vol} are carried out using the spatial scheme AUSMP+(P);
- Eventually, to respond to industrial requirements, a “non-zonal" approach is of primary interest and has been investigated. A well-known approach, the Delayed Detached Eddy Simulation (DDES) [201] has quickly been assessed for simulating round jets. However, the first comparison with ZDES suggests an important issue in the development of instabilities in both external and internal mixing layers (see figure 4.4). This dramatic delay in the development of instabilities, due to an excessive turbulent viscosity in the shear-layer, had already been addressed by Deck [81]. Actually, to treat “automatically" the switch between RANS and LES areas, the mode 2 of the ZDES is preferred. It is implemented in a computation using Δ_ω with the AUSM+(P) scheme, and is compared with the mode 1.

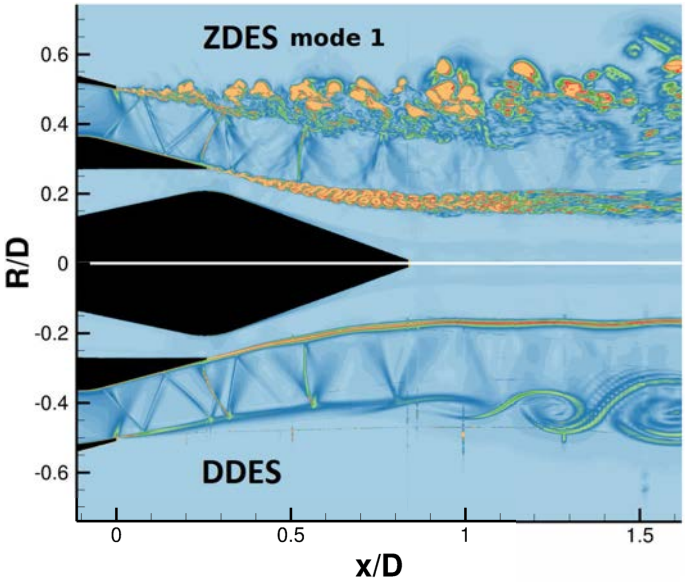

Figure 4.4: Density gradient magnitude : ZDES mode1 (top) versus DDES (bottom)

The features of the different simulations are summarized in Table 1. To refer to the

different simulations, the following taxonomy is used:

Model - Spatial scheme - Subgrid length-scale - Mode of ZDES

with RANS or ZDES for the model, J (Jameson) or A (AUSM+(P)) for the scheme, vol (Δ_{vol}) or ω (Δ_ω) for the subgrid length-scale and mode2 for the mode 2 of ZDES.

Calculation	RANS	ZDES-Jω	ZDES-Aω	ZDES-Avol	ZDES-Aω-mode2
Spatial Scheme	Jameson	Jameson	AUSM+(P)	AUSM+(P)	AUSM+(P)
Subgrid length scale	-	Δ_ω	Δ_ω	Δ_{vol}	Δ_ω
ZDES mode	0	1	1	1	2

Table 4.1: Summary of simulations. Naming used for ZDES simulations: MODEL - SPATIAL SCHEME - SUBGRID LENGTHSCALE - MODE (J=Jameson, A=AUSM+(P), vol=Δ_{vol}, $\omega = \Delta_\omega$).

4.4 Results and discussion

4.4.1 Instantaneous fields

A first glimpse of the instantaneous field is provided in figure 4.5. The instantaneous fields show that in all the ZDES computations the Kelvin-Helmotz instabilities in the external shear-layer become quasi-immediately toward a 3D turbulent state, which is already a clear asset of the method. The density gradient magnitude and the dilatation fields are plotted figure 4.5, and in the external mixing layer region, no major difference can be noticed between the 4 calculations, neither regarding the beginning of instabilities appearance nor about the growth of vortical structures. The velocity gradient between the fan flow and the ambient is so high that the effect of numerical parameters is small in this area. However, the Q-criterion iso-surfaces seem to exhibit smaller structures in the calculations using the AUSM+(P) schemes (figure 4.6(c)) than the one using the Jameson scheme (figure 4.6(a)).

On the core cowl wall, just upstream of the trailing edge, some Q-criterion isosurfaces features are distinguishable in all computations. Those may be the marker of a shallow shock-induced separation, caused by the first strong shock in the fan jet.

Regarding the internal mixing layer, in all computations the Kelvin-Helmholtz instabilities grow very quickly after the trailing edge, but the 3D transition is very long. One can depict two small shear layers that develop on both sides of the core cowl, then merge in a vortex-pairing-like process leading to turbulent transition. Nevertheless, large discrepancies can be observed between the three cases. In the case using the Jameson scheme, the 2D coherence of the structures is maintained excessively far from the trailing edge, as if the small structures were immediately dissipated and could not participate to the mixing of the shear-layer. Figure 4.7(a), shows distinct structures evolving in the azimuthal direction but with a significant length of coherence, even in the $x/D = 1$ plane, giving to the structures a reticulated aspect. Conversely, the two computations using the spatial scheme AUSM+(P) (figures 4.7(c) and 4.7(b)) exhibit a lesser azimuthal coherence, even if the 3D destabilization happens also too late. For these two computations the effect of the subgrid length-scale plays a major role in the early azimuthal destabilization and in the radial mixing efficiency. Using the subgrid length-scale Δ_ω it appears clearly in the Q-criterion visualizations figure 4.6 that azimuthal instabilities occur earlier than when

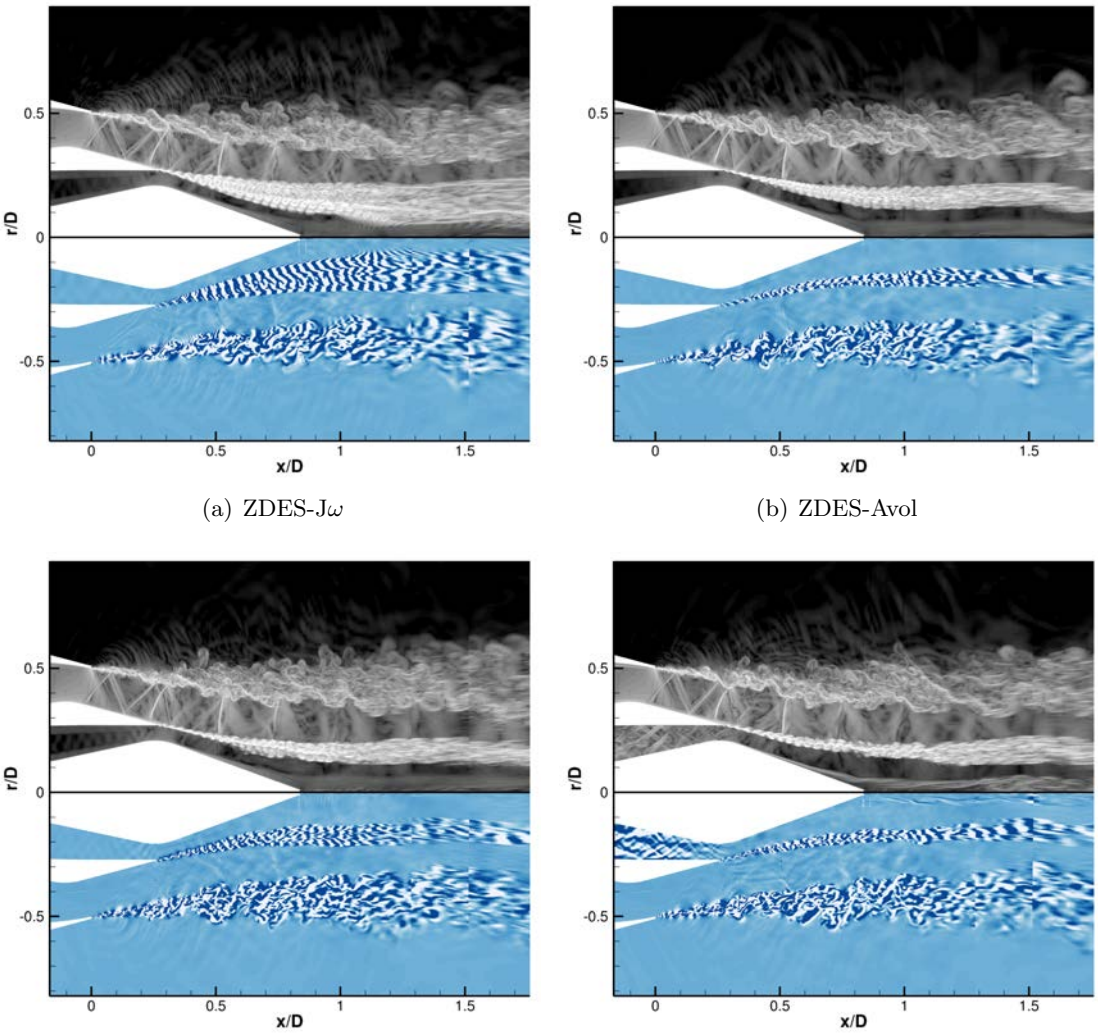

(a) ZDES-Jω (b) ZDES-Avol

(c) ZDES-Aω (d) ZDES-Aω-mode2

Figure 4.5: Instantaneous fields : density gradient magnitude $\| grad(\rho) \|$ (gray scale) and dilatation field $(1/\rho)div(\rho u)$ (blue scale)

using Δ_{vol} and the mixing in the radial directions is slightly improved. The last computation using the mode 2 of ZDES does not present either significant qualitative differences with the mode 1 simulation in the external mixing layer. It exhibits stronger acoustic waves in the internal duct of the nozzle (figure 4.5(d)), but it does not seem to affect the mixing layers development. Another discrepancy lies in the flow development in the plug wake. The vorticity magnitude contours in figure 4.7(d) show a more intense turbulent activity downstream of the plug than in the mode 1 simulations. This suggests that the flow in this area is highly disturbed, even tough no flow separation on the plug has been identified in the simulations data.

4.4.2 Averaged fields

4.4.2.1 Mean quantities

One can observe in figures 4.8(a) to 4.8(d) that the mean velocity agrees well with the available experimental data. No difference can be depicted between the several ZDES cases and the RANS calculation up to $x/D = 0.5D$, except for the internal mixing layer of the case ZDES-Jω. Some discrepancies between RANS and ZDES first appear from

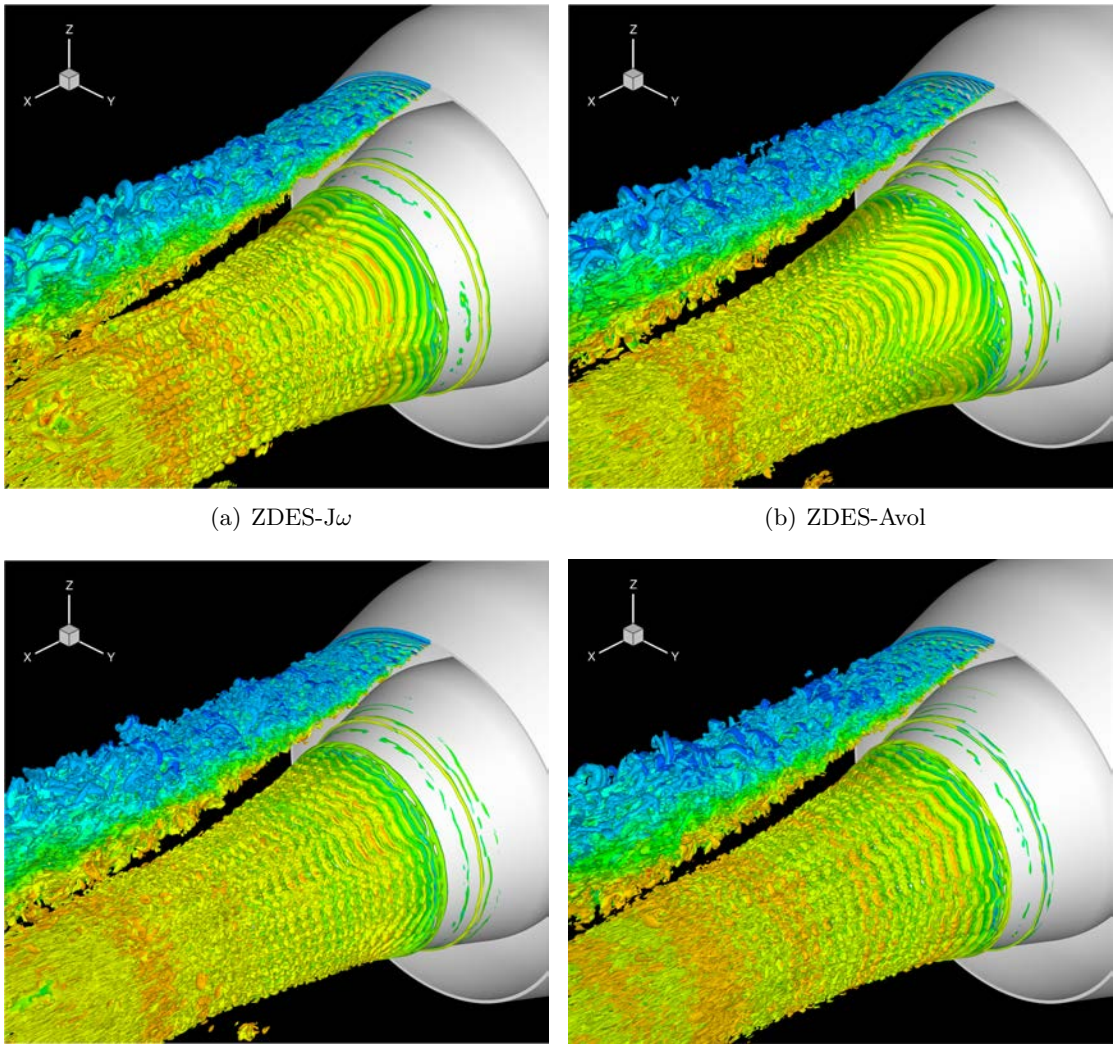

(a) ZDES-Jω (b) ZDES-Avol

(c) ZDES-Aω (d) ZDES-Aω-mode2

Figure 4.6: Q-criterion iso-surface $Q(D^2/\Delta U^2) = 10$ coloured by streamwise velocity magnitude

x/D=1 on the velocity level in figure 4.8(c) in the core of the jet, and further downstream, also on the mixing layer prediction. Discrepancies between simulations and experiment are more important at $x/D = 1.5$ which can be attributed to the wrong prediction of the shock-cell width and positioning in all the simulations. Besides, as exhibited on the fan and core lines (figures 4.8(e) and 4.8(f)), the RANS simulation features the larger phase lag, which is reduced with the ZDES, as well as an excessive velocity damping downstream of $x/D = 1$. On the contrary, the amplitude of oscillations is overestimated with ZDES, particularly between $x/D = 1$ and $x/D = 2.25$.
The discrepancies on the radial velocity profiles are negligible between the four ZDES cases in the external mixing layer. The main discrepancies appear in the internal mixing layer, especially when changing the spatial scheme. In this region, the AUSM+(P) results get closer to the experiment. Indeed, at $x/D = 0.5$, the case inplementing the Jameson scheme exhibits an inverted velocity peak in the core mixing layer instead of a smooth deficit of velocity as in all the other computations and in the experiment (see figure 4.8(b)). This non-physical behavior is not fully understood yet, but could be linked to the unexpected

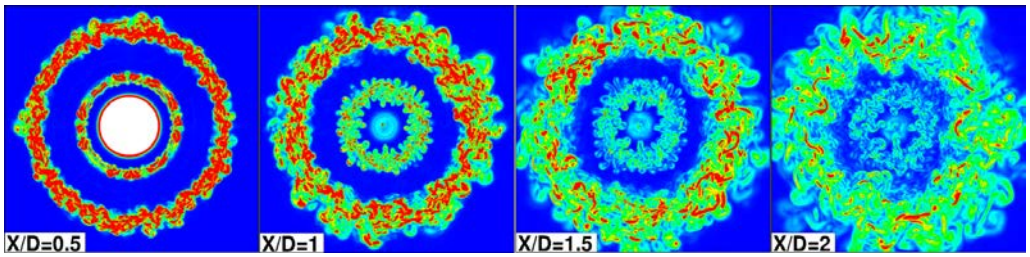

(a) ZDES-Jω

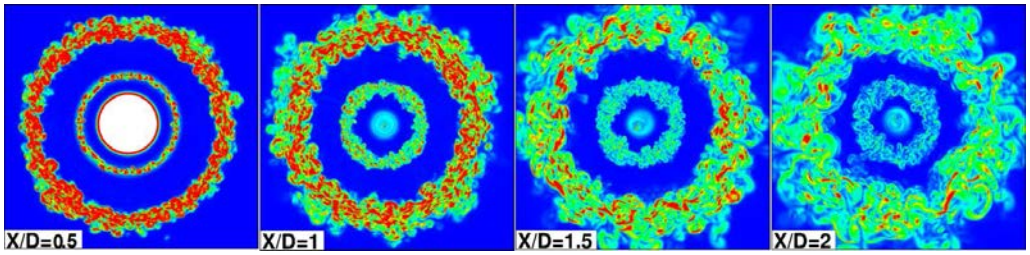

(b) ZDES-Avol

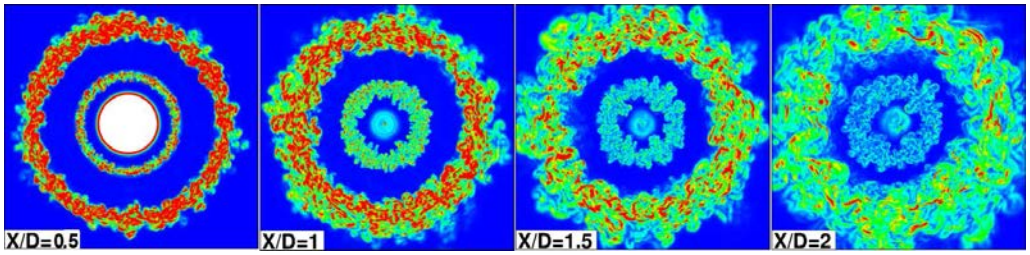

(c) ZDES-Aω

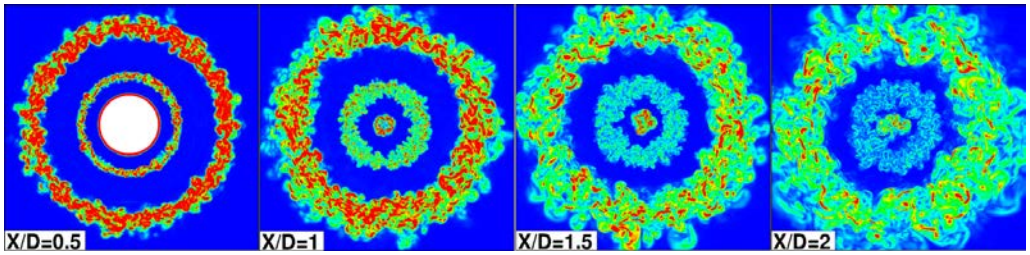

(d) ZDES-Aω-mode2

Figure 4.7: Vorticity Magnitude at various axial locations

vortex-pairing which occurs at this location in this simulation.
Some discrepancies between ZDES simulations also appear on the fan line in figure 4.8(e). From $x/D = 1.5$, the intensity of velocity fluctuations becomes smaller in cases using the AUSM+(P) scheme and the shock cell width is larger with the Jameson scheme. This behavior could be linked to the grid stretching downstream from $x/D = 1$ that dissipates the small structures more present in AUSM+(P) cases. On the core line in figure 4.8(f), the same characteristics are observed.

Overall, the mean velocity does not seem dramatically affected by the change of subgrid length-scale. Indeed, the main discrepancies between the case with Δ_{vol} and the one with Δ_{ω} lies in the slightly smoother velocity profile in the inner mixing layer when using the latter, due to a higher mixing. Downstream of $x/D = 1.5$, the mean level of velocity fluctuations is also slightly higher using Δ_{vol}, as presented in figure 4.8(f).

The only significant difference observed between ZDES mode 1 and mode 2 simulations

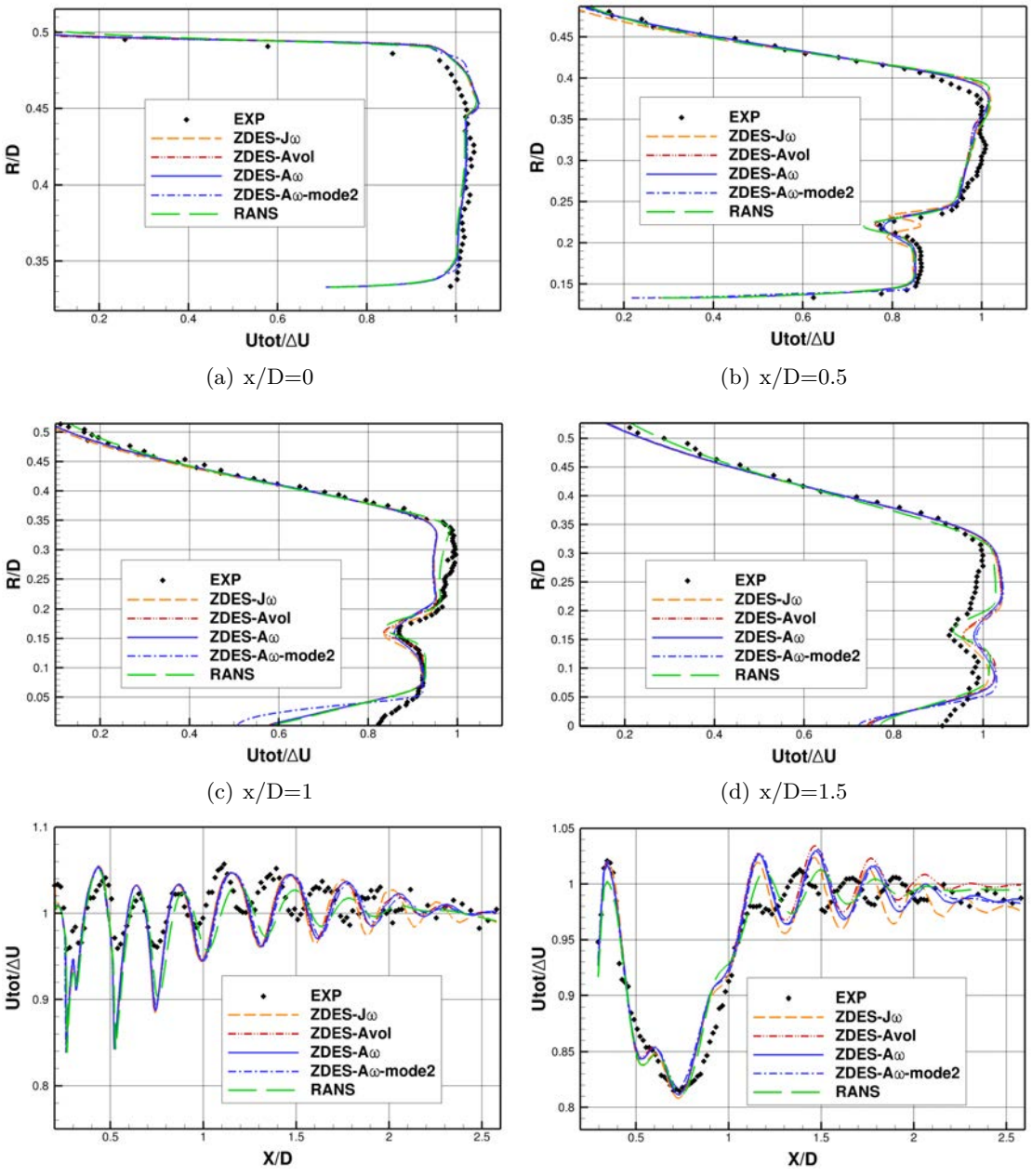

(a) x/D=0 (b) x/D=0.5

(c) x/D=1 (d) x/D=1.5

(e) Fan line (f) Core line

Figure 4.8: Magnitude of velocity: (a) 0D line, (b) 0.5D line (c) 1D line, (d) 1.5D line, (e) Fan line, (f) Core line

lies downstream of the plug at $r/D = 0$, $x/D = 1$ where mode 2 results display a higher velocity deficit. However, this local discrepancy is quickly compensated thanks to a higher mixing downstream of the plug in mode 2 (see the visualizations in figure 4.7) and all simulations results collapse at $r/D = 0$, $x/D = 1.5$.

4.4.2.2 External mixing layer streamwise evolution

The streamwise evolution of the vorticity thickness of the external mixing layer is plotted in figure 4.9. The interactions between the shear layer and the shock-cells result in some pinchings/widenings of the mixing layer. At axial locations where a shock intersects

the mixing layer, this one widens and the local maximum of the velocity gradient increases. The vorticity thickness is thus smaller at these locations as it can be seen in figure 4.9(a). In particular, ZDES simulations exhibit a significant drop around $x/D = 0.8$ whose width is larger than for previous shock/mixing layer intersections. At this location, no shock appears in the RANS simulation, but it can be seen in the time evolution of the ZDES simulations that a shock appears and vanishes successively at this location in a large oscillating movement, which explains the width of the irregularity observed. Downstream from $x/D = 1.5$, the intensity of velocity fluctuations is lower and the impact on the external mixing layer less noticeable.

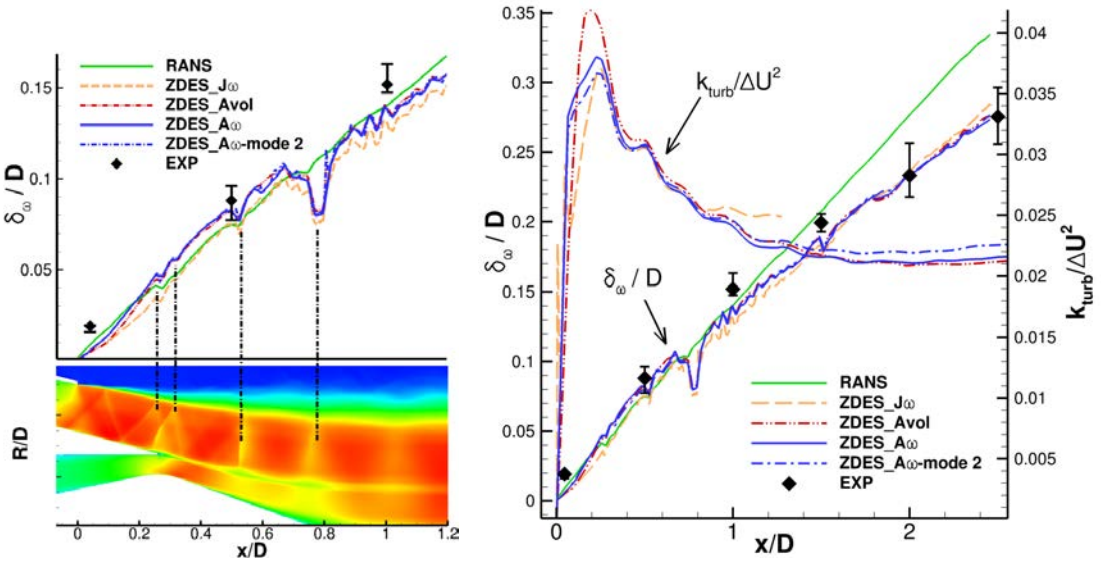

(a) Correlation between shocks and δ_ω

(b) δ_w and k_{turb} vs the axial positon

Figure 4.9: External mixing layer development: (a) Effect of the shock cell pattern on the vorticity thickness, (b) vorticity thickness δ_w and turbulent kinetic energy k_{turb} evolution along the mixing layer.

The evolution of vorticity thickness, figure 4.9(b), shows that in all simulations, the shear-layer thickness is smaller than in the experiment up to $x/D = 1.5$, which could affect the compression/expansion wave reflections and partly explain the wrong shock-cell positioning previously mentioned. A change of slope appears around $x/D = 0.75$ in all ZDES simulations. This change of spreading rate is also observable in the experimental results, slightly downstream, but it does not occur for the RANS simulation whose growth rate value stagnates around 0.135. Despite irregularities due to shocks, the values of spreading rate computed in the region extending from the trailing edge up to $x/D = 0.65$ varies from 0.15 to 0.17 from one ZDES simulation to another. In the same region, the experimental slope is also in this range, estimated at 0.15. This region corresponds to the transition area of the shear layer, presenting an initial peak of turbulent kinetic energy in the early beginning of the shear layer, before decreasing up to x/D around 0.8 (figure 4.9(b)). Then, in the fully turbulent area, the turbulent kinetic energy is stabilized and the growth rate of the mixing layer becomes constant.

Figure 4.9(a) shows that minor discrepancies appear on the vorticity thickness of the external shear layer when changing the subgrid length scale. Only the initial peak of turbulent kinetic energy is slightly higher using Δ_{vol}, but this does not impact the vorticity thickness.

A slightly larger thickness is observed with the AUSM+(P) scheme. However the spreading rate $d\delta_\omega/dx$ is almost the same for both schemes, only the very early development of the shear-layer up to $x/D = 0.2$ is faster using the AUSM+(P) scheme, since it seems to accelerate instabilities development. Beyond $x/D = 0.8$, where the transition is achieved, the growth rates calculated range from 0.095 (AUSM+(P)) to 0.106 (Jameson) for ZDES calculations whereas it is rather around 0.091 in the experiment.

As presented in section 2.1.1.4, compressibility effects on the growth rate evolution of a canonical shear layer are commonly taken into account through a constant C_δ dependent on the convective Mach number M_c. In the case of the external mixing layer with a static outer flow and small density differences, the expression can be reduced to C_δ. Dimotakis [87] proposed the expression for $C_\delta(M_c)$

$$\frac{C_\delta}{C_\delta(M_c = 0)} = 0.8e^{-3M_c^2} + 0.2, \tag{4.4.1}$$

later refined by Murakami & Papamoschou with:

$$\frac{C_\delta}{C_\delta(M_c = 0)} = 0.77e^{-3.5M_c^2} + 0.23. \tag{4.4.2}$$

Thus, for a convective Mach number of 0.52 the growth rate should be situated between 0.093 (using equation 4.4.2) and 0.097 (using equation (4.4.1)) which matches very well with the values extracted from ZDES calculations with AUSM+(P) in the fully turbulent region of the external mixing layer, and is a little bit smaller than values given by the ZDES simulation using the Jameson scheme. The agreement with the experimental value of 0.091 is also reasonable although the value 0.91 is slightly smaller than values coming from equations (4.4.1) and (4.4.2). However, the experimental uncertainty is an important source of error on the calculation of gradients, and therefore on the vorticity thickness, which appears in figure 4.9(b) within the error bars. Regarding the values of C_δ extracted in the close-to-exit region, they are very high compared to those given in the literature for fully developed shear layers, since the turbulent transition is not finished. Nevertheless, the order of magnitude of C_δ in all calculations remains in the range of values referenced by Aupoix [13] from experimental results at similar Mach numbers, namely C_δ inferior to 0.17. In addition, the initial vorticity thickness in the experiment is slightly larger than in simulations, which might be caused by the small remaining delay in the instability development or by a difference of boundary layer thickness at the nozzle exit.

In the region downstream from $x/D = 0.8$, the constant growth rate in the RANS calculation is also much higher than values predicted by models and the absence of slope change might directly originate from the turbulence modeling. Aupoix [13] already mentioned that standard RANS models do not take into account the effect of compressibility on the spreading rate. Last, it is important to notice that both mode 1 and mode 2 of ZDES give exactly the same results regarding the vorticity thickness growth in the external mixing layer, which is an important achievement for the non-zonal mode of ZDES. A summary of the results regarding the growth rate of the external mixing layer is given in Table 4.2.

In the internal mixing layer, the velocity difference between the flows surrounding each side of the core cowl is relatively low, the velocity profiles in this region looking like wake profiles with low velocities in the wake of the core cowl trailing edge and two opposite gradients of velocities around. Thus, an accurate computation of the vorticity thickness is difficult to obtain.

Model	Dimotakis	Murakami et al.	Exp	RANS	ZDES-Jameson	ZDES-AUSM+(P)
$\frac{d\delta_\omega}{dx}$	0.097	0.093	0.091	0.135	0.106	0.095

Table 4.2: Summary of the growth rates computed for the fully developed mixing layer using different models. Dimotakis and Murakami et al. refer to the results obtained from the equations (4.4.1) and (4.4.2).

4.4.2.3 Turbulent quantities

Turbulent variables are plotted at $X/D = 0$, $X/D = 0.5$, $X/D = 1$ and $X/D = 1.5$ in figure 4.10. The turbulent RMS velocities are defined by: $u_{rms} = \sqrt{\overline{u_x'^2}}$ and $v_{rms} = \sqrt{\overline{u_r'^2}}$. These expressions represent the resolved part of the velocity fluctuations. As experimental measurements do not give access to the azimuthal fluctuations, the turbulent kinetic energy is computed only with axial and radial components of RMS velocity: $k_{uv} = \frac{1}{2}(u_{rms}^2 + v_{rms}^2)$. A good agreement between simulations and experiments is observed in the plots of $k_{uv}/\Delta U^2$ in the external mixing layer, up to $x/D = 1$. From $x/D = 1$, the turbulent levels in the simulations implementing the AUSM+(P) scheme decrease in comparison to the cases implementing the Jameson one, and deviate from the experimental results. This decrease is associated to the dissipation of the more numerous small structures by the mesh which is stretched in the streamwise direction from $x/D = 1$.

In the internal mixing layer the agreement between simulations and the experiments is

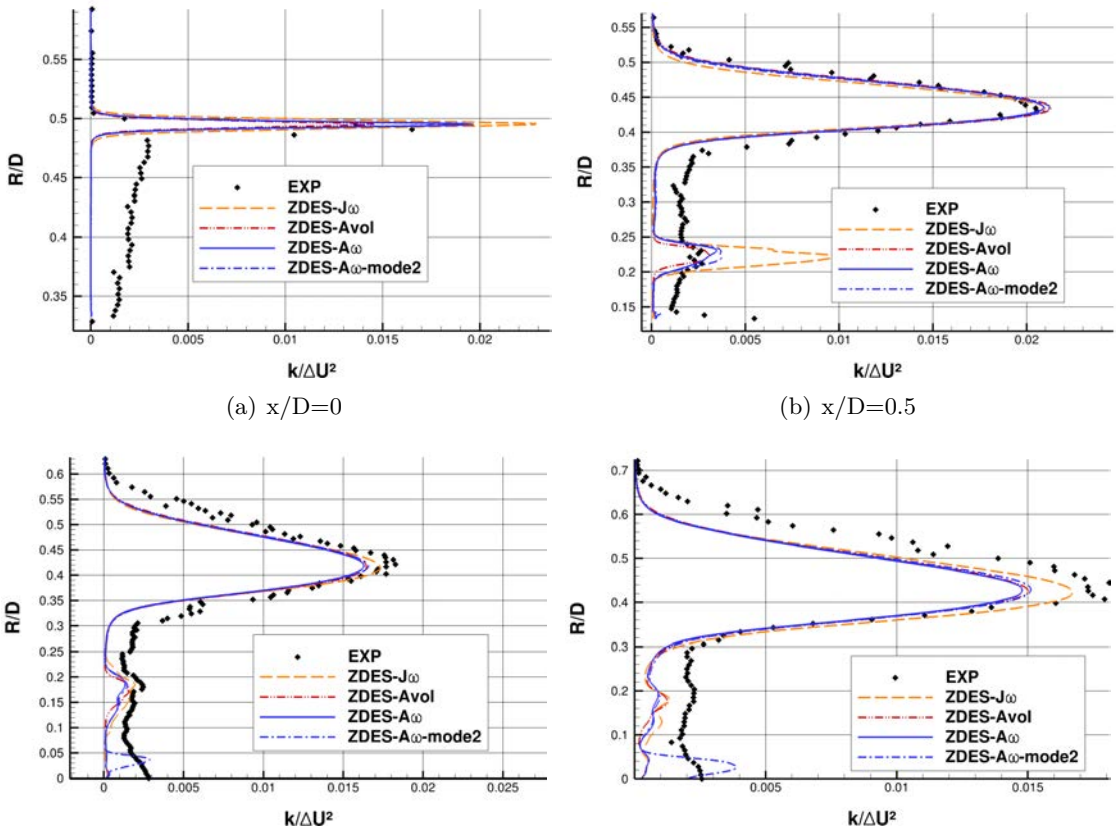

(a) x/D=0 (b) x/D=0.5

(c) x/D=1 (d) x/D=1.5

Figure 4.10: Turbulent kinetic energy $k_{uv}/\Delta U^2$: (a) 0D line, (b) 0.5D line (c) 1D line, (d) 1.5D line

satisfactory for AUSM+(P) cases but the case with the Jameson scheme presents a very high level of turbulence at $x/D = 0.5$, where the shear layer is still transitional as seen previously (figure 4.9(b)). Indeed, the instantaneous visualizations for this simulation, figure 4.6(a), exhibit very large structures which are likely to carry much energy and produce such turbulent levels. Nevertheless, at further downstream stations where transition is achieved, presented in figures 4.10(c) and 4.10(d), the level of k_{uv}falls down to the one obtained with simulations using the AUSMP scheme.

The effect of the subgrid length-scale appears in the internal mixing layer at $X/D = 0.5$ by widening the thickness of the shear layer when using Δ_ω instead of Δ_{vol}. Meanwhile, the influence of using the mode 2 instead of the mode 1 of ZDES, does not appear in the mixing layers but on the jet axis downstream from the plug where the simulation with mode 2 exhibits higher turbulent levels as previously mentioned. One can also notice that the average level of turbulent kinetic energy outside the shear layers, in the center of the fan and core jets, is significantly lower than the experimental one. It is mainly explained by the absence of injected turbulence at the inlet boundary conditions. Indeed, the addition of inlet random flow perturbations has shown to improve this aspect of the simulation [55] and will be the topic of future work.

The study of the resolved shear-stress component (figure 4.11) leads almost to the same remarks, with a very good matching match between experiments and simulations up to $x/D = 1$, except for the cases with the Jameson scheme, in the inner mixing layer. Using the Jameson scheme, the bi-dimensional nature of vortical structures between the fan and

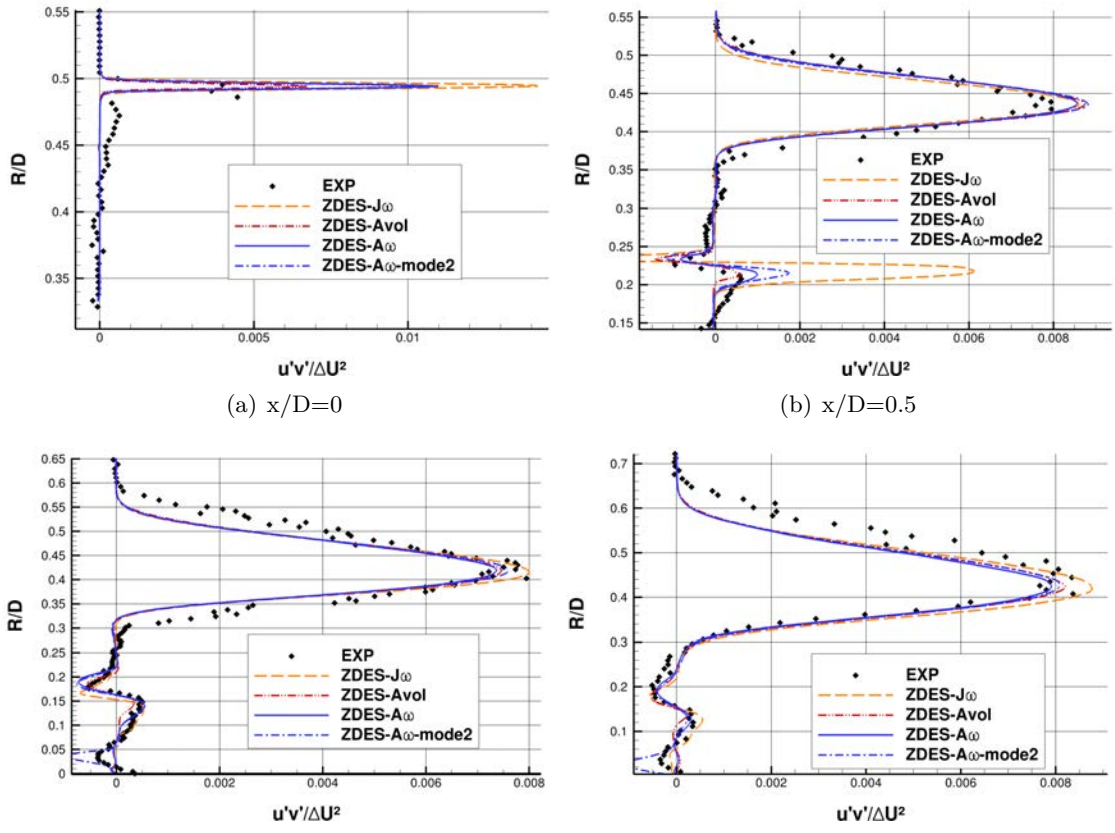

(a) x/D=0 (b) x/D=0.5

(c) x/D=1 (d) x/D=1.5

Figure 4.11: Shear-stress component $u'v'/\Delta U^2$: (a) 0D line, (b) 0.5D line (c) 1D line, (d) 1.5D line

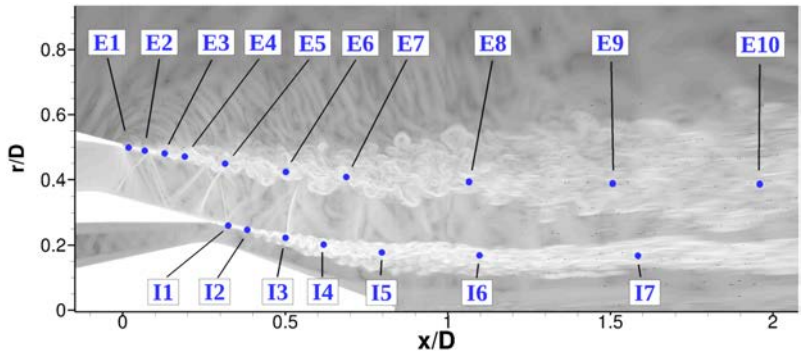

Figure 4.12: Probes location

core jets induces very high shear-stress levels of the component $\overline{u'v'} = \overline{u'_x u'_r}$. The shear-stress level in the external mixing layer is lower using AUSM+(P) than using Jameson scheme which is consistent with the k_{uv} levels. A small difference can also be depicted in the inner shear layer at $x/D = 0.5$, but the major discrepancies between the mode 1 and the mode 2 are again located in the vicinity of the plug. Actually, it seems that the physics in the boundary layer of the plug was not properly described neither by the mode 1 nor by the mode 2, due to a too strong adverse pressure gradient which does not impair the shielding properties for the mode 2 simulation as commented previously but may be challenging for the underlying RANS model of the present ZDES simulations. As a matter of fact, let us be reminded that in both mode 1 and mode 2, the boundary layers are treated in RANS which may not be fully reliable in this area where the boundary layer is highly disturbed as seen previously. Unfortunately, no near-wall experimental data is available to accurately assess the state of the plug boundary layer in the experiments and further evaluate the computations. If a shallow separation occurs on the plug, it can be noted that this is beyond the scope of classical DES-type methods which are suited for massive separations and would require more advanced and costly approaches such as Wall Modelled LES. To mitigate the cost of such a computation, one could take advantage of the flexibility of the ZDES formulation to locally use the ZDES mode 3 only in the plug area for instance.

4.4.3 Spectral analysis

The Power Spectral Density (PSD) of a quantity Φ (e.g. velocity component, pressure,...) indicates how the energy of fluctuations is distributed in the frequency domain since

$$\sigma_\Phi^2 = \int_0^\infty PSD_\Phi(f)df \tag{4.4.3}$$

with σ_Φ^2 the variance of Φ. Hence, to get a better understanding of the physics of the turbulence in the mixing-layers, it is important to scrutinize the spectral content of the flow in these regions. The numerical probe locations are presented figure 4.12. The power spectral densities of the radial velocity and of the pressure are presented figures 4.13 and 4.14 , for two sensors located in the external mixing layer and for two others located in the inner mixing layer. The Strouhal number $St_D = fD/\Delta U$ based on the fan nozzle diameter is used to normalize the frequency.

Regarding the probes E2 and I1 located close the trailing edges (i.e. the very beginning of shear layers), very distinct high frequency peaks can be distinguished, on both

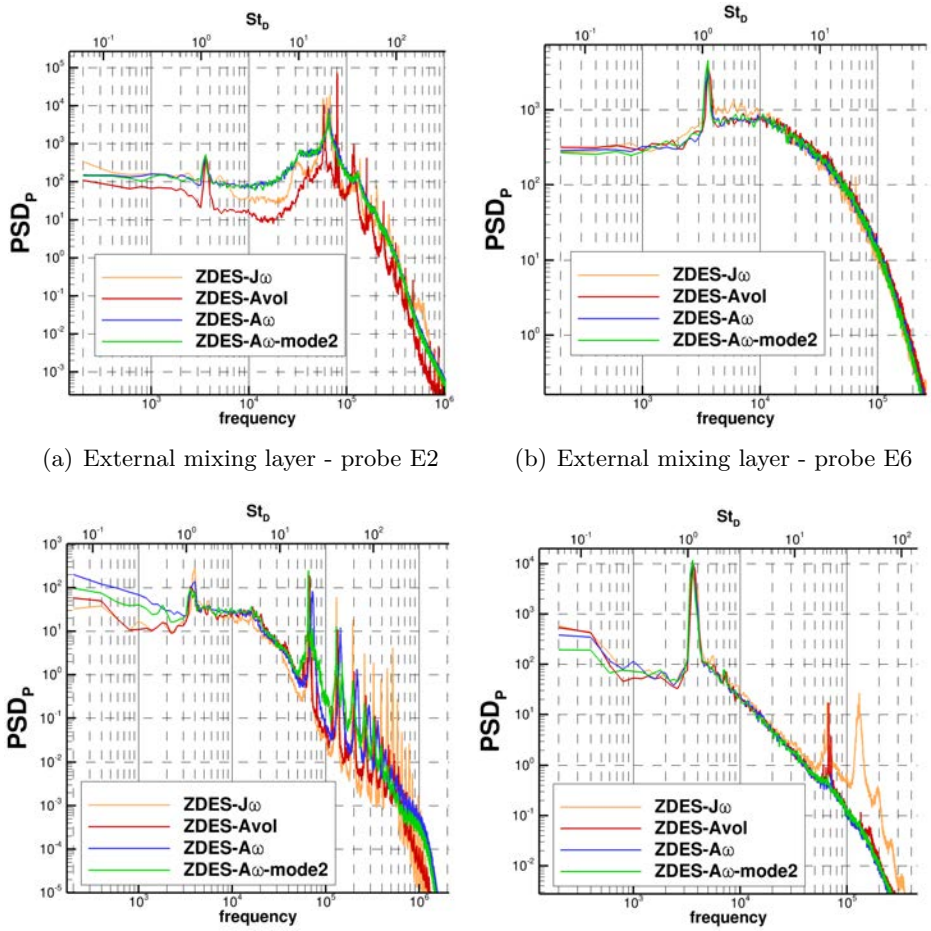

(a) External mixing layer - probe E2

(b) External mixing layer - probe E6

(c) Internal mixing layer - probe I1

(d) Internal mixing layer - probe I6

Figure 4.13: Power Spectral Density of pressure : (a)-(b)External mixing layer (c)-(d) Internal mixing layer

pressure (figures 4.13(a) and 4.13(c)) and velocity spectra (figures 4.14(a) and 4.14(c)). In the external mixing layer, the frequency of the first peak lies in the range $St_D = 15 - 25$ (50-80 kHz) depending on the simulation, and around $St_D = 18$ (60 kHz) for the internal mixing layer. These frequencies are associated with Kelvin-Helmholtz instabilities, which are typical of shear-layers development and recognizable by the development of bi-dimensional eddies. According to the frequency given by eq (2.1.10), and based on the vorticity thickness at probes locations, the theoretical frequencies in the present case lie in the range $St_D = 14 - 17$ (45-55 kHz) for the external mixing layer probe. For the internal one, the estimation of δ_ω gives a theoretical frequency for the Kelvin-Helmholtz instability around $St_D = 37$ (120 kHz) whose order of magnitude is similar to the one in the simulations. It confirms that the nature of high frequency peaks is linked to the instability birth mechanism. On both external and inner mixing layers some harmonics of the Kelvin-Helmholtz frequencies appear close to the trailing edge. In the external mixing layer, all these frequencies disappear totally half a diameter downstream whereas in the inner mixing layer the fundamental frequency peak remains, which is consistent with previous comments about the longer delay in the growth of instabilities for the internal mixing layer. The fact that the main frequency peak persists up to $x/D = 1$ in

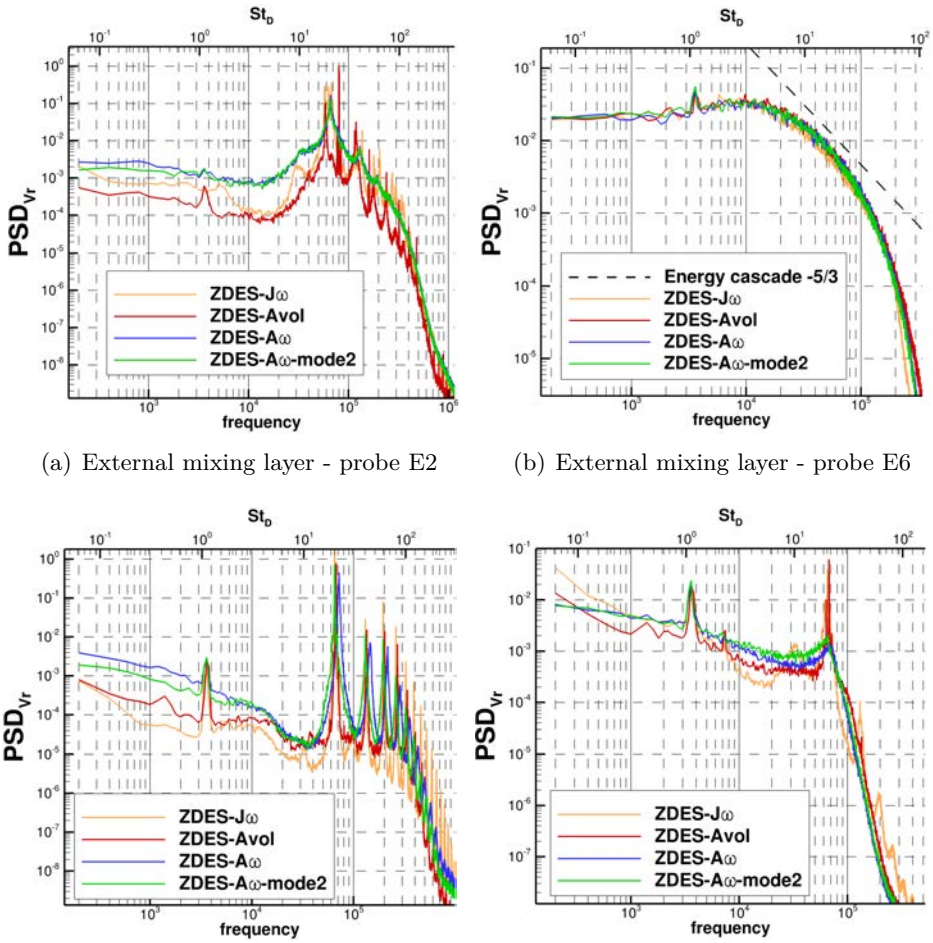

(a) External mixing layer - probe E2

(b) External mixing layer - probe E6

(c) Internal mixing layer - probe I1

(d) Internal mixing layer - probe I6

Figure 4.14: Power Spectral Density of radial velocity : (a)-(b)External mixing layer (c)-(d) Internal mixing layer

all simulations is consistent with the too long transition toward a fully three dimensional turbulence. Besides, the main discrepancies between simulations state around this location in the inner layer, where only the simulation with the Jameson scheme still presents residual harmonics. In the case with the Jameson scheme, the longer transition phase is also revealed on the spectra further downstream (not presented here), where the main frequency peak can still be depicted. It is noteworthy that the simulation with mode 2 of ZDES provides the same frequency distribution and PSD levels as the simulations with mode 1.

Another peak is clearly observable in all the pressure spectra in the mixing layers, whose frequency around $St_D = 1.1$ (3600Hz) is largely lower than the ones typical of shear layer instabilities. This peak which also appears on most of radial velocity spectra seems to be linked to the oscillatory shock motion and its interaction with the mixing layers. Its origin may be found in the literature among shock-associated noise investigations. In particular, in the screech phenomenon primarily observed by Powell [171], that generates such peaks in pressure spectra. As presented in section 2.1.3.3 the screech frequency f_s is given by:

$$f_s = \frac{U_c}{L_s(1 + M_c)} \tag{4.4.4}$$

with $M_c = U_c/c_0$ the convective Mach number. Several models have been proposed to

determine the shock cell length of a single jet, as the models of Prandtl [172] or of Pack [162]. In the present case, instead of using a model for the length of shock cell, we directly measured it in the simulations, as it has been seen in figure 4.8(e) that ZDES simulations predict correctly at least the 3 first shock-cells. Then, using $(u_{fan} + u_{ext})/2$ i.e. $\Delta U/2$ for U_c, the previous expression gives a theoretical frequency around $St_D = 1.2$ (3800Hz), which is in a good agreement with the frequency appearing on pressure spectra. The same frequency appears in the inner mixing layer spectra which indicates that the dominant interaction that generates screech tones in the jet are the interactions between shocks and the external mixing layer. Indeed, if the interactions between shocks and the inner shear layer would be the cause of a screeching peak, as the convective velocity in this shear layer given by $(u_{fan} + u_{core})/2$ is almost twice the convective velocity of the external mixing layer, the peak frequency would be around $St_D = 1,6$ (5300Hz). However, the screech phenomenon in dual-stream jets is highly complex and the role of the interactions between the inner shear-layer and the shocks is not completely obvious. Unfortunately, no near-field spectral data is available from the experiment that could corroborate the existence of these screech tones. Nevertheless, such screech tones have already been measured experimentally in dual-stream nozzle models, but the analysis focused mostly on the broadband shock associated noise [222]. In the literature, many authors mention the sensitivity of the screech to experimental conditions, that prevent the screech to occur. They also link the screech amplitude to the trailing edge thickness [174] [169]. For instance, to suppress the screeching phenomenon experimentally observed, Shur et al [191] used a very thin nozzle edge in their simulations (one grid cell size). The sensitivity to the boundary layer thickness at the nozzle exit has also been mentioned by [124] as a cause of potential discrepancies with the experiment. Nonetheless, even though the screech phenomenon rarely occur in real engine jets of civil aircraft, due to the non-axisymmetry of the flow and to steps and gaps effects, it is interesting to note the ability of the ZDES to capture such phenomenon, without frequency variation with the spatial scheme or the subgrid length-scale used.
As a conclusion, the investigation of the spectral content of both inner and external mixing layers confirms the previous analysis based on averaged quantities. The longer transition distance obtained with the Jameson scheme leads to stronger Kelvin-Helmholtz peaks. The use of Δ_{vol} produces a similar effect, to a lesser extent. Eventually, no significant differences can be depicted between mode 1 and mode 2 spectra.

4.5 Conclusion

In this chapter, a parametric analysis have been performed through four ZDES calculations of a dual-stream jet with an external plug whose secondary jet is choked. The effect of the spatial scheme, of the subgrid length-scale, as well as the mode 2 of the ZDES have been investigated. Both flow field and spectral content have been analysed and compared to experimental data.

A fairly good agreement with the available experimental data is observed up to 1 diameter for the mean flow, then a phase-lag in the shock-cells positioning appears. This phase-lag is significanltly reduced compared to RANS calculations. The development of the external mixing layer is well reproduced and few discrepancies appear between the four ZDES simulations. The turbulent levels are in a good agreement with the experimental ones. The streamwise evolution in the external mixing layer given by all ZDES simulations is very close to the experimental growth rate. Actually, the investigation of the internal mixing layer lays emphasis on the effect of the parameters investigated. Indeed,

in this area, a too long transitional region is observed in all simulations compared to the experiment, and large discrepancies exist from one simulation to the other. The use of the subgrid length scale Δ_ω based on the local vorticity orientation instead of Δ_{vol} accelerates the azimuthal destabilization of the initial Kelvin-Helmholtz instabilities. The use of the less dissipative AUSM+(P) scheme instead of the Jameson one enables also to reduce the length of the transition toward a full 3D turbulence. Eventually, experimental turbulent profiles in the internal mixing layer are recovered less than 0.2 diameter downstream the trailing edge in the best case and less than 0.5 diameter in the worst case.

Another key result of the present study is that the (non-zonal) mode 2 of the ZDES provides almost the same growth rate, turbulent intensity and spectral content in both mixing layers than the (user-defined) mode 1. The only difference observed lies in the vicinity of the plug on the jet axis line, where larger velocity deficits are observed in the simulations than in the experiments. This is attributed to the RANS treatment of the plug boundary layer (which is shielded manually in mode 1 or via the f_d function in mode 2) which may not be sufficient to properly capture the effect of the strong adverse pressure gradient in this area.

In fact, the treatment of the plug boundary layer remains very challenging. Despite a severe increase of the computational cost, since the dynamics of the boundary layer is a key point in this area, the use of the mode 3 of the ZDES (which acts as a Wall-Modelled LES) could be necessary to increase the accuracy of the simulation. Actually a major asset of the ZDES lies in the possibility to use the different modes of the ZDES in the same calculation. Besides, mode 2 of ZDES has shown to be as proficient as mode 1 for the treatment of the shear-layers which enables to turn towards the simulation of more complex geometries. For instance, the analysis of interactions between hot engine jets and the pylon of an industrial configuration seems to be a natural way forward for the method, as initiated in Ref. [57, 55].

Moreover, in the framework of the use of ZDES for industrial applications, since one known weakness of the modified AUSM+P scheme remains its robustness, future work should be devoted to the investigation of a low dissipative scheme also robust for a large range of flow Mach numbers. The AUSM+UP specifically developed by Liou to extend the AUSM+ family to transsonic flows [146] could be considered.

Last, to further reduce the delay in the formation of instabilities, the issue of turbulent content injection at the inlet boundary of fan and core ducts is also a major field of investigation in simulations of jets. Even though some turbulent injection techniques can induce some spurious noise (see [83]) which is a drawback for acoustic analysis, they can also bring serious enhancements of aerodynamic results (see section 2.2). Thus, in the frame of vibrational and thermal concerns such features are investigated in the chapter 5 to improve aerodynamic predictions.

Chapter 5

Turbulence injection in ZDES jet simulations

After some investigations of the numerical setup of ZDES, this chapter analyses the effect of Random Flow Generation at fan and core inlets on the jet flow development, by varying the characteristic turbulent length scale and the turbulence rate injected.

Contents

It has been shown in the previous chapter that a good numerical setup of ZDES enables to improve shear layer development, but does not prevent from a remaining delay in the formation of instabilities in the inner mixing layer and neither provide satisfactory shock-cell locations.

In this chapter, the objective is to take into account the upstream turbulence experimentally measured in fan and core ducts and further assess the effect of a synthetic turbulence inlet on the mixing layers and jet development. As presented in section 2.2.3.2, several methods have been developed over the last two decades to treat such turbulent boundary conditions for LES/DNS simulations. Among these methods, turbulent boundary conditions based on the Random Flow Generation technique developed by Smirnov et al.[197] from an idea of Kraichnan[135] appears as an interesting trade-off between efficiency and ease of implementation. Therefore, this method is used to generate inflow content at nozzle inlets. A parametric study of turbulent parameters is performed in this chapter and results compared to are compared to a reference simulation performed with steady uniform boundary conditions and to experimental results.

The chapter is organized as follows. As the dual-stream nozzle configuration used is the same as in the previous chapter, only changing parameters are presented as well as a summary of the different simulations carried out. The behavior of injected turbulence inside the nozzle is analyzed together with the effect of the turbulence rate on the overall jet flow development. Eventually, the instantaneous, time-averaged and spectral features

of shear layers development are scrutinized.

5.1 Numerical settings

5.1.1 Computational description

RANS and ZDES simulations are both based on the Spalart-Allmaras turbulence model. Although the mode 2 of ZDES applied to jet simulation has been validated in the previous chapter, the goal in the present study being to focus only on the injection of turbulence, the mode 1 of ZDES is used to ensure a RANS treatment of duct boundary layers since the validation experience with mode 1 was stronger at the time when the simulations were performed. The physical time step used for unsteady simulations is $\Delta t = 1.5.10^{-7}s$, leading to the reduced time step $\widetilde{\Delta t} = \frac{\Delta t \Delta U}{D}$ of $4.86.10^{-4}$. As in chapter 4, the acoustic CFL number $CFL = \frac{(u+c)\Delta t}{min(\Delta_x,\Delta_y,\Delta_z)}$ in the domain is lower than 1 almost everywhere in the domain except in the close vicinity of trailing edges where it reaches a value of 15. Regarding boundary conditions, far field free-stream conditions are again modeled by non-reflective conditions while the skin boundaries are modeled by adiabatic no-slip conditions. At upstream boundaries, the total pressure and temperature are imposed while at the downstream interface the pressure is prescribed. Turbulent fluctuations are introduced at the inlet of core and fan ducts through the RFG technique as depicted in figure 5.1.

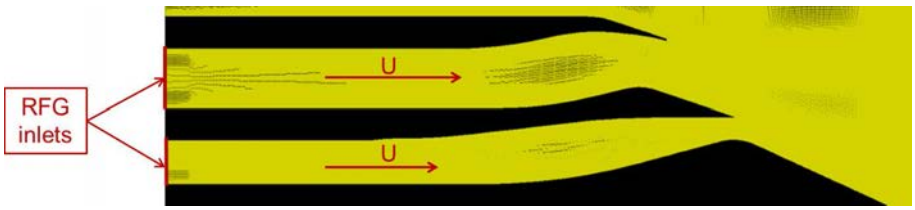

Figure 5.1: RFG boundaries at fan and core duct inlets.

In the frame of this PhD work, the RFG technique has been used with both Jameson and AUSM+(P) schemes, but simulations run with AUSM+(P) have encountered robustness issues, especially when increasing the turbulence rate. However, last successful attempts with lower turbulence rates let appears interesting perspectives for the RFG method in combination with the AUSM+(P) scheme. A way forward not studied in this work would be the numerical setup of AUSM+(P) in order to gain robustness when used with RFG (for instance the choice of the coefficients $C1$ and $C2$ in eq (3.1.56) and (3.1.57)). In the following, only computations run with the Jameson scheme are thus described. The following taxonomy is used for the different computations:

- Jω stands for Jameson spatial scheme and Δ_ω subgrid lengthscale;
- Turbulence rate expressed in % is the turbulent ratio defined by $T_u = \sqrt{\frac{2}{3}k}/U_{inj}$ related to the inlet velocity U_{inj} of the considered duct, with $k = \frac{1}{2}\overline{u_i' u_i'}$ the prescribed turbulent kinetic energy (see eq. (3.1.66));
- Turbulence lengthscale (see sec. 3.1.4) is expressed as a fraction of the considered inlet height H.

In this chapter, the values T5 (5%) and T10 (10%) for the turbulence level and H/10 and H/5 for the length scale have been used after preliminary tests. In each computation, the same values of turbulence rate and length scale related to inlet characteristics are used for both primary and secondary ducts.

Calculation	RANS	Jω	Jω-T10-H/10	Jω-T5-H/10	Jω-T5-H/5
Spatial Scheme	Jameson	Jameson	Jameson	Jameson	Jameson
Subgrid length scale	-	Δ_ω	Δ_ω	Δ_ω	Δ_ω
ZDES mode	0	1	1	1	1
Turb. level	-	0	10	5	5
Turb. length scale	-	-	$H/10$	$H/10$	$H/5$

Table 5.1: Summary of simulations. Nomenclature used for ZDES simulations: MODEL-SUBGRID LENGTHSCALE (J=Jameson, $\omega = \Delta_\omega$).

5.1.2 Spectral acquisition

The spectral analysis has been carried out using a time signal of $T = 36$ms corresponding to $\widetilde{T} = \frac{T\Delta U}{D} = 116$. Several probes have been placed in the flowfield, as presented in figure 5.2. In particular, some probes are located in mixing layers (probes E1 to E10 in the external mixing layer, from I1 to I7 in the inner mixing layer) while some probes aim at investigating the core of the jets (probe C1 in the primary jet, probes F1 to F4 in the secondary jet). Last, the probe O1 is located just outside the external mixing layer and allows to obtain information on the near-field outside the jet. Unfortunately, no probe provides spectral content in the far-field as the grid was not designed to propagate accurately acoustic waves over large distances. The Reynolds averaged statistics are computed on the fly during the calculation.

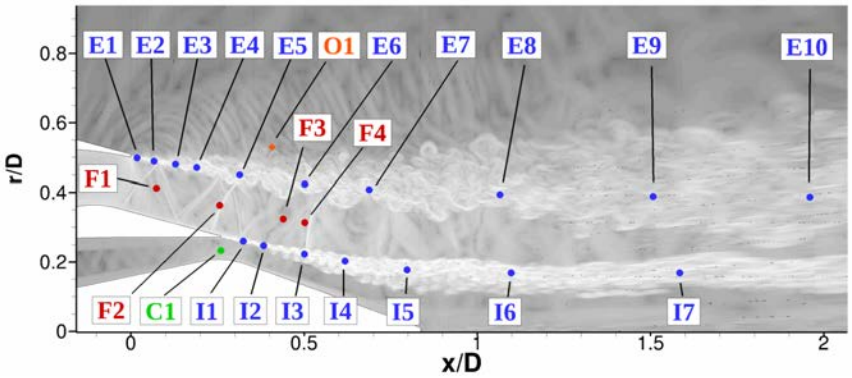

Figure 5.2: Probes location

5.2 Results - discussion

5.2.1 Advection of the turbulence in the ducts

Prior to focus on the jet properties, the flow field in the ducts is scrutinized in order to properly characterize the nozzle exit turbulence and assess the role of the mesh and the modeling on the inflow content.

5.2.1.1 Streamwise evolution of the flow

The streamwise velocity inside the ducts follows the evolution of the area as shown in figure 5.3. The area increase followed by a strong contraction induces a deceleration of the flow before an acceleration close to the nozzle exit. Such a convergent nozzle is likely to induce a favorable pressure gradient. No discrepancy appears here between the different

simulations, with and without turbulent boundary conditions, as the synthetic velocity fluctuation has a zero mean.

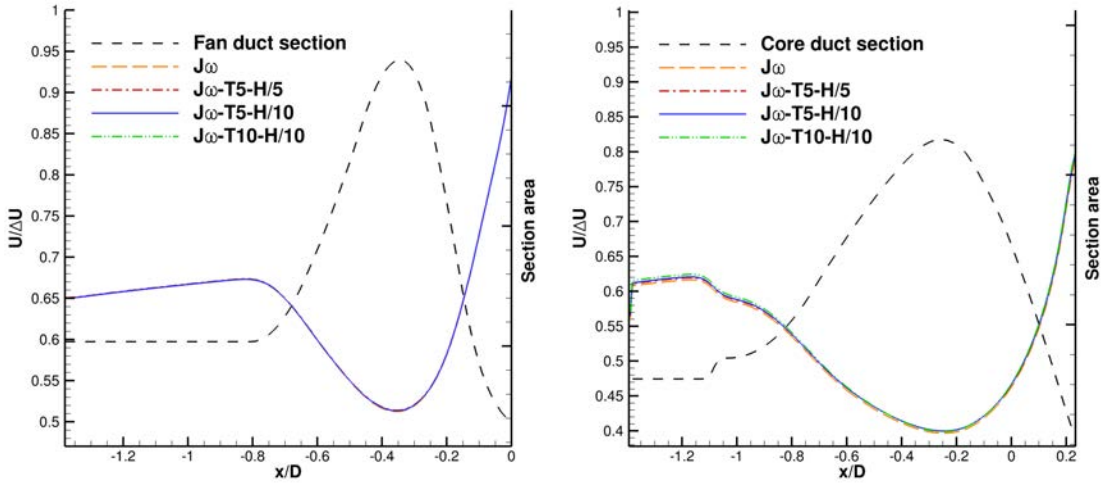

(a) Fan duct (b) Core duct

Figure 5.3: Evolution of the axial velocity $U/\Delta U$ along the fan and core ducts

The effect of the turbulent injection is clearly observable in figure 5.4. Radial velocity contours are distorted by the injected turbulent structures. Moreover, the intensity and amplitude of these distortions seem to scale with the length scales and turbulent rates prescribed at the inflow planes.

In order to assess how turbulence is advected in the ducts, the evolution of the different components of the turbulent velocity along the ducts are plotted in figure 5.5. As expected, turbulent levels in the cases using turbulence injection are significantly increased in the ducts compared to the baseline computation. It can be noted that the streamwise

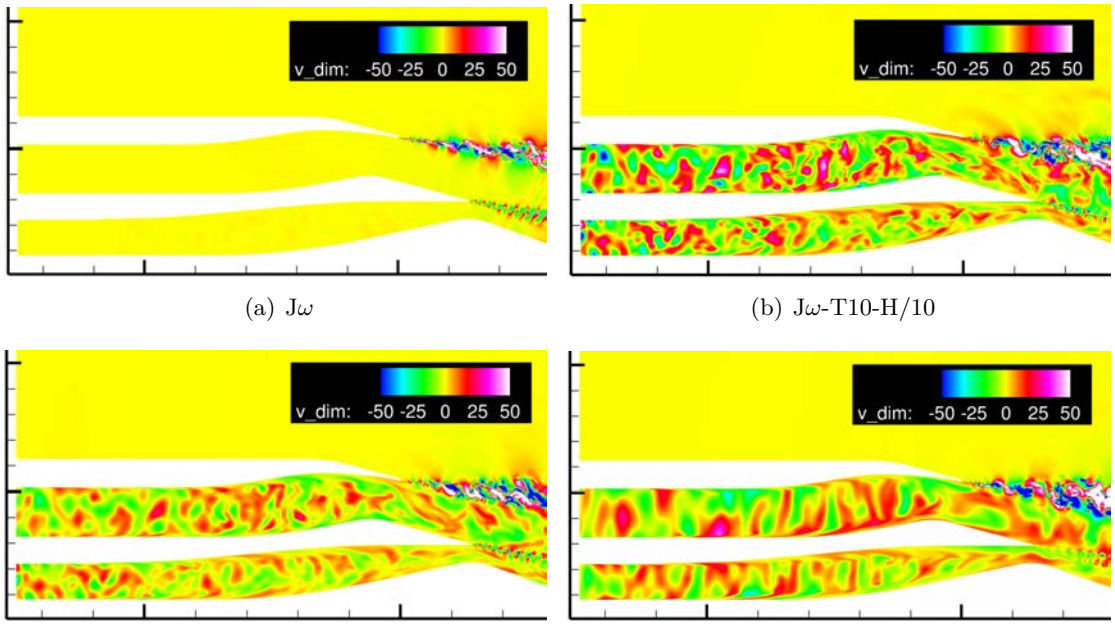

(a) Jω (b) Jω-T10-H/10

(c) Jω-T5-H/10 (d) Jω-T5-H/5

Figure 5.4: Instantaneous field : radial velocity field in the ducts

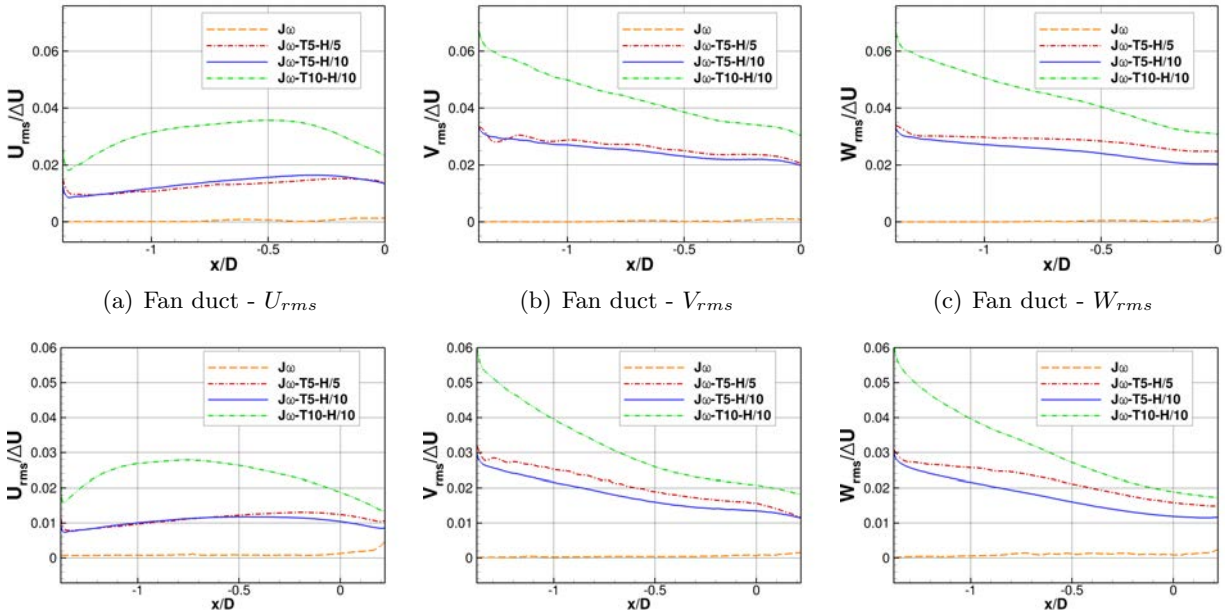

(a) Fan duct - U_{rms} (b) Fan duct - V_{rms} (c) Fan duct - W_{rms}

(d) Core duct - U_{rms} (e) Core duct - V_{rms} (f) Core duct - W_{rms}

Figure 5.5: Evolution of r.m.s. velocities along the fan and core ducts

velocity fluctuations undergo a significant drop downstream of the inlet interface which is partly attributed to the damping of non-physical perturbations in the first cells and to the grid stretching, which may also alter injected turbulent structures. It is noteworthy that the actual turbulent rate reached in the inflow plane at x/D=-1.38 is not exactly the one prescribed in the RFG boundary condition, which is due to the numerical treatment of the boundary condition in the elsA software (see table 5.2). Downstream of the inflow planes, U_{rms}, V_{rms} and W_{rms} present the same streamwise evolution for all simulations with injected turbulence, which is mainly driven by the evolution of the streamwise velocity (see figure 5.3). Eventually, the turbulent rate $Tu = \sqrt{\frac{2}{3}K_{turb}}/U_{inj}$ with $K_{turb} = \frac{1}{2}(U_{rms}^2 + V_{rms}^2 + W_{rms}^2)$ reached at the nozzle exit plane in each duct is given in Table 5.2. It can be remarked here that, though U_{inlet} is used to calculate Tu, the turbulence rate perceived by the exit sections based on the nozzle exit velocity is different.

Simulation case	RFG value	Fan duct inlet $X/D = -1.38$	Fan duct exit $x/D = 0$
Jω-T10-H/10	10%	7.6%	4.4%
Jω-T5-H/10	5%	3.9%	2.8%
Jω-T5-H/5	5%	4%	3.1%
Jω	0%	0%	0.2%
EXP	-	-	7.5%
Simulation case	RFG value	Core duct inlet $X/D = -1.38$	Core duct exit $x/D = 0.22$
Jω-T10-H/10	10%	6.9%	2.6%
Jω-T5-H/10	5%	3.4%	1.6%
Jω-T5-H/5	5%	3.6%	1.98%
Jω	0%	0%	0.3%
EXP	-	-	7.9%

Table 5.2: Turbulence rate in percentage of the inlet mean velocity at different locations.

5.2.1.2 Radial profiles in the ducts

The mean velocity field in fan and core ducts are presented in figure 5.6 to illustrate the effect of upstream turbulence on the mean boundary layers development. Although a smoothing of the profile and a slight increase of the boundary layer momentum thickness can be identified in the case with 10% of injected turbulence, giving a boundary layer profile more typical of turbulent boundary layers, the discrepancies appear very small. Moreover, the effect of the turbulence length-scale is not observable here. This result is consistent with the shielding of boundary layers that are treated through the URANS modelling.

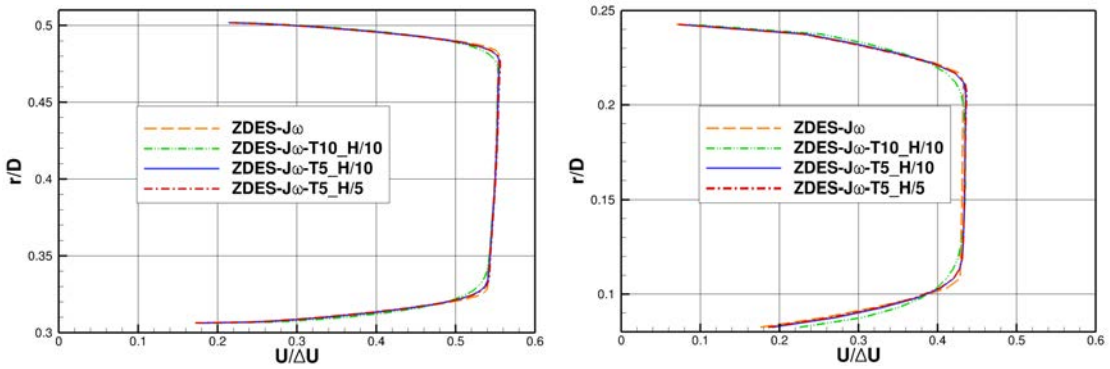

(a) fan duct x/D=-0.5 (b) core duct x/D=-0.5

Figure 5.6: Axial velocity profiles at x/D=-0.5 in the fan and core ducts

However, the radial profiles of velocity fluctuations in figure 5.7 show that using the RFG technique at the inlet, some resolved turbulence, especially for U_{rms}, appears to penetrate into the attached boundary layers treated in URANS and not only in the center

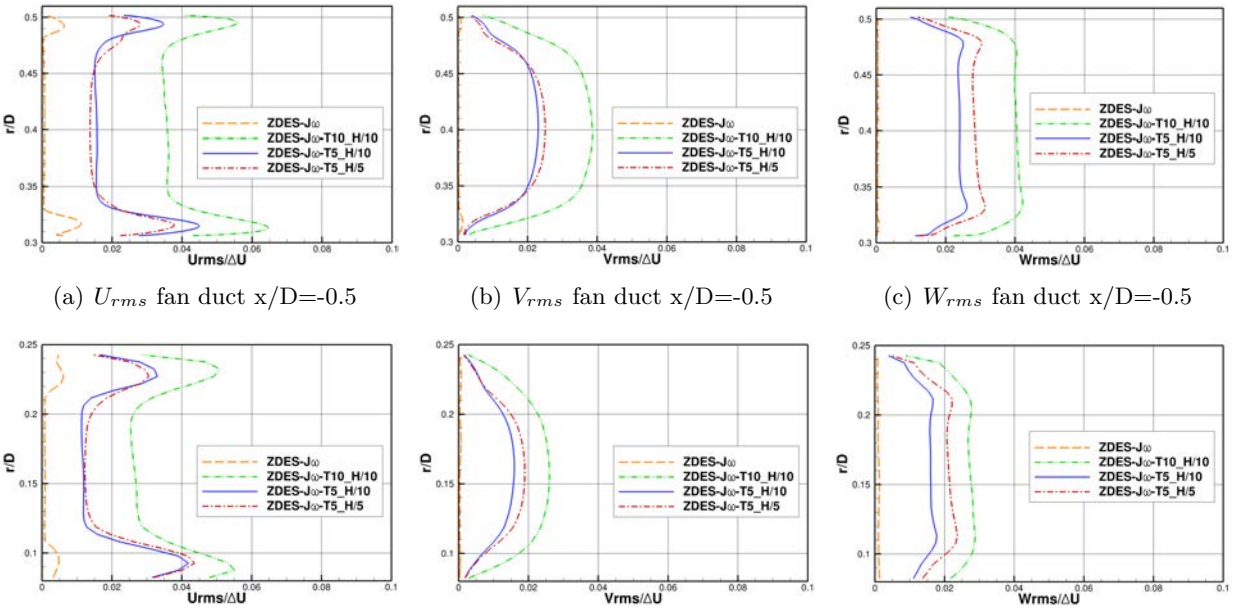

(a) U_{rms} fan duct x/D=-0.5 (b) V_{rms} fan duct x/D=-0.5 (c) W_{rms} fan duct x/D=-0.5

(d) U_{rms} core duct x/D=-0.5 (e) V_{rms} core duct x/D=-0.5 (f) W_{rms} core duct x/D=-0.5

Figure 5.7: Turbulent velocity profiles U_{rms}, V_{rms} and V_{rms} at x/D=-0.5 in the fan and core ducts

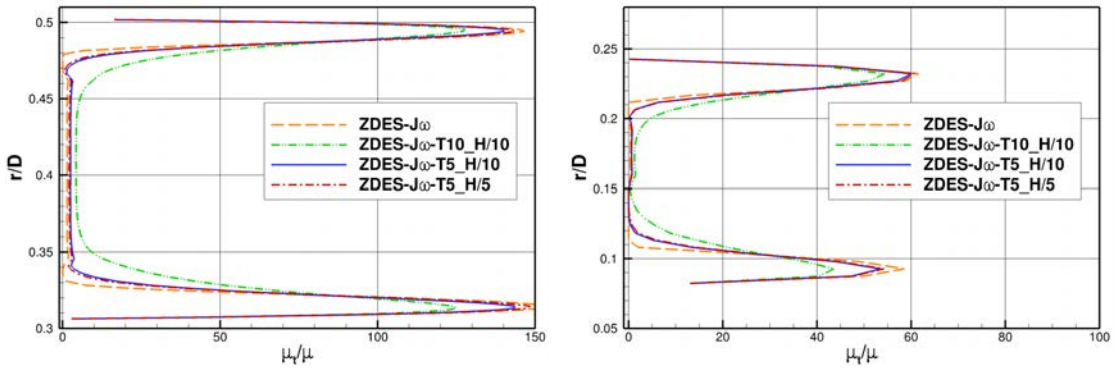

(a) fan duct x/D=-0.5 (b) core duct x/D=-0.5

Figure 5.8: Turbulent viscosity profiles at x/D=-0.5 in the fan and core ducts

of the duct. Besides, turbulent level discrepancies in the core of the ducts as in boundary layers are consistent with the difference of injected levels.

The characteristic length scale of the injected turbulence induces many discrepancies on the three components of the fluctuating velocity U_{rms}, V_{rms} and W_{rms}. In figures 5.7(a) and 5.7(d), one can see that the peaks of streamwise velocity fluctuations are wider and attenuated when the length scale is increased. This result reflects the mixing effect scaling with the turbulent structure size. Regarding the core of the duct, a smaller level appears on V_{rms} and W_{rms} when using $l = H/10$ instead of $l = H/5$, as shown in figures 5.7(b) and 5.7(c). This tendency suggests that larger injected structures enable to maintain higher turbulent levels in the ducts and are less likely to undergo a dissipation by the mesh which can occur when the size of vortical structures is too small with regards to the mesh refinement. The streamwise component of the velocity does not present such a behavior, even though the axial direction is the less refined direction.

Although the mean velocity profiles are not significantly affected, the turbulent boundary condition impacts also turbulent viscosity profiles in the boundary layer, as plotted in figure 5.8. Indeed, a large dependency on the injected turbulence intensity appears. The profile of μ_t in the boundary layers is slightly wider spread with a 10% inlet turbulent rate than with 5%. On the contrary to R.M.S. velocities, the size of the injected turbulence length-scale does not seem to affect the profile of turbulent viscosity. This result is consistent with the safe treatment of the boundary layers in RANS mode which does not appear to be impaired by the penetration of resolved turbulence in the boundary layers.

5.2.1.3 Spectral content of the inner turbulence at the exit

The spectra of axial and radial velocity signals at the nozzle exit, i.e. from the probes C1 an F1, are displayed in figure 5.9. Contrary to the baseline computation with a steady inflow, the spectra obtained with turbulence injection are broadband and display milder peaks both at low and high frequencies due to the increased mixing. Besides, the overall spectra levels scale with the turbulent rate reached in the exhaust planes given in Table 5.2. It also seems that the spectra do not present spurious features that could be attributed to the RFG technique.

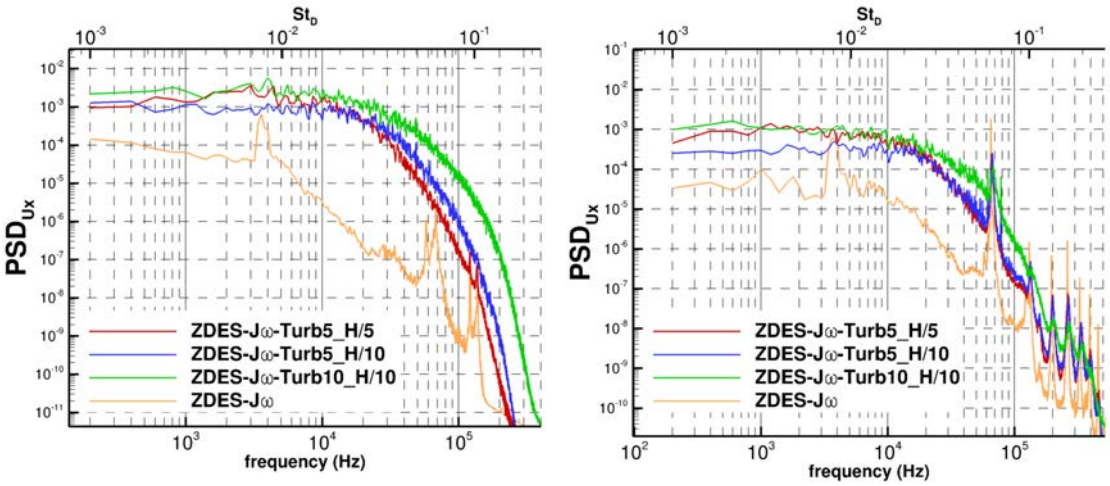

(a) Fan exit - probe F1

(b) Core exit - probe C1

Figure 5.9: PSD of axial velocity u_x at the nozzle exit. Top axis: $St_D = fD/\Delta U$.

5.2.2 Effects on the overall structure of the jet

Although the mean velocity profiles in the ducts are not significantly affected, the overall jet development is likely to be impacted by the different turbulent content at the nozzle exit.

5.2.2.1 Shock-cells system

As an effect of turbulence injection, several turbulent structures can be observed in the inner part of the jet in the nozzle exit plane in figure 5.4, which are likely to affect the shock cell dynamics. As a matter of fact, the density gradient magnitude fields depicted in figure 5.10 show that simulations with upstream turbulence display slightly less sharp expansion and compression waves.

More quantitatively, it appears that the injection changes the shock-cell positioning as shown in figure 5.11. As observed in the previous chapter for the baseline simulation without upstream turbulence, a phase lag appears between experimental and simulation data from the third shock-cell, associated with a widening of the cell width. Figure 5.11 shows that the injection of turbulence at channel inlets tends to reduce again the phase-lag with the experiments. In the cases with 5% prescribed turbulence rate, the phase-lag is approximately reduced by half. With 10% of turbulence at the inlet, the phase-lag is almost fully suppressed. This evolution is consistent with the turbulence rate achieved at the nozzle exit in the simulations (see table 5.2) which is close to the experimental one for the fan duct in case Jω-T10-H/10. This effect can be explained by the influence of upstream turbulence on the development of mixing layers, which is investigated in the next section. From the aerodynamic point of view, it is a major improvement brought on by the method and emphasizes the need to take into account upstream turbulence in the simulations.

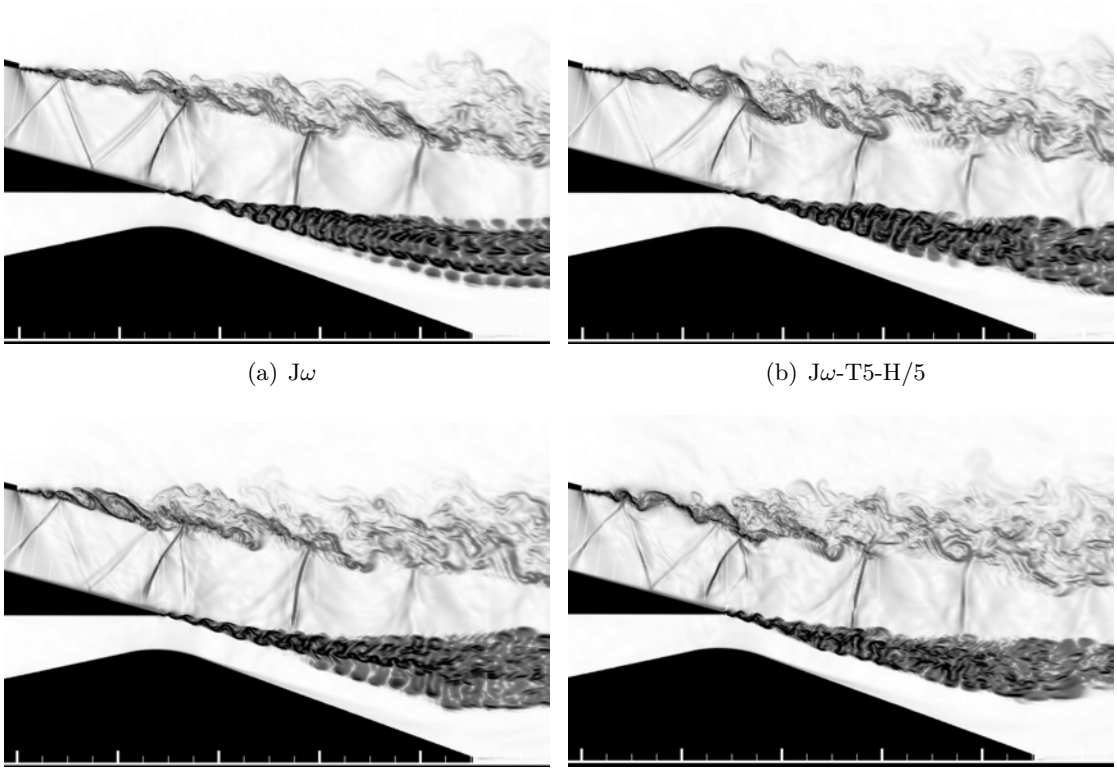

(a) Jω (b) Jω-T5-H/5

(c) Jω-T5-H/10 (d) Jω-T10-H/10

Figure 5.10: Instantaneous fields : pseudo-schlieren field (gray scale)

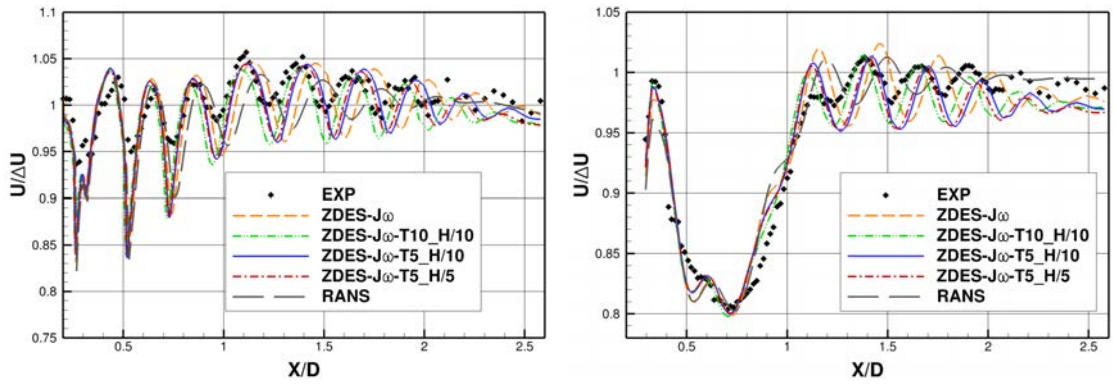

(a) Fan line (b) Core line

Figure 5.11: Mean field of axial velocity : Fan and Core lines

5.2.2.2 Turbulent levels in the jet

The vorticity contours in cross-planes presented in figure 5.12 illustrate the spatial organization and intensity of the upstream turbulence in the fan and core jets of the simulations. Conversely to the baseline Jω case, simulations with RFG exhibit resolved structures outside the mixing layers which increases mixing and affects the shock-cells positioning as previously described. As can be expected, more intense eddies are found at x/D=0.5 with 10% turbulence rate (figure 5.12(d)) than with 5% turbulence rate (figure 5.12(b)). Similarly, the length scale of the injected structures is not affected by the con-

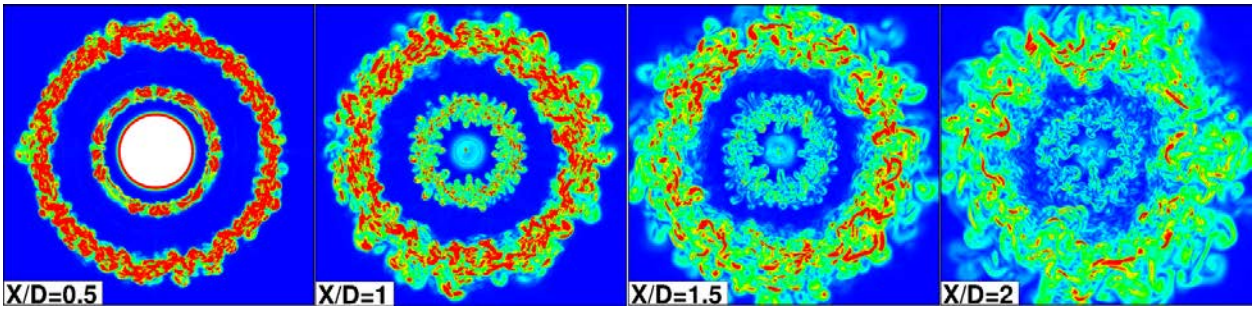

(a) ZDES-Jω

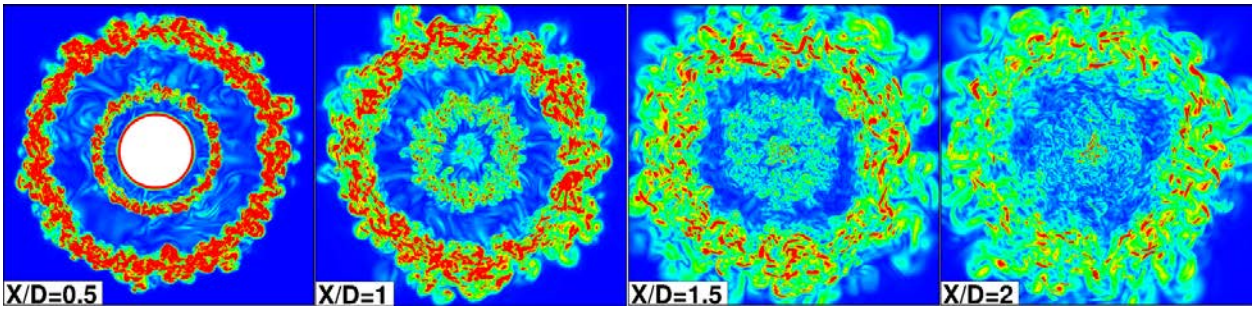

(b) Jω-T5-H/5

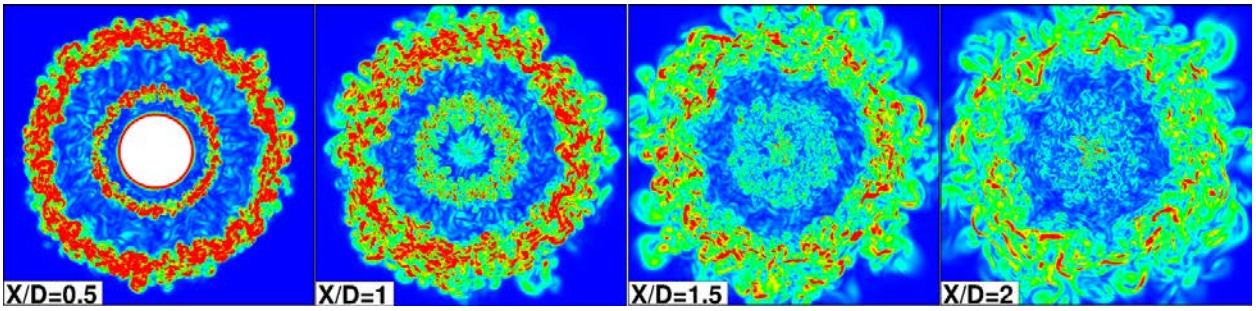

(c) Jω-T5-H/10

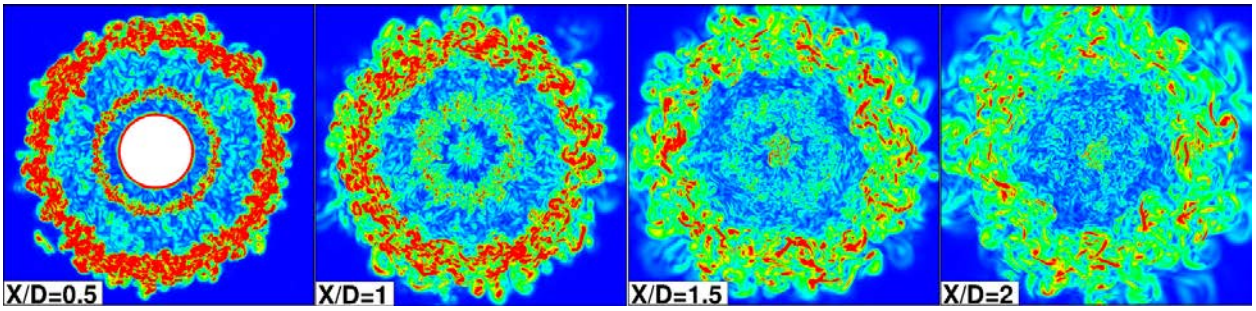

(d) Jω-T10-H/10

Figure 5.12: Vorticity magnitude at various axial positions

vection through the ducts and smaller structures are found at x/D=0.5 in the simulation

Jω-T5-H/10 than in the simulation Jω-T5-H/5.

The profiles of turbulent kinetic energy along the fan and core lines are depicted in figure 5.13(b). Along the core line, few discrepancies are observed close to the exit between the calculations as a result of the turbulence advection presented previously (see figure 5.7). Besides, the turbulent level is lower than in the experiments which shows that the setup of the RFG boundary condition needs to be further refined to accurately reproduce the experimental conditions.

More differences are observed along the fan line, although none of the current simulations reaches the experimental turbulent rate, as commented in section 5.2.1. The turbulence level downstream of the fan exhaust scales with the one prescribed in the RFG inflow condition. Of interest, it appears that using larger structures in simulation Jω-T5-H/5 results in an increased mixing (meaning a higher growth rate) than the one with finer structures Jω-T5-H/10.

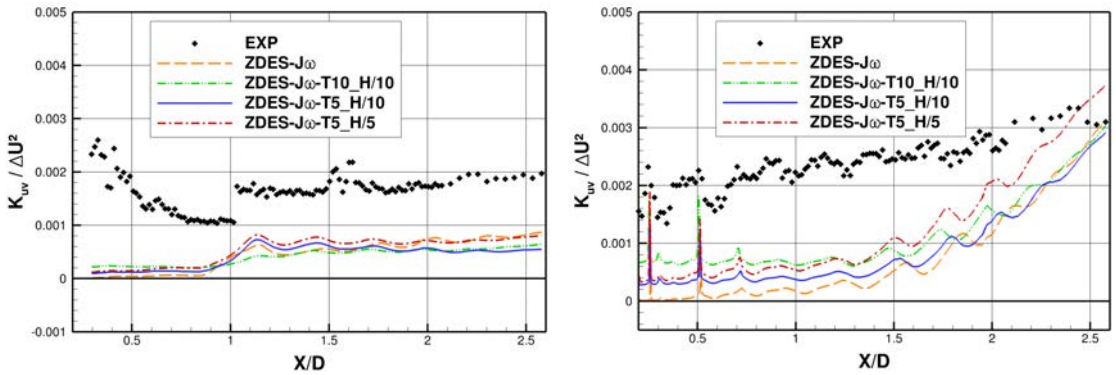

(a) Core line (b) Fan line

Figure 5.13: Axial evolution of the turbulent kinetic energy K_{uv} : (a) core line, (b) fan line

5.2.2.3 Spectra in the inner part of the jets

In order to assess the acoustic influence of turbulence injection in the inner part of jets, the Sound Pressure Level (SPL) defined from the PSD of pressure by:

$$SPL(f) = 20log\left(\frac{\sqrt{PSD_p(f)}}{p_{ref}}\right) \tag{5.2.1}$$

with $p_{ref} = 2.10^{-5}$, is displayed in figure 5.14 for the signal extracted from the probe F3. Even though 4 probes (F1, F2, F3 and F4 in figure 5.2) were located along the fan line, only probe F3 is shown since the other probes are affected by the change of the shock cell location which makes difficult the comparison between simulations. It can be noticed in particular that the probes F2 and F4 are located very close to if not right on a strong shock location.

At probe F3, the SPL is much lower without turbulent inflow and also more peaky. The screech frequency at $St_D = 0.015$ and Kelvin-Helmholtz-like frequencies around $St_D = 20$ can be depicted (see description in previous chapter in section 4.4.3).

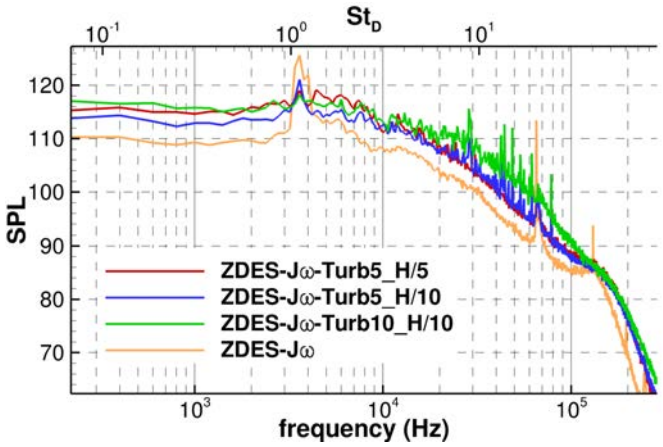

Figure 5.14: Sound Pressure Level in the inner fan jet area

5.2.3 Mixing layers development

The strong impact of the turbulence injection on the shock-cell positioning and the turbulent levels in all regions of the jet has been exposed in the previous section. In particular, it has been shown that the use of the RFG technique allows to take into account the turbulence rate in the inner part of the jet even if some tuning remains necessary to match experimental levels. In this section, the focus is put on the influence of the turbulent rate on mixing layer development.

5.2.3.1 Effect on the internal mixing layer

The density gradient magnitude snapshots in figure 5.15 illustrate the RANS-to-LES transition delay issue. As mentioned in the introduction, conversely to what happens in massively separated flows, the absence of large-scale flow instabilities in the case of jets makes the turbulence development in mixing layers challenging, even more in the case of the core mixing layer due to the low velocity difference between the core and fan streams. This issue appears critical in figure 5.15(a) for the baseline simulation with steady

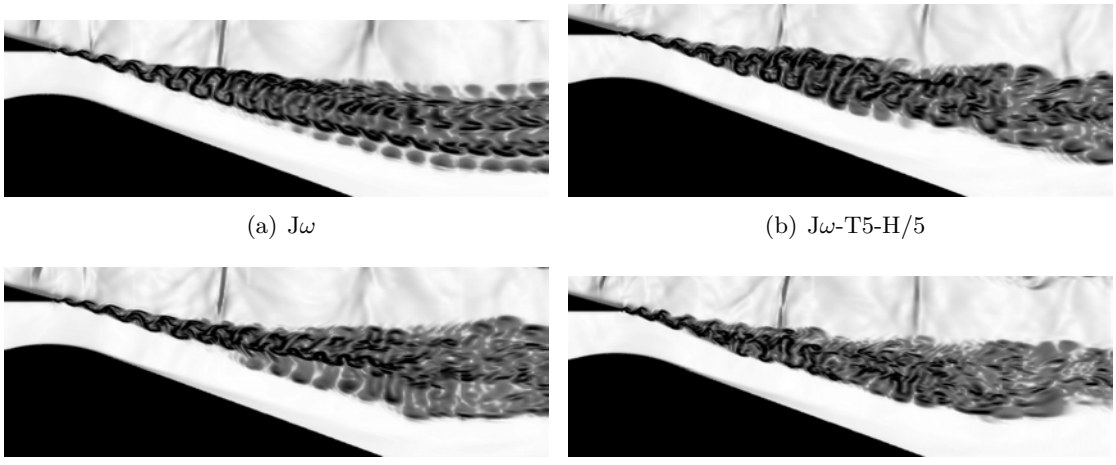

(a) Jω (b) Jω-T5-H/5

(c) Jω-T5-H/10 (d) Jω-T10-H/10

Figure 5.15: Instantaneous fields : pseudo-schlieren in the inner mixing layer area.

inflow which displays large coherent structures far from the nozzle trailing edge. This behavior has already been highlighted in the previous chapter and would be attenuated by using AUSM+(P), which was not possible here for the aforementioned robustness aspects. Conversely, it seems that the RANS-to-LES transition in the core mixing layer is shorter in simulations with RFG inflows, especially so when the turbulence rate is high and the structures small.

To get a better understanding of the physics of the turbulence in the inner mixing-layer, the spectral content of the flow is scrutinized in this region. Regarding the probe I1 located close to the trailing edge, the baseline computation Jω exhibits very distinct high frequency peaks, on both pressure (figure 5.16(a)) and velocity spectra (figure 5.16(c)). The high frequency peaks appear from $St_D = 18$ (60kHz) and still exist at probe I6 around x/D=1.1. As described in the previous chapter, these high frequencies are associated to Kelvin-Helmholtz instabilities, which are typical of shear-layer development and recognizable by the development of bi-dimensional eddies. A lower frequency peak around $St_D = 1.1$ (3.6kHz) is also clearly evidenced. This peak is related to shock-mixing layer interactions,

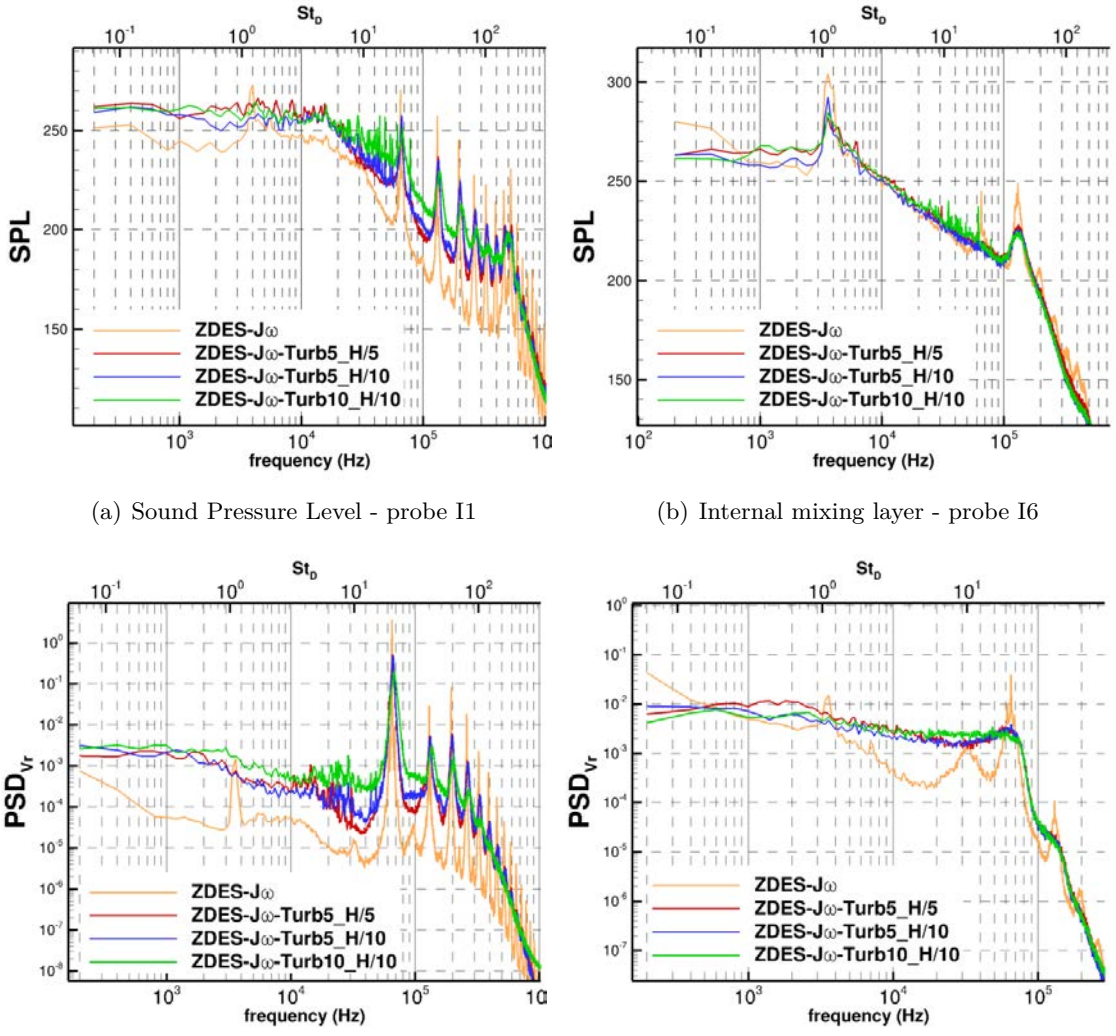

(a) Sound Pressure Level - probe I1

(b) Internal mixing layer - probe I6

(c) Radial velocity PSD - probe I1

(d) Radial velocity PSD - probe I6

Figure 5.16: Sound Pressure Level (SPL) and Power Spectral Density (PSD) of radial velocity in the internal mixing layer

the screech phenomenon, also described in ref [220].

Upstream turbulence appears to smooth the high frequency peaks and reduce their intensity, which is particularly evidenced in figures 5.16(b) and 5.16(d) for the probe I6. This indicates that the strong 2D coherence of Kelvin-Helmholtz vortices observed in the baseline computation is altered by the upstream turbulence. It can be explained by a faster transition at the early beginning of the shear layer, due to upstream velocity fluctuations at the nozzle exit and especially the fluctuations which penetrate into the boundary layers.

Regarding the screech tone, it still exists as shown in figure 5.16(a), but with an intensity significantly reduced by the turbulent inflow. Nevertheless, it must be noticed that with the RFG inlet the broadband aspect of the spectra in low frequencies makes the distinction of this screech peak more difficult.

5.2.3.2 Effect on the external mixing layer

The inner mixing layer therefore appears to transition quicker with turbulent injection. The vorticity magnitude contours in figure 5.17 show that shear layer instabilities in the external mixing layer follow the same trend. In comparison with all turbulent cases, the computation Jω exhibits a much thinner mixing layer with a delayed destabilization of Kelvin-Helmholtz vortices. Besides, the coherence of the vortex sheet seems to remain slightly longer in the case Jω-T5-H/5 (figure 5.17(b)) than in both cases using $l = H/10$ (figures 5.17(c) and 5.17(d)), which could indicate that using small length scales for the prescribed RFG inlet triggers more efficiently the transition. This might be linked to higher values of U_{rms} obtained in the nozzle boundary layers when injecting smaller turbulent

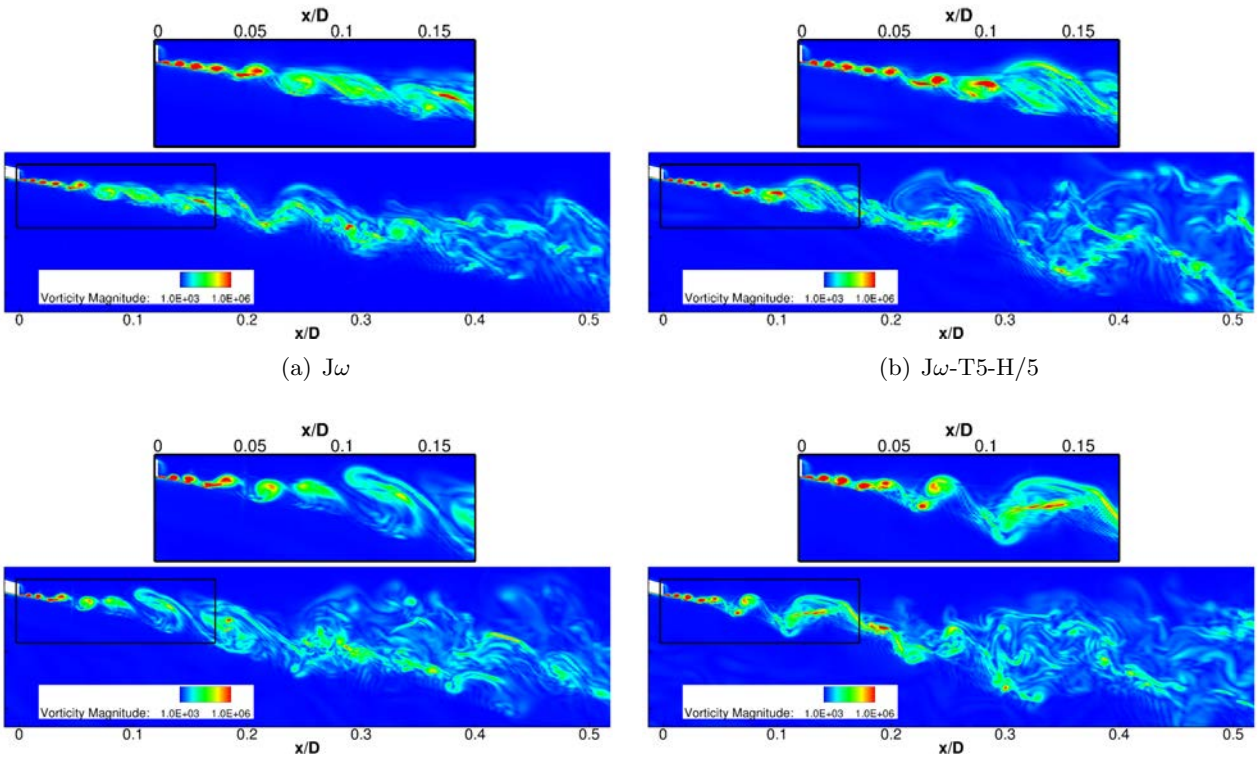

(a) Jω

(b) Jω-T5-H/5

(c) Jω-T5-H/10

(d) Jω-T10-H/10

Figure 5.17: Instantaneous fields : vorticity magnitude in the fan mixing layer area.

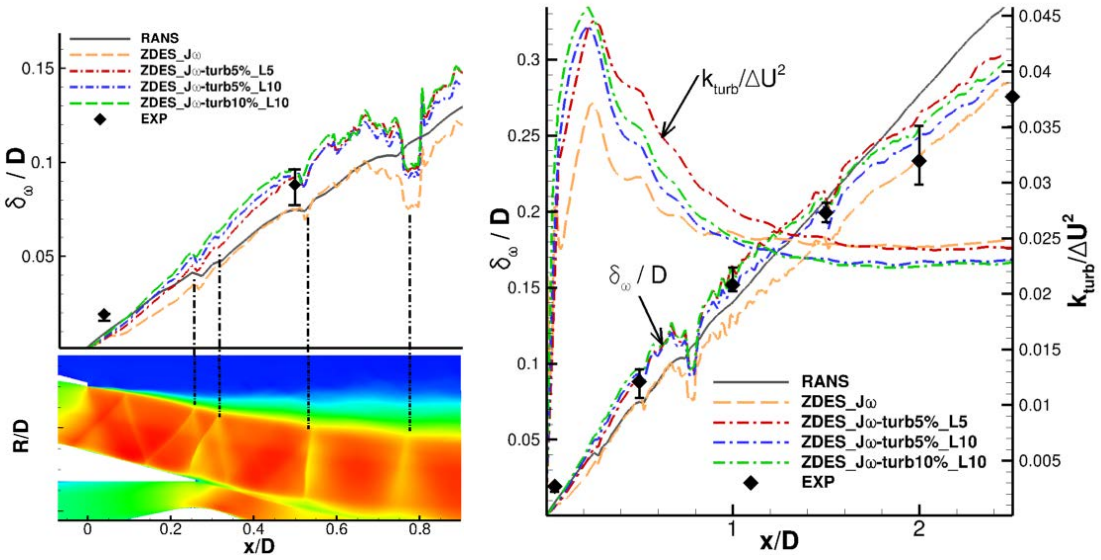

(a) Correlation between shocks and δ_ω

(b) δ_w and k_{turb} vs the axial positon

Figure 5.18: External mixing layer development: (a) Effect of the shock cell pattern on the vorticity thickness, (b) vorticity thickness δ_w and turbulent kinetic energy k_{turb} evolution along the mixing layer.

length scales.

Regarding the vorticity thickness evolution in figure 5.18, simulations with turbulent inflows present a better agreement with the experimental data. The vorticity thickness exhibits a faster growth rate for the simulations with turbulent inflow in the transition area, i.e. up to $x/D = 0.5 - 0.8$. Actually, the growth rate seems to be dependent on the turbulence injection parameters. The case with $l = H/5$ suffering a very small delay while the case Jω-T10-H/10 growing the fastest. For the case without turbulent injection, the initial delay is more significant than the one observed with turbulent inflow and the vorticity thickness does not reach the experimental value, even downstream of the transition area. The too thin mixing layer in this region induces a larger effective section for the 3 first shock-cells compared to cases with turbulent inflow, which could also partly explain the discrepancies observed on the shock-cell positioning.

The difference of spreading rate in the early growth of the shear layer can be related to the evolution of the turbulent kinetic energy in the mixing layer in figure 5.18. In the transition area, all cases, with and without turbulent injection, exhibit a peak of turbulent kinetic energy approximately at the same streamwise location, but whose intensity scales with the prescribed turbulent rate. Thus, the case Jω-T10-H/10 exhibits the steepest increase of K_{turb} to reach the highest peak value, whereas the baseline case Jω presents significantly lower values of $K_{turb} = \frac{1}{2}(U_{rms}^2 + V_{rms}^2 + W_{rms}^2)$ in this transition area. This is in agreement with the vorticity thickness evolution. The effect of using a larger turbulent length scale seems to affect the width of this turbulent kinetic energy peak rather than its intensity, by widening the peak as observed in the case Jω-T5-H/5. Downstream of the transition area, from $x/D = 1$, the Jω and the Jω-T5-H/5 curves of K_{turb} returns to an asymptotic level which is higher than the one obtained in computations Jω-T5-H/10 and Jω-T10-H/10. This is in agreement with the vorticity thickness growth rate after the transition, in the fully turbulent area, which is lower in cases with $l = H/10$. The lower level of K_{turb} actually reached at the end of the transition area when injecting smaller

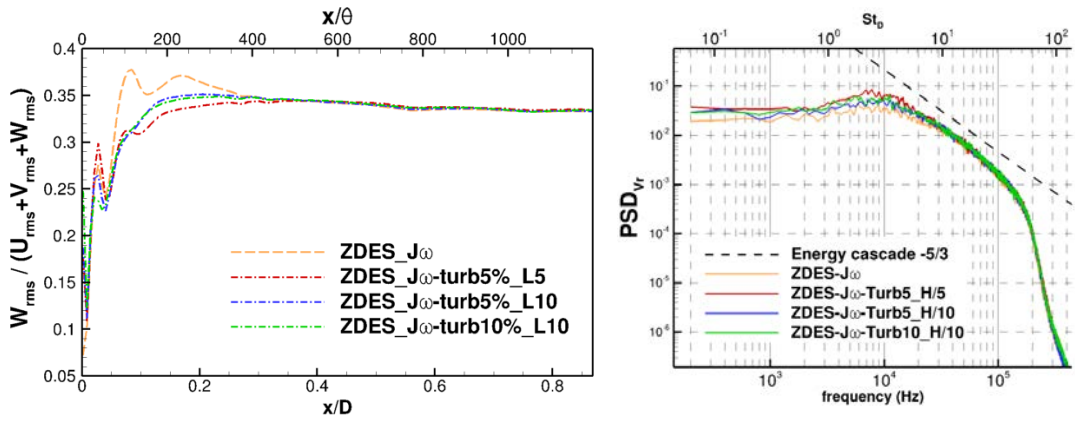

(a) $W_{rms}/(U_{rms}+V_{rms}+W_{rms})$ (b) Radial velocity PSD - probe E6

Figure 5.19: Three-dimensionality and fully-developed turbulence in the external mixing layer: (a) Evolution of $W_{rms}/(U_{rms}+V_{rms}+W_{rms})$ along the fan lip line, (b) Radial velocity spectrum at probe E6.

structures can be interpreted as follows: prescribing a smaller turbulent length scale at the RFG inlet produces a more broadband turbulence with more small scales during the transition process which then dissipate faster the turbulent kinetic energy by both the energy cascade process and the numerical dissipation due to the grid stretching (which starts around $x/D = 1$).

In order to assess the tridimensionality of the mixing layer, the evolution of the ratio $W_{rms}/(U_{rms}+V_{rms}+W_{rms})$ is plotted in figure 5.19. All the computations exhibit an secondary peak in the first part of the curve. According to Zaman & Hussain[242] such a dual-peak shape is typical of a vortex pairing whose location does not change significantly over time. This dual-peak shape is less pronounced for the cases with turbulent inflow, in particular for the cases using $l = H/10$ as injected characteristic length scale, which suggests that the vortex pairing is stronger in the computation without turbulent injection. The ratio, $W_{rms}/(U_{rms}+V_{rms}+W_{rms})$, also enables to assess the three-dimensional nature of the turbulence. The location where the value of the ratio reaches 0.33, location from which the turbulence can be regarded as fully three-dimensional, lies around $x/D \simeq 0.17$ for $l = H/10$ instead of $x/D \simeq 0.3$ for both other cases. The external mixing layer turns three-dimensional earlier when using a smaller injected length scale.

Slightly further downstream, at $x/D = 0.5$, the PSD of radial velocity at probe E6 exhibits for all simulations a broadband spectrum with a -5/3 slope over almost one decade, which indicates a fully developed turbulence in the mixing layer at this location.

To further investigate the initial vortex pairing development, the spectral content at the beginning of the transition area of the outer mixing layer is analyzed. The Power Spectral Density previously used also satisfies the equation:

$$\sigma_\Phi^2 = \int_{-\infty}^{\infty} f \cdot PSD_\Phi(f) d[log(f)] \tag{5.2.2}$$

where σ_Φ is the variance of Φ, which means that plotting $f \cdot PSD_\Phi(f)$ as a function of f in the linear-log axis gives directly the contribution to the total energy of the considered frequency band.

Such a representation of $f \cdot PSD_{V'}(f)$ for the radial velocity fluctuations is given in figure 5.20. As the computation of momentum thickness θ of the fan internal boundary

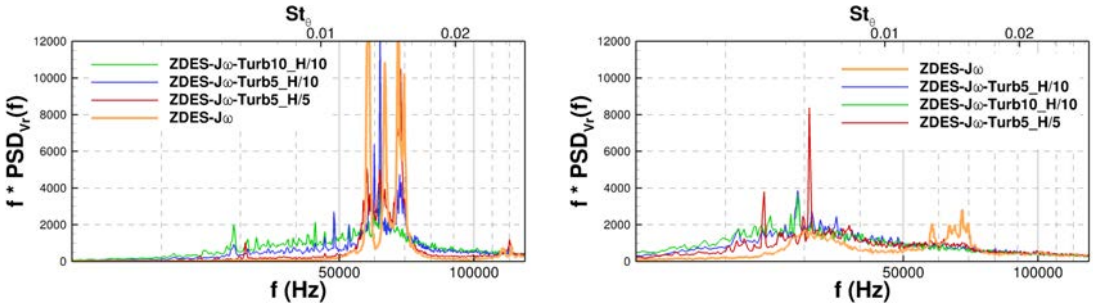

(a) PSD of radial velocity $x/D = 0.066$ (b) PSD of radial velocity $x/D = 0.13$

Figure 5.20: Power Spectral Density of radial velocity at probe location $x = 0.066D = 92\theta$ (a) and $x = 0.13D = 179\theta$ (b).

layer at the nozzle exit does not differ significantly between the 4 computations, the momentum boundary layer thickness of the baseline case $\theta = 7.77 \cdot 10^{-2} mm$ is used to calculate the Strouhal number $St_\theta = f\theta/\Delta U$, as well as the normalized axial coordinate x/θ.

The plot at $x/D = 0.066$ (probe E2) in figure 5.20(a) exhibits pronounced peaks for the curve Jω, that are still existing for cases Jω-T5-H/5 and Jω-T5-H/10 with the 5% turbulence rate. The peak frequencies lie in the range $St_\theta = 0.012 - 0.014$. In the case with 10% turbulence injected, peaks are further attenuated leading rather to a broadband hump centered on the same frequencies. These frequencies are in good agreement with the most amplified frequencies of the shear-layer mode predominating in the initial part of annular mixing layers, which have been established around $St_\theta = 0.017$ in stability analysis by Morris [158] or Michalke [156] but found slightly lower, around 0.012-0.013, in many experimental (see for instance Drubka & Nagib [90], Zaman & Hussain [243] or Bridges & Hussain [49]) and numerical (e.g. Bogey et al. [41], Kim and Choi [127]) studies (see chapter 2). This confirms the presence of roll-ups of Kelvin-Helmholtz-like vortices in the external mixing layer in all simulations, in a similar way that they can be found in the inner mixing layer. It seems however that a high turbulent rate in the jet core attenuates this phenomena.

In figure 5.20(b), the spectra of radial velocity are now displayed at the location $x/D = 0.13$ (probe E3). It can be observed that the main peak/hump frequencies occur now in the range $St_\theta = 0.0065 - 0.0068$ except for the baseline case which exhibits two humps, around $St_\theta = 0.0065$ and $St_\theta = 0.014$ respectively. The frequency $St_\theta = 0.0065$ is a sub-harmonic of the shear layer mode typical of the vortex pairing[49, 34, 41]. Hence, it seems to indicate that in all turbulent cases with turbulent inflow the vortex pairing occurs between the locations $x/d = 0.066$ and $x/D = 0.13$ whereas in the case without turbulent injection the vortex pairing occurs over a larger streamwise distance. This location of the vortex pairing is consistent with the vortex pairing observed around $x/D = 0.07 - 0.08$ for the case Jω-T10-H/10 in figure 5.17(d). Furthermore, in both cases with $l = H/10$, the spectra at $x/D = 0.13$ exhibit more broadband features, which indicates a more developed turbulence.

As an intense vortex pairing can be the source of tonal noise, it is interesting to scrutinize the density and pressure fluctuations in the vicinity of the transition area. The instantaneous field of dilatation $(1/\rho)div(\rho u)$ is plotted in figure 5.21 and gives access to the time variation of density. In all computations, a wave patterns appears (identified by

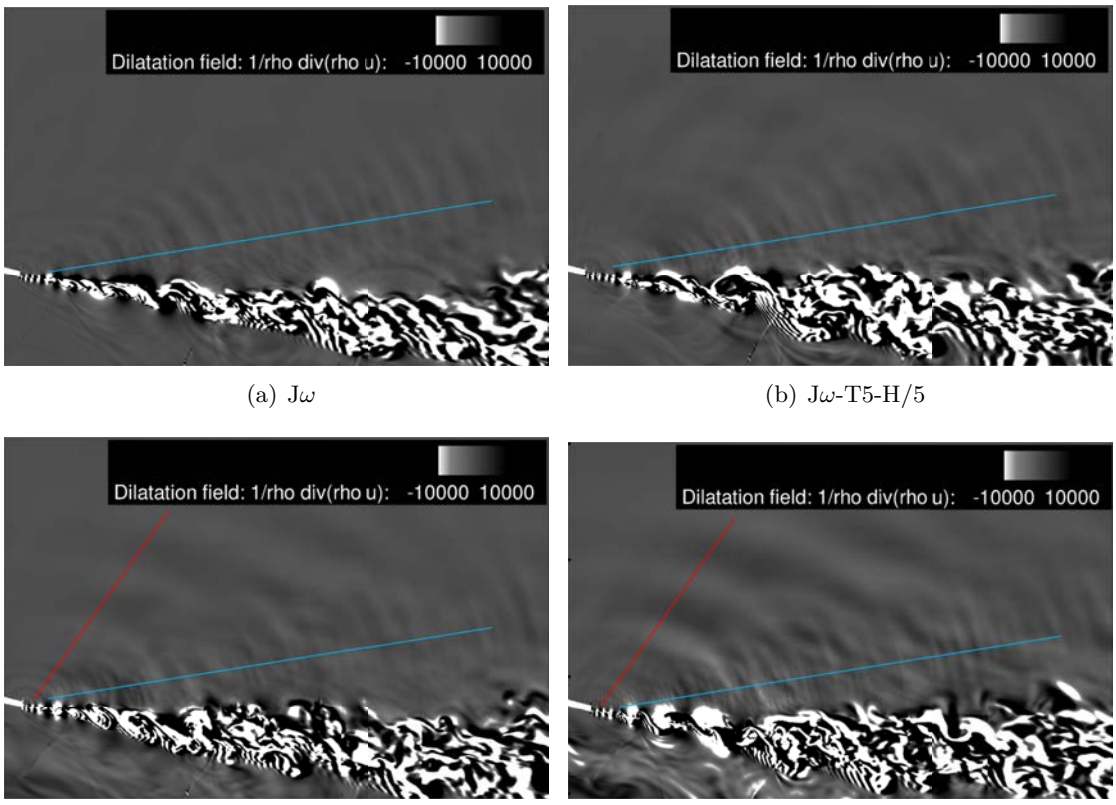

(a) Jω (b) Jω-T5-H/5

(c) Jω-T5-H/10 (d) Jω-T10-H/10

Figure 5.21: Instantaneous fields : dilatation field. The red and blue lines are used to identity the different acoustic waves emanating from the nozzle trailing edge area.

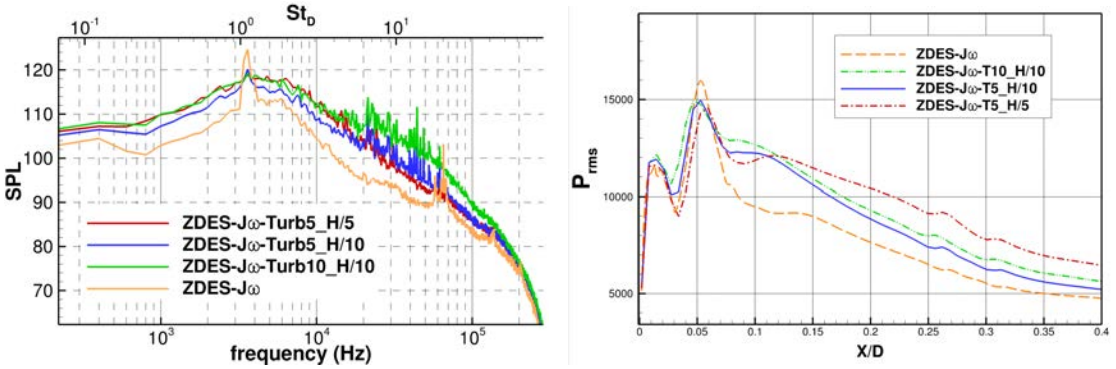

(a) Sound Pressure Level - probe Ext2 (b) P_{rms}

Figure 5.22: Sound Pressure Level outside the external mixing layer at $x/D = 0.4$ and P_{rms} along the external mixing layer

blue lines), emitted downstream from the trailing edge with an emission angle around 45 degrees, which is probably due to the initial Kelvin-Helmholtz-like roll up vortices and the subsequent vortex pairings. Another wave pattern (identified by red lines) appears in the turbulent cases with $l = H/10$, whose emission angle and wave length is much larger than the previous one. This noise emission could be directly linked to synthetic turbulence injection and seems to be only created when using a smaller length scale. Although the

grid was not designed to sustain acoustic waves over a sufficient distance from the jet to allow a proper acoustic post-processing and far-field noise analysis (which is beyond the primary objectives of the thesis), some insights on the acoustic content of the simulations can be gained with the SPL spectra at the probe O1 located just above the mixing layer (at $x/D = 0.4$, see figure 5.2 for the exact location). It shows a higher global level with turbulent inlets, but no specific peak frequency. This attenuation of the tonal frequencies is corroborated by the plot of the R.M.S. of pressure along the fan lip line in figure 5.22(b) with lower values for the peak of fluctuations. Conversely, the injection of turbulence appears to provide higher broadband noise. Actually, it seems that there may be at least two sources of broadband noise in the simulations : the BBSCN - which is physical - and another source related to the turbulent inlet - which can be regarded as a spurious one. This point would require further investigations in order to quantify the acoustic consequences of the turbulent injection in comparison with the aerodynamic benefits it can provide.

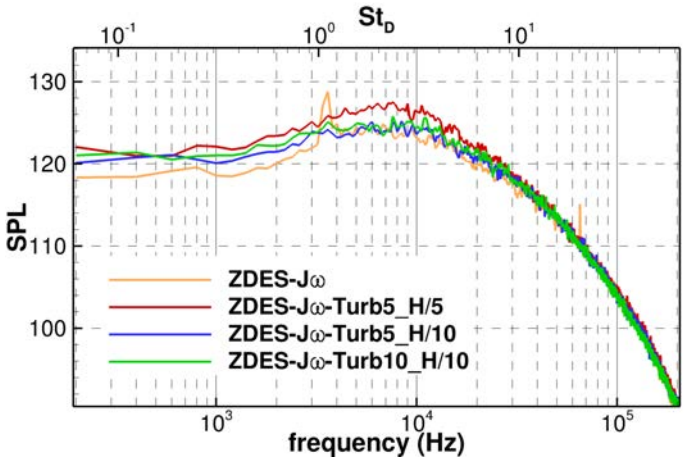

Figure 5.23: Sound Pressure Level in the External mixing layer

Regarding now the spectrum of pressure a bit further downstream, at $x/D = 0.5$ (probe E6) (see figure 5.23), it exhibits a broadband hump whatever the computation considered with slightly higher levels in low frequencies for the case Jω-T5-H/5 (still due to larger turbulent structures in that case). However, for the baseline computation, a small peak around $St_D = 1.1$ (3600Hz) characteristic of the screech tone is distinguishable. The injection of turbulence appears to have removed this tone and conserved only the broadband shock-cell noise component. Focusing on the radial velocity spectra, it shows a slope of decaying turbulence close to -5/3 over almost one decade, with few discrepancies between the four simulations, which indicates that the mixing layer is fully developed at this location for all simulations.

5.3 Conclusion

In this chapter, a parametric analysis of the RFG technique has been performed through four ZDES calculations of a dual-stream jet with an external plug. The motivation for upstream turbulence injection is twofold. On the one hand, it aims at improving the numerical/experimental agreement by taking into account an additional experimental parameter in the simulations. On the second hand, turbulence injection was evaluated as a mitigation solution for the delay in the formation of instabilities in mixing layers, as

observed in the previous chapter on the baseline simulation with steady inflow. In particular, two different turbulent length scales have been injected, and two different turbulent intensities.

The analysis of the way the turbulence is advected up to the nozzle exit has shown that the mesh refinement in the fan duct is satisfying whereas it is a bit coarser in the core duct, inducing an important dissipation of the injected turbulent content by the mesh before the exit. Moreover, realistic turbulence develops quickly downstream from the boundary condition but close to the exit, the three components of turbulent fluctuations of velocity undergo the local section contraction which slightly smooths the discrepancies from one simulation to the other. Nonetheless, the spectral content of the turbulence at the exit exhibited higher levels when the initial turbulent ratio was high and highlighted as expected that the smaller the turbulent injected length scale, the broader the spectrum, with more energy in the high frequencies.

Then, the study focused on the global development of the jet. The major result in this section, besides a higher turbulent level in the inner area of the jets, lies in the improvement of the shock-cells positioning when injecting turbulence. For this aspect, the most important parameter appears to be the turbulent ratio injected rather than the turbulent length scale. With an initial injected ratio of 10% of the mean velocity at the inlet, it has been possible to reach the experimental shock-cells positioning which is a significant achievement from an aerodynamic point of view. It highlights the necessity to account for all experimental parameters to achieve a satisfactory mean flowfield.

Besides, it has been observed that the initial delay in the formation of instabilities in the mixing layer is attenuated in simulations with turbulent inflow. The mixing layer development seems to be fed by the presence of freestream turbulence as well as by the injected turbulence which penetrates into the nozzle boundary layer. A clear effect has been observed in the cases injecting a smaller turbulent length scale $l = H/10$, the transition toward a three-dimensional behavior being even quicker when the inlet turbulent ratio was 10%. With an injected length scale twice larger, the acceleration of the transition is lower but can still be evidenced by the reduced Kelvin-Helmholtz peaks compared to the case with no injected fluctuation. In the external mixing layer, the same trend is observed. A first discrepancy is located in the vorticity thickness evolution when using the RFG inlet. Indeed, the transition is accelerated and the mixing layer thickness grows faster in the early stages of the shear-layer, reaching the experimental mixing layer thickness faster downstream of the exit than in the simulation without perturbation. This thickening of the early mixing layer could partly explain the better shock-cell positioning with injected turbulence, by the relative reduction of the efficient section in the first shock-cell. Vortex pairing appears also to be less intense and to occur somewhat earlier with injected turbulence. The higher the turbulent ratio and the smaller the length scale are, the higher the acceleration of the transition is. As a consequence, the spectral content indicates lower tonal noise resulting from the roll-up and vortex pairing at the beginning of the external shear-layer. However, some wave patterns seem to appear due to the turbulent inlet boundary conditions that could lead to additional broadband noise. This remains to be further investigated by acoustic studies, as the current mesh and numerical settings did not fit such requirements.

Actually, it appears preferable to inject relatively small structures at the inlet in order to obtain a quite broad spectrum of turbulent scales at the nozzle exit, which results in a more efficient transition of the mixing layers. Regarding the initial injected turbulence ratio, no generic recommendation can be expressed from this work, since it was found to be very case dependent and should be tuned to match the experimental level in the first

place.

In the end, this study has demonstrated the strong interest of the RFG method for the aerodynamic prediction of the dual-stream jets, which remains to be validated for aero-acoutic purposes since it could induce some spurious noise.

Chapter 6
Conclusions and perspectives

Conclusions

The objectives of this thesis were to assess the maturity of the multi-resolution approach ZDES developed by ONERA [81] for the accurate simulation of propulsive jets representative of aircraft engine configurations and to investigate the influence on the jet development of upstream turbulence in the core of the jet. The industrial solver elsA has been used in the framework of this thesis.

After having provided the main features of jet physics, chapter 2 focused on the numerical methods currently existing to simulate turbulent jets. This review laid emphasis on two key aspects which need to be further addressed especially for realistic geometries: on the one hand, in realistic configurations, the issue of the widely laminar mixing layers which occurs almost systematically with significant consequences on the jet development, on the other hand, the inflow turbulence in the core of jets - quite important in real engines - which had not been thoroughly studied in the open literature.

In the first part of this work, a study of ZDES numerical settings has provided deeper insights on different ways to reduce RANS-to-LES transition issues in the mixing layer recurrently encountered in DES-like simulations of turbulent jets.

Some comparisons between two different spatial schemes have been performed and the effect on the mixing layer development assessed, using the mode 1 of ZDES. One spatial scheme is the commonly used centered scheme of Jameson, and the second one is the lower dissipation upwind scheme AUSM+(P). While a strong bi-dimensional behavior associated to Kelvin-Helmholtz vortices is observed in the internal mixing layer with the Jameson scheme, the results evidence a reduction of this behavior and a faster transition of mixing layers toward three-dimensional turbulence when using the lower dissipation AUSM+(P) scheme. However, it does not completely suppress the initial bi-dimensional development of the inner shear-layer which remains nonphysical.

The effect of the subgrid length scale definition has also been conducted by comparing the time-honored length scale Δ_{vol} only based on the local grid characteristics to the subgrid length scale Δ_ω introduced by Chauvet et al. [65] which takes into account both local grid spacing and vorticity. As for the spatial scheme effect, a significant reduction of the transition length in the inner mixing layer is observed using Δ_ω instead of Δ_{vol}, nevertheless without preventing the delay in the apparition of fully developed turbulence.

Both effects of the subgrid length scale and of the spatial scheme dissipation level on the inner mixing layer transition appear to be of the same order of magnitude.

Conversely, in the outer mixing-layer, the velocity difference which triggers the shear-layer is so large that the initial Kelvin-Helmholtz process is very quickly destabilized in all ZDES simulations, such that the discrepancies between simulations are less observable. In all ZDES simulations of this study, once the transition is fully achieved, the growth of the vorticity thickness of the outer mixing layer is close to the experimental one and is in better agreement with experimental data than the results obtained with RANS modeling. ZDES simulations also induce a better prediction of shock-cell locations than RANS, but an important phase-lag with experimental results remains. This phase-lag is attributed to a different efficient section of the fan jet in simulations due to the transition from laminar to turbulent state of the mixing layer, whereas in the experiment the mixing layer is initially fully turbulent.

Last, the mode 2 (the "automatic" mode) of ZDES has been compared with the mode 1. A very similar mixing layer development is observed, but some discrepancies appears in the vicinity of the plug, with amplified unsteady features using the mode 2. In this latter region, both mode 1 and mode 2 of ZDES appear to differ from the experimental flow field. Unfortunately, few measurements are available in the plug area to further assess the reliability of the simulations.

In a second part of this work, the influence of accounting for upstream turbulence in ZDES simulations has been investigated with the RFG technique developed by Smirnov et al. [197]. Several computations have been carried out, by changing the prescribed turbulence rates and turbulent length scales. Despite a decrease of the overall turbulent kinetic energy level along nozzle ducts, a significant amount of the injected turbulence is advected up to the nozzle exit. Even in the boundary layer treated in RANS mode of ZDES, significant velocity fluctuations are observed at the nozzle exit. These fluctuations promote a fast transition in the mixing layers, which can be seen as a favorable side-effect of the injection of upstream turbulence in the whole inflow plane.

The analysis of the mixing layer development has indeed revealed the acceleration of the process leading to a fully developed turbulence in both inner and outer mixing layers. In the outer mixing layer, the turbulent injection provides a higher turbulent level at the beginning of the mixing layer transition, which induces a larger initial thickness of the mixing layer than in the computation with steady inflow, as in the experiment. Besides, this positive effect is increased when injecting a smaller turbulent length scale. In the inner mixing layer, the injection of turbulence reduces the intensity of the Kelvin-Helmholtz vortices and accelerates the three-dimensional destabilization of the vortex sheet. However, only the case with the highest inlet turbulence rate succeeded in suppressing the bi-dimensional behavior of the inner mixing layer. As a general recommendation, the use of smaller turbulent structures in the synthetic turbulence method appears more efficient to achieve a rapid transition of mixing layers, although this setup must be done consistently with the grid spacing in the ducts.

Regarding the consequences of upstream turbulence on the overall jet development, the major effect is the modification of the shock-cell positioning. Indeed, the phase-lag between simulated and experimental results is significantly reduced when injecting upstream turbulence. Besides, this effect increases with the turbulence rate injected. The suppression of the phase-lag is for instance suppressed in the case with the highest turbulence rate at nozzle inlets. The reason of this effect seems to be twofold. A part of the explanation undoubtedly lies in the better prediction of the mixing layer thickness in the transition area, which changes the local efficient section of the fan jet and favorably modifies the shock-cell pattern. Another part of the explanation could be directly linked

to the increased mixing in the core of the jet that could attenuate shocks and modify shock-cell width.

To summarize, this parametric study conducted on a 200 million points mesh with the industrial solver elsA has helped identify some key numerical parameters and best practices to improve the accuracy of ZDES simulations of propulsive jets. The interest of using a low dissipative scheme associated to the subgrid length scale Δ_ω has proved to enhance the rapid transition toward fully turbulent mixing layers. The interest of accounting for upstream turbulence to increase the jet physics representativity has also been demonstrated using the RFG technique. This method was shown to be well suited to this purpose.

Perspectives

The fair agreement between ZDES simulations and experimental results achieved in this work appears today sufficient to consider ZDES as a reliable tool for predicting most of the jet physics of real engine configurations. In particular, the development of the external mixing layer triggered by high velocity gradients is satisfactorily reproduced, even by the "automatic" mode of ZDES, the mode 2. Thus, the increased accuracy of simulations can be envisaged for the treatment of more complex cases such as the flow field at the junction between the nacelle trailing edge and the pylon fairing , in order to predict pressure fluctuations on the aft pylon fairing. More generally, all issues related to the outer mixing layer, since they occur at flight conditions likely to induce very high velocity gradients (ground and take-off conditions), can be investigated by means of ZDES with a fair level of reliability insomuch as the grid spacings and numerics are carefully controlled. Further validation of the mode 2 of ZDES on installed configurations like nacelle-to-wing geometries should now be conducted as initiated in Ref. [57, 55].

However, several limitations pointed out by the present results continue to deserve attention and should be the topic of future work.

First, the correct prediction of the inner mixing layer development remains challenging. Only a significant level of upstream turbulence permitted to achieve a satisfactory destabilization of the initial vortex sheet. To equally obtain a rapid transition for lower upstream turbulence, the combination of the turbulent injection with lower dissipative scheme could be advantageous. Unfortunately, the spatial scheme AUSM+(P) used in the present work, even though it has demonstrated the interest of this kind of scheme, has also exhibited recurrent problems of robustness, especially in presence of upstream turbulence.

The use of low dissipation spatial schemes appears mandatory for the future of hybrid RANS-LES simulations. Therefore, a necessary work should be devoted to the development and validation of affordable and robust low dissipative schemes to treat industrial configurations. For instance, the extension of AUSM+(P) to transsonic Mach numbers by Liou [146] within the scheme AUSM+UP could be of interest. For acoustic purposes, the robustness of high order schemes as those studied in [98] should also be investigated.

Regarding the influence of upstream turbulence on the jet, further studies would also be necessary. In this work, only 2 turbulence rates and 2 turbulent length scales have been investigated, identical in fan and core ducts, and the nozzle exit experimental level of turbulent kinetic energy has not been reached. Additional efforts could be made with the RFG method to properly rescale turbulent levels and to investigate a wider range of

RFG parameters. It could also be interesting to compare this technique with another technique of synthetic turbulence generation.

One important result of this thesis is the shock-cell positioning evolution with upstream turbulence. Nonetheless, it is not clear which part is due to the earlier thickening of mixing layers and which part is directly linked to upstream turbulence in the core of jets. Some ZDES simulations involving turbulent excitation only in boundary layers could help to discriminate the origin of the change in shock-cell location when injecting turbulent content. Additional wind tunnel test campaigns dedicated to this would also be of high value.

An aeroacoustic analysis of the simulations was beyond the scope of the thesis but in the frame of acoustic studies using ZDES, it would be interesting to assess the effect of the reduction of the mixing layer transition brought on by the use of Δ_ω and of a low dissipation scheme. Furthermore, the present study has evidenced the increased accuracy of the ZDES simulations when taking into account upstream turbulence with the RFG technique, but the use of such synthetic turbulence method is bound to create some spurious noise, the evaluation of which should be the topic of future work.

Last, an issue pointed out by this work is the behavior of the flow field in the vicinity of the plug which remains very challenging to simulate. Both mode 1 and mode 2 fail to reproduce velocity levels downstream from the plug on the jet axis. Despite no separation has been evidenced on the plug in simulations, instantaneous visualizations suggest unsteady features in the plug boundary layer which are significantly amplified with mode 2. The boundary layer in this region appears very thick and is submitted to a small radial velocity gradient combined with a significant adverse pressure gradient. The RANS treatment with the Spalart-Allmaras model of the boundary layer in mode 1 and mode 2 of ZDES is not tailored to efficiently treat the dynamics of such type of flow and could fail to reproduce an incipient separation which may occur in such conditions. Unfortunately, no measurement was available in the plug boundary layer that could confirm such an hypothesis.

In order to get a deeper insight on the dynamics of the plug boundary layer, the mode 3 of ZDES (acting as WMLES) could offer an affordable solution. Indeed, the mode 3 of ZDES can be used locally in the plug boundary layer area in combination with mode 1 and mode 2 in the rest of the domain, which limits the increase of computational cost. One could also take advantage of the chimera technique to allow a grid density consistent with a WMLES modelling only in the plug area. Such a simulation would bring significant improvements to the understanding of the mixing on the jet axis. Since the jet axis is the location of highest temperatures, the comprehension of the local physics is necessary to further predict accurately the temperature evolution in the jet. Additional measurements would also help to better understand this issue in the plug area.

Appendix A

Preliminary study: steady generative boundary conditions setting

Prior to investigating the jet physics and ZDES modeling, the sensitivity of steady state simulations to generative conditions has been studied. As a matter of facts, jet experiments raise several issues regarding results accuracy and reliability. In particular, the variations of ambient and generative conditions between runs is commonly acknowledged. In addition, it appears out of reach to simulate the complete domain of ducts from the upstream tranquilization chamber, where generative conditions are measured, up to the nozzle exit. Thus, in simulation the mockup geometry (see section 3.2) is truncated to conserve only the nozzle part, which induces another cause of uncertainty about the generative conditions to impose at nozzle inlets.

Those issues have motivated the present investigation on the jet sensitivity to fan and core generative conditions. Several approaches exist to assess the sensitivity of a simulation to a set of parameters, as uncertainty propagation techniques or data assimilation. Such techniques are cumbersome to implement and out of the scope of this preliminary study which aims at simply and quickly investigating the potential impact of total pressure and temperature variations on the flow field. Another objective is to generate the best input data set of boundary conditions for the initialization of ZDES computations.

Several variations of generative pressures and temperatures have been performed with both uniform and non-uniform boundary conditions and their effects are given in the end of this section. In the following, the procedure that has enabled to accurately rescale the mass flow rate in primary and secondary ducts is presented in more details.

A.1 Numerical setup

The present numerical study has been performed with the 2D axisymmetrical RANS approach on the truncated nozzle geometry of the MARTEL experiment as illustrated in figure A.1.

The 2D-axisymetric mesh forms a thin wedge of 10 degrees in the azimuthal direction with an increased refinement in mixing layers. Almost 0.7 million grid points per azimuthal plan are used to reach an actual 2 million points mesh.

The effect of different RANS turbulence models has been widely investigated by Giner in his PhD[102], concluding to insignificant discrepancies over a distance of a few diameters downstream of the nozzle exit. For the sake of consistency with the remaining of the thesis based on ZDES simulations relying on the Spalart-Allmaras [200] model, the Spalart-

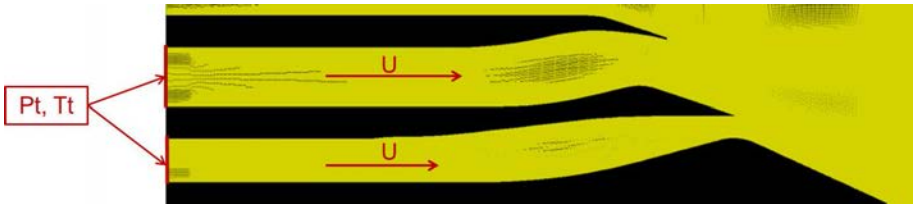

Figure A.1: Inlet boundaries of fan and core ducts.

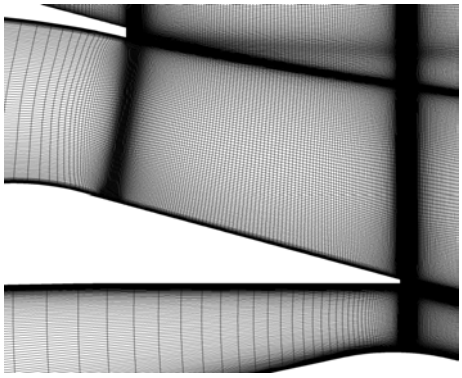

Figure A.2: Mesh in the region of nozzle trailing edges

Allmaras model was used for this preliminary study.

The numerical scheme used is the centered second order scheme of *Jameson*. No preconditioning is imposed. A first run with 3 levels of multigrid is performed, before a simple grid restart which aims at improving the convergence in the wakes of thick trailing edges.

Adiabatic, no-slip conditions were imposed at all walls.. A non-reflective condition is imposed on the top radial boundary and a periodicity condition on the azimuthal boundaries. Subsonic injection boundary conditions are used at the inlet of the domain. In particular, the total temperature and total pressure are fixed at the inlet of the fan and core ducts. For the sake of robustness, as no preconditioning is used, the external Mach number is set at $M_\infty = 0.01$ instead of 0. The inlet ratio μ_t/μ is set at 0.01.

A.2 Effect of of total quantity variations on mass flow rates

The objective is to define Pt and Tt that provide the best match with the experimental values. The baseline computation is run with:

- fan pressure ratio $NPR_{fan} = 2.452$
- core pressure ratio $NPR_{core} = 1.608$
- fan temperature ratio $Tt_{fan}/Tt_0 = 1.0172$
- core temperature ratio $Tt_{core}/Tt_0 = 1.8026$

First, variations of total pressure over a range of $\pm 5\%$ around the values of a baseline computation are imposed at the fan and core inlets. These variations are carried out separately in the core and the fan, in order to understand their respective effects. Therefore, the pressure ratio of the fan duct ranges in $NPR_{fan} = 2.32 - 2.57$ whereas the core pressure ratio ranges in $NPR_{core} = 1.52 - 1.69$. The same procedure is operated for the total temperature ratio which varies between 0.96 and 1.07 for the secondary stream and between 1.71 and 1.89 for the primary flow. Then some total pressure variations

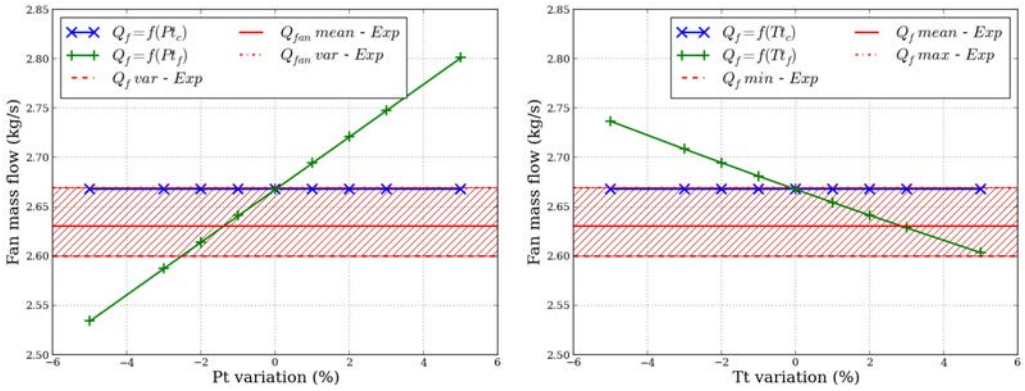

(a) $Q_{fan} = f(NPR)$ (b) $Q_{fan} = f(T_t)$

Figure A.3: Evolution of the fan mass flow depending on the total temperature and pressure variations in the core and the fan

concomitant in both fan an core ducts are operated. The fan mass flow rate is plotted in function of fan and core pressure ratios in figure A.3(a) and in function of fan and core total temperatures in figure A.3(b).

The fan mass flow evolution appears to be an increasing linear function of NPR_{fan}. Conversely, the fan mass flow rate decreases linearly depending on the total temperature imposed at the fan inlet. On the one hand, the velocity is increased, on the other hand, the density is decreased, but this latter is predominant in the mass flow rate evolution. Regarding the dependency on core inlet generative conditions, it appears that the fan mass flow rate is neither influenced by the total temperature imposed at the core inlet, nor by the variations of NPR_{core}, which was expected since the fan exit is shocked. The averaged fan mass flow in experiments is 2.630kg/s, with a significant scatter from one run to the other, experimental values ranging between 2.600 and 2.669 kg/s (±1.5%).

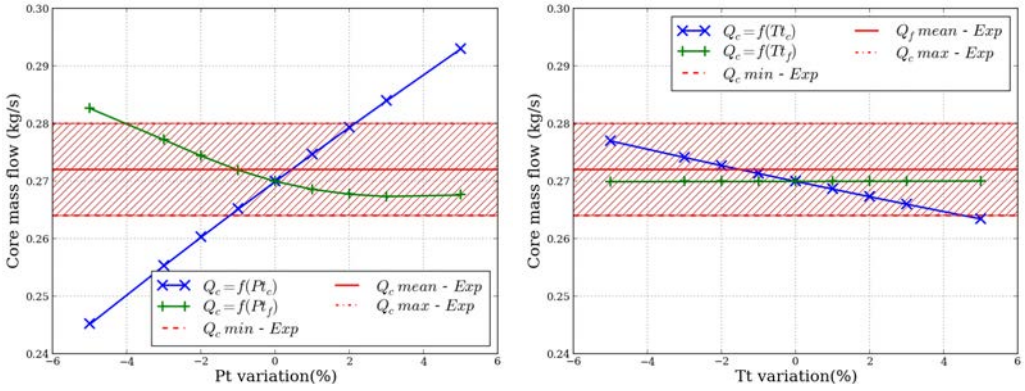

(a) $Q_{core} = f(NPR)$ (b) $Q_{core} = f(T_t)$

Figure A.4: Evolution of the core mass flow depending on the total pressure and temperature variations in the core and the fan

It is shown in figure A.4(b), that the core mass flow rate is not influenced by Tt_{fan} and decreases linearly with Tt_{core} (see figure A.4(b)). The dependency of the core mass flow rate on the pressure ratios, it appears less straightforward. Figure A.4(a) shows that

the core mass flow rate increases linearly with the NPR_{core}. Over the range investigated for NPR_{core}, a variation of almost 18% on the core mass flow is observed. Conversely, the core mass flow rate decreases linearly with the fan pressure ratio,then reaches a plateau at higher pressure ratios. This dependency of the primary flow on the secondary flow generative conditions is due to the variations of the core exit pressure induced by NPR_{fan} variations. For low values of NPR_{fan}, a NPR_{fan} increase induces a displacement of the strong shock at the end of the first cell up to the core cowl trailing edge, which increases the adverse pressure at the core exit and reduces the core mass flow rate. Once the shock positioning is fixed at the core cowl trailing edge, the core exit pressure does not significantly evolve and the core mass flow rate appears stabilized.

The averaged core mass flow in experiments is 0.272kg/s, which is not so far from the computed value for the baseline simulation. However, an important experimental scatter exists, core mass flow rates varying between 0.264 and 0.280 kg/s from one run to the other ($\pm 3.5\%$). Consequently, the ranges of variation of Tt_{core} provide core mass flow rates within the experimental scatter range.

Actually, it appears that all mass flow curves can easily be fitted by a linear function except the core mass flow depending on the NPR_f. But in this latter case, linear approximation remains valid for low fan pressure ratios (lower than -1% of the baseline value). Since the experimental fan mass flow rates are reached for fan pressure ratios in the linear part of the curve, it appears reasonable to consider a global linear behavior of mass flow rates depending on generative pressure and temperature, as long as considered NPR values are lower than baseline ones.

Moreover, the concomitant variations of total pressure between the fan and the core have shown that the slope of the linear fitting curve does not change when changing the pressure ratio in one channel (it just shifts the curve) as plotted in figure A.5.

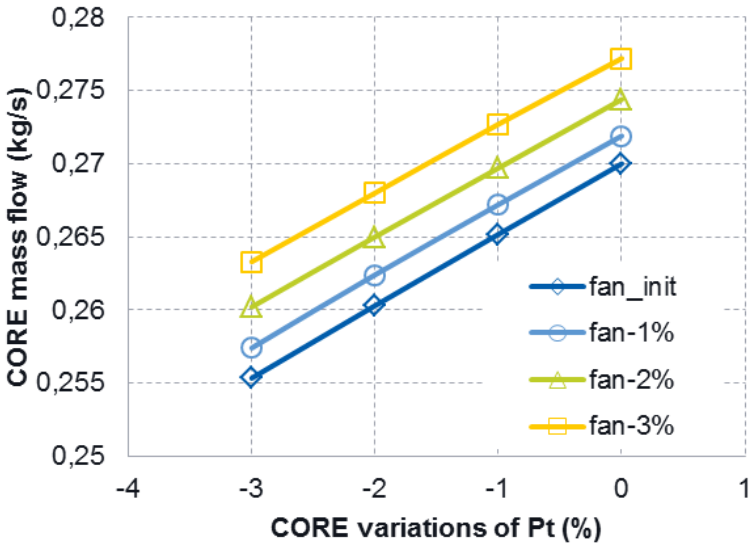

Figure A.5: Core mass flow rate vs Pt core for different values of NPR_{fan}

Therefore, it can be taken advantage of this linear mass flow behavior to estimate mass flow rates depending on total quantities injected. The primary mass flow Q_c can be

modeled in the following manner:

$$Q_c = Q_c(REF) + \alpha_c \Delta Pt_c + \beta_c \Delta Pt_f + \gamma_c \Delta Tt_c + \delta_c \Delta Tt_f \tag{A.2.1}$$

and the secondary mass flow Q_f as follows:

$$Q_f = Q_f(REF) + \alpha_f \Delta Pt_c + \beta_f \Delta Pt_f + \gamma_f \Delta Tt_c + \delta_f \Delta Tt_f \tag{A.2.2}$$

where $Q_c(REF)$ and $Q_f(REF)$ are core and fan mass flows obtained in the reference simulation and α_c, β_c, γ_c, δ_c, α_f, β_f, γ_f and δ_f are the slopes of the core and fan mass flow curves. In particular, β_c is the slope of the linear part of the curve figure A.4(a). Considering that δ_c, α_f and γ_f are almost null, it comes:

$$Q_c = Q_c(REF) + \alpha_c \Delta Pt_c + \beta_c \Delta Pt_f + \gamma_c \Delta Tt_c \tag{A.2.3}$$

and

$$Q_f = Q_f(REF) + \beta_f \Delta Pt_f + \delta_f \Delta Tt_f \tag{A.2.4}$$

The question is then to know which values among ΔPt_c, ΔPt_f, ΔTt_c and ΔTt_f have to be estimated at the inlets to retrieve experimental mass flows. At this stage, still 4 unknowns remain for only 2 equations. As previously seen, total temperature variations essentially impact the amplitudes of flow field variables, mainly in the stream whose inlet is modified (primary stream for ΔTt_c, secondary stream for ΔTt_f), but no shifting of axial location or shape modification of velocity profiles is observed. Thus, the variation of total temperature is considered as slightly affecting the flow physics, and can be fixed first, more less arbitrarily (see discussion below). Therefore, the problem is mainly reduced to the determination of ΔPt_c and ΔPt_f with equations (A.2.3) and (A.2.4), knowing the target values $Q_{core_{exp}}$ and $Q_{fan_{exp}}$. Several tests, with different choices of ΔTt_c and ΔTt_f have been performed using this approach. This led each time to a discrepancy lower than 2% between the target core mass flow and the one obtained in the simulation. The linear assumption is less exact when injected levels are increased, which explains that 2% of discrepancy can casually be reached. Conversely, discrepancies on the fan mass flow are systematically lower than 0.1%. The choice of total temperatures such as the one measured in experiments would be legitimate. However, between the different runs of the experiment, non-negligible variations of the temperature existed, inducing noticeable discrepancies of total temperatures from one measurement station to the other. Actually, the temperature profile at $x/D = 0.5$ has been chosen as target for total temperature prescriptions, since it is the closest from the nozzle exit including both primary and secondary streams. The procedure has also been operated with the temperature profile at $x/D = 1$, but with less success, which confirms the initial choice. It led to the following values of ΔPt_{core}, ΔPt_{fan}, ΔTt_{core} and ΔTt_{fan} relatively to the reference calculation:

$$\begin{array}{llllll} \Delta Pt_c = -1.02\% & \Longrightarrow & NPR_c = 1.591 & \Delta Pt_f = -1.91\% & \Longrightarrow & NPR_f = 2.404 \\ \Delta Tt_c = -1.5\% & \Longrightarrow & T_{t_c}/T_0 = 1.776 & \Delta Tt_f = -1\% & \Longrightarrow & T_{t_f}/T_0 = 1.006 \end{array}$$

The resulting mass flows are $Q_{core} = 0.2714 kg/s$ and $Q_{fan} = 2.630 kg/s$, *i.e.* 0.22% in the core and 0% in the fan compared with averaged values of the experiment, thus significantly in the range of uncertainty of measurements. The results at $x/D = 0.5$ and along the fan line are presented in figure A.6. It shows less discrepancies in the external

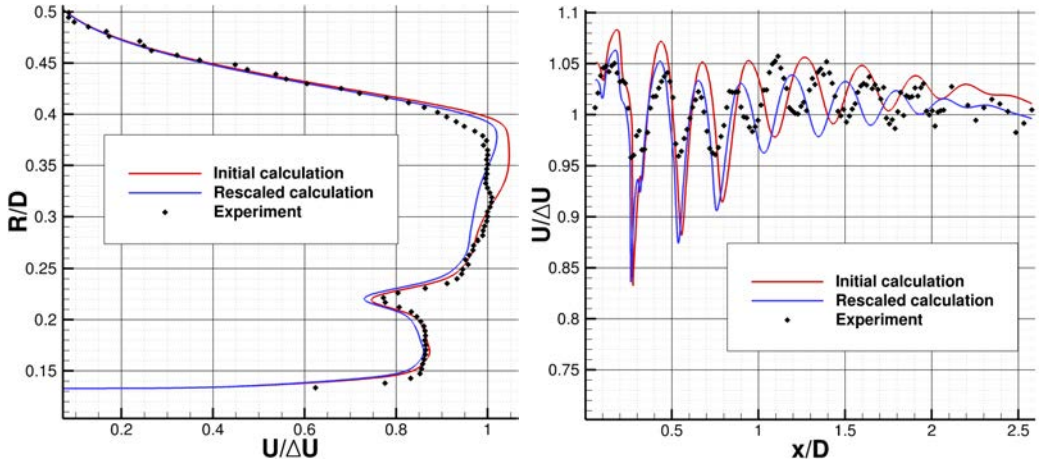

(a) 0.5D line (b) Fan line

Figure A.6: Velocity profiles of the rescaled calculation versus the initial one

region of the radial velocity profile, but slightly more in the core area than the baseline computation. Along the fan line, the location of velocity extrema, i.e. the shock-cell location, the phase-lag with the experimental curve is reduced.

However, the shape of the radial velocity profile in the secondary stream remains far from the experimental shape, with a curvature oriented toward the nozzle instead of downstream, which is attributed to the RANS modeling rather than the generative conditions.

A.3 General remarks about generative conditions

This preliminary study investigated RANS inlet boundary conditions for simulating the MARTEL experiment. The influence on the flow field of total temperatures and pressures injected at fan and core inlets has been analyzed focusing on three main aspects: radial velocity profiles, shock-cell pattern and mass flow rates. All these aspects have been compared with experimental results.

As exposed in the previous section, the linear dependency on generative boundary conditions of shock-cell characteristics and of mass flow rates have been observed. In particular, the fan pressure ratio appeared as the most influential parameter, which actually impacts the shock-cell positioning, while core pressure ratio and total temperatures only affect the mean level of velocity.

The effect of non-uniform injection has also been studied, only the main findings of this study are given below for the sake of concision. Several profiles with a deficit of total pressure for higher radius have also been prescribed at the fan inlet in order to improve the agreement of the nozzle exit velocity profiles with the experiment. It provided slight improvements of exit velocity profiles, but significantly increases the complexity to obtain at the same time satisfactory mass flow rates. Investigations on the shape of inlet P_t profiles have been limited, but the complexity to both match experimental profiles and mass flow rates appears as a significant drawback.

Actually, for the sake of simplicity, generative boundary conditions obtained from the mass flow rate rescaling method with uniform injection have been preferred for ZDES simulations.

Appendix B

Post-processing

B.1 The turbulent stress-tensor

B.1.1 Definitions and hypothesis about the Reynolds stress tensor

Following the formulation proposed by Vreman et al (1997) for a compressible flow, the fluctuating velocity is defined by:

$$u_i^f = u_i - \frac{<\rho u_i>}{<\rho>} \tag{B.1.1}$$

where $<\cdot>$ refers to the statistical averaging.

The Reynolds stress tensor for unfiltered variables is then defined by:

$$r_{ij} = \frac{<\rho u_i^f u_j^f>}{<\rho>} \tag{B.1.2}$$

In the case of our compressible simulations, the filtered variables are referred to by $\overline{\cdot}$ and $\widetilde{u_i} = \overline{\rho u_i}/\overline{u_i}$ refers to the Favre filtering of the velocity. Then, the fluctuating filtered velocity is defined by:

$$u' = \widetilde{u} - \frac{<\overline{\rho}\widetilde{u_i}>}{<\overline{\rho}>} \tag{B.1.3}$$

Introducing the Favre averaging $[\cdot] = <\overline{\rho}\widetilde{\cdot}> / <\overline{\rho}>$, it comes:

$$u' = \widetilde{u} - [u] \tag{B.1.4}$$

so u' verifies $<\overline{\rho}u'> = [u'] = 0$. We define R the Reynolds stress tensor of filtered velocity by:

$$R_{ij} = \frac{<\overline{\rho}\widetilde{u_i'}\widetilde{u_j'}>}{<\overline{\rho}>} = [u_i'u_j'] \tag{B.1.5}$$

It must be noted that the exact definition of the resolved and the modeled parts of the Reynolds stress tensor is not trivial. Following Vreman et al [230] it is assumed that :

$$r_{ij} \approx R_{ij} + \frac{<\tau_{ij}>}{<\overline{\rho}>} \tag{B.1.6}$$

where R_{ij} represents the resolved part of the shear-stress tensor and $<\tau_{ij}>$ the modeled part.

B.1.2 Calculation of the filtered Reynolds stress tensor R_{ij}

The simulation only provides access to the variables:

$$[u_i] = \frac{<\overline{\rho}\widetilde{u_i}>}{<\overline{\rho}>} \quad , \quad [u_j] = \frac{<\overline{\rho}\widetilde{u_j}>}{<\overline{\rho}>} \quad and \quad [u_i u_j] = \frac{<\overline{\rho}\widetilde{u_i}\widetilde{u_j}>}{<\overline{\rho}>} \tag{B.1.7}$$

but by application of the Favre averaging to $\overline{\rho}\widetilde{u}\widetilde{u}$, it is possible to write:

$$R_{ij} = \frac{<\overline{\rho}\widetilde{u_i}\widetilde{u_j}>}{<\overline{\rho}>} - \frac{<\overline{\rho}\widetilde{u_i}>}{<\overline{\rho}>}\frac{<\overline{\rho}\widetilde{u_j}>}{<\overline{\rho}>} \tag{B.1.8}$$

$$R_{ij} = [u_i u_j] - [u_i][u_j] \tag{B.1.9}$$

B.1.3 Calculation of the modeled part τ_{ij}^{SGS}

Within the frame of ZDES, the subgrid stress tensor is similar to the Smagorinsky one and thus based on a turbulent viscosity. The subgrid stress tensor verifies:

$$<\tau_{ij}^{SGS}> = -<\mu_t>\left(\frac{\partial[u_i]}{\partial x_j} + \frac{\partial[u_i]}{\partial x_i} - \frac{2}{3}\frac{\partial[u_k]}{\partial x_k}\delta_{ij}\right) + \frac{1}{3}<\tau_{kk}^{SGS}>\delta_{ij} \tag{B.1.10}$$

which gives:

$$<\tau_{u_x u_r}^{SGS}> = -<\mu_t>\left(\frac{\partial[u_r]}{\partial x} + \frac{\partial[u_x]}{\partial r}\right) \tag{B.1.11}$$

(To be more exact, some terms including products of μ_t fluctuations with gradients fluctuations should be taken into account, but a recent estimation of these terms for a turbulent boundary layer by Deck et al [84] showed they were negligible. Even though present flows are compressible, it is assumed that this observation remains valid. Let it be reminded that $<\tau_{ij}^{SGS}> / <\rho>$ is already an approximation of the discrepancies between r_{ij} and R_{ij} and the calculation of these additional terms is too heavy to be carried out in our study.)

Unfortunately, the computational process within the industrial environment provides μ_t/μ instead of μ_t, therefore μ has to be estimated. The molecular viscosity is estimated thanks to the Sutherland's law with μ_∞ and T_∞ as reference values:

$$\mu(<T>) = \mu_\infty\left(\frac{<T>}{T_\infty}\right)^{\frac{3}{2}}\frac{<T>+110.4}{T_\infty+110.4} \tag{B.1.12}$$

then $<\tau_{ij}>$ is computed by means of the Boussinesq expression:

$$<\tau_{u_x u_r}^{SGS}> = -\left(\mu(<T>)<\frac{\mu_t}{\mu}>\right)\left(\frac{\partial[u_r]}{\partial x} + \frac{\partial[u_x]}{\partial r}\right) \tag{B.1.13}$$

Regarding the subgrid turbulent kinetic energy $<k_{SGS}> = 1/2(<\tau_{kk}^{SGS}>)$, the components of the subgrid tensor verify:

$$<\tau_{ij}^{SGS}> = -2<\mu_t>\widetilde{S_{ij}} + \frac{2}{3}<k_{SGS}>\delta_{ij} \tag{B.1.14}$$

which does not permit the direct computation of the subgrid turbulent kinetic energy. Nevertheless, Vreman [227] established that the formula $k_{SGS} = 2\sqrt{2}\mu_t \parallel \widetilde{S_{ij}} \parallel$ is a good approximation for the case of a Smagorinsky model.

B.1.4 Practical estimation of the Reynolds stress tensor

The extraction of the relative weight of each contribution (resolved and modeled) has been performed on the reference calculation presented in Chapter 4. The shear-stress component r_{uv} and both resolved part $u'v'$ and modeled part τ_{uv} are plotted in figure B.1. It appears that the contribution of the modeled part is negligible everywhere in the free shear areas and is preponderant in the plug boundary layer due to the RANS treatment of boundary layers. Therefore, the approximation $r_{ij} \approx R_{ij}$ is justified and has been done for the estimation of the Reynolds stresses in mixing layers in this PhD work. Besides, it illustrates that far from the walls the ZDES behavior is similar to LES.

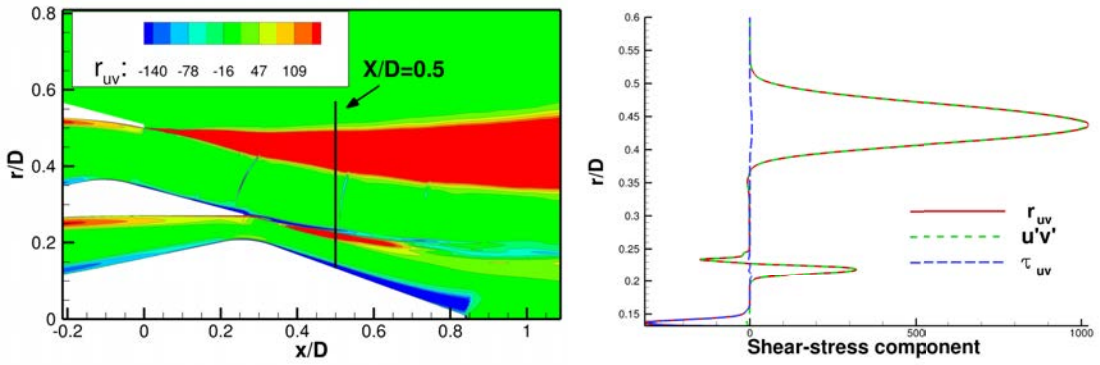

(a) Total shear-stress component r_{uv} (b) $x/D = 0.5$

Figure B.1: Shear-stress component estimation: (a) contour of the total estimation, (b) breakdown of the shear-stress component at $x/D = 0.5$

B.2 The azimutal average

In the case of an axisymetrical flowfield using the cylindrical coordinates and the Favre averaging, as demonstrated in [170], the components of the Reynolds tensor $r_{u\theta}$ and $r_{r\theta}$ must be null. Numerically these components appear to be negligible compared to the other components, as exposed in figure B.2, which legitimates the azimuthal averaging.

Two possibilities exist to perform the azimutal average:

- First, to calculate and carry out the azimuthal average of primitive and other various interesting variables expressed in the cartesian frame (u_x, u_y, u_z, u_xu_y,...) and then operate the frame to frame transformation to get the radial and azimuthal components using the cartesian to cylindrical relations for tensors and vectors,
- Or, to convert primitive variables in the cylindrical frame (u_x, u_r, u_θ, u_xu_r,...), to calculate all the interesting terms in the volume thanks to operators ($\overrightarrow{grad}$, div, ...) also expressed in the cylindrical frame, and then only, to carry out the azimuthal average.

The second approach has been developped to operate the azimuthal averaging. Moreover, it is noticeable that this approach enables to access more information as radial and azimuthal contributions to a global term.

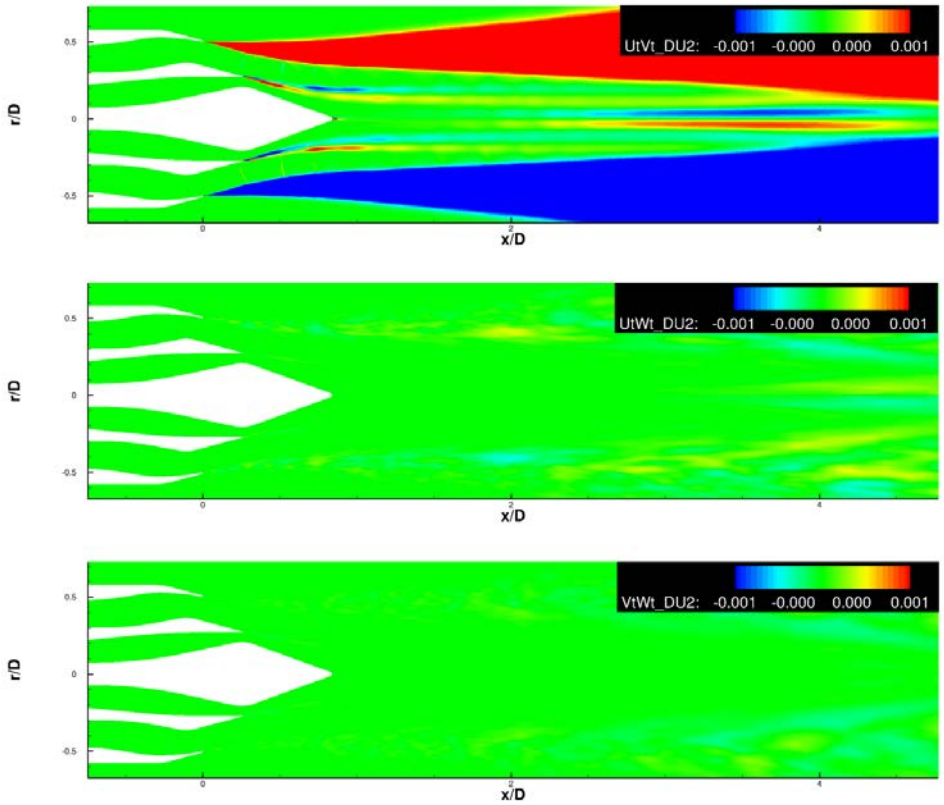

Figure B.2: Comparison of the resolved shear-stress components, azimuthally averaged on 12 ms, of a ZDES calculation. The components $u'w'$ and $v'w'$ are negligible compared to $u'v'$.

Bibliography

[1] A350xwb website. http://www.a350xwb.com/photo-gallery/., consulted 26-05-2016.

[2] Acare vision h2020. http://www.acare4europe.org/sites/acare4europe.org/files/document/Vision%202020_0.pdf, consulted 26-05-2016.

[3] Massachusetts institute of technology website. (from epstein, 1998). http://web.mit.edu/16.unified/www/FALL/thermodynamics/notes/node84.html, consulted 26-05-2016.

[4] Rolls-royce website gallery. https://www.flickr.com/photos/rolls-royceplc/16699406026/in/album-72157658567683743/., consulted 26-05-2016.

[5] Stanford university website. (dennis berry, courtesy of boeing). http://adg.stanford.edu/aa241/propulsion/sfc.html, consulted 26-05-2016.

[6] Virginia tech. university website. http://www.engapplets.vt.edu/fluids/CDnozzle/cdinfo.html, consulted on 05-02-2016.

[7] Andersson, N., Eriksson, L.-E., and Davidson, L. Large-eddy simulation of subsonic turbulent jets and their radiated sound. *AIAA journal 43*, 9 (2005), 1899–1912.

[8] André, B. *Étude expérimentale de leffet du vol sur le bruit de choc de jets supersoniques sous-détendus*. PhD thesis, Ecole Centrale de Lyon, 2012.

[9] André, B., Castelain, T., and Bailly, C. Experimental study of flight effects on screech in underexpanded jets. *Physics of Fluids (1994-present) 23*, 12 (2011), 126102.

[10] André, B., Castelain, T., and Bailly, C. Shock-tracking procedure for studying screech-induced oscillations. *AIAA journal 49*, 7 (2011), 1563–1566.

[11] Antonia, R., and Zhao, Q. Effect of initial conditions on a circular jet. *Experiments in Fluids 31*, 3 (2001), 319–323.

[12] Au, H., and Ko, N. Coaxial jets of different mean velocity ratios, part 2. *Journal of sound and vibration 116*, 3 (1987), 427–443.

[13] Aupoix, B. Modelling of compressibility effects in mixing layers. *Journal of Turbulence 5*, 7 (2004).

[14] Aupoix, B., and Bézard, H. Compressible mixing layers : Data analysis and modelling. *ERCOFTAC Bulletin* (September 2006), 13–17.

[15] Bailly, C., and Bogey, C. Contributions of computational aeroacoustics to jet noise research and prediction. *International Journal of Computational Fluid Dynamics 18*, 6 (2004), 481–491.

[16] Bailly, C., and Comte-Bellot, G. *Turbulence*. Springer International Publishing, 2015.

[17] Balarac, G. *Etude numérique de la dynamique tourbillonnaire et du mélange dans les jets coaxiaux turbulents*. PhD thesis, Institut National Polytechnique de Grenoble, 2006.

[18] Bardina, J., Ferziger, J. H., and Reynolds, W. Improved subgrid-scale models for large-eddy simulation. In *American Institute of Aeronautics and Astronautics, Fluid and Plasma Dynamics Conference, 13th, Snowmass, Colo., July 14-16, 1980, 10 p.* (1980), vol. 1.

[19] Batchelor, G., and Gill, A. E. Analysis of the stability of axisymmetric jets. *Journal of Fluid Mechanics 14*, 04 (1962), 529–551.

[20] Batten, P., Goldberg, U., and Chakravarthy, S. Interfacing statistical turbulence closures with large-eddy simulation. *AIAA journal 42*, 3 (2004), 485–492.

[21] Bellaud, S. *Mesures et analyse détaillée des champs turbulents en couches de mélange annulaires supersoniques*. PhD thesis, Université de Poitiers, 1999.

[22] Bianchi, S., Corsini, A., and Sheard, A. A critical review of passive noise control techniques in industrial fans. *Journal of Engineering for Gas Turbines and Power 136*, 4 (2014), 044001.

[23] Bocquet, S., Sagaut, P., and Jouhaud, J. A compressible wall model for large-eddy simulation with application to prediction of aerothermal quantities. *Physics of Fluids (1994-present) 24*, 6 (2012), 065103.

[24] Bodart, J., and Larsson, J. Wall-modeled large eddy simulation in complex geometries with application to high-lift devices. *Annual Research Briefs, Center for Turbulence Research, Stanford University* (2011).

[25] Bodony, D. The prediction and understanding of jet noise. *Center for Turbulence Research Annual Research Briefs 367377* (2005).

[26] Bodony, D. J., and Lele, S. K. On using large-eddy simulation for the prediction of noise from cold and heated turbulent jets. *Physics of Fluids (1994-present) 17*, 8 (2005), 085103.

[27] Bodony, D. J., and Lele, S. K. Current status of jet noise predictions using large-eddy simulation. *AIAA Journal 46 n2* (2008), 364–380.

[28] Bogdanoff, D. W. Compressibility effects in turbulent shear layers. *AIAA Journal 21*, 6 (1983), 926–927.

[29] Bogey, and Bailly. Computation of a high reynolds number jet and its radiated noise using large eddy simulation based on explicit filtering. *Computers and Fluids* (2006).

[30] Bogey, C. Direct computation of jet noise using large eddy simulation. In *Colloque MUSAF II, Toulouse, September 2013* (2013).

[31] Bogey, C., and Bailly, C. Les of a high reynolds, high subsonic jet : effects of the inflow conditions on flow and noise. *AIAA/CEAS , AIAA 2003-3170* (2003).

[32] Bogey, C., and Bailly, C. Effects of inflow conditions and forcing on subsonic jet flows and noise. *AIAA journal 43*, 5 (2005), 1000–1007.

[33] Bogey, C., and Bailly, C. Investigation of downstream and sideline subsonic jet noise using large eddy simulation. *Theoretical and Computational Fluid Dynamics 20*, 1 (2006), 23–40.

[34] Bogey, C., and Bailly, C. Influence of nozzle-exit boundary-layer conditions on the flow and acoustic field of initially laminar jets. *Journal of Fluid Mechanics 663* (2010), 507–538.

[35] Bogey, C., Bailly, C., and Juvé, D. Noise investigation of a high subsonic, moderate reynolds number jet using a compressible large eddy simulation. *Theoretical and Computational Fluid Dynamics 16*, 4 (2003), 273–297.

[36] Bogey, C., and Marsden, O. Numerical investigation of temperature effects on properties of subsonic turbulent jets. In *19th AIAA/CEAS Aeroacoustics Conference AIAA 2013-2140* (2013), pp. 1–19.

[37] Bogey, C., and Marsden, O. Influence of nozzle-exit boundary-layer profile on high-subsonic jets. In *Proceedings of the 20th AIAA/CEAS Aeroacoustics Conference AIAA 2014-2600* (2014).

[38] Bogey, C., and Marsden, O. Simulations of initially highly disturbed jets with experiment-like exit boundary layers. *AIAA Journal 54*, 2 (2016), 1–14.

[39] Bogey, C., Marsden, O., and Bailly, C. Large-eddy simulation of the flow and acoustic fields of a reynolds number 10^5 subsonic jet with tripped exit boundary layers. *Physics of Fluids (1994-present) 23*, 3 (2011), 035104.

[40] Bogey, C., Marsden, O., and Bailly, C. Effects of moderate reynolds numbers on subsonic round jets with highly disturbed nozzle-exit boundary layers. *Physics of Fluids (1994-present) 24*, 10 (2012), 105107.

[41] Bogey, C., Marsden, O., and Bailly, C. Influence of initial turbulence level on the flow and sound fields of a subsonic jet at a diameter-based reynolds number of 10^5. *Journal of Fluid Mechanics 701* (2012), 352–385.

[42] Boussinesq, M. *Théorie de l'écoulement tourbillonnant et tumultueux des liquides: Étude des régimes graduellement variés*. Gauthier-Villars, 1897.

[43] Brancher, P., Chomaz, J., and Huerre, P. Direct numerical simulations of round jets: vortex induction and side jets. *Physics of Fluids (1994-present) 6*, 5 (1994), 1768–1774.

[44] Brès, G., Bose, S. T., Ham, F. E., and Lele, S. K. Unstructured large eddy simulations for nozzle interior flow modeling and jet noise predictions. *AIAA Paper 2014-2601* (2014).

[45] Brès, G., Ham, F., Nichols, J., and Lele, S. Nozzle wall modeling in unstructured large eddy simulations for hot supersonic jet predictions. *AIAA paper 2013-2142, 19th AIAA/CEAS* (2013).

[46] Brès, G., Jaunet, V., M., L. R., Jordan, P., Colonius, T., and Lele, S. Large eddy simulation for jet noise: the importance of getting the boundary layer right. *AIAA Paper, AIAA 2015-2535, 21st AIAA/CEAS Aeroacoustics Conference, 22-26 June 2015, Dallas, TX* (2015).

[47] Brès, G., Jordan, P., Colonius, T., Le Rallic, M., Jaunet, V., and Lele, S. Large eddy simulation of a mach 0.9 turbulent jet. In *Proceedings of the Summer Program* (2014), p. 221.

[48] Brichet, G., Koenig, M., and Bailly, C. Installation noise of a turbofan jet engine under an airfoil. In *21st AIAA/CEAS Aeroacoustics Conference* (2015), p. 2208.

[49] Bridges, J., and Hussain, A. Roles of initial condition and vortex pairing in jet noise. *Journal of Sound and Vibration 117*, 2 (1987), 289–311.

[50] Bridges, J., and Wernet, M. Measurements of the aeroacoustic sound source in hot jets. *AIAA paper 3130* (2003), 2003.

[51] Bridges, J., Wernet, M., and Brown, C. Control of jet noise through mixing enhancement. *NASA Report NASA/TM2003-212335* (2003).

[52] Bridges, J., and Wernet, M. P. Cross-stream piv measurements of jets with internal lobed mixers. *AIAA paper 2004-2896* (2004).

[53] Bridges, J., and Wernet, M. P. Effect of temperature on jet velocity spectra. *AIAA paper 2007-3628* (2007).

[54] Brown, G. L., and Roshko, A. On density effects and large structure in turbulent mixing layers. *Journal of Fluid Mechanics 64*, 04 (1974), 775–816.

[55] Brunet, V. Random flow generation technique for civil aircraft jet simulations with zdes approach. *Progress in Hybrid RANS-LES Modelling NNFM, vol. 117, Springer, Heidelberg (2012)* (2012), pp. 193–204.

[56] Brunet, V. Random turbulent flow generation coupled with zdes for civil aircraft jet configurations. In *30th AIAA Applied Aerodynamics Conference* (2012), no. 2012-2896.

[57] Brunet, V., Molton, P., Bezard, H., and Deck, S. Advanced experimental and numerical investigations of an aircraft powerplant configuration. *AIAA paper 2010-4814, 28th AIAA Applied Aerodynamics Conference, Chicago* (2010).

[58] Br G., Nichols, J., Lele, S., and Ham, F. Towards best practices for jet noise predictions with unstructured large eddy simulations. –.

[59] Bui, T. T. A parallel, finite-volume algorithm for large-eddy simulation of turbulent flows. *Computers & fluids 29*, 8 (2000), 877–915.

[60] Cai, X., Ladeinde, F., Reba, R., and Schinkler, R. Hybrid les/rans calculation of high speed jet noise. *AIAA paper, AIAA 2007-3870* (2007).

[61] Cambier, L., Heib, S., and Plot, S. The onera elsa cfd software: input from research and feedback from industry. *Mechanics & Industry 14*, 3 (2013), 159–174.

[62] Caruelle, B., and Ducros, F. Detached-eddy simulations of attached and detached boundary layers. *International Journal of Computational Fluid Dynamics 17*, 6 (2003), 433–451.

[63] Casalino, D., and Lele, S. Lattice-boltzmann simulation of coaxial jet noise generation. In *CTR, Proceedings of the Summer Program* (2014), p. 231.

[64] Chauvet, N. *Simulation numérique et analyse physique d'un jet propulsif contrôlé par des injections radiales*. PhD thesis, UPMC, 2007.

[65] Chauvet, N., Deck, S., and Jacquin, L. Numerical study of mixing enhancement in a supersonic round jet. *AIAA Journal 45*, 7 (2007), 1675–1687.

[66] Chauvet, N., Deck, S., and Jacquin, L. Shock patterns in a slightly underexpanded sonic jet controlled by radial injections. *Physics of Fluids (1994-present) 19*, 4 (2007), 048104.

[67] Chauvet, N., Deck, S., and Jacquin, L. Zonal detached eddy simulation of a controlled propulsive jet. *AIAA journal 45*, 10 (2007), 2458–2473.

[68] Choi, H., and Moin, P. Grid-point requirements for large eddy simulation: Chapmans estimates revisited. *Physics of Fluids 24*, 011702 (2012).

[69] Choi, H., Moin, P., and Kim, J. Direct numerical simulation of turbulent flow over riblets. *Journal of fluid mechanics 255* (1993), 503–539.

[70] Choi, M.-R., and Lele, S. K. Prediction of shock-cell structure using parabolized stability equations. *AIAA paper 2001-744* (2001).

[71] Cohen, J., and Wygnanski, I. The evolution of instabilities in the axisymmetric jet. part 1. the linear growth of disturbances near the nozzle. *Journal of Fluid Mechanics 176* (1987), 191–219.

[72] Coles, D. Prospects for useful research on coherent structure in turbulent shear flow. *Proceedings of the Indian Academy of Sciences Section C: Engineering Sciences 4*, 2 (1981), 111–127.

[73] Constantinescu, G., and Lele, S. Large eddy simulation of a near sonic turbulent jet and its radiated noise. *AIAA paper 376* (2001), 2001.

[74] Crighton, D. Acoustics as a branch of fluid mechanics. *Journal of Fluid Mechanics 106* (1981), 261–298.

[75] Crighton, D., and Gaster, M. Stability of slowly diverging jet flow. *Journal of Fluid Mechanics 77*, 02 (1976), 397–413.

[76] Crow, and Champagne. Orderly structure in jet turbulence. *Boeing Technical Note* (1971).

[77] Daude, F., Mary, I., and Comte, P. Implicit time integration method for les of complex flows. *ERCOFTAC SERIES 10* (2006), 771.

[78] Debonis, J. Progress toward large-eddy simulations for prediction of realistic nozzle systems. *Journal of Propulsion and Power 23*, 5 (2007), 971–980.

[79] Debonis, J. R., and Scott, J. N. Large-eddy simulation of a turbulent compressible round jet. *AIAA journal 40*, 7 (2002), 1346–1354.

[80] Deck, S. Zonal-detached eddy simulation of the flow around a high-lift configuration. *AIAA Journal Vol. 43, No. 11* (2005), 2372–2384.

[81] Deck, S. Recent improvements in the zonal detached eddy simulation (zdes) formulation. *Theoretical Computational Fluid Dynamics 26* (2012), 523–550.

[82] Deck, S., Gand, F., Brunet, V., and Ben Khelil, S. High-fidelity simulations of unsteady civil aircraft aerodynamics: stakes and perspectives. application of zonal detached eddy simulation. *Philosophical Transactions of the Royal Society of London. A 372*, 2022 (2014).

[83] Deck, S., and Laraufie, R. Numerical investigation of the flow dynamics past a three-element aerofoil. *Journal of Fluid Mechanics 732* (2013), 401–444.

[84] Deck, S., Renard, N., Laraufie, R., and Sagaut., P. Zonal detached eddy simulation (zdes) of a spatially developing flat plate turbulent boundary layer over the reynolds number range $3150 \leq Re_\theta \leq 14000$. *Physics of Fluids 26*, 025116 (2014).

[85] Deck, S., Weiss, P., Pamies, M., and Garnier, E. On the use of stimulated detached eddy simulation (sdes) for spatially developing boundary layers. In *Advances in Hybrid RANS-LES Modelling*. Springer, 2008, pp. 67–76.

[86] Deck, S., Weiss, P.-É., Pamies, M., and Garnier, E. Zonal detached eddy simulation of a spatially developing flat plate turbulent boundary layer. *Computers & Fluids 48*, 1 (2011), 1–15.

[87] Dimotakis, P. Turbulent free shear layer mixing and combustion. *High Speed Flight Propulsion Systems 137* (1991), 265–340.

[88] Dimotakis, P. E. Two-dimensional shear-layer entrainment. *AIAA journal 24*, 11 (1986), 1791–1796.

[89] Drubka, R. E. Instabilities in near field of turbulent jets and their dependence on initial conditions and reynolds number. *PhD thesis from Inst. Tech. of Chicago, Illinois* (1981).

[90] Drubka, R. E., and Nagib, H. M. Instabilities in near field of turbulent jets and their dependence on initial conditions and reynolds number. Tech. rep., DTIC Document, 1981.

[91] Du, Y., and Morris, P. J. The separation of radiating and non-radiating near-field pressure fluctuations in supersonic jets. *Journal of Sound and Vibration 355* (2015), 172–187.

[92] Eastwood, S., and Tucker, P. Hybrid les-rans of complex geometry jets. *International Journal of Aeroacoustics 10*, 5-6 (2011), 659–684.

[93] Eastwood, S., Tucker, P., and Xia, H. Large-eddy simulations and measurements of a small-scale high-speed coflowing jet. *AIAA Journal 48* (2010), 963–974.

[94] Edwards, J., and Liou, M. S. Low-diffusion flux-splitting methods for flows at all speeds. *AIAA Journal 36*, 9 (1998), 1610–1617.

[95] Elliott, G. S., Samimy, M., and Arnette, S. A. The characteristics and evolution of large-scale structures in compressible mixing layers. *Physics of Fluids (1994-present) 7*, 4 (1995), 864–876.

[96] Forsythe, J., Fremeaux, C., and Hall, R. . Calculation of static and dynamic stability derivatives of the f/a-18e in abrupt wing stall using rans and des. In *ICCFD3, Toronto, Canada, July* (2004).

[97] Fosso-Pouangué, A., Sanjosé, M., and Moreau, S. Jet noise simulation with realistic nozzle geometries using fully unstructured les solver. *AIAA paper 2012-2190* (2012).

[98] Fosso Pouangué, A., Sanjosé, M., Moreau, S., Daviller, G., and Deniau, H. Subsonic jet noise simulations using both structured and unstructured grids. *AIAA Journal 53*, 1 (2015), 55–69.

[99] Freund, J. B., Lele, S. K., and Moin, P. Compressibility effects in a turbulent annular mixing layer. part 1. turbulence and growth rate. *Journal of Fluid Mechanics 421* (2000), 229–267.

[100] Freund, J. B., Moin, P., and Lele, S. K. Compressibility effects in a turbulent annular mixing layer. part 2. mixing of a passive scalar. *Journal of Fluid Mechanics 421* (2000), 269–292.

[101] Gand, F., Brunet, V., and Mancel, G. Zonal detached eddy simulation (zdes) using turbulent inflow and high order schemes: Application to jet flows. *Progress in Hybrid RANS-LES Modelling, Springer International Publishing. 130* (2015), 141–152.

[102] Giner, P. *Simulation numérique des jets et sillages instationnaires dans la conception de formes aérodynamiques, 1, 2, 10, 16, 8.* PhD thesis, ISAE - Universite de Toulouse, 2012.

[103] Giner, P., Sylla, A., Dezitter, F., Aupoix, B., and Brunet, V. Attempt to improve the prediction of engine jet development. *4th european conference for aerospace sciences* (2011).

[104] Girard, S., Collin, E., Delville, J., Bonnet, J. P., Benyahia, A., Fourment, C., Lebedev, A., Foulon, H., Braud, P., Royer, A., Laurent, P., and Huet, L. Etude adynamique de jets coaxiaux. *Technical report CEAT-LEA Poitiers, France* (2009).

[105] Goebel, S. G., and Dutton, J. C. Experimental study of compressible turbulent mixing layers. *AIAA journal 29*, 4 (1991), 538–546.

[106] Gutmark, E., and Ho, C.-M. Preferred modes and the spreading rates of jets. *Physics of Fluids (1958-1988) 26*, 10 (1983), 2932–2938.

[107] Hall, J. L., Dimotakis, P. E., and Rosemann, H. Experiments in non-reacting compressible shear layers. *AIAA Journal 31*, 12 (1993), 2247–2254.

[108] Harper-Bourne, M. Jet noise measurements: past and present. *International Journal of Aeroacoustics 9*, 4-5 (2010), 559–588.

[109] Harper-Bourne, M., and Fisher, M. The noise from shock waves in supersonic jets. *AGARD Noise Mech. 13 p(SEE N 74-22640 14-02)* (1974).

[110] Harten, A. High resolution schemes for hyperbolic conservation laws. *Journal of computational physics 49*, 3 (1983), 357–393.

[111] Hill Jr, W. G., Jenkins, R. C., and Gilbert, B. L. Effects of the initial boundary-layer state on turbulent jet mixing. *AIAA journal 14*, 11 (1976), 1513–1514.

[112] Ho, C., and Huerre, P. Pertubed free shear layers. *Annual Review of Fluid Mechanics* (1984), pp. 365–424.

[113] Ho, C.-M., and Hsiao, F.-B. Evolution of coherent structures in a lip jet. In *Structure of Complex Turbulent Shear Flow*. Springer, 1983, pp. 121–136.

[114] Huang, S., Li, Q., and Wu, J. A general inflow turbulence generator for large eddy simulation. *Journal of Wind Engineering and Industrial Aerodynamics 98*, 10 (2010), 600–617.

[115] Huber, J., Drochon, G., Pintado-Peno, A., Cléro, F., and Bodard, G. Large-scale jet noise testing, reduction and methods validation exejet: 1. project overview and focus on installation. In *Proceedings of the 20th AIAA/CEAS Aeroacoustics Conference* (2014), pp. 1–17.

[116] Husain, Z., and Hussain, A. Axisymmetric mixing layer: influence of the initial and boundary conditions. *AIAA Journal 17*, 1 (1979), 48–55.

[117] Hussain, A., and Zedan, M. Effects of the initial condition on the axisymmetric free shear layer: Effect of the initial fluctuation level. *Physics of Fluids (1958-1988) 21*, 9 (1978), 1475–1481.

[118] Hussain, A., and Zedan, M. Effects of the initial condition on the axisymmetric free shear layer: Effects of the initial momentum thickness. *Physics of Fluids (1958-1988) 21*, 7 (1978), 1100–1112.

[119] Hussain, A. K. M. F., and Zaman, K. The 'preferred mode' of the axisymmetric jet. *Journal of Fluid Mechanics 110* (1981), pp. 39–71.

[120] Jameson, A., Schmidt, W., and Turkel, E. Numerical solutions of the euler equations by finite volume methods using runge-kutta time-stepping schemes. *AIAA paper 1981-1259* (1981).

[121] Janardan, B., Yamamoto, K., Majjigi, R., and Brausch, J. Experimental investigation of shock-cell noise reduction for dual-stream nozzles in simulated flight. *Final Report General Electric Co., Cincinnati, OH. Aircraft Engine Business Group. 1* (1984).

[122] Jarrin, N., Benhamadouche, S., Laurence, D., and Prosser, R. A synthetic-eddy-method for generating inflow conditions for large-eddy simulations. *International Journal of Heat and Fluid Flow 27*, 4 (2006), 585–593.

[123] Jarrin, N., Prosser, R., Uribe, J.-C., Benhamadouche, S., and Laurence, D. Reconstruction of turbulent fluctuations for hybrid rans/les simulations using a synthetic-eddy method. *International Journal of Heat and Fluid Flow 30*, 3 (2009), 435–442.

[124] Jothi, T. J. S., and Srinivasan, K. Role of initial conditions on noise from underexpanded pipe jets. *Physics of Fluids 21 (066103)* (2009).

[125] Keating, A., Piomelli, U., Balaras, E., and Kaltenbach, H. A priori and a posteriori tests of inflow conditions for large-eddy simulation. *Physics of Fluids 16*, 12 (2004), pp. 4696–4712.

[126] Kibens, V. The limit of initial shear layer influence on jet development. *AIAA paper 81-1960* (1981).

[127] Kim, Afshari, Bodony, and Freund. Les investigation of a mach 1.3 jet with and without plasma actuators. *AIAA/ASME* (2009).

[128] Kim, J., and Choi, H. Large eddy simulation of a circular jet: effect of inflow conditions on the near field. *Journal of Fluid Mechanics 620* (2009), 383–411.

[129] Kleinstein, G. Mixing in turbulent axially symmetric free jets. *Journal of Spacecraft and Rockets 1*, 4 (1964), 403–408.

[130] Ko, and Kwan. The initial region of subsonic coaxial jets. *Journal of Fluid Mechanics 73* (1976), 305–332.

[131] Ko, N., and Au, H. Initial region of subsonic coaxial jets of high mean-velocity ratio. *Journal of Fluids Engineering 103*, 2 (1981), 335–338.

[132] Ko, N., and Au, H. Spreading rate and reattachment of coaxial jets of high mean-velocity ratio. *Journal of Fluids Engineering 104*, 3 (1982), 400–401.

[133] Ko, N., and Au, H. Coaxial jets of different mean velocity ratios. *Journal of Sound and Vibration 100*, 2 (1985), 211–232.

[134] Konrad, J. H. *An experimental investigation of mixing in two-dimensional turbulent shear flows with applications to diffusion-limited chemical reactions*. PhD thesis, California Institute of Technology, 1977.

[135] Kraichnan, R. H. Diffusion by a random velocity field. *Physics of Fluids 13*, 1 (1970), pp. 22–31.

[136] Kwan, A., and Ko, N. The initial region of subsonic coaxial jets. part 2. *Journal of Fluid Mechanics 82*, 02 (1977), 273–287.

[137] Laraufie, R. *Simulations avancées de turbulence pariétale ut nombre de Reynolds sur des géométries curvilignes par une approche hybride RANS/LES*. PhD thesis, ONERA/UPMC, 2012.

[138] Laraufie, R., Deck, S., and Sagaut, P. A dynamic forcing method for unsteady turbulent inflow conditions. *Journal of Computational Physics 230*, 23 (2011), 8647–8663.

[139] Lau, J. Effects of exit mach number and temperature on mean-flow and turbulence characteristics in round jets. *Journal of Fluid Mechanics 105* (1981), 193–218.

[140] Lau, J. C., Morris, P. J., and Fisher, M. J. Measurements in subsonic and supersonic free jets using a laser velocimeter. *Journal of Fluid Mechanics 93*, 01 (1979), 1–27.

[141] Le Bras, S., Deniau, H., Bogey, C., and Daviller, G. Development of compressible large-eddy simulations combining high-order schemes and wall modeling. In *21st AIAA/CEAS Aeroacoustics Conference* (2015), p. 3135.

[142] Lesieur, M. *Turbulence in fluids*. Kluwer Academic Publishers, 1997.

[143] Lew, P., Blaisdell, G., and Lyrintzis, A. Recent progress of hot jet aeroacoustics using 3-d large eddy simulation. *AIAA paper 2005-3084* (2005).

[144] Liepmann, D., and Gharib, M. The role of streamwise vorticity in the near-field entrainment of round jets. *Journal of Fluid Mechanics 245* (1992), 643–668.

[145] Liou, M. S. A sequel to AUSM: AUSM+. *Journal of Computational Physics 129* (1996), 364–382.

[146] Liou, M. S. A sequel to AUSM, part ii: AUSM+ - UP for all speeds. *Journal of Computational Physics 214* (2006), 137–170.

[147] Liu, J., Kailasanath, K., Boris, J., Heeb, N., Munday, D., and Gutmark, E. Effect of the initial turbulence level on an underexpanded supersonic jet. *AIAA journal 51*, 3 (2012), 741–745.

[148] Lund, T. S., Wu, X., and Squires, K. D. Generation of turbulent inflow data for spatially-developing boundary layer simulations. *Journal of Computational Physics 140*, 2 (1998), 233–258.

[149] Marty, J. Numerical investigations of separation-induced transition on high-lift low-pressure turbine using rans and les methods. *Proceedings of the Institution of Mechanical Engineers, Part A: Journal of Power and Energy 228*, 8 (2014), 924–952.

[150] Mary, I. *Méthode de Newton approchée pour le calcul d'écoulements instationnaires comportant des zones ès faibles nombres de Mach.* PhD thesis, Université Paris Sud Orsay, 1999.

[151] Mary, I., and Sagaut, P. Large eddy simulation of flow around an airfoil near stall. *AIAA Journal 40*, 6 (2002), 1139–1145.

[152] Menter, F., and Kuntz, M. Adaptation of eddy-viscosity turbulence models to unsteady sseparate flow behind vehicles. *Symposium "The aerodynamics of heavy vehicles: trucks, buses and trains." Monterey, USA, DEC. 2-6, 2002. R. Mc-Callen, F. Browand and J. Ross, eds. Springer* (2004), 339–352.

[153] Menter, F., Kuntz, M., and Bender, R. A scale-adaptative simulation model for turbulent flow predictions. *AIAA Paper AIAA Paper 03-0767, 41th AIAA ASME, Reno, Nevada, January* (2003).

[154] Michalke, A. On the inviscid instability of the hyperbolictangent velocity profile. *Journal of Fluid Mechanics 19*, 04 (1964), 543–556.

[155] Michalke, A. On spatially growing disturbances in an inviscid shear layer. *Journal of Fluid Mechanics 23*, 03 (1965), 521–544.

[156] Michalke, A. Survey on jet instability theory. *Progress in Aerospace Sciences 21* (1984), 159–199.

[157] Michalke, A., and Hermann, G. On the inviscid instability of a circular jet with external flow. *Journal of Fluid Mechanics 114* (1982), 343–359.

[158] Morris, P. Viscous stability of compressible axisymmetric jets. *AIAA Journal 21*, 4 (1983), pp. 481–482.

[159] Morris, P. J., and Zaman, K. B. Velocity measurements in jets with application to noise source modeling. *Journal of sound and vibration 329*, 4 (2010), 394–414.

[160] MQ Zaman, K., and Dahl, M. Noise and spreading of subsonic coannular jets-comparison with single equivalent jet. *AIAA journal 45*, 11 (2007), 2661–2670.

[161] Murakami, E., and Papamoschou, D. Mean flow development in dual-stream compressible jets. *AIAA journal 40*, 6 (2002), 1131–1138.

[162] Pack, D. C. A note on prandtl´s formula for the wave-length of a supersonic gas jet. *The quaterly journal of mechanics and applied mathematics 3*, 2 (1950), 173–181.

[163] Pamies, M., Weiss, P.-E., Garnier, E., Deck, S., and Sagaut, P. Generation of synthetic turbulent inflow data for large eddy simulation of spatially evolving wall-bounded flows. *Physics of Fluids (1994-present) 21*, 4 (2009), 045103.

[164] Panda, and Seasholtz. Measurement of shock structure and shockvortex interaction in underexpanded jets using rayleigh scattering. *Physics of Fluids* (1999).

[165] Panda, J., Seasholtz, R., and Elam, K. Investigation of noise sources in high-speed jets via correlation measurements. *Journal of Fluid Mechanics 537* (2005), 349–385.

[166] Pantano, C., and Sarkar, S. A study of compressibility effects in the high-speed turbulent shear layer using direct simulation. *Journal of Fluid Mechanics 451* (2002), 329–371.

[167] Papamoschou, D., and Roshko, A. The compressible turbulent shear layer : an experimental study. *Journal of Fluid Mechanics 197* (1988), 453–477.

[168] Petersen, R., and Samet, M. On the preferred mode of jet instability. *Journal of Fluid Mechanics 194* (1988), 153–173.

[169] Ponton, M. K., and Seiner, J. M. The effects of nozzle exit lip thickness on plume resonance. *Journal of Sound and Vibration 154*, 3 (1992), 531–549.

[170] Pope, S. B. Turbulent flows. p.104, 2001.

[171] Powell, A. On the mechanism of chocked jet noise. *Proceedings of the Physical Society*, B66 (1953), 316–327.

[172] Prandtl, L. über die stationn wellen in einem gasstrahl. *Physikalische Zeitschrift 5* (1904), 599–601.

[173] Ramamurti, R., Corrigan, A., Liu, J., Kailasanath, K., and Henderson, B. Jet noise simulations for complex nozzle geometries. *International Journal of Aeroacoustics 14*, 7 (2015), 947–975.

[174] Raman, G. Cessation of screech in underexpanded jets. *Journal of Fluid Mechanics 336* (1997), 69–90.

[175] Raman, G. Supersonic jet screech: half-century from powell to the present. *Journal of Sound and Vibration 225*, 3 (1999), 543–571.

[176] Raman, G., Rice, E., and Reshotko, E. Mode spectra of natural disturbances in a circular jet and the effect of acoustic forcing. *Experiments in fluids 17*, 6 (1994), 415–426.

[177] Raman, G., Zaman, K. B., and Rice, E. J. Initial turbulence effect on jet evolution with and without tonal excitation. *Physics of Fluids A: Fluid Dynamics (1989-1993) 1*, 7 (1989), 1240–1248.

[178] Rhie, C., and Chow, W. Numerical study of the turbulent flow past an airfoil with trailing edge separation. *AIAA journal 21*, 11 (1983), 1525–1532.

[179] Roe, P. L. Characteristic-based schemes for the euler equations. *Annual Review of Fluid Mechanics 18*, 1 (1986), 337–365.

[180] Roidl, B., Meinke, M., and Schröder, W. A zonal rans–les method for compressible flows. *Computers & Fluids 67* (2012), 1–15.

[181] Sagaut, P. *Large eddy simulation for incompressible flows: an introduction.* Springer Science & Business Media, 2006.

[182] Sagaut, P., Deck, S., and Terracol, M. *Multiscale and Multiresolution Approaches in Turbulence, LES, DES and Hybrid RANS/LES Methods: Applications and Guidelines (2nd Edition).* Imperial College Press, London UK, 2013.

[183] Saiyed, N. H., Mikkelsen, K. L., and Bridges, J. E. Acoustics and thrust of quiet separate-flow high-bypass-ratio nozzles. *AIAA journal 41*, 3 (2003), 372–378.

[184] Sanjosé, M., Fosso-Pouangué, A., Moreau, S., Wang, G., and Padois, T. Unstructured les of the baseline exejet dual-stream jet. *AIAA paper 3037* (2014).

[185] Saxena, S., and Morris, P. J. Noise predictions for high subsonic single and dual-stream jets in flight. *AIAA/CEAS, AIAA 2012-2082* (2012).

[186] Schadow, K., Gutmark, E., and Wilson, K. Compressible spreading rates of supersonic coaxial jets. *Experiments in fluids 10*, 2-3 (1990), 161–167.

[187] Shur, M., Spalart, P., and Strelets, M. Noise prediction for increasingly complex jets. part i: Methods and tests. *International Journal of Aeroacoustics 4* (2005), 213–246.

[188] Shur, M., Spalart, P., and Strelets, M. Further steps in les-based noise predicition for complex jets. *AIAA paper 2006-485, AIAA 44th Aerospace Sciences Meeting and Exhibit, 9-12 January, 2006, Reno, Nevada* (2006).

[189] Shur, M., Spalart, P., and Strelets, M. A hybrid rans-les approach with delayed-des and wall-modelled les capabilities. *International Journal of Heat and Fluid Flow 1638-1649* (2008).

[190] Shur, M., Spalart, P. R., Strelets, M., and Travin, A. A rapid and accurate switch from rans to les in boundary layers using an overlap region. *Flow, turbulence and combustion 86*, 2 (2011), 179–206.

[191] Shur, M. L., Spalart, P. R., and Strelets, M. K. Noise prediction for underexpanded jets in static and flight conditions. *AIAA Journal 49*, 9 (2011), 2000–2017.

[192] Shur, M. L., Spalart, P. R., Strelets, M. K., and Travin, A. K. Synthetic turbulence generators for rans-les interfaces in zonal simulations of aerodynamic and aeroacoustic problems. *Flow, turbulence and combustion 93*, 1 (2014), 63–92.

[193] Simon, F. *Simulations numérique hybrid RANS/LES de l'aérodynamique des projectiles et application au contrle des écoulements.* PhD thesis, UPMC, 2007.

[194] Simon, F., Deck, S., Guillen, P., Sagaut, P., and Merlen, A. Numerical simulation of the compressible mixing layer past an axisymmetric trailing edge. *Journal of Fluid Mechanics 591* (2007), 215–253.

[195] Slessor, M., Zhuang, M., and Dimotakis, P. Turbulent shear-layer mixing: growth-rate compressibility scaling. *Journal of Fluid Mechanics 414* (2000), 35–45.

[196] Smagorinsky, J. General circulation experiments with the primitive equations: I. the basic experiment*. *Monthly weather review 91*, 3 (1963), 99–164.

[197] Smirnov, A., Shi, S., and Celik, I. Random flow generation technique for large eddy simulations and particle-dynamics modeling. *Journal of Fluids Engineering 123*, 2 (2001), pp. 359–371.

[198] Spalart, P. Trends in turbulence treatments. *AIAA Paper AIAA paper 00-2306, Fluids 2000, Denver, CO, USA* (2000).

[199] Spalart, P. Young's person's guide to detached eddy simulation grids. *NASA Report Technical Report CR-2001-211032, July* (2001).

[200] Spalart, P., and Allmaras, S. A one equation turbulence model for aerodynamics flows. *La Recherche Aspatiale 1* (1994), 5–21.

[201] Spalart, P., Deck, S., Shur, M., Squires, K., Strelets, M., and Travin, A. A new version of detached-eddy simulation, resistant to ambiguous grid densities. *Theoretical and Computational Fluid Dynamics 20* (2006), 181–195.

[202] Spalart, P., Jou, W., Strelets, M., and Allmaras, S. Comments on the feasibility of les for wings, and on a hybrid rans/les approach. *Advances in LES/DNS, First AFOSR International Conference on DNS/LES. Greyden Press, Louisiana Tech University.* (1997).

[203] Spalding, D. A single formula for the law of the wall. *Journal of Applied Mechanics 28*, 3 (1961), 455–458.

[204] Stanley, S., and Sarkar, S. Influence of nozzle conditions and discrete forcing on turbulent planar jets. *AIAA journal 38*, 9 (2000), 1615–1623.

[205] Tabor, G., and Baba-Ahmadi, M. Inlet conditions for large eddy simulation: A review. *Computers & Fluids 39*, 4 (2010), pp. 553567.

[206] Tam, C., Seiner, J., and Yu, J. Proposed relationship between broadband shock associated noise and screech tones. *Journal of Sound and Vibration 110*, 2 (1986), 309–321.

[207] Tam, C. K. On the noise of a nearly ideally expanded supersonic jet. *Journal of Fluid Mechanics 51*, 01 (1972), 69–95.

[208] Tam, C. K., Jackson, J. A., and Seiner, J. A multiple-scales model of the shock-cell structure of imperfectly expanded supersonic jets. *Journal of Fluid Mechanics 153* (1985), 123–149.

[209] Tam, C. K., Pastouchenko, N. N., and Viswanathan, K. Broadband shock-cell noise from dual stream jets. *Journal of Sound and Vibration 324*, 3 (2009), 861–891.

[210] Tanna, H. An experimental study of jet noise part ii: shock associated noise. *Journal of Sound and Vibration 50*, 3 (1977), 429–444.

[211] Tanna, H. Coannular jets - are they really quiet and why? *Journal of Sound and Vibration 72*, 1 (1980), 97–118.

[212] Toubin, H. *Prediction and Phenomenological Breakdown of Drag for Unsteady Flows*. PhD thesis, University Pierre et Marie Curie, 2015.

[213] Tyacke, J. C., Mahak, M., and Tucker, P. G. Les of jet flow and noise with internal and external geometry features. *53rd AIAA Aerospace Sciences Meeting, 5-9 january 2015, AIAA 2015-0503* (2015).

[214] Uzun, A., Bin, J., and Hussaini, M. Y. High-fidelity numerical simulation of a chevron nozzle jet flow. *International Journal of Aeroacoustics 10*, 5-6 (2011), 531–564.

[215] Uzun, A., and Hussaini, M. Y. Investigation of high frequency noise generation in the near-nozzle region of a jet using large eddy simulation. *Theoretical and Computational Fluid Dynamics 21*, 4 (2007), 291–321.

[216] Uzun, A., and Hussaini, M. Y. High-fidelity numerical simulations of a round nozzle jet flow. *AIAA/CEAS Paper 2010-4016* (2010).

[217] Uzun, A., Lyrintzis, A., and Blaisdell, G. Coupling of integral acoustics methods with les for jet noise prediction. *International Journal of Aeroacoustics 3*, 4 (2004), 297–346.

[218] Van Leer, B. Towards the ultimate conservative difference scheme. v. a second-order sequel to godunov's method. *Journal of computational Physics 32*, 1 (1979), 101–136.

[219] Verhelst, S., and Wallner, T. Hydrogen-fueled internal combustion engines. *Progress in Energy and Combustion Science 35*, 6 (2009), 490–527.

[220] Verrière, J., Gand, F., and Deck, S. Zonal detached eddy simulations of a dual-stream jet. *AIAA Journal submitted Nov 2015, accepted May 2016* (2015).

[221] Viswanathan, and Clark. Effect of nozzle internal contour on jet aeroacoustics. *AIAA paper* (2004).

[222] Viswanathan, K. Parametric study of noise from dual-stream nozzles. *Journal of Fluid Mechanics 521* (2004), 35–68.

[223] Viswanathan, K., Czech, M., and Lee, I.-C. Towards prediction of dual-stream jet noise: Database generation. *AIAA journal 49*, 12 (2011), 2695–2712.

[224] Viswanathan, K., Shur, M., Spalart, P., and Strelets, M. Comparisons between experiment and large-eddy simulation for jet noise. *AIAA Journal 45*, 8 (2007), 1952–1966.

[225] Viswanathan, K., Shur, M., Spalart, P., and Strelets, M. Flow and noise predictions for single and dual-stream beveled nozzles. *AIAA journal 46*, 3 (2008), 601–626.

[226] Viswanathan, K., Spalart, P., Czech, M. J., Garbaruk, A., and Shur, M. Tailored nozzles for jet plume control and noise reduction. *AIAA Journal 50*, 10 (2012), 2115–2134.

[227] Vreman, A. An eddy-viscosity subgrid-scale model for turbulent shear flow: Algebraic theory and applications. *Physics of Fluids (1994-present) 16*, 10 (2004), 3670–3681.

[228] Vreman, A., Sandham, N., and Luo, K. Compressible mixing layer growth rate and turbulence characteristics. *Journal of Fluid Mechanics 320* (1996), 235–258.

[229] Vreman, B., Geurts, B., and Kuerten, H. A priori tests of large eddy simulation of the compressible plane mixing layer. *Journal of Engineering Mathematics 29*, 4 (1995), 299–327.

[230] Vreman, B., Geurts, B., and Kuerten, H. Large-eddy simulation of the turbulent mixing layer. *Journal of Fluid Mechanics 339* (1997), 357–390.

[231] Vuillot, F., Lupoglazoff, N., and Huet, M. Effect of a pylon on double stream jet noise from hybrid caa computations. In *16th AIAA/CEAS Aeroacoustics conference, AIAA-2010-4029* (2010).

[232] Wang, P., and McGuirk, J. J. Large eddy simulation of supersonic jet plumes from rectangular con-di nozzles. *International Journal of Heat and Fluid Flow 43* (2013), 62–73.

[233] Weiss, P.-E. *Simulation numérique et analyse physique d'un écoulement d'arrière-corps axisymétrique et application au contrôle des charges latérales.* PhD thesis, Université Pierre et Marie Curie, Paris 6, 2010.

[234] WITZE, P. . Centerline velocity decay of compressible free jets. *AIAA journal 12*, 4 (1974), 417–418.

[235] Xia, Karabasov, Graham, Tucker, Dowling, Depuru, and Hynes. Hybrid rans-les modeling of chevron nozzles with prediction of far field sound. *AIAA/ASME*, 2011-21 (2011).

[236] Xia, H., Tucker, P., and Eastwood, S. Towards jet flow les of conceptual nozzles for acoustic predictions. *AIAA/ASME, AIAA 2008-10* (2008).

[237] Xia, H., Tucker, P., Eastwood, S., and Mahak, M. The influence of geometry on jet plume development. *Progress in Aerospace Sciences 52* (2012), 56–66.

[238] Xiao, F., Dianat, M., and Mcguirk, J. A recycling/rescaling method for les inlet condition generation. In *8th International ERCOFTAC Symposium (ETMM8), Marseille, France, June* (2010), pp. 9–11.

[239] Xu, G., and Antonia, R. Effect of different initial conditions on a turbulent round free jet. *Experiments in Fluids 33*, 5 (2002), 677–683.

[240] Zaman, K. Far-field noise of a subsonic jet under controlled excitation. *J. Fluid Mech 152* (1985), 83–111.

[241] Zaman, K. Effect of initial boundary-layer state on subsonic jet noise. *AIAA journal 50*, 8 (2012), 1784–1795.

[242] Zaman, K., and Hussain, A. K. M. F. Vortex pairing in a circular jet under controlled excitation. part 1. general jet response. *Journal of Fluid Mechanics 101*, 3 (1980), pp. 449– 491.

[243] Zaman, K., and Hussain, A. K. M. F. Turbulence suppression in free shear flows by controlled excitation. *Journal of Fluid Mechanics 103* (February 1981), pp. 133–159.

[244] Zeman, O. Dilatation dissipation: the concept and application in modeling compressible mixing layers. *Physics of Fluids A: Fluid Dynamics (1989-1993) 2*, 2 (1990), 178–188.

[245] Zeman, O. On the decay of compressible isotropic turbulence. *Physics of Fluids A: Fluid Dynamics (1989-1993) 3*, 5 (1991), 951–955.

[246] Zhao, W., Frankel, S., and Mongeau, L. Large eddy simulations of sound radiation from subsonic turbulent jets. *AIAA journal 39*, 8 (2001), 1469–1477.

List of Figures

List of Tables

Jonas Verrière **September 23, 2016**

Sujet : Simulations ZDES de jets propulsifs: Analyse physique et influence de la turbulence amont

Résumé : Ce travail porte sur l'évaluation de la méthode ZDES pour la simulation de jets propulsifs. L'analyse se concentre sur le positionnement des cellules de chocs et le développement des couches de mélange d'une tuyère double-flux avec plug externe, typique des moteurs d'avions modernes. Les champs statistiques sont comparés aux résultats expérimentaux et discutés en termes de grandeurs moyennes, fluctuantes et dans le domaine fréquentiel. L'intérêt d'utiliser un schéma spatial peu dissipatif ainsi qu'une échelle de longueur sous-maille basée sur la vorticité locale est mis en évidence, notamment pour le dévelopement de la couche de mélange interne, et le mode 2 ("automatique") de la ZDES a démontré un comportement similaire au mode 1 ("manuel") dans les couches de mélange. Par ailleurs, la technique Random Flow Generation (RFG) mise en oeuvre afin de reproduire la turbulence amont existant au coeur des jets primaire et secondaire a permis d'accélérer la transition RANS-LES dans les deux couches de mélanges, plus conformément à l'expérience. La transition est d'autant plus rapide que le taux de turbulence est élevé et l'échelle de la turbulence injectée est petite. Le positionnement des cellules de choc est également amélioré, soulignant l'importance de prendre en compte la turbulence amont dans les simulations de jets.

Mots clés : jet, hybride RANS/LES, turbulence, couche de mélange, choc, transition

Subject : ZDES simulations of propulsive jets: Physical analysis and influence of upstream turbulence

Abstract : In this thesis, the ZDES method is assessed for the simulation of propulsive jets. This work focuses on the shock-cell positioning and the mixing layer development of a dual-stream nozzle configuration with an external plug, typical of modern aircraft engines. Reynolds averaged data are discussed in terms of mean and fluctuating quantities as well as in the frequency domain and compared with experimental data. First, the advantage of using a low dissipative spatial scheme as well as a subgrid length scale based on the local vorticity is demonstrated, especially for the development of the core mixing layer. Besides, the "automatic" mode of ZDES (mode 2) is found to provide similar mixing layers as the user defined mode. Then, the use of the Random Flow Generation (RFG) technique at the inlet boundaries of the core and fan channels in order to reproduce the turbulence rate at the center of the nozzle ducts is shown to accelerate the RANS-to-LES transition in both external and internal mixing layers, which is in better agreement with the experimental results. The transition length is further reduced when the injected turbulent ratio is higher, but also when the injected turbulent length scale is smaller. Of interest, the shock-cell positioning in the fan jet is also improved using RFG, which emphasizes the importance of accounting for upstream turbulence for this type of simulations.

Keywords : jet, hybrid RANS/LES, turbulence, mixing layer, chock, transition